

An investigation of nanoscale materials and their incorporation in patch antenna for high frequency applications

PhD Thesis

Ahmad Ali Bahar

Emerging Technologies Research Centre
Faculty of Technology
De Montfort University
England

1st Supervisor:

Richard Cross

This thesis is submitted in partial fulfillment of the
requirements for the Doctor of Philosophy.

July, 2019



And mankind have not been given of knowledge

Except a little. Quran surah Al Isra 85 (QS 17:85)

Abstract

The rapid development in the polymer-based electronic contribute a strong determination for using these materials as substitute to the high-cost materials commonly used as medium substrate in the fabrication of Microstrip Patch Antenna (MPA). Antenna technology can strongly gain from the utilisation of low-cost, flexible, light weight with suitable fabrication techniques.

The uniqueness of this work is the use of variety of common but unexplored different polymer materials such as Polyethylene (PE), Polypropylene (PP), Polyvinyl chloride, (PVC) Polystyrene (PS), Polystyrene fibre (PSF) as the substrates for the design and fabrication of different MPAs for communication and sensing applications in millimetre wave (MMW) region.

Electrospinning (ES) technique is used to reconstruct PS and produced PSF material of low dielectric constant. A co-solvent vehicle (comprising 50:50 ratio) of Dichloromethane (DCM) and acetone was utilised with processing condition of solution infusion flow-rate of $60\mu\text{L}/\text{min}$ and an applied voltage of $12\pm$ kV yielded rigid PSF substrates. The PSF Produced has complex permittivity of $1.36\pm 5\%$ and a loss tangent of $2.4\text{E}-04\pm 4.8\text{E}-04$ which was measured using Spilt-Post Dielectric Resonators (SPDR) technique at National Physics Laboratory, Teddington, London.

A diamond-shaped MPAs on RT Duriod material were simulated and fabricated using photo-lithography for different inner lengths to work in the frequencies range from (1-10 GHz). The resonant frequency is approximated as a function of inner length L_1 in the form of a polynomial equation. The fabricated diamond-shaped MPA more compact (physical geometry) as compared with a traditional monopole antenna. This MPAs experimentally measured and have a good agreement with the simulated results.

The coplanar waveguide (CPW) diamond-shaped MPA working in the MMW region was designed and fabricated with polymer materials as substrates using thermal evaporation technique and the RF measurement was carried out using Vector Network

Analyser (VNA). The resonant frequencies of the CPW diamond shaped MPAs for (PE, PP, PVC, PS and PSF) were found to be 67.5 GHz, 72.36 GHz, 62.41 GHz, 63.25 GHz and 80.58 GHz, respectively. The antenna fabricated on PSF were resonating at higher frequency when compared to the other polymers materials. In adding an air-bridge to the CPW diamond-shaped MPA the resonating frequency increased from ≈ 55 GHz to ≈ 62 GHz.

Three different shaped nano-patch antennas (Diamond shaped, diamond shaped array and T-shaped) have been designed, simulated and fabricated on Silicon substrate with DLC deposition using focused Ion Beam (FIB) technique, these antennas were found to resonate at 1.42 THz with (-19 dB return loss), 2.42 THz with (-14 dB return loss) and 1.3 THz with (-45 dB return loss) respectively.

Acknowledgement

My welfare is only in Allah. In Him I trust and unto Him, I turn. I would like to use this opportunity to express my appreciation to my supervisor Dr Richard Barrie Michael Cross for his support, advice, patience and encouragement during the period of this research. Furthermore, I would like to thank Prof Shashi Paul Head, Emerging Technology Research Centre (EMTERC), Paul Taylor, Principal Research Technician (EMTERC) for providing much needed materials, creating a vibrant study atmosphere and facilities. My appreciation also goes to Mark Cuckow, Senior Technician in Mechanical Engineering Laboratory for his assistance and help in many of the resources needed for this research. I would like to also thank Prof Zeeshan Ahmad and Dr Irina Ermolina for their unlimited support during my study. Moreover, I would like to thank Dr Mohamed Ismaeel Maricar from Nottingham University and Dr Scott Doak from Loughborough University for their unflinching support in some of the fabrication and measurements needed in this research. I cannot forget Dr Abdulaziz Alayed who without his help I would be unable to start or complete this research. Words cannot express how grateful I am to my parents for all their support and encouragement over the years. In addition, a special thanks to my family, I love you all unconditionally as your needs and welfare are my priority. Finally, I would like to express my appreciation to all my friends who have supported me during this period of my studies.

Declaration

I declare that this thesis which has been submitted as a requirement for a PhD degree in De Montfort University is completely my own work and all materials cited from other sources have been clearly identified and referenced. The work which is contained in the thesis has not been submitted in full or part for any other degree at De Montfort University...

Ahmad Bahar

Publications

- Design and characterization of a diamond-shaped monopole antenna *Maricar, M., Bahar, A., Greedy, S., Phang, S., Gradoni, G., Cross, R., Creagh, S., Tanner, G. and Thomas, D.* (2017). Design and characterization of a novel diamond shaped monopole antenna, Microwave and Optical Technology Letters (accepted: 13/6/17)
- Preliminary Design and Characterisation of a Novel T-shaped Nanoantenna on Diamon Like Carbon Material *Bahar, A. Maricar, M. I. and Cross, R. B. M.,* (2015). Preliminary Design and Characterisation of a Novel T-shaped Nanoantenna on Diamon Like Carbon Material, International Journal of Antennas, [Online]. Vol. 1 Iss.1, 77-84. Available at: <https://doi.org/10.6084/m9.figshare.6880364.v1>
- DSP Control of Smart Antennas *Mohamed Ismaeel Maricar, Ahmad Bahar, Yamini Raju, James Glover, Krishna Nama, Richard Cross* (2014). DSP Control of Smart Antennas. IEEE – International Conference on Advances in Engineering and Technology (ICAET 2014)
- Participated in De Montfort poster competition with A poster titled "A Novel Nanoantenna for Terahertz Frequency Application".

Abbreviations

2D	Two Dimension
3D	Three Dimensions
AC	Alternating Current
AF	Array Factor
AFM	Atomic Force Microscopy
AL	Aluminium
BW	Bandwidth
C-V	Current-Voltage
CPW	Coplanar waveguide
dB	Decibel
dB _i	Decibel-isotropic
DBS	Direct Broadcast Satellite
DC	Direct Current
DCM	Dichloromethane
DLC	Diamond Like Carbon
DSC	Differential Scanning Calorimetry
DTG	Differential Thermogram
DUT	Device Under Test
EBL	Electron-Beam Lithography
EBS _D	Electron Backscatter Diffraction
EDS	Energy Dispersive Spectroscopy
EFIE	Electric Field Integral Equation
EM	Electromagnetic waves
EMTERC	Emerging Technologies Research Centre
ES	Electrospinning
ESAs	Electrically Small Antennas

FCC	Federal Communication Commission
FCVA	Filtered Cathodic Vacuum Arc (FCVA)
FDTD	Finite Difference Time Domain
FEM	Finite Element Method
FIB	Focused Ion Beam
FTIR	Fourier Transform Infra-red Spectroscopy
GHz	Giga Hertz
GPS	Global Positioning System
GSM	Global System for Mobil
HPBW	Half Power Beam Width
ICPAS	Inductively Coupled Plasma Assisted Sputtering (ICPAS)
IEEE	Institute of Electrical and Electronics Engineers
IF	Intermediate Frequency bandwidth
LCP	Liquid Crystal Polymers
LDPE	Low-density polyethylene
LED	Light-Emitting Diode
LRL	Line-Reflect-Line
LRM	Line-Reflect-Match
LTE	Long Term Evolution
MEM	Micro-Electromechanical devices (MEMs)
MFP	Mean Free Path
MHz	Miga Hertz
MICs	Microwave Integrated Circuits
MMICs	Monolithic Microwave Integrated Circuits
MMW	Millimeter wave
MOM	Methods of Moments
MPA	Microstrip Patch Antenna
NSOM	Nearfield Scanning Optical Microscopy
PAN	Personal Area Networks
PDMS	polydimethylsiloxane
PE	Polyethylene
PECVD	Plasma-enhanced chemical vapor deposition
PET	Polyethylene terephthalate
PLD	Pulsed Laser Deposition (PLD)
PP	Polypropylene
PS	Polystyrene

PSF	Polystyrene Fibre
PVC	Polyvinyl chloride
PVD	Physical Vapour Deposition
Radar	Radio Detection and Ranging
RF	Radio Frequency
RFID	Radio Frequency Identification
RIE	Reactive-Ion Etching
RL	Return Loss
SEM	Scanning Electron Microscopy
SERS	Surface-Enhanced Raman Scattering
Si	Silicon
SOLR	Short-Open-Load-Reciprocal
SOLT	Short-Open-Load-Thru
SPDR	Split-Post Dielectric Resonators
SPP	Surface Plasmon Polariton
SSLR	Short-Short-Load-Reciprocal
SSLT	Short-Short-Load-Thru
SSSR	Short-Short-Short-Reciprocal
SSST	Short-Short-Short-Thru
SWR	Standing wave ratio
TDD	Time Division Duplexing
TEM	Transverse Electromagnetic
TGA	Thermal Gravimetric Analysis
TM	Transversal Magnetic Field Distribution
TRL	Transmission line-Reflect-Line
TRM	Transmission line-Reflect-Match
VNA	Vector Network Analyser
VSWR	Voltage Standing Wave Ratio
WiFi	Wireless Fidelity
WiMax	Worldwide Interoperability for Microwave Access
WLNA	Wireless Local Area Network

Glossary

symbol	Glossary
N_A	Avogadro's Number
zettabytes	10^{21}
f_c	Center Frequency
dB	Decibel
dB _i	Decibel-isotropic
ρ	Density
ϵ_r	Dielectric Constant Of Substrate
α_d	Dipole Polarisability
D	Directivity
r	Distance To Observation Point
ϵ_{reff}	Effective Dielectric Constant
e	Efficiency
J	Electric Current Density (A/m^2)
E	Electric Field Density (V/m)
Z_0	Free Space Impedance
λ_0	Free Space Wavelength
Δ	Frings Factor
G	Gain
h	High of Substrate
E	Incident electric field
V_o^-	Incident Voltage
a_i	Incident Wave
J	induced current
f_e	linear operator
Z_1	Load Impedance

f_l	Lower Frequency
M	Magnetic Current Density (V/m^2)
H	Magnetic Field Intensity (A/m)
ω_{max}	Maximum Frequency
M	Molar Mass Of The Material(Molecular Weight)
L_{eff}	Patch Effective Length
W	Patch Width
μ_0	Permeability Of Free Space
ϵ_0	Permittivity Of Free Space
α	Polarisability
Q	Quality Factor
Q_c	Quality Factor Due To Conduction Losses (ohmic)
Q_d	Quality Factor Due To Dielectric Losses
Q_{rad}	Quality Factor Due To Radiation (space Wave) Losses
Q_{sw}	Quality Factor Due To Surface Waves
P_{rec}	Receiving Power
P_r	Reflected Power
V_o^-	Reflected Voltage
b_i	Reflected Wave
Γ	Reflection Coefficient
τ	Relaxation Time
RC	Resistance-Capacitance
L	Resonance Length Direction
f_r	Resonant Frequency
RL	Return Loss In dB
S-parameters	Scattering Parameters
C	Speed of Light
h	Substrate Thickness
P_i	The Incident Power
ϵ	The Permittivity Of A Material
ϵ_o	The Permittivity Of Free Space
h	Thickness
P_r	Total power received by the antenna (watts)
P_t	Total Power transmitted by the antenna (watts Per Square Meter)
Q_t	Total Quality Factor
f_u	Upper Frequency

λ

Wavelength In The Dielectric Substrate

Contents

1	INTRODUCTION	23
1.1	Communication in The millimeter wave (sub-terahertz) and terahertz region	24
1.2	Important Outcomes of the Research	26
1.3	Thesis structure	27
2	ANTENNA BACKGROUND	28
2.1	History	28
2.2	Introduction	30
2.3	Antennas Parameters	32
2.3.1	Polarisation	32
2.3.2	Radiation Characteristics	34
2.3.3	Half Power Beam Width (HPBW)	36
2.3.4	Directivity	36
2.3.5	Antenna Gain	37
2.3.6	Voltage Standing Wave Ratio (VSWR)	38
2.3.7	Return Loss	38
2.3.8	S-Parameters	39
2.3.9	Bandwidth	40
2.3.10	Field Region	40
2.3.11	Dielectric Medium	41
2.4	Microstrip Patch Antennas (MPA)	42
2.4.1	MPA History	42
2.4.2	Advantages and Disadvantages	43
2.4.3	Types of MPAs	45
2.4.4	MPA structure	45
2.4.5	Applications	49

2.4.6	Basic principle of MPAs operation	51
2.4.7	Efficiency and Quality Factor of MPAs	52
2.4.8	Feeding Techniques	55
2.4.9	Methods of Analysis for Patch Antennas	60
2.5	Antenna Arrays	70
2.5.1	Simple Array Theory	70
2.6	Summary	72
3	POLYMERIC DIELECTRIC MATERIALS	73
3.1	Introduction	73
3.1.1	Background	73
3.1.2	Application of polymeric dielectric materials	75
3.2	Theory of dielectric properties in polymer	76
3.2.1	Mechanism of interaction with electric field	76
3.2.2	Effect of chain polarity	79
3.2.3	Effect of temperature	82
3.2.4	Effect of a cross-link between chains	83
3.3	Structure-properties relationship	87
3.3.1	Dielectric relaxation	87
3.3.2	Dielectric breakdown	90
3.4	Designing of polymer dielectric materials	92
3.4.1	Free volume	92
3.4.2	Copolymerisation	95
3.5	Summary	97
4	CLEANING, FABRICATION AND CHARACTERISATION	99
4.1	Plasma Cleaning	99
4.2	Thermal Evaporation	100
4.3	PLASMA – ENHANCED CHEMICAL VAPOUR DEPOSITION (PECVD)	101
4.4	Lithography	103
4.4.1	Photolithography	103
4.5	Electrospinning (ES)	104
4.6	Focused Ion Beam (FIB)	106
4.7	Profilometer	107
4.8	Scanning Electron Microscopy (SEM)	108
4.9	Fourier Transform Infra-red Spectroscopy (FTIR)	109
4.10	S-Parameter	110

4.11	Vector Network Analyser (VNA)	113
4.11.1	Networks measuring using VNA	114
4.12	Non-Contact THz Probe Measurement	122
4.12.1	Analysis Of The Non-Contact THz Probe	123
4.12.2	Calibration Of Non-Contact Probes	123
4.13	Thermal Gravimetric Analysis (TGA)	125
4.14	Differential Scanning Calorimetry (DSC)	126
4.15	C-V measurements	127
4.16	Dielectric Measurements	128
4.17	Summary	137
5	POLYMER CHARACTERISATION	138
5.1	Introduction	138
5.2	Optimisation of Polystyrene fibre(PSF) Deposition Using Electrospinning	139
5.2.1	Electrospinning and Polymer Layer Optimisation	139
5.3	Characterisation of polymer materials	145
5.3.1	Fourier Transform Infra-Red Spectroscopy (FTIR)	145
5.3.2	Thermogravimetric Analysis (TGA)	148
5.3.3	Differential Scanning Calorimetry (DSC)	152
5.4	Broadband dielectric spectroscopy (BDS)	155
5.4.1	Split-Post Dielectric Resonator (SPDR)	158
5.5	Summary	160
6	DESIGN AND CHARACTERISATION OF POLYMERS PATCH ANTENNAS AND DLC NANO-PATCH ANTENNAS	161
6.1	Design And Characterisation Of A Diamond-Shaped Monopole Patch Antenna	161
6.1.1	Introduction	161
6.1.2	Design Of A Diamond-Shaped Monopole Antenna	163
6.1.3	Simulation Results Of A Diamond Shaped MPA and Fabrication	164
6.1.4	Experimental Results Of A Diamond shaped MPA	166
6.2	Coplanar Waveguide (CPW) Diamond Shaped MPAs	167
6.2.1	Fabrication process of a CPW Diamond shaped antennas	172
6.2.2	Experimental Results of a CPW Diamond shaped antennas	172
6.3	Design And Simulation Of Nano-Patch Antennas On Diamond-Like Carbon Substrate	176
6.3.1	Design and simulation of a diamond shaped nano-patch antenna	177

6.3.2	Design and simulation of a diamond shaped nano-patch antenna array	179
6.3.3	Design and simulation of T-Shaped nano-patch antennas	179
6.3.4	Fabrication process for nano-patch antennas	180
6.3.5	DLC Measurements	183
6.3.6	Thickness	183
6.3.7	C-V measurements	184
6.3.8	RF measurements of the nano-patch antennas	185
6.4	Conclusion	185
7	CONCLUSION AND FUTURE WORK	187
7.1	Conclusion	187
7.2	Future Work	188

List of Figures

1.1	Electromagnetic spectrum demonstrating the millimeter wave and terahertz region[2]	24
1.2	Millimeter-wave and terahertz networks for personal area networks (a) and wireless backhauls (b)[2]	25
2.1	History of wireless systems	30
2.2	Hertz's Experiment[20]	30
2.3	Three types of Polarisation	33
2.4	Polar radiation pattern (2D)[41]	34
2.5	Radiation pattern (3D)[41]	35
2.6	3dB Beam Width[43]	36
2.7	Bandwidth[42]	41
2.8	Primary conformal array fed with microstrip transmission line which has been designed by Deschamps [52].	43
2.9	Well known types of MPA	45
2.10	Micro-strip antenna structure	46
2.11	Cross section of a patch antenna in its basic form[77]	51
2.12	Geometry of antenna equivalent cavity[78]	53
2.13	Microstrip Line Feed[29]	56
2.14	Coaxial Feed[79]	56
2.15	Aperture Coupled Feed[29]	58
2.16	Proximity Coupled Feed[79]	58
2.17	Equivalent Circuit of Feed Techniques[29][79]	59
2.18	Microstrip line[29]	60
2.19	Electric field lines[29]	60
2.20	Transmission line model for patch antenna[29]	61
2.21	Planar transmission lines (a) Microstrip (b) Parallel Plate line (c) Slotline (d) coplanar waveguide[29]	63

2.22 Coplanar waveguide[29]	64
2.23 Charge distribution and current density creation on MPA[38][79]	65
2.24 Antenna Array[40]	70
3.1 Application of dielectric polymers in IC packaging	76
3.2 PTFE (a) and PVC (b) with arrow showing the net dipole moment[98]	80
3.3 Dielectric constant and loss dispersion of dielectric materials against frequency[98]	80
3.4 Schematic dielectric loss curve for polymer as temperature is increased[98]	83
3.5 Affect of crosslink network on rigidity of polymer chains[98]	84
3.6 Effect of degree of reaction on the α and β relaxation time of DGEBA-DETA system[98]	84
3.7 (a) Effect of cross-link density on dielectric constant (ϵ' above) (b) dielectric loss (ϵ'' below) for DGEBA-DETA system[98]	85
3.8 Repeat unit of the polyimide[111]	85
3.9 (a) Adamantane structure incorporated into polyimide chain[115] (b) the generic structure for polynorbonene[98]	87
3.10 Debye dielectric dispersion curve[115]	88
3.11 Cole-Cole Plot showing the relationship between dielectric constant and dielectric loss[98]	89
3.12 Plot of (a) dielectric constant and (b) dielectric loss with the change in frequency and temperature for polyvinylchloride[121].	90
3.13 Triblock polyimide structure illustrating the thermally labile and stable segments[98]	93
3.14 Relation between the dielectric constant with the void fractional volume in PMDA/3FDA/PPO triblock system [125]	93
3.15 Preparation of porous Polyimide using sol-gel method[98]	94
3.16 SEM scan of fracture surface of pure (a) PI/SiO ₂ 10% (b) and PI/SiO ₂ 20% porosity (c)[98]	95
3.17 Series of PI-polysiloxane copolymers[126]	96
4.1 Internal structure of thermal evaporator	100
4.2 The block diagram of Plasma – Enhanced Chemical Vapour Deposition[129]	102
4.3 Electrospinning set-up	105
4.4 Focused Ion Beam set-up	106
4.5 Scanning Electron Microscope (SEM)	108
4.6 FTIR spectrometer set up[144]	110

4.7	Block Diagram of S-Parameters[147]	111
4.8	A schematic block diagram of a Vector Network Analyser (VNA)	113
4.9	Vector Network Analyser (VNA)	114
4.10	S-Parameter measurement setup using Agilent E8364B VNA up to 110GHz	115
4.11	Two S-parameter measurement setup using Agilent VNA up to 325GHz	115
4.12	Schematic view of the SOL calibration substrate	117
4.13	set-up of the VNA with the antenna	117
4.14	One port calibration Smith chart	118
4.15	Schematic view of the SLOT calibration substrate[147]	119
4.16	Block diagram of two-port network calibration	119
4.17	Two port calibration Smith chart[147]	119
4.18	Alignment marker on the wafer	120
4.19	Illustration of Non Contact Probes Set-up[158]	122
4.20	Radiation Patterns of Thru Connected Non-Contact Probes[158]	124
4.21	Scattering for different terminations of non-contact probes[158]	125
4.22	Thermal Gravimetric Analysis block diagram[163]	126
4.23	Schematic set up of differential scanning calorimetry	127
4.24	CV measurements set-up	128
4.25	Different dielectric measurements methods[167]	129
4.26	A Split-Post Dielectric Resonator (SPDR) cell for dielectric measurements[169]	132
4.27	10 GHz resonator	134
4.28	SPDR measurements process	135
4.29	Schematic diagram of Broadband dielectric/Impedance Alpha-A-analyser	136
5.1	PSF produced with 4% PS concentration using DCM solvent only at 50 $\mu\text{l}/\text{min}$ (14.6 ± 2)kV	140
5.2	Polystyrene fibre produced with 4% PS concentration using DCM solvent only at 60 $\mu\text{l}/\text{min}$ (14.6 ± 2)kV	141
5.3	PSF produced with 3% PS concentration using DCM solvent only at 60 $\mu\text{l}/\text{min}$ (14.6 ± 2)kV	141
5.4	PSF produced with 3% PS concentration using DCM and Acetone (1:1) at 60 $\mu\text{l}/\text{min}$ (14.6 ± 2)kV	142
5.5	Polystyrene fibre produced with 5% PS concentration using DCM and Acetone (1:1) at 60 $\mu\text{l}/\text{min}$ (14.6 ± 2)kV	142
5.6	PSF produced with 7% PS concentration using DCM and Acetone (1:1) at 60 $\mu\text{l}/\text{min}$ (14.6 ± 2)kV	143

5.7	PSF produced with 6% PS concentration using DCM and Acetone (1:1) at 60 $\mu\text{l}/\text{min}$ (14.6 ± 2)kV	143
5.8	SEM image of PSF produced from PS with 6% PS concentration using DCM and Acetone (1:1) at 60 $\mu\text{l}/\text{min}$ (14.6 ± 2)kV after heating	144
5.9	FTIR for different polymer materials	147
5.10	Thermogram curve Analysis	148
5.11	Derivative of weight change for different polymers materials	151
5.12	DSC for different polymer materials	154
5.13	Different polymer Broadband dielectric spectroscopy	157
6.1	Diamond shaped monopole antenna	163
6.2	Simulated resonant frequency of a diamond-shaped MPAs for different inner length L_1 and by fixed sectorial angle	164
6.3	Diamond shaped monopole antenna fabrication Process	165
6.4	Fabricated diamond shaped antennas	165
6.5	Comparison of the resonant frequency of Diamond shaped and monopole antennas as a function of inner length L_1 (simulation and measurements)	166
6.6	Comparison of the bandwidth of diamond-shaped MPAs and monopole antennas for different length	167
6.7	Diamond Shaped antenna with and without air-bridge	168
6.8	Diamond Shaped antenna with and without air-bridge	169
6.9	Schematic of a CPW Diamond Shaped MPA	169
6.10	Simulation results for different polymers materials (single MPA antennas)	170
6.11	Schematic of a CPW Diamond Shaped MPAs	171
6.12	Simulation results for different polymers materials (MPA array)	171
6.13	High-frequency Diamond shaped antennas fabrication Process	172
6.14	Fabricated CPW Diamond Shaped MPAs using different polymers substrates	173
6.15	Fabricated high-frequency Diamond Shaped MPAs arrays using different polymers substrates	174
6.16	Measurements and simulation results of a diamond-shaped MPA fabricated on a PVC	175
6.17	Measurements and simulation results of a diamond-shaped MPA fabricated on a PSF	175
6.18	Diamond shaped nano-patch antenna	178

6.19 FIB fabricated diamond shaped nano-patch antenna on DLC with Si substrate	178
6.20 Diamond shaped nano-patch antenna array	179
6.21 FIB fabricated diamond shaped nano-patch antenna arrays on DLC with Si substrate	180
6.22 Schematic view of the T-shaped nano-patch antennas	181
6.23 Return loss, gain and directivity of the T-shaped nano-patch antennas . . .	181
6.24 Front view of 3D directivity pattern	182
6.25 FIB fabrication	182
6.26 Cross section on copper on DLC	183
6.27 Fabricated t-shaped nano-patch antenna	183
6.28 Thickness measurements for Al and DLC layers	184
6.29 Capacitance of DLC materials	184

List of Tables

2.1	Advantages and disadvantages for MPAs [29][35][38][54]	44
2.2	Six categories of dielectric materials used for patch antennas[51][66][67] .	48
2.3	Comparison between the different feed techniques used for MPA[81] . . .	59
3.1	Dielectric constant of different polymers and inorganic materials [99][98]	74
3.2	The effect of Fluorine content on the dielectric constant of a polyimide[98]	86
3.3	Dielectric parameters for some polymers at various frequencies[98]	91
3.4	Dielectric constant of a series of polyimides at varying TEOS content[98]	94
3.5	Effect of silicone content in silicon-polyimide copolymers on dielectric constant[126]	97
4.1	Different kinds of calibration techniques[147][151][152][153][154][155][156]	121
4.2	Different dielectric measurements methods[167][168]	131
5.1	Parameters for polystyrene fibre optimisation	140
5.2	Thermal decomposition of polymer materials	149
5.3	SPDR- comparison of some selected polymer materials	158
6.1	Dielectric parameters for different polymers at various frequencies	170
6.2	Simulation frequency VS Measured frequency for different polymers ma- terials	176
6.3	PECVD deposition parameters for growth of DLC	183

Chapter 1

INTRODUCTION

There has been an enormous increase in recent years in the usage of personal electronic systems, with growth in smart phone and tablet usage increasing by 79% and 104% respectively [1]. This has inevitably led to a drastic increase in the levels of data being transmitted around the globe. In 2017, 1.4 zettabytes of data have been shared across the world[2]. Around 3.6 billions of people connect to the internet every day, with the number of connections having increased to 19 billion compared to 12 billion in 2016)[1].

All these factors have led to huge increases in connectivity and data sharing. Nevertheless, increasing data rates beyond current limits could have negative effects on energy efficiency due to bandwidth limitations. However, on the optical spectrum, data rates up to 20 Gbps have been illustrated[3]. Nonetheless, their performance is in general affected by the huge laser power as well as the devices sensitivity to the temperature. The present wireless such as 4G LTE (30 Mbps for uplink and 100 Mbps for peak data rate) as well as LTE-Advanced (500 Mbps – uplink and peak data rate of 1 Gbps for download link) are standard supporting data rates for smart phones[4][5]. Therefore, the growth in data transfer expected in the future necessitates high bandwidth devices for high communication system connections[6]. The millimetre wave (sub-terahertz) and terahertz region of spectrum offers potential to accomplish this goal due to the availability of many gigahertz of spectrum in the this band (figure (1.1)).

The millimeter wave band spectrum is defined from 30 GHz to 300 GHz (corresponding to wavelengths between 1 cm to 1 mm), with the terahertz band spectrum is between 300 GHz to 3 THz (corresponding to wavelengths from 1mm to 0.1mm) [2]. Most of the electronic devices are operating in the low frequencies band of this spectrum (Radio and Microwave) and their performance reduces as their cut-off fre-

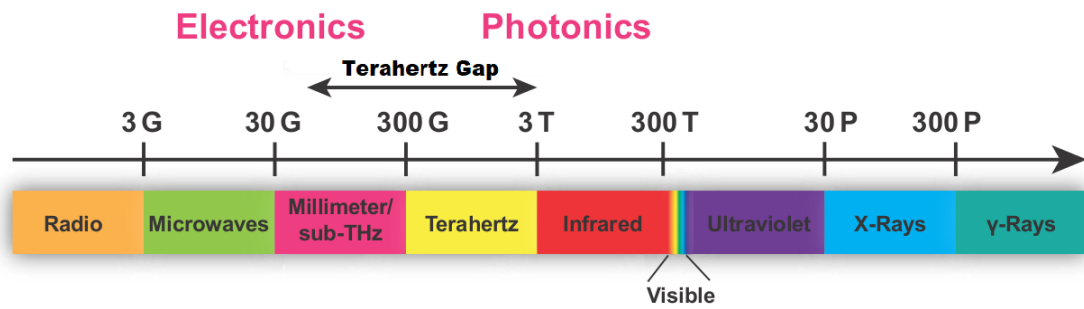


Figure 1.1: Electromagnetic spectrum demonstrating the millimeter wave and terahertz region[2]

quencies are approached. An important region of the electromagnetic spectrum that has been the focus of recent research starts from 50 GHz to 3 THz, which is well-known as the terahertz gap. Investigations have focused on a number of different frequencies within this band including the 60 GHz band for high data rate communication in both indoor and outdoor networks and 94 GHz, 140 GHz and 220 GHz for imaging applications[7]. Molecular spectroscopy or terahertz chemical imaging is another rising field of application where specific substances can be detected depending on their high degree of absorption at these particular frequencies. This can be utilised to discover harmful gases e.g carbon monoxide (which is responding at 230 GHz) or phosphine (which is responding at 266 GHz) [8].

1.1 Communication in The millimeter wave (sub-terahertz) and terahertz region

In the V-band (50-75 GHz), 60 GHz is famous for commercial products and there are availability of unlicensed band spectrum between 57 and 64 GHz. [9]. This gives opportunity to utilise very high data rate communications in different applications including media sharing in Personal Area Networks (PANs) and wireless backhails as shown in figure (1.2). The WiGig standard (IEEE 802.11ad)[10], which is a section of the Wi-Fi alliance which is a non-profit organisation that certifies Wi-Fi products. This organisation grants the entire band to be utilised in Time Division Duplexing (TDD) mode which is facilitates high data rates and can be used for high-definition video streaming and files transfer. Currently, technology with the 802.11ac Wireless LAN standard supports a maximum of 2.5 Gbps with three 160 MHz channels. On the contrary, 60 GHz has the ability to provide throughputs of up to 10 Gbps with higher effi-

ciencies. Moreover, the V-band can be utilised for supporting backhaul networks[11].

The millimeter wave link system is basically for short-to medium-range broadband wireless data transmission[12]. They are expected to manage a major part of data transfer with the average backhaul data rate scaling up to 1 Gbits/cell in the next five years[5]. This could work towards targets of the Federal Communication Commission (FCC) with aim being to achieve maximum transmission power of 82 dBm with antenna gain of 51 dBi for outdoor communication applications over a mile in term of distance [5]. In this regard, it is the planar antenna structure that is most often utilised for such applications due to their low-cost fabrication and ability to (currently) scale their dimensions; this consequently allows for them to be operated in the millimetre waves range. Whilst the V-band is suitable for high speed applications, the terahertz



Figure 1.2: Millimeter-wave and terahertz networks for personal area networks (a) and wireless backhauls (b)[2]

regime offers even higher data rates. Smart phones and tablets integrate many wireless antennas (Bluetooth, GPS, 4G LTE and so on) and signal processing units (CPU, multi-standard baseband and graphics) on one single board. The high density combination of these devices in physical size and shape is becoming a significant problem from integration prospective[13]. One potential solution would be to employ short-range wireless communication systems which can complement or replace wires buses, as a result of that extra space can be utilised for different features such as high capacity battery[14].

The rapid developments in the polymer based electronic contribute a strong determination for using these materials as substitutes to the high cost materials in terms of design and fabrication of the Antenna. Antenna technology can strongly gain from the utilisation of low-cost, flexible, light-weight with suitable fabrication techniques[15].

In using polymer-based materials, antenna of small size, mechanical ruggedness, light weight and physical comfort in terms of flexibility can be design with omni-directional radiation pattern, wide bandwidth and stable gain[16][17][18]. Inclusion of an antenna into the flexible electronics, make such electronic systems received a huge attention recently due to their different applications which include flexible displays, wearable products and smart tags[17]. Such antenna must be flexible or stretchable and it requires flexible substrates of low permittivity which makes polymer materials falls into these categories. Polymers such as Liquid Crystal Polymers (LCP), Polyetherimide (PEI) or Polyethylene terephthalate (PET)) and polydimethylsiloxane (PDMS) are among widely accepted substrates for microwave system[17][19].

The uniqueness of this work is to use variety of common but unexplored different polymer materials such as polyethylene (PE), polypropylene (PP), polyvinyl chloride (PVC), polystyrene (PS) and polystyrene fibre (PSF) as the substrates for the design and fabrication of different Micro-strip Patch Antenna (MPA) for communication and sensing applications in millimetre wave region. These substrates of low cost, possess low permittivity and can be easily fabricate in case if need arise for such. For terahertz region, nano-antennas of different shapes are going to be fabricated using different polymer substrates and a proposed RF testing method for the devices.

1.2 Important Outcomes of the Research

- Investigation, characterisation and assessment of different polymer materials (PE, PP, PVC, PS and PSF) as dielectric substrates for their suitability to be utilised as dielectric medium substrates for different patch antennas working in millimetre wave frequency.
- Fabrication and optimisation of PSF as this polymer material is not available in the market. The fabrication and optimisation is done with 6% PS concentration using DCM and acetone solvent only at ratio 1:1, (a solution infusion flow-rate of $60\mu\text{l}/\text{min}$), $(12.6\pm 2)\text{kv}$ using electrospinning technique.
- The successful design, fabrication and characterisation of different MPAs working in MMW frequency using different polymer materials as a dielectric medium.
- Proposed design of a nano-patch antenna working in Terahertz frequency using DLC material as a dielectric medium. This data will be presented in chapter (6).

1.3 Thesis structure

Chapter 1: Introduction The chapter provides information about the nature of the research, a summary of important outcomes and thesis structure.

Chapter 2: Antenna Background Covers and explains antenna fundamentals, fundamentals of MPA and their applications.

Chapter 3: Polymeric Dielectric Materials The chapter gives a background for polymeric dielectric materials, their applications and relevance to this work.

Chapter 4: Fabrication And Characterisation Techniques The chapter gives an overview of the device fabrication techniques and characterisation methods employed in this research.

Chapter 5: Polymer Characterisation This chapter details the synthesis and optimisation of the polymeric materials using electrospinning methods. These include PE, PP, PVC, PS and PSF; their characterisation and an analysis of their suitability as a dielectric medium for MPA.

Chapter 6: Design And Characterisation Of Polymers Patch Antennas And DLC Nano-Patch Antennas The chapter covers the design, simulation, fabrication and investigation of different diamond-shaped antennas which have been fabricated using polymer substrates with resonant frequencies ranging from 4.5 GHz to 110 GHz. Also, it covers the design, simulation and fabrication of a diamond shaped nano-patch antennas and a novel T-shaped nano-patch antenna fabricated using DLC as dielectric medium which working in the terahertz band.

Chapter 7: Conclusions and future work This chapter describes the main findings of the work, the limitations encountered and suggested future avenues of investigation.

F

Chapter 2

ANTENNA BACKGROUND

2.1 History

The origin for the development of wireless systems can be traced back to two European scientists in particular, James Clerk Maxwell (1831-1879) and Heinrich Rudolf Hertz (1857–1894). In 1864, Maxwell derived equations by integrating the works of Gauss, Ampere, Faraday and Lorentz. He postulated that electromagnetic waves propagate at the speed of light in free space and assumed that light is an electromagnetic physical phenomena of a specific wavelength; and that different types of radiation could be correlated with different wavelengths. His theoretical work was first explored experimentally later by Hertz who created a system illustrated in figure 2.2 to initiate and receive radio waves; the main objective being to demonstrate the existence of electromagnetic waves.

The transmitter consisted of a variable voltage source attached to a dipole ended with two conducting spheres. The space between the two spheres was adjustable for circuit resonance in order to generate sparks. Consequently, when voltage was accumulated to a certain amount, a spark was generated. The receiver consisted of a simple wire loop ended with two conducting spheres whose separation could again be modified. The space between the spheres was painstakingly adjusted in order to effectively received the spark. This was placed in a darkened box so as clearly view the sparks. As the spark was generated at the transmitter so also at the same time the spark was observed at the receiver. This demonstrated that the information from location A was transmitted to location B in a wireless mode.

Hertz validated radio frequency (RF) production, propagation and reception in the laboratory. In fact, the information used in this research was really in binary form,

which is represented by tuning the spark either on or off. This can be considered as a first digital wireless system[20]. For this research work, Hertz is known as the father of radio and the frequency unit (Hz) in International standard (SI) is named after him [20][21].

Hertz's work stayed as a laboratory activity without any practical applications for almost two decades, when a young Italian inventor, Guglielmo Marconi (1874–1937), developed and commercialised a method for a wireless communication system using electromagnetic waves to transfer information from one continent to another; he did this by introducing the radiotelegraph system.

The most well-known experiment that he conducted was in 1901, when he validated transatlantic communication from Poldhu in UK to St Johns, Newfoundland in Canada, utilising untuned systems. In 1909, he shared with Karl Ferdinand Braun the Nobel prize for physics for their contributions and efforts to develop the telegraphy wireless system. Monopole antennas (vertical and almost quarter-wavelength) which were commonly utilised in Marconi's experiments; are named Marconi antennas. [21][20]

In 1920s Detroit, police cars were first equipped with a one-way broadcasting system[22]. Subsequently, the use of wireless broadcasting systems was improved and allowed for the communications between mobile and fixed stations. Therefore, these systems was exceptionally increased in public applications including land transportations, maritime services and public safety systems and so on[22][23].

During World War II, wireless systems became essential for military and army unit manoeuvres with early detection of enemy combatants playing a vital role. For this reason, American and British scientists developed radar technology (Radio Detection And Ranging)[24]. As the resolution of these systems were proportional to wavelength, higher frequencies - i.e. microwave frequencies and higher - were needed to discover small targets such as military aircraft at distance.

After the war, relay systems and tropospheric scattering were used for long distance telecommunication communications systems. In 1955, John R. Pierce and Rudolf Kompfner visualized overseas communications by satellites and this was the cornerstone for the development of global satellite communications[25][26]. Satellite systems have operating frequencies in gigahertz use broadband high-frequency systems which can support many data links, hundreds of TV channels and thousands of telephone calls simultaneously[27].

In the present time, mobile phone technology with the aid of wireless communication system provides all-in-one services including calling, messaging and data service.

Other applications related to wireless communication services include global positioning systems (GPS), remote sensing, Radio Frequency Identification (RFID) systems and surveillance systems[28]. Figure (2.1) summarises the history of these wireless systems.

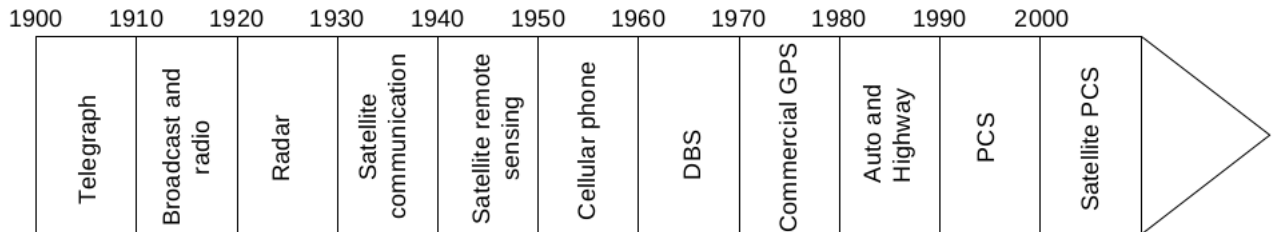


Figure 2.1: History of wireless systems

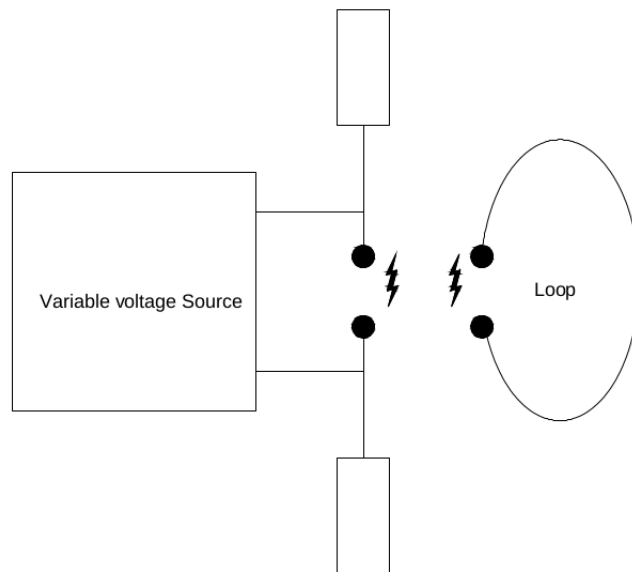


Figure 2.2: Hertz's Experiment[20]

2.2 Introduction

An antenna is the fundamental component of all the wireless system[20][29][30][31][32][33][34][35]. It is a device which is utilised to radiate and receive an electromagnetic wave in

space[38]. Each type of antenna is designed to work in a specific frequency, any others than the operating band will be rejected. Therefore, an antenna can be considered as a combination of a transducer and a band pass filter. Antennas can be classified into nine forms which are[39]

1. Wire Antennas(e.g. loops and dipoles).
2. Active Integrated Antennas.
3. Antenna Arrays(considering smart antennas).
4. Dielectric Antennas.
5. MPA.
6. Lens Antennas(sphere).
7. Aperture Antennas (e.g. pyramidal horns).
8. Reflector Antennas (e.g. parabolic dish antennas).
9. Leaky wave antennas.

The first form of antenna ever used was the dipole antenna, also it is the simplest type of antenna to interpret. It is formed from straight wire fed from the centre. The length of the dipole antenna should be half the wavelength of the operating frequency. An example for a dipole antenna is to use 0.5 meter antenna for a frequency of 300 MHz which has 1 meter wavelength[40].

In order to understand the working mechanism of an antenna, it should be considered as it was enclosed by surface volume and radiates in free space (homogeneous space) also it can be replaced by equivalent of electric current density (J) and magnetic current density (M) of an electromagnetic source[40]

$$J = \vec{n} \times H \quad (2.1)$$

$$M = -\vec{n} \times H \quad (2.2)$$

where,

H = Magnetic field intensity (A/m).

E = Electric field density (V/m).

$$E_{\theta} = \sqrt{\frac{\mu_0}{\epsilon_0}} H_{\phi} \quad (2.3)$$

$$H_{\phi} = \sqrt{\frac{\epsilon_0}{\mu_0}} E_{\theta} \quad (2.4)$$

$$Z_0 = \frac{\epsilon_0}{\mu_0} \quad \text{free space impedance.} \quad (2.5)$$

where,

ϵ_0 is the permittivity of free space.

μ_0 is the permeability of free space.

r = distance to observation point.

$$S = E * H = k_0^2 \sqrt{\frac{\epsilon_0}{\mu_0}} \frac{Idz \sin^2\theta}{16\pi^2 r^2} \vec{r} \quad (2.6)$$

Isotropic antennas are used to measure the designed antennas and it is usually radiates equally in every direction in space. This antenna is considered as a radiation reference for other antennas. The parameters [which will be discussed later in this chapter] of an antenna is measured with reference to this isotropic radiator and are rated in decibels with respect to an isotropic radiator (dB)[39].These parameters are necessary to perform design and analysis of any antennas.

2.3 Antennas Parameters

Each antenna has its own set of parameters which distinguish it from other types of antennas. These parameters describe the performance of an antenna, which can then help to highlight its relative suitability for particular applications. Some of these properties are interconnected. Therefore, for a complete description of antenna performance, not all properties need to be detailed. Consequently, a description for the relevant antenna parameters for this work will be explained below.

2.3.1 Polarisation

Polarisation can be defined as the direction of wave propagated (radiated) by the antenna. It is a characteristic of an electromagnetic wave which describes the time changing direction and magnitude of the electric field vector. There are three types of polarisation which are shown on figure (2.3)

1. Linear Polarisation
2. Circular Polarisation
3. Elliptical Polarisation

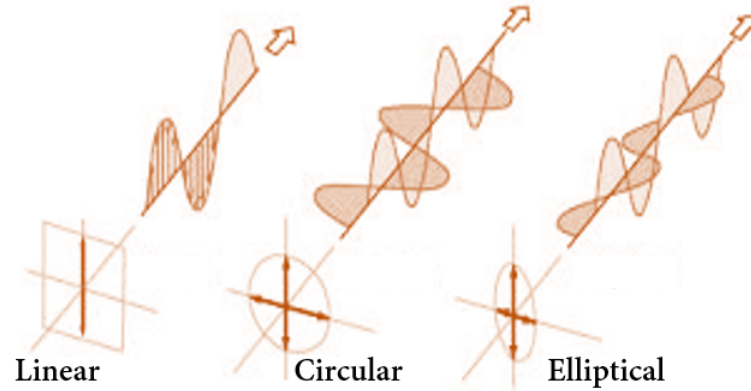


Figure 2.3: Three types of Polarisation

Figure (2.3) illustrates the polarisation and orientation of the electric field vector component. When transmitting and receiving a signal in line-of-sight communication, the polarisation should be the same (horizontal, vertical or circular), while in non-line-of-sight communication the wave changes indiscriminately since the received signal can go through multiple reflections.

The polarisation has been expressed by Maxwell's Equations:

$$\nabla \times E = -j\omega\mu H \quad (2.7)$$

$$\nabla \times E = (\sigma + j\omega\epsilon)E \quad (2.8)$$

$$\nabla \cdot E = \frac{\rho}{\epsilon} \quad (2.9)$$

$$\nabla \cdot H = 0 \quad (2.10)$$

Famous solution of these equations is as following[20][29][31][32][34][37]

$$\nabla^2 E - \gamma^2 E = \nabla(\rho/\epsilon) \quad (2.11)$$

While in free space ($\rho = 0$)

$$\nabla^2 E - \gamma^2 E = 0 \quad (2.12)$$

$$E = E_0 e^{j\omega t + \gamma z} \hat{X} \quad (2.13)$$

$$E = E_0 e^{j\omega t + \gamma z} \hat{Y} \quad (2.14)$$

$$E = E_0 e^{j\omega t + \gamma z} \hat{Z} \quad (2.15)$$

2.3.2 Radiation Characteristics

The radiation characteristics also known as radiation patterns, antenna patterns or far field patterns are defined as by either graphical illustration or mathematical relation, which describe the antennas' radiation properties as a function of space coordinates[29]. Radiation characteristics include field strength, power flux density, radiation intensity and polarisation or directivity phase. Radiation characteristics give information that explains how an antenna directs the energy it emits and it is observed in the far field region. The radiation characteristics can be illustrated in 2D as a form of a polar plot for vertical and horizontal (azimuth) as shown in figure (2.4) or can be illustrated in 3D as shown in figure (2.5)[41].

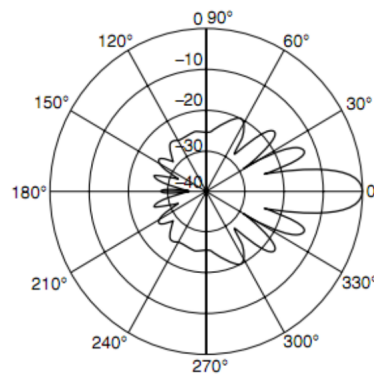


Figure 2.4: Polar radiation pattern (2D)[41]

The Radiation characteristics consist of the following:

1. Main lobes

The main lobe is the radiation of the major lobe which represents the path of the maximum radiation.

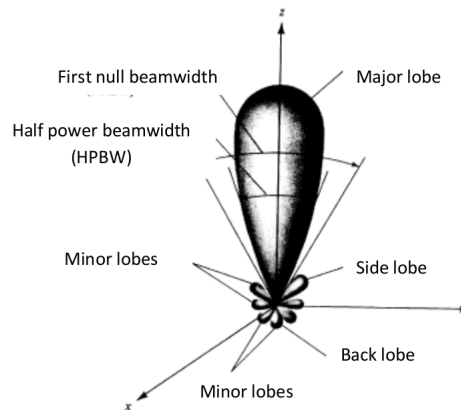


Figure 2.5: Radiation pattern (3D)[41]

2. Side lobes

The side lobes are the minors lobes which surrounding the main lobe. In an ideal situation, there are no side lobes for a perfect antenna. Furthermore, the existence of the side lobes causes electromagnetic interference which is undesirable in the receiving antenna system.

3. Back Lobes

The back lobe is a minor lobe which is in the opposite direction to the main lobe.

Antennas can be classified in three types of radiations patterns:

1. Omnidirectional Antennas

Omnidirectional antenna is an antenna which has uniform radiation patterns and they are equally propagating in one plane usually the horizontal plane. Many applications such as cellular phones, cordless phones, wireless computer network, GPS and FM radios needed antennas that can emitting evenly in a plane. The radiation patterns of omnidirectional antenna's have the doughnut shaped. Examples of omnidirectional antennas includes discone antenna, dipole antenna and slot antenna[42].

2. Directional Antennas

Directional Antennas also known as beam antennas are antennas which focused their radiations in a specific direction. They are used in point to point communication such as satellite communications or can be used in base station antenna for transmitting energy for a special purpose or sector[42].

3. Isotropic Antenna

An Isotropic antenna is an antenna which radiates all the feed power equally in all the directions. It is an imaginary antenna which is practically not available. It is used as a reference for all others antennas[42].

2.3.3 Half Power Beam Width (HPBW)

Half Power Beam Width (HPBW) is the angle in which the radiation drops 3dB (one half of it's maximum). The 3dB beam width is shown in figure (2.6). The antenna's beam width is a figure of merit in antenna performance and there is usually a trade-off between it and the side lobe level. The gain of the antenna can also be manipulated by controlling the beam width i.e. the gain can be increased by narrowing the beam width[39].

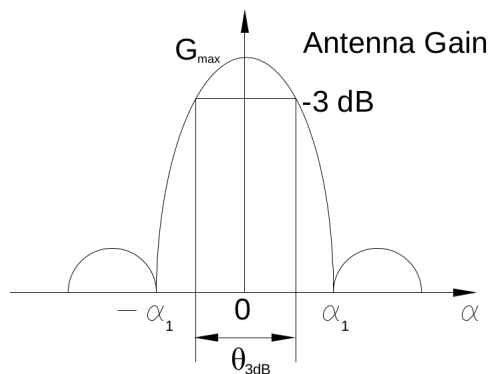


Figure 2.6: 3dB Beam Width[43]

2.3.4 Directivity

Directivity is the capability of an antenna for focusing energy in a specific direction. It is an essential demand if the antenna is functioning as a receiver. According to IEEE standard 145-1983 the definition of the directivity “is the ratio of the radiation intensity in a given direction from the antenna to the radiation intensity averaged over all directions”. In fact, radiation intensity is equal to the entire power emitted by the antenna divided by 4π [29][35][36].

The directivity of an antenna is equal 1 if the antenna emits equally in every direction, or equal 0dB if it is measured with respect to isotropic antenna. Directivity can

be represented by an easy form which is the ratio of maximum radiation intensity to average radiation intensity as follows[42]:

$$Directivity = \frac{\text{maximum radiation intensity}}{\text{average radiation intensity}} \quad (2.16)$$

2.3.5 Antenna Gain

The antenna gain which is also known as power gain or plainly gain is defined (with respect to IEEE Std 145-1983) “as the ratio of the radiation intensity, in a given direction to the radiation intensity that would be obtained if the power accepted by the antenna were radiated isotropically” [36]. Antenna gain (unit dB) is a measure of efficiency and the directivity characteristics of an antenna.

The gain for a transmitting antenna represents the efficient ability of an antenna in order to emit the input power into space in a specific path. On the other hand, for receiving antenna it states the performance of antenna in converting the received electromagnetic waves to electrical power.

The efficiency (e) is considered in the gain and this is what it makes it differ from the directivity. Furthermore, the antennas’ gain can be explained as how far the signal can travel. The gain is proportional with propagated wave’s area (not with the power) [38]. The gain can be obtained from the directivity if the efficiency is known (the gain and the directivity of an antenna will have the same value if the efficiency of the antenna is 100%).

$$G = eD \quad (2.17)$$

If the directivity with a specific direction is presented, then it is called directive Gain.

$$Directive G(\Theta, \pi) = eD(\Theta, \pi) \quad (2.18)$$

There are two different antennas which can be used as a reference to the antenna gain; the first is the isotropic antenna in which the gain is measured in dB and the second is the half wave dipole antenna in which the gain is measured in dB. Gain can be calculated by the following equation[38][44]:

$$G = \frac{p_t}{p_r} / 4\pi r^2 \quad (2.19)$$

where,

P_t is the total power transmitted by the antenna (watts per square meter).

P_r is the total power received by the antenna (watts).

It should be noted that the microstrip antenna directivity is directly proportional with substrate thickness (h) and patch width (W). Conversely the beamwidth is inversely proportional with h & W [35].

2.3.6 Voltage Standing Wave Ratio (VSWR)

Voltage Standing Wave Ratio (VSWR) is the ratio of the amplitude voltage at antinode (maximum) to the amplitude at the next node (minimum) on the feeding line on the antenna[45]. The phenomenon of standing wave occurs as a result of two waves moving in opposite directions. In antenna systems, that can happen when the input power is reflected which causes forward loss or return loss of energy. In the ideally matched systems VSWR is 1:1

$$VSWR = V_{MAX}/V_{MIN} \quad (2.20)$$

VSWR is one of the most important measurements at microwave frequencies. The impedance at any point in a microwave system can be calculated using VSWR as follows:

$$VSWR = \frac{Z_0}{R_L} \quad or \quad VSWR = \frac{R_L}{Z_0} \quad (2.21)$$

2.3.7 Return Loss

The return loss can be characterised as the ratio of the incident power of the antenna to the reflected power returned back from the source. So it the loss of power in the reflected signal by discontinuity in a transmission line, it is generated when not all the power is transferred to the load (the load is mismatched). Return loss can be calculated as a ratio using the formula[46]:

$$RL = 10 \log_{10} \frac{P_i}{P_r} \quad (2.22)$$

where,

RL is the return loss in db.

P_r is the reflected power.

P_i is the incident power.

For more explanation, if the return loss is 0 dB that means all the power has been reflected; which means the matching is very bad. On the other hand, -10dB return loss means that 10% of incident power is reflected and 90% of the power is accepted by the antenna. In another words, having -10dB as a return loss is an assumption that 10% of the energy is lost[47].

The return loss can be described as the difference in dB among the power transmitted towards the antenna and reflected power from it. So, it will be negative if the antenna is active and positive if the antenna is passive.

2.3.8 S-Parameters

S-Parameters are those which describe the relationship between input and output terminals (or ports) in an electrical system. In general, S-parameters are a function of frequency (i.e. alter with frequency). S_{12} correspond to the power transferred from Port 2 to Port 1. S_{21} correspond to the power transferred from Port 1 to Port 2 (S_{12} and S_{21} are the reverse and forward transmission gains). In general, SNM illustrates the power transferred from Port M to Port N in a multi-port network. Furthermore, S_{11} represents the reflected power from the antenna and it is the most quoted parameter in respect to antenna for that reason it is known as the reflection coefficient (some times written as Γ). Return loss is related to the reflection coefficient Γ and standing wave ratio (SWR) as explained in the following formulas:

$$RL = -20 \log |\Gamma| \text{ dB} \quad (2.23)$$

$$\Gamma = \frac{V_o^-}{V_o^+} = \frac{Z_1 - Z_0}{Z_1 + Z_0} \quad (2.24)$$

where,

Γ is the reflection coefficient.

V_o^- is the reflected voltage.

V_o^+ is the incident voltage.

Z_1 is the load impedance.

Z_0 is the characteristics impedance.

Return loss is a measure which indicates how good lines and devices are matched; if the return loss is high then the match is good, higher return loss means lower SWR. The modern practice prefers return loss to SWR since it has better resolution in the small values of reflected waves [46].

2.3.9 Bandwidth

The antenna's bandwidth is the range of frequencies in which the antenna fulfil some required properties. In fact, there is no unique definition of bandwidth [48] it can be represented due to Impedance, gain, or VSWR. i.e the bandwidth on basis of impedance is the scope of frequencies where the antenna's input impedance is perfectly matching the impedance of the feeding transmission line, this impedance bandwidth can be described as follows:

$$Bandwidth = \frac{VSWR - 1}{Q\sqrt{VSWR}}; \quad (2.25)$$

where,

Q is the Quality factor.

But in general, fractional bandwidth is utilised widely in Microstrip antennas. It is specified as a percentage of the difference among the upper frequency to the lower frequency or the ratio of upper frequency to the lower frequency as follows:

$$BW = \frac{f_u - f_l}{f_r} \quad (2.26)$$

Where,

f_r is the resonant frequency.

f_u is the upper frequency.

f_l is the lower frequency.

2.3.10 Field Region

The waves radiation from antennas is changing over distance. The field region can be classified as Near Field Region (Fresnel) and Far Field Region (Fraunhofer) which is the region where the radiation pattern does not change over distance, far field region is

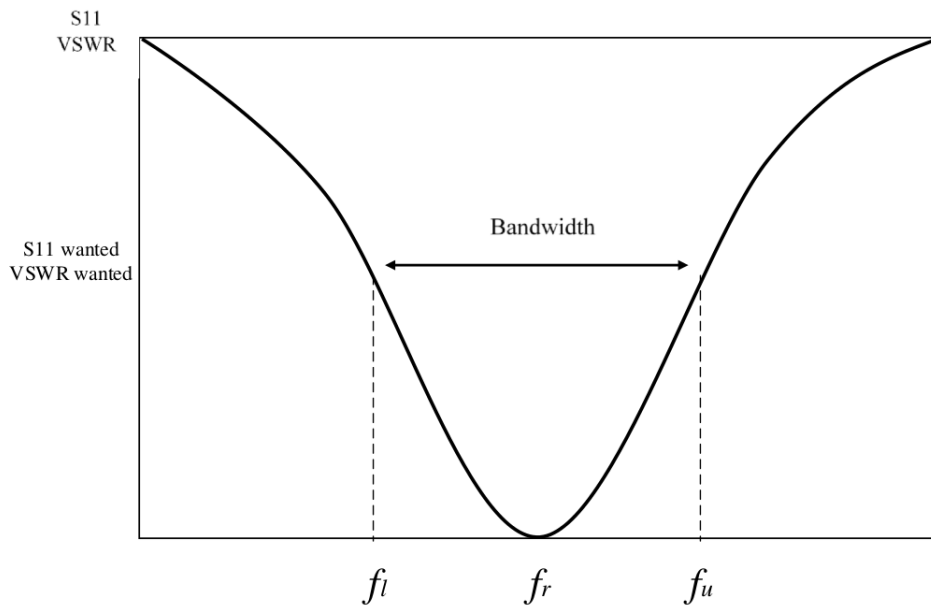


Figure 2.7: Bandwidth[42]

proportional to the antenna dimension and can be determined by the equation[42]:

$$R = \frac{2D^2}{\lambda} \quad (2.27)$$

Where,

R is distance from antenna.

D is the larger dimension of antenna.

λ is the wavelength in free space.

2.3.11 Dielectric Medium

The dielectric constant is the ratio of the permittivity of a material ϵ to the permittivity of free space ϵ_0

$$\text{Dielectric Constant } \epsilon_r = \frac{\epsilon}{\epsilon_0} \quad (2.28)$$

where,

$$\epsilon_0 = 8.854 \cdot 10^{12} [F/m].$$

2.4 Microstrip Patch Antennas (MPA)

Microstrip patch antennas are the most popular kind of printed antennas[49]. The major factor for the current progression on MPA is the recent revolution in miniaturization of electronic circuits[29].

A patch antenna consists of a metallic patch, a dielectric substrate that has permittivity ϵ_r and a ground plane. It has many advantages compared to other kinds of antennas such as wire and aperture antennas[29][50]. These include low fabrication cost, small size, light weight and low profile configuration. Currently, MPAs are widely used in the area of the Global Positioning System (GPS), the Direct Broadcast Satellite (DBS) and mobile satellite Communications. Moreover, they are used in medical applications such as hyperthermia application and remote sensing, aviation and defence[51].

2.4.1 MPA History

During the 19th century, twin parallel wires and coaxial cables were used as transmission lines in microwave circuits. By the mid 20th century, printed circuit board technology facilitated the fabrication of transmission lines in a repeatable and economically useful way. These printed transmission lines were known as microstrip lines, where there was a metallisation layer at the bottom of the board representing the ground plane and coaxial line cable acting as the stripline. The idea of using this microstrip structure as an antenna was first proposed by Deschamps in 1953 and was known as a microstrip radiator as shown on figure (2.8)[52][53].

Subsequently two years after, a patent on microstrip was recorded in France by both Gutton and Baissinot[53][54][55]. In view of this achievement, much was not done on microstrip for another 15 years except an unpublished work produced by Kaloi in the United States. This device was tested in part by U.S Navy in the Missile range in California as the non-availability of good substrates that can work at microwave region[51]. During that period, much interest was developed on stripline circuits as well as antennas which lead to thinner, lower cost as an alternative to waveguide components. The rapid development of thin conformal microstrip started in early 1970s for missile and spacecraft applications in[29][51][56][57][58].

An extension of microstrip transmission line is a microstrip antenna. It was first proposed by Grieg and Englemann in 1952[58]. This antenna was initially outweighed

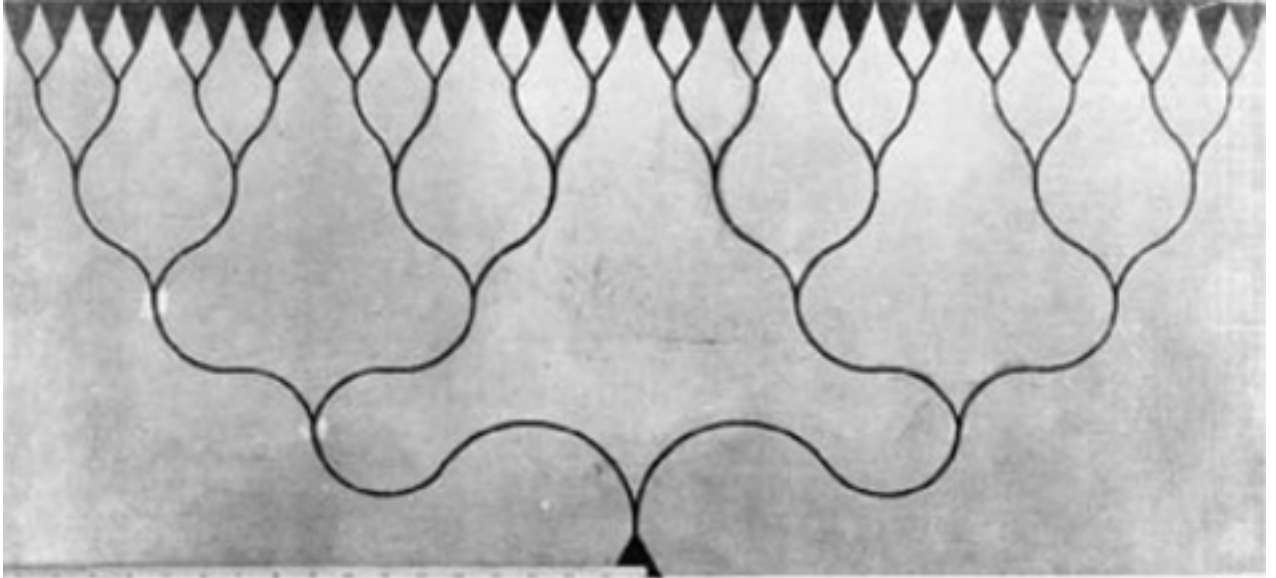


Figure 2.8: Primary conformal array fed with microstrip transmission line which has been designed by Deschamps [52].

by the uses of stripline antenna on printed circuit media for microwave components application. The support of stripline by transverse wave made the design and analysis of this antenna easier. The sandwich structure of stripline antenna is passive in nature but not suitable for any application that requires space for bonding wires. In the advents of microwave transistors and other active devices, the popularity of microstrip antenna increases as it make complete circuits in amplifiers, mixers and phase shifter for hybrid system[51].

2.4.2 Advantages and Disadvantages

The significance of Microstrip patch antennas cannot be overlooked any more due to some of the possessed characteristics usually link to several advantages as compared to the conventional microwaves antennas in terms of applications. They are widely used in the broad region of microwave frequency (100 MHz – 100 GHz) due to their simplicity and compatibility with the technology of Printed Circuit Board (PCB), this is usually makes the device to be easy to fabricate either as a stand-alone elements or as arrays of elements[35][59].

In fact, although MPA suffering from some disadvantages but recent researches shows that there are different methods works to defeat these limitations. For example, MPA have a high quality factor (Q) which represents the losses within the antenna where a high Q causes low efficiency and narrow bandwidth. However, the quality fac-

tor can be reduced by increasing the height or thickness of the dielectric medium. Nevertheless, the increasing of the thickness will increase the fraction of the overall power delivered by the source and converted to a form of surface wave. This surface wave effect is considered as discarded power because at long last it is scattered at the dielectric bends and leads to degradation of the antennas properties. Bandwidth of MPA can be increased by utilizing various method such as defected ground plane strategy, slotted patches, stacked patches and parasitic patch[42][60]. Other disadvantages such as lower power and lower gain can be defeated by configuring an array of antennas[61].

Advantages	Disadvantages
Small mass and light weight	High quality factor
Low profile planar shape	Narrow bandwidth
Low fabrication cost (can be fabricated in big quantity)	Low gain
Can be fabricated easily	Low power handling capability
Can be fixed easily on any surface	Extraneous radiation from feeds and junctions
Their characteristics are reconfigurable	low RF power due to the small separation between the radiation patch and the ground plane(not suitable for high-power applications)[40]
Supports linear and circular polarisation	Suffers from Surface wave when high dielectric constant material is used (Surface wave excitation)
Integrable with Microwave Integrated Circuits (MICs)	Sensitive to environment conditions like temperature and humidity
Capable of dual and multiple frequency resonance	
Mechanically robust if affixed on rigid surfaces. Resist vibration and shock	

Table 2.1: Advantages and disadvantages for MPAs [29][35][38][54]

2.4.3 Types of MPAs

There are many different form of MPAs, each shape has been designed to have specific properties in order to work in particular application. Figure (2.9) shows some well known types of MPA, the most famous kinds in millimetre waves frequencies are rectangular and circular patches.

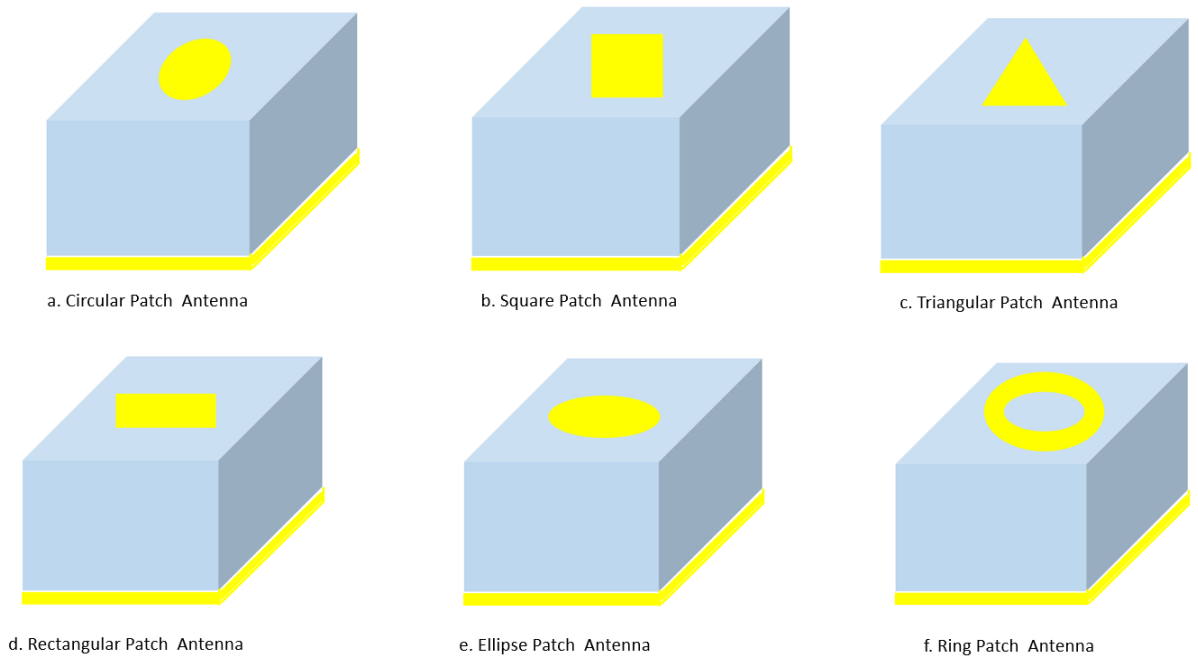


Figure 2.9: Well known types of MPA

Determining the substrate material is an essential part in designing MPAs as it is necessary to consider the temperature, humidity and the atmospheric conditions of anticipated operations. Moreover, the substrate's thickness (h) has an impact on the resonant frequency f_r and bandwidth BW. The bandwidth of MPA is proportional to the substrate thickness h but with cut-off point, otherwise the antenna will not resonate[40].

2.4.4 MPA structure

The basic form of a MPA is a dielectric medium sandwiched between two conducting layers. The upper layer is called a patch or metallisation layer and the bottom is named a ground plane. The patch shape determines the nomenclature with its size being proportional to the wavelength of the operation frequency f_r as illustrated in

figure (2.10).

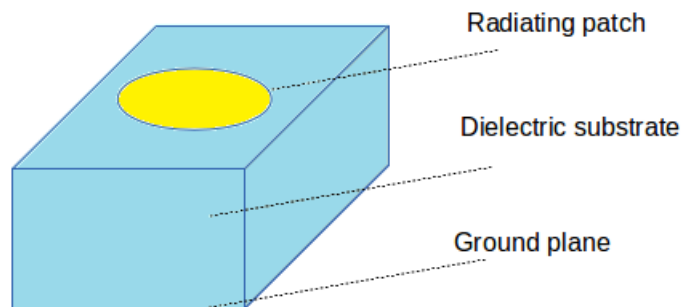


Figure 2.10: Micro-strip antenna structure

Conducting Layers and the ground plane

The patch or conducting layer is a very thin ($t \ll \lambda_0$, where λ_0 is the free space wavelength) metallic strip (or array of strips) placed on one side of a dielectric substrate[40]. It should be fabricated with a material that has a high conductivity and there are many materials that have been used for the conducting layer such as copper and aluminum [20][62]. Moreover, the ground plane is fabricated with the same material properties of the patch on the other side of the dielectric substrate.

There are different techniques used to fabricate this layer such as photo-lithography, conductive ink printing and thermal evaporation[63][64]. Each of these techniques has its own advantages and disadvantages which make designers prefer one technique rather than others[20].

A photo-lithographic technique is the most common process to form the patch shape. This process is an etching method (subtractive process) since the metal is removed.

Similar to the metal layer is a conductive ink which has many advantages; it can be printed easily in different designs without having to use lithography methods which reduces cost significantly. Moreover, potential oxidation issues can be overcome by using an ink that has high resistance to oxidation[62][65].

As a part of the antenna, the ground plane should be infinite in size as for a monopole antenna[20], the length of ground plane should be at least one wavelength, meaning that the length of the patch is equal or less than one half wavelength ($L \leq \lambda_0/2$), thus the ground plane will extend $\lambda/4$ from the edge of the patch.

Dielectric Substrate

The most important dielectric material properties that affect the performance of these devices are the relative permittivity, which is represented by the dielectric constant ϵ_r , the loss tangent δ and their variation with respect to temperature and frequency.

Also it should be taken into consideration that the dielectric substrate should be able to withstand a temperature in the atmosphere in which it is intended to be of use; and be sufficiently robust to withstand chemical processes during fabrication. Moreover, the surface roughness of the substrate should be minimised to reduce losses and to increase the ability to adhere to the conducting layers. The relative permittivity ϵ_r of the substrate is usually in the range from 2 to 12[51]. It should be noted that the substrate layer thickness is of the order of 0.01–0.05 of free-space wavelength (λ_0)[51], consequently by using a thicker dielectric substrate will increase the bandwidth. However, a surface wave propagation will emerge which can be solved by using materials of low dielectric constants[51]. Low dielectric constant substrates are generally preferred for maximum radiation[66].

There are a number of materials utilised in the commercial fabrication of MPAs. Some of these materials are high loss materials or are very difficult to fabricate with thicknesses of less than 4 mm, expensive and non-flexible[67]. A list of the most common materials and their advantages and disadvantages are summarised in table 2.2. In the proposed work, common but unexploited polymer substrates of low permittivity, low loss tangent, flexible, and relatively cheaper will be investigated and used for this research.

Materials	Dielectric Constant	Loss Tangent	Advantages	Disadvantages
Ceramic - Alumina	9.5	0.0003	1-low loss 2-Good resistance versus chemical and heat	Brittle
Synthetic materials- Teflon	2.08	0.0004	Have good electric characteristics	1-Low melting point 2-Poor stickiness
Composite materials – Duroid	2.2 /6.0/ 10.8	0.0017	Good electrical and physical characteristics	Expensive
Ferromagnetic - Ferrite	9 - 16	0.001	This kind of dielectric materials is biased by an electric field.	High loss
Semiconductor - Silicon	11.9	0.0004	Cheap and available	High loss
Fibreglass - Woven fibreglass	4.882	0.002	Relatively low in cost for such low loss tangent.	Tend to be anisotropic which is unwanted in many designs

Table 2.2: Six categories of dielectric materials used for patch antennas[51][66][67]

To sum up, for optimal MPA performance, a thick dielectric medium substrate with a low dielectric constant is desired since this gives better efficiency, wider bandwidth and movable free fields for radiation into space[68]. However, such configurations lead to antennas of on-ideal, larger dimensions[68]. In order to design a compact MPA however, dielectric substrates with high dielectric constants lead to less efficient and a narrow bandwidth, therefore a trade-off must be considered between the antenna geometry and antenna performance[68] .

2.4.5 Applications

The various simple and cost-effective fabrication techniques, planar or flat configuration, lightweight and high-class portability, simple of conformal, convenient for arrays and simple integration with other devices has made micro patch antennas to found its applications in various fields as discussed below[59][69]:

- Mobile communications

Most mobile communications use small devices such as UHF pagers, walkie talkie, cellular phones and so on. Due to their small size, they need smaller size and light weight antennas. For these reasons, MPAs are the suitable type of antennas for these type of applications because they own all of these properties[35][70]. It is good to mention that the communication and the telemetry antennas on missiles are usually MPAs[51].

- Radio Frequency Identification (RFID)

RFID is a method where data stored on a chip or in an integrated circuit (IC), which can be read remotely without physical contact. Generally, an RFID technology consists of a tag and a reader. MPA is perfect choice to be used in RFID applications due to their characteristics including low cost fabrication, conformability and versatility. Moreover, their suitability of integration with planar structures make them more attracted to be used in this field [71][72].

- Radar and remote sensing Communications

Another area where MPAs have been used is the radar applications in transport e.g. cars, planes and ships. Different kinds of MPA which designed from desired gain and bandwidth are successfully utilised for radar applications including surveillance radar, marine radar and for remote sensing e.g. sensing of the direction of the ocean wave and its speed[35]. MPA arrays have been utilised

on satellite imaging systems including SEASAT and SIR-A, due to their size and efficiency requirements[51].

- WiMax

The IEEE 802.16 standard which is called as WiMax (worldwide interoperability for microwave access). It can cover up to 30 mile (48km) radius area with data rate of 70 Mbps. One advantage of MPAs they can resonate at more than one frequency. Hence, they are used in WiMax-based communication[73][74].

- Satellite Communication

One of the major advantage of MPA is that it can be designed for a desired polarisation by using dual feed networks and since the polarisation for the satellite applications antennas should be circular. In other words, MPA is perfect antennas for that purposes. Moreover, in the satellite communication a parabolic dish antenna is used for broadcasting while a flat MPA array is used in the parabolic reflector[35][51].

- Global Positioning System

At the beginning the satellite based GPS system was used only in military purposes. However, GPS nowadays used commercially in many applications(automobile navigation, vehicle tracking, airport surveillance, digital network timing and synchronization etc.)[75]. GPS satellites transmit signals in L-band which are received by huge numbers of receivers antennas on earth, these receivers have to be circularly polarised. MPA can be well designed to operate as GPS antenna receiver[35][51][76].

- Direct Broadcast Satellite System (DBS)

Many countries around the world are using DBS to broadcast the television services. For this system an antenna with high gain ($\approx 33\text{db}$) should be used at the ground in the user side, a huge parabolic reflector antennas are usually used which cover a big space and affected by the weather conditions e.g. rain and snow. However, an array of circularly polarised MPA can be used DBS reception, which are cheaper, smaller, easy to install and has less effect from the weather conditions[35].

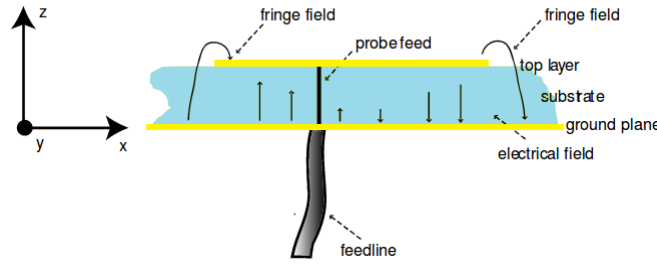


Figure 2.11: Cross section of a patch antenna in its basic form[77]

2.4.6 Basic principle of MPAs operation

Figure (2.11) shows the cross-section of an MPA. The top layer is the patch, while the bottom layer is the ground plane and the material in between is the dielectric medium substrate. The probe is used to feed electromagnetic energy to the patch which generates an electric field basically equal to zero at the centre with a minimum value (negative) at one side and the maximum value (positive) on the other side of the patch[66].

The conductive patch creates a resonant cavity at the boundaries of which are determined by geometry of the patch itself. The patch edges act as an open-circuit boundary (a cavity) which is surrounded by a perfect electric conductor from the top and the bottom, as well as a perfect “magnetic conductor” from the edges[61].

The electric field does not stop suddenly at the patch’s boundary, as it extends the outer boundary for some value and these expansions are known as fringing fields which lead the patch to emit energy. This concept is known as a leaky-cavity and many popular analytic modeling techniques for MPA are based on its theory[66][77].

The cavity modes are represented by a double index (m,n). For a rectangular patch the (m,n) cavity mode is represented by the form[61]

$$E_z(x, y) = A_{mn} \cos\left(\frac{m\pi x}{L}\right) \cos\left(\frac{n\pi y}{W}\right) \quad (2.29)$$

Where,

L is the length of the patch.

W is the width of the patch.

Consequently, the basic mode of a rectangular MPA is usually denoted adopting cavity theory as the TM_{10} mode, where TM is the transversal magnetic field distribu-

tion.

In this mode, the electric field is in the z direction and the magnetic field elements are in x and y directions thus adopting a Cartesian coordinate system, where the x and y axes are parallel with the patch and the z -axis is perpendicular[66][77]. The surface current of the patch is x directed and the patch length, L , is one-half wavelength in the dielectric.

The modes are TM_{nmz} , as TM represents distribution of magnetic field between the patch and the ground plane.

Where,

n and m denotes the field changing in x and y directions.

While,

z value is ignored because the electric field alteration in the z -axis is negligible.

In the y direction, the electric field alteration (impedance width direction) is neglected therefore $m = 0$. While in x direction, the field has one minimum to maximum variation (resonance length direction (L)). The maximum current will be at the centre of the patch ($x = L/2$) and the maximum electric field will be at the two radiating sides ($x = 0$ and $x = L$); therefore $n = 1$ and the notation is TM_{10} in case of fundamental form[66][77].

At first glance, it may be seems that MPA is not effective if its substrate is thin (due to the probability of short circuit happening between the patch and the ground plane). However, if the amplitude (A_{10}) is constant, then the radiated field strength is proportional to thickness (h), and since h is inversely proportional to the radiation Q , then the cavity (Q) will be increased as h decreased. Therefore, the amplitude A_{10} of the modal field is inversely proportional to h . However, if the losses are ignored, then the radiated field strength from the patch is basically independent of h . Similarly, the input resistance is approximately independent of h . This explains the reason why MPAs can be an effective antenna even if very thin substrates are used[61].

2.4.7 Efficiency and Quality Factor of MPAs

Efficiency can be characterised as the ratio of total power transmitted or radiated (P_r) to the total power received or accepted (P_{in}) by an antenna from the transmitter as connected. Linearly-polarised microstrip patch antenna under consideration where fringe effect is been neglected as shown in figure (2.12)[78].

with the condition $h \ll a < b$, as the electric field of the resonant mode TM_{mn}

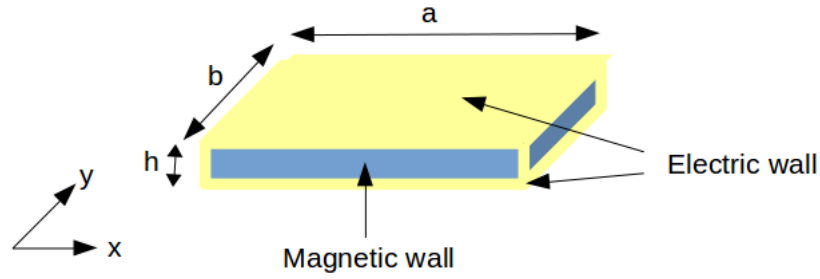


Figure 2.12: Geometry of antenna equivalent cavity[78]

moved inside the cavity is given by

$$E_z = \frac{V_{mn}}{h} \cos\left(\frac{m\pi x}{a}\right) \left(\frac{n\pi y}{b}\right) \quad (2.30)$$

Where V_{mn}/h stand for the intensity of electric field on the magnetic walls. If this antenna consider in the fundamental mode (TM_{10}), the dielectric power losses (P_d) and metallic losses will be calculated as expressed in both equation (2.31) and (2.32).

$$p_d = \frac{\sigma_d}{2} \int_V |E_z|^2 dV = \frac{V_{10}^2 ab \sigma_d}{4h} \quad (2.31)$$

$$p_m = \frac{R_s}{2} \int_S |\vec{J}_s|^2 dS = \frac{V_{10}^2 R_s ab \epsilon_0 \epsilon_r}{2h^2 \mu_0} \quad (2.32)$$

Where,

ϵ_r is the relative permittivity of the substrate.

σ_d is the electric conductivity of the substrate.

R_s is the surface resistance.

\vec{J}_s is the current density of the surface on the metallic walls.

ϵ_0 is the electric permittivity.

μ_0 is the magnetic permeability of free space.

The power obtained by radiation obtained as shown

$$p_r = \int_0^{2\pi} \int_0^{\pi/2} \frac{1}{2\eta_0} (|E_\Theta|^2 + |E_\Phi|^2) r^2 \sin\Theta d\Theta d\Phi \quad (2.33)$$

Where,

η_0 indicate intrinsic impedance of free space.

E_{Θ} and E_{Φ} represent the components of electric field radiated by the antenna.

When the surface wave losses of the antennae is been neglected, in which the dielectric is truncated, the efficiency of this antenna can be expressed as

$$\eta = \frac{P_r}{P_d + P_m + P_r} \quad (2.34)$$

Quality factor The quality (Q) factor of an antenna is characterised as the computation between the power stored in the reactive field of an antenna and the radiated power. It is usually considered as a frequent and simple way to estimate the efficiency of an antenna. There are several approaches to express the Q factor in the impedance circuit of the antenna. However, in term of efficiency there is a dielectric loss, surface wave loss, radiation loss and conduction loss as expressed[29][32][35][40]:

$$e = \frac{1/Q_{rad}}{1/Q_t} = \frac{Q_t}{Q_{rad}} \quad (2.35)$$

$$\frac{1}{Q_t} = \frac{1}{Q_{rad}} + \frac{1}{Q_c} + \frac{1}{Q_d} + \frac{1}{Q_{sw}} \quad (2.36)$$

where,

Q_t = total quality factor.

Q_{rad} = quality factor due to radiation (space wave) losses.

Q_c = quality factor due to conduction losses (ohmic).

Q_d = quality factor due to dielectric losses.

Q_{sw} = quality factor due to surface waves.

There are approximative mathematical statement to figure the quality factor[29]:

$$Q_c = h\sqrt{\pi f \sigma \mu} \quad (2.37)$$

$$Q_d = \frac{1}{\tan \delta} \quad (2.38)$$

$$Q_{rad} = \frac{2\omega \epsilon_r}{hGt/l} K \quad (2.39)$$

where,

$\tan \delta$ = the loss tangent of the dielectric medium.

σ = the conductivity of the conductors.

Gt/l = the entire conductance per unit length.

2.4.8 Feeding Techniques

There are many methods of feeding techniques that can be used to feed MPA. Each technique has its own advantages and disadvantages. Therefore, there are a number of elements which must be considered in choosing the suitable technique for a designed antenna [40][42][66][79].

Transferring the maximum power is the most important factor that should be considered in the feed techniques, which can be reached by matching the input impedance of the MPA with the feed technique in question [40].

Techniques such as impedance transformers and stubs can be used for impedance matching. Simplicity of fabrication is also considered [42]. Also the side effect of spurious feed radiation and surface waves created by the feeding method are major factors which affect the characteristics of the MPA; the efficiency of an MPA is decreased by surface waves and the undesired radiation created by the spurious feed emission which will increase both the level of the side lobe and the level of cross polarisation. Another primary characteristic is that the feed method utilised should be applicable for use with an array [42].

The feeding methods can be categorised into two classifications: contacting or non-contacting. In the contacting scheme, the RF power is directly fed the radiation patch by using a connection component which is contacting the patch. The most popular contacting feed techniques are micro-strip transmission line and coaxial probe. However, in the non-contacting category, the power is transferred to the radiation patch by using electromagnetic field coupling. The most popular non-contacting feed techniques are aperture coupling and proximity coupling [66][79].

The main disadvantage of contacting feeding techniques is that it demonstrates inherent asymmetry which creates higher order modes leading to increase the cross polarisation. For this reason, non-contacting feeding techniques are used to minimise these effects [42].

Contacting Feeding Techniques

Microstrip Line Feed In this technique, a small conducting strip is attached directly to the edge of the patch as shown on figure (2.13). The main advantages of this method is that it is easy to fabricate - the feed element can be fabricated on the same substrate to give planar construction, and the impedance of the feed line can be matched to

the patch without any extra matching element, providing simplicity in modeling. On the other hand, spurious feed emission and surface wave creation is proportional to the thickness of the substrate, which affects the bandwidth of the MPA. Moreover, the radiation occurs because the feed line can lead to unwanted cross polarised emission[29][79].

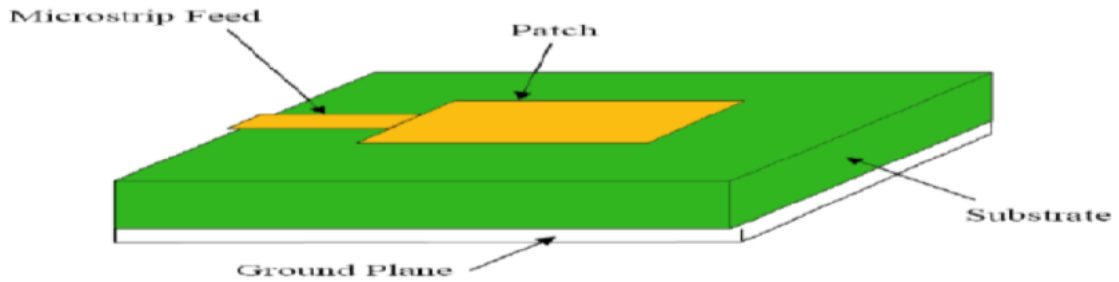


Figure 2.13: Microstrip Line Feed[29]

Coaxial Feed Another technique which is very common in feeding MPA is the coaxial feed (probe feed). Figure (2.14) illustrates its configuration where the coaxial connector is connected to the dielectric via the inner conductor. However, the outer conductor is attached to the ground plane. The major advantages of this kind of feeding is the flexibility of locating it in any required place in order to match the input impedance. It is easy to fabricate and has reduced spurious radiation[79]. However, the main disadvantages is that it results in narrow bandwidth, is challenging to model as a hole is needed in the substrate and the connector out the ground plane, which reduces planarity of the substrate. Moreover, a longer probe length which is needed for thicker substrates makes the input impedance more inductive causing matching problems[79][80]

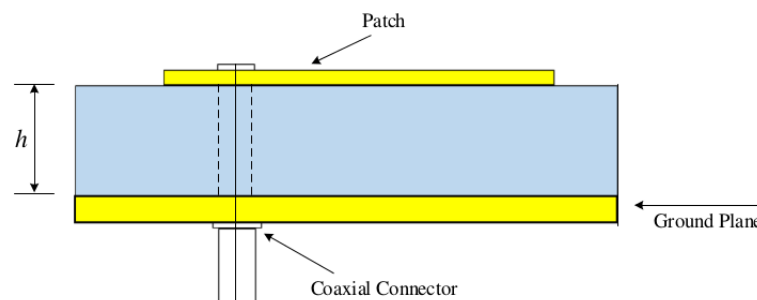


Figure 2.14: Coaxial Feed[79]

Non-Contacting Feeding Techniques

It is seen from above that for a thick dielectric substrate, which provides broad bandwidth, the microstrip line feed and the coaxial feed suffer (Contacting Feeding Techniques) from numerous disadvantages. The non-contacting feed techniques which have been discussed below, solve these problems[79].

Aperture Coupled Feed In the aperture coupled feed, the patch and the microstrip feed line are isolated by the ground plane as shown in figure (2.15). Coupling among the radiation patch and feed line is made by an aperture or a slot in the ground plane. The coupling aperture is normally centred below the patch, directing to lower cross-polarisation due to the symmetry of the configuration. The shape, size and the location of the aperture are determining the amount of coupling from the patch to the feed line. Hence, spurious radiation is minimized because the ground plane isolates the patch and the feed line[29].

In general, in order to optimise the radiation from the patch, a thick and low dielectric constant material is used for the upper substrate and a high dielectric constant material is used for the lower substrate[29]. The main disadvantages of this technique is the difficulty in fabricating since it contains multiple layers which is lead to an increase on the antenna thickness and narrow bandwidth.

Proximity Coupled Feed This kind of feed scheme is called the electromagnetic coupling scheme. In this technique as illustrated in figure (2.16) two dielectric substrates are used and the feed line is located between them as the radiation patch is on the upper part of the top substrate[29]. The major benefit of this technique is that it gets rid of spurious feed radiation and gives higher bandwidth comparing to the other feeding schemes (as high as 13%) , which is due to overall increase in the thickness of MPA [29]. Matching in this scheme can be achieved by manipulating the length of the feed line and the width-to-line ratio of the patch[79].

The main drawbacks of this feed technique is that it is challenging to construct because of the two dielectric layers which demand proper alignment and an increase in the total thickness of the antenna.

Figure (2.17) demonstrates the equivalent electrical circuit of the four kinds of feed techniques[29] while Table (2.3) summarise the different between them.

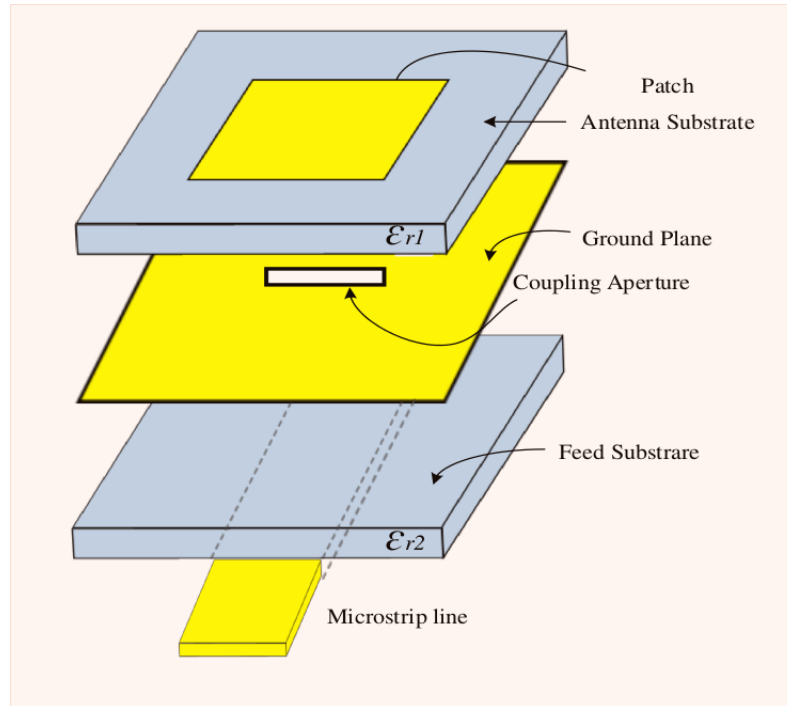


Figure 2.15: Aperture Coupled Feed[29]

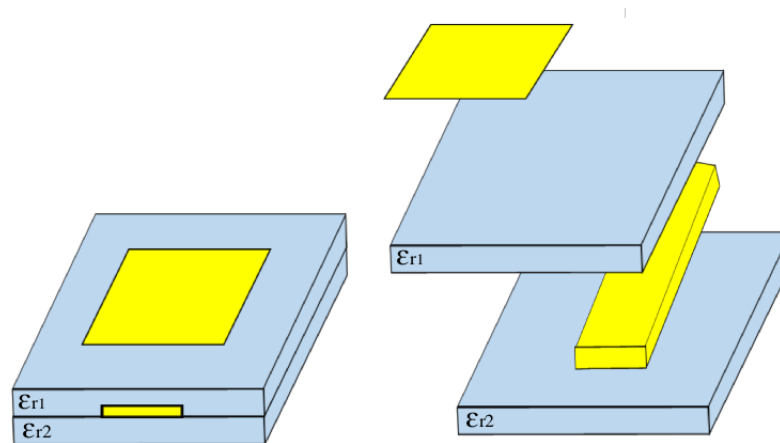


Figure 2.16: Proximity Coupled Feed[79]

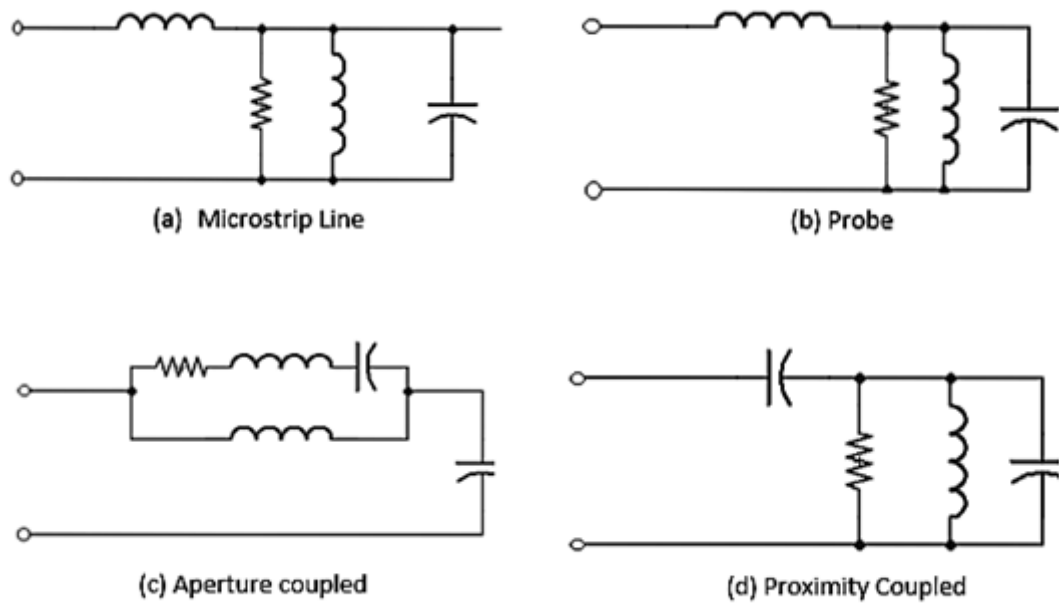


Figure 2.17: Equivalent Circuit of Feed Techniques[29][79]

Characteristics	Microstrip Line Feed	Coaxial Feed	Aperture Coupled Feed	Proximity Coupled Feed
Spurious feed radiation	Much	Much	Less	Minimal
Reliability	Amended	Poor due to soldering	Good	Good
Simplicity of fabrication	Easy	Drilling and soldering needed	Alignment needed	Alignment needed
Impedance matching	Easy	Easy	Easy	Easy
Bandwidth (achieved with impedance matching)	2-5%	2-5%	2-5%	13%

Table 2.3: Comparison between the different feed techniques used for MPA[81]

2.4.9 Methods of Analysis for Patch Antennas

There are many models used for MPA analysis including: transmission line model, cavity model and the full-wave model, which includes primarily integral equations and moment method[29]. However, the most preferred model and the simplest to implement is the transmission line model in which the patch is assumed as a transmission line or a part of it. Conversely, the cavity model (in which the patch is assumed as a dielectric – loaded cavity) is more accurate in this regard and it gives improved physical insight, but is more complex in nature[40][79][82]. The full wave methods are exceedingly accurate, versatile and can deal with single element, finite and infinite arrays, stacked elements, arbitrary shaped elements and coupling. However, it is complex in nature which leads less visualisation as compared to the previous two models[79][82]. Briefly, an explanation of these model will be given as follows:

Transmission Line Model

In this model, the MPA is represented by two slots separated by a transmission line. Generally, the microstrip is considered as a non-homogeneous line of two dielectric materials, the substrate and the air. A symbolic microstrip line is illustrated in figure (2.18) and the electric field lines related to it are shown in figure (2.19).

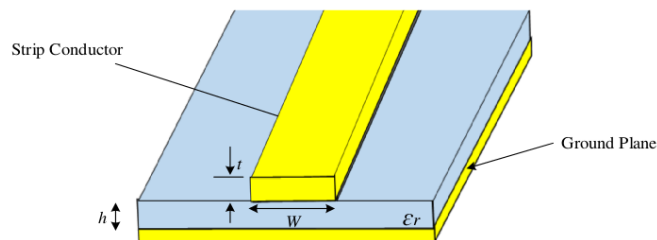


Figure 2.18: Microstrip line[29]

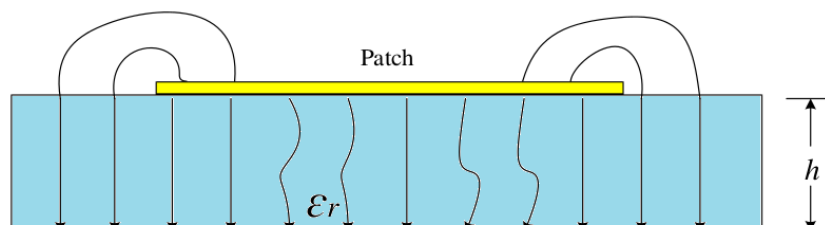


Figure 2.19: Electric field lines[29]

As observed from figure (2.19) most of the electric field lines are located in the substrate although a few field lines can be found in the air. Correspondingly, this transmission line cannot assist pure Transverse Electric Magnetic (TEM) mode of transmission due to the different of the phase velocities in the substrate and the air. Alternatively, the effective mode of propagation would be the quasi-TEM mode. Therefore, obtaining an effective dielectric constant (ϵ_{reff}) is essential in order to explain the fringing and the wave propagation in the line.

The ϵ_{reff} has less value than ϵ_r , since the fringing fields surrounding the boundary of the patch are not confining in the dielectric substrate but are also spreading in the air as illustrated in figure (2.19) above. ϵ_{reff} can be calculated by using the expression given by Balanis [32] as:

$$\epsilon_{reff} = \frac{\epsilon_r + 1}{2} + \frac{\epsilon_r - 1}{2} \left[1 + 12 \frac{h}{w} \right]^{-\frac{1}{2}} \quad (2.40)$$

where,

ϵ_{reff} represents effective dielectric constant.

ϵ_r denotes for dielectric constant of substrate.

h stands for the height of dielectric substrate.

W refers to the width of the patch.

Figure (2.20) demonstrates the transmission line model for patch antenna, where figure (2.20a) is the top view and figure (2.20b) is the side view of the antenna.

For the operation in the fundamental TM_{10} mode, the patch length must be marginally less than $\lambda/2$, where λ is the wavelength in the dielectric substrate which

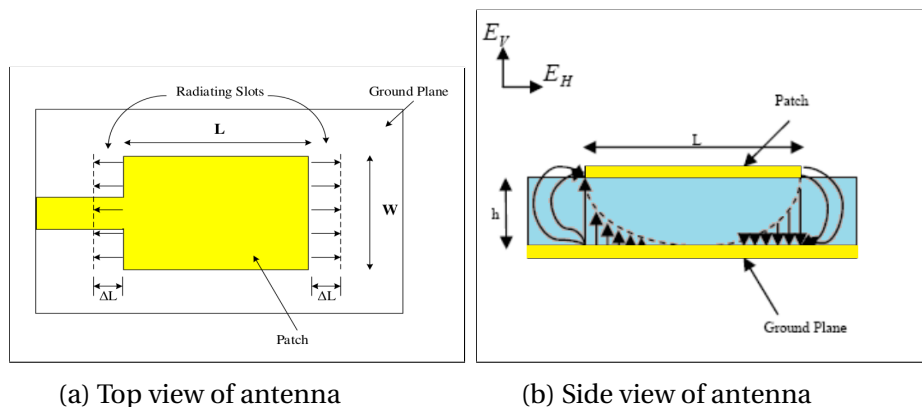


Figure 2.20: Transmission line model for patch antenna[29]

is equal to $\lambda_0/\epsilon_{reff}$ ($\lambda_0/$ is the free space wavelength). The TM_{10} model signify that the field change one $\lambda/2$ cycle along the length of the patch. However, there is no alteration along the width.

In figure (2.20a) it is shown that, the MPA is represented by two slots which are isolated by a transmission line of length L and open circuited at the both ends. Onward the width of the patch, the current is minimum and the voltage is maximum as a result of the open ends. The fields at the borders can be resolved into normal and tangential components with respect to the ground plane.

It can be seen from figure (2.20b) that the electric field at the two sides along the width are contradictory directions and this out of phase because the patch is $\lambda/2$ long as they cancel each other in the edge-side direction. The tangential elements (seen in figure (2.20b)), which are in phase, means that the consequent fields combine to afford maximum radiated field normal to the surface of the structure.

Therefore, the borders along the width can be depicted as two radiating slots, which are $\lambda/2$ apart, stimulated in phase and radiating in the half space above the ground plane. Moreover, the fringing fields on the width can be represented as radiating slots and electrically the patch of the MPA appears larger than its physical dimensions. The patch dimensions onward its length have now been protracted on each end by a distance ΔL [79], which is given practically by Hammerstad [83] as:

$$\Delta L = 0.412h \frac{(\epsilon_{reff} + 0.3) \left(\frac{W}{h} + 0.264\right)}{(\epsilon_{reff} - 0.258) \left(\frac{W}{h} + 0.8\right)} \quad (2.41)$$

The patch effective length L_{eff} is given by

$$L_{eff} = L + 2\Delta L \quad (2.42)$$

For a resonance frequency f_r , the effective length becomes [80] as

$$L_{eff} = \frac{c}{2f_r \sqrt{\epsilon_{reff}}} \quad (2.43)$$

For a rectangular MPA, the resonance frequency for any TM_{nm} mode is presented by James and Hall [48] as

$$f_r = \frac{c}{2\sqrt{\epsilon_{reff}}} \left[\left(\frac{m}{L}\right)^2 + \left(\frac{n}{W}\right)^2 \right]^{\frac{1}{2}} \quad (2.44)$$

where m and n are modes along L and W , respectively.

The width W For efficient radiation is given by Bahl and Bhartia[84] as:

$$W = \frac{c}{2f_0 \sqrt{\frac{(\epsilon_{reff}+1)}{2}}} \quad (2.45)$$

Planar Transmission Line One of the elementary principles of the transmission line structure is that if the structure is planar in configuration, then it is suitable to be used as a circuit component in Microwave Integrated Circuits (MICs). A planar design is used to determine the properties of the component in a single plane. For instance the microstrip line width can be adjusted to have the desired impedance for the matching circuits[85]. There are many transmission line structures which can fulfill the requirement of being planar. The most common designs are as follows[86]:

Microstrip - which has metallisation side on the bottom as a ground plane.

Coplanar Waveguide (CPW) - which consists of a conductor that is separated by a slot from two ground planes.

Slotline - it is the opposite of Microstrip.

Coplanar Strips - it is the opposite of the CPW.

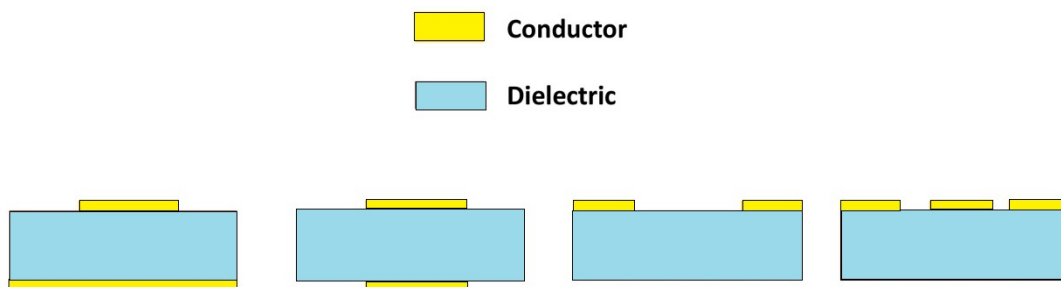


Figure 2.21: Planar transmission lines (a) Microstrip (b) Parallel Plate line (c) Slotline (d) coplanar waveguide[29]

Figure (2.21) displays the various kinds of planar transmission lines which are utilised in monolithic microwave integrated circuits (MMICs)[87]. Microstrip line and

coplanar waveguide are the most favourite from these structures as a result of the mode propagation in them as well as transfer electromagnetic (TEM), which allows simple approximation analysis and produce wide band circuits.

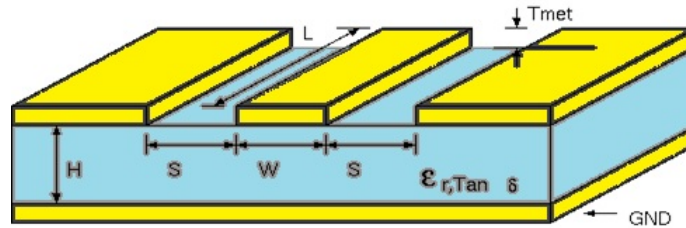


Figure 2.22: Coplanar waveguide[29]

Cavity Model

Despite the fact that the transmission line model reviewed earlier is easy to use, it suffers from inherent drawbacks. Generally, it is useful for the design of rectangular patches only and it disregards the field radiation onward from the radiation borders. These disadvantages can be defeated by using the cavity model. In the cavity model, the internal part of the dielectric substrate is modeled as a cavity surrounded by electric walls from top and bottom. The following observations for thin substrates ($h \ll \lambda$) is the foundation of this hypothesis[35]:

- The fields in the internal part do not change to any large degree in the z direction, i.e. normal to the patch due to the thin substrate.
- the electric field is on z direction only, however, the magnetic field has only transverse elements H_x and H_y in the area surrounded by the metallisation patch and the ground plane.

By considering figure (2.23) when the patch is supplied with power, a charge distribution is occurred on the top and bottom surfaces of the patch and at the ground plane. Two mechanisms are responsible for distribution, which are an attractive and repulsive mechanism which discussed by Richards[88]. The attraction mechanism occurs between the opposite charges located on the bottom of the patch and the charges on the ground plane, thus the charge concentration kept intact at the lower surface of the patch. On the other hand, the repulsion mechanism is among the same charges on the bottom of the patch which forcing some charges to travel to the top of the patch.

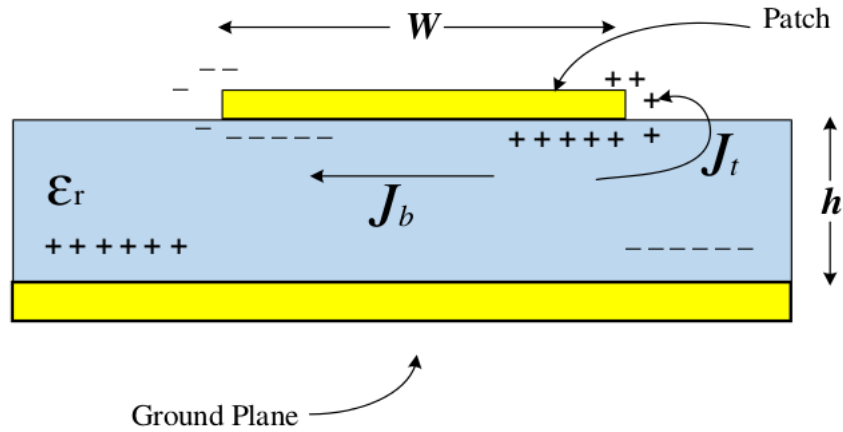


Figure 2.23: Charge distribution and current density creation on MPA[38][79]

Corresponding to this charge movement, a current flow occurs on the top and on the bottom of the patch.

The height to width ratio (I.e. height of substrate and width of the metallisation patch) considered on the cavity model is too small, thus the attractive mechanism take the control and leads most of the charge concentration as well as the current to be under the patch surface. Less current would travel on the upper surface of the patch and as height to the width ratio more decreases, the current flow on the upper surface would be nearly equal to zero (in practice, the height to width ratio never be zero), which prevent any creation of tangential magnetic field elements on the patch borders. Therefore, the four sidewalls can be considered as perfect magnetic conducting surfaces. This means that the electric and the magnetic fields under the patch will not be disturbed[29].

Since the materials are cavity walls are lossless, the cavity will not radiate with purely reactive input impedance. Therefore, a radiation resistance R_r and loss resistance R_L should be introduced in order to account for radiation and a loss execution. A lossy cavity can represents an antenna with taken in to consideration the effective loss tangent δ_{eff} which is given by:

$$\delta_{eff} = \frac{1}{Q_T} \quad (2.46)$$

where,

Q_T represents the total quality factor of the antenna which can be also calculated by the following formula:

$$\frac{1}{Q_T} = \frac{1}{Q_d} + \frac{1}{Q_c} + \frac{1}{Q_r} \quad (2.47)$$

where,

Q_d is denotes the quality factor of the dielectric and given by the formula

$$Q_d = \frac{\omega_r W_T}{P_d} = \frac{1}{\tan\delta} \quad (2.48)$$

where,

ω_r represents the angular resonant frequency.

W_T denotes for the total energy stored in the patch at resonance.

P_d stands for the dielectric loss.

$\tan\delta$ is the loss tangent of the dielectric.

However, Q_c denotes the quality factor of radiation and calculated by the formula:

$$Q_c = \frac{\omega_r W_T}{P_c} = \frac{h}{\Delta} \quad (2.49)$$

where,

P_c is the conductor loss.

Δ is the skin depth of the conductor.

h is the height of the substrate.

Q_r represents the quality factor for radiation and expressed by the following equations:

$$Q_r = \frac{\omega_r W_T}{P_r} \quad (2.50)$$

where,

P_r is the power radiated from the patch.

Substituting Equations 2.47, 2.48, 2.49, 2.50, into Equation (2.46), we get :

$$\delta_{eff} = \tan\delta + \frac{\Delta}{h} + \frac{P_r}{\omega_r W_T} \quad (2.51)$$

Thus, Equation (2.51) describes the total effective loss tangent for the MPA[79].

Full Wave Solution – Method of Moments (MOM)

One of the ways that supply the full wave analysis for the MPA is the Method of Moments (MOM). In this method, the surface currents are utilised to model the patch and the volume polarisation currents are used to model the fields in the dielectric slab.

It has been illustrated by Newman and Tulyathan[89] how an integral equation is derived for these unknown currents and using the Method of Moments. These electric field integral equations are converted into matrix equations which can be solved by several algebraic methods to give the result.

A brief summary of the(MOM) explained by Balanis[29] and Harrington[90] will be discussed here. The basic structure of the equation to be solved by the (MOM) is

$$F(g) = h \quad (2.52)$$

where,

F is a known linear operator.

g is an unknown function.

h is the source or excitation function.

The purpose here is to find g , since F and h are known.

The unknown mathematical function g can be expanded as a linear sequence of N terms and can be expressed as:

$$g = \sum_{n=1}^N a_n g_n = a_1 g_1 + a_2 g_2 + a_3 g_3 + \dots + a_n g_n \quad (2.53)$$

where,

a_n is an unknown constant.

g_n is a known function normally known as a basis or expansion function.

Substituting equation (2.53) into equation (2.52) and by utilising the linearity characteristics of operator F , it can be written:

$$\sum_{n=1}^N a_n F(g_n) = h \quad (2.54)$$

The basis functions g_n must be chosen in such a way that all $F(g_n)$ in the previous equation can be calculated. The unknown constants a_n could not be observed directly because N is unknowns.

One way to determine these constants is by using the method of weighted residuals.

In this approach, a set of trial solutions is established with one variable parameter or more. The residuals are a measurement of the difference among the trial and the true solution. The variable parameters are then chosen in such a way that gives the best fit of the trial functions depends on the minimisation of the residuals. This is through defining a set of N testing (or weighting) functions $\{w_m\}=w_1, w_2, w_3, \dots, w_N$ in the domain of the operator F , by taking the inner product of these functions, equation (2.54) becomes:

$$\sum_{n=1}^N a_n \langle W_m, F(g_n) \rangle = \langle W_m, h \rangle \quad (2.55)$$

where,

$$m = 1, 2, 3, \dots, N.$$

paraphrase it in matrix form, it will be [29]:

$$[F_{mn}] [a_n] = [h_m] \quad (2.56)$$

where,

$$[F_{mn}] = \begin{bmatrix} \langle w_{1,F(g_1)} \rangle \langle w_{1,F(g_2)} \rangle \dots \\ \langle w_{2,F(g_1)} \rangle \langle w_{2,F(g_2)} \rangle \dots \\ \cdot \\ \cdot \\ \cdot \\ \cdot \\ \cdot \\ \cdot \end{bmatrix}, \quad [a_n] = \begin{bmatrix} a_1 \\ a_2 \\ a_3 \\ \cdot \\ \cdot \\ \cdot \\ a_N \end{bmatrix}, \quad \text{and } [h_m] = \begin{bmatrix} \langle w_1, h \rangle \\ \langle w_2, h \rangle \\ \langle w_3, h \rangle \\ \cdot \\ \cdot \\ \cdot \\ \langle w_N, h \rangle \end{bmatrix} \quad (2.57)$$

a_n which is the unknown constant can be found now using algebraic schemes e.g. Gaussian elimination. It should be taken into consideration that the weighting functions have to be chosen suitably so that elements of $\{w_n\}$ are linearly independent and they minimise the computations needed to evaluate the inner product. One selection of the weighting functions is to make them equal to the basis functions ($W_n = g_n$) and this was described by Kantorovich and Akilov as the Galerkin's procedure [91].

From antenna theory perspective, the Electric Field Integral Equation (EFIE) can be written as :

$$\underline{E} = f_e(\underline{J}) \quad (2.58)$$

where,

\underline{E} is the known incident electric field.

\underline{J} is the unknown induced current.

f_e is the linear operator.

The solution process in the MOM starts with expanding \underline{J} as a finite sum of basis functions as

$$\underline{J} = \sum_{i=1}^M J_i b_i \quad (2.59)$$

where,

b_i is the i^{th} basis function.

J_i is unknown coefficient.

The next step is to determine a set of M linearly independent weighting functions (W_j), then, taking the inner production on both sides and substitute equation (2.59) into equation (2.58) which ended up with the formula:

$$\langle w_i, \underline{E} \rangle = \sum_{i=1}^M \langle w_j, f_e(J_i, b_i) \rangle \quad (2.60)$$

where,

$j = 1, 2, \dots, M$.

Paraphrase it in matrix form:

$$[Z_{ij}] [J] = [E_j] \quad (2.61)$$

where,

$Z_{ij} = \langle w_j, f_e(b_i) \rangle$

$E_j = \langle w_j, H \rangle$

\underline{J} is the current vector containing the unknown quantities.

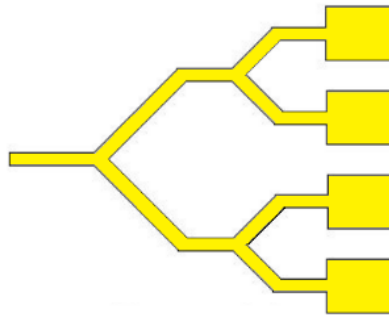
The vector \underline{E} includes the known incident field quantities while the phrases of the \underline{Z} matrix are functions of geometry. The unknown coefficients of the induced current are the phrases of the \underline{J} vector. These equations can be solved by utilising any of the algebraic method cited earlier, in order to determine the current and then another elements including the scattered electric and magnetic fields which can be counted directly from the induced currents[79].

2.5 Antenna Arrays

MPA can be used as a single device or in arrays[35][38][92]. MPA array is used to enhance the performance of MPA including directivity, increasing gain and other parameters which are challenging to do with the single antenna[35][38][92]. MPA array feeding can be series feed network as illustrated in figure (2.24a), or corporate feed network as shown in figure (2.24b).



(a) Series feed



(b) Corporate feed

Figure 2.24: Antenna Array[40]

2.5.1 Simple Array Theory

A single MPA can supply desirable, however a group of them combined in an array can improve the MPA characteristics including directivity, increasing gain and other parameters which are challenging to do with the single antenna. Arrays of MPA normally consist of repeating multiple radiation patches in a specific design. The radiating elements can be identical or different also their constructions can be designed as linear, planar or volume. In order to create the desired radiation pattern, the distance between the elements should be well calculated since it causes addition or subtraction in the entire far fields[38]. Each patch element is analysed as an isotropic source in the simple array theory. However, their contributions which is derived in the far

field called the array factor (AF). The AF depends on the array geometry and the phase among each component. Then, the far field radiation pattern is determined by pattern multiplying the AF with the pattern of the patch. Nevertheless, mutual coupling is neglected in the operation because all the patches are treated individually as well as their effect on each other are not considered. Moreover, the simple array theory does not consider the existence of the other components such as obstructions and the feeding techniques[35][38][40][92].

Several physical properties such as optical, mechanical, electrical change as the dimensions of a material is reduced from micro to nanoscale. The statistical and quantum mechanical effects become significant or notice at this scale. The increase in surface area to volume ratio is another phenomenon that altered the catalytic, heat as well as mechanical properties of the material at the nanoscale. At this scale, the reaction and diffusion of nanomaterials will be fast enough to give leverage for the transportation of ions which is important in the fabrication of nano-antenna[93][94].

2.6 Summary

The history about the evolution of antennas were discussed extensively in this chapter. General parameters which include polarisation, radiation characteristics, directivity and return loss were all considered. The S-parameter, bandwidth and field region, which formed the basis for the antenna performances were mentioned in this discussion. Further brief on the history of MPAs, it's operation principle, structural types, and it's applications were provided. Basics explanation about the efficiency , quality factor and feeding techniques and the antennas arrays were also discussed.

Chapter 3

POLYMERIC DIELECTRIC MATERIALS

3.1 Introduction

As mentioned in chapter 2, the basic form of MPA consists of a metallisation layer, ground plane and a dielectric substrate. This chapter is going to give an overview of the polymeric dielectric materials fundamentals which is going to be used in this research.

3.1.1 Background

The term permittivity (ϵ) refers to the ability of the material to undergo polarisation when applying an electric field. It is presented as the ratio between dielectric permittivity of a material related to the vacuum. The physical implication of the statement means the greater dielectric constant the greater polarisation that is developed by a material in an applied field of given strength. Conventionally, inorganic substances such as silicon dioxide, silicon nitride and mica were employed for the manufacturing of dielectric materials. Recently, the use of polymers as dielectric materials is expensive, which can be attributed to the properties such as flexibility, specific use customization, easier processing and better resistance to chemical attack[95]. In capacitors, the use of polyvinyl fluoride[95] and aromatic-containing polymers[96] is evident since as early as mid-60's, as dielectric materials. In addition, the US Patent 4153925[97] revealed the establishment of further improvement in organic film fabrication. There are several methods, which can be used to fabricate polymers into a thin film; which include (i) solution casting and spin coating, (ii) electron or UV radiation, (iii) glow discharge methods and (iv) immersion in the organic substrate[98]. The primary reasons for considering these materials are, lower thermal properties, including melting temperature and glass transition, which in turn added to a lower temperature

processing windows. It has controllable solubility without any disturbance to the intrinsic properties of the material[98].

Inorganic and ceramic materials present relatively higher thermal properties and this can be linked to extremely high processing temperatures. However, polymers are susceptible to significantly high temperatures, present large thermal expansion coefficient while ceramic materials are due to atmospheric and hydrolytic degradation. Table 3.1 presents dielectric values of several polymers in concurrent comparisons with several inorganic materials.

It has been observed that as against polymers, inorganic/ceramics materials present a higher dielectric constant, for example, water constitutes relatively high dielectric constant[98]. In turn, this is concerning as the desired dielectric properties are altered with any moisture traces.

It is also observed that in comparison to polymeric materials, inorganic materials generally present higher dielectric constant compared, owing to their intrinsic ions and polar groups. Herein, with a 1.02 dielectric constant air is considered as reference dielectric.

Materials	Dielectric constant (ϵ)	Materials	Dielectric constant (ϵ)
Air	1.02	Polyimide	2.8 – 3.2
Teflon AF	2.1	Fluorosilicate glass	3.2 – 4.0
Polyethylene	2.3 – 2.7	SiO ₂	3.9 – 4.5
Fluorinated polyimide	2.5 – 2.9	PVDF	6.0
Polystyrene	2.5 – 2.9	neoprene	9.8
Methylsilsesquioxane	2.6 – 2.8	H ₂ O	78
Polyarelene ether	2.8 – 2.9	TiO ₂	100

Table 3.1: Dielectric constant of different polymers and inorganic materials [99][98]

3.1.2 Application of polymeric dielectric materials

In electronic industries, there is a high significance use of both dielectrics materials with low and high dielectric constant. Specifically, the low dielectric constant is commonly known as passivation materials and primarily used as an insulator. These present wide area of applications such as:

1. Isolating signal-carrying conductors from each other.
2. Fast signal propagation.
3. Interlayer dielectric to reduce the resistance-capacitance (RC) time delays.
4. Crosstalk and power dissipation in the high density and high-speed integration[100].

This show necessary utility in very dense multi-layered IC's, which can be attributed to the need suppressed coupling between very close metal lines towards the prevention of device performance, as this role entails packaging and encapsulation[98]. Particularly, they provide isolated pathways and separate interlayers in multilayer printed circuit boards electronic devices connection. Furthermore, the harmful effect of stray and coupling capacitances were reduced with relative permittivity decrease and miniaturization trends in microprocessor fabrication. For the encapsulation of balls which bridge the die and substrate, dielectric materials are used, which is referred to as underfill. It ensures protection against any circuitry failures and contributes to the reduction of a thermal mismatch as seen between the bridging layers in figure (3.1)[98]. Low dielectric materials are used for insulation purposes in LED encapsulation at the lead frame housing.

The main focus of designing active components is oriented towards high permittivity value, which attributes to its high use as polarisable media. This wide application is seen in:

1. Capacitors - in apparatus used for the propagation or reflection of electromagnetic waves.
2. For a variety of artefacts, such as rectifiers and semiconductor devices, piezoelectric transducers, dielectric amplifiers and memory elements.

In these materials, which are insulators and thus non-polar, with the introduction of small amount of impurities, it is possible to convert them into polar materials. In this mixed stage, the material presents with properties of a large amount of charges

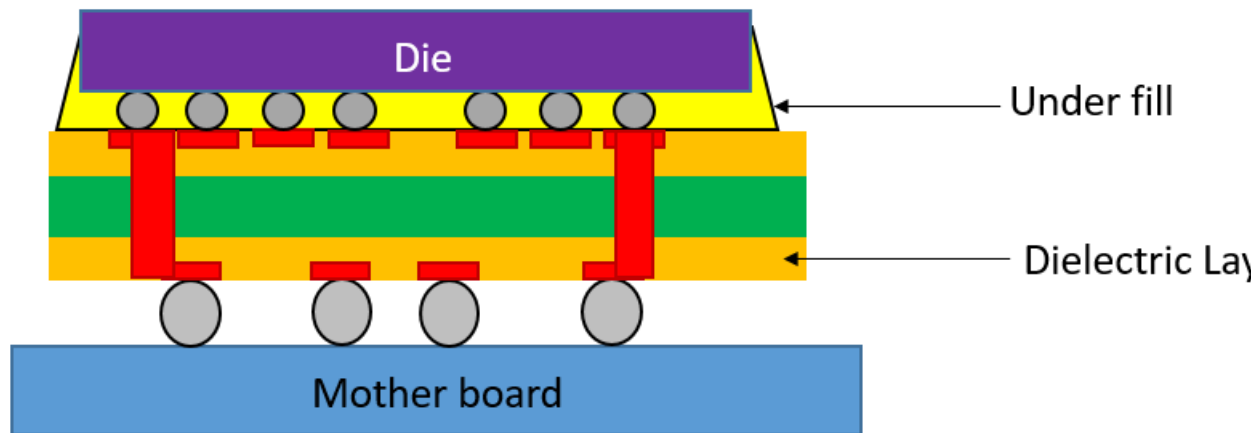


Figure 3.1: Application of dielectric polymers in IC packaging

storage at the small applied electrical field, for example, polyvinylidene fluoride with chlorotrifluoroethylene impurities introduction[101]. However, polymers showed an improved dielectric constant in polyimides with introduced Al_2O_3 , $BaTiO_3$ and ZrO_3 'impurities' [102][103][104]. A large charge storage allows for ready on-demand release, as evident in a capacitor, in a rectifier, to be useful in smoothing off direct pulsating current[102][103][104].

3.2 Theory of dielectric properties in polymer

3.2.1 Mechanism of interaction with electric field

The Clausius-Mossotti equation can be used to summarize the quantitative treatment of a dielectric in an electric field (equation3.1.)

$$P = \frac{\epsilon_r - 1}{\epsilon_r + 2} \cdot \frac{M}{\rho} = \frac{N_A \alpha}{3\epsilon_0} \quad (3.1)$$

For clarity,

- ϵ_r is the relative dielectric constant of a material.
- ϵ_0 is the permittivity of a vacuum.
- M is the molar mass of the material(molecular weight).

- ρ is the density.
- N_A is the Avogadro's number.
- α is the polarisability.

According to this equation, the factors of the free volume of the constituents and polarisability of the element present in the materials governed the dielectric constant[105]. The term, polarisability, specifically pertains to the proportionality constant for the dipole formation under the electric field influence, such that for each different type of atom or molecule, it presents a typical value[105]. The following Equation(3.2), presents the intersect between dielectric material permittivity and polarisability:

$$\epsilon_r = 1 + \frac{N_A \alpha}{\epsilon_0} \quad (3.2)$$

Then, the equation presents that relative permittivity is the ratio of the total permittivity of one mole of material with that in a vacuum. Therefore, the origin of free volume dependency of relative permittivity is in the one mole of the material volume. Furthermore, each molecule or atom presents a distinctive characteristic molar volume. Hence, the introduction of molar volume into these derivations is referred to as molar polarisation, which in turn leads to Clausius–Mossotti equation[106].

The application of electric field induces polarisability, while in its absence there is an even distribution of the electrons around the nuclei. When the electric field is applied the electron cloud is displaced from the nuclei in the direction opposite to the applied field. This result in separation of positive and negative charges and the molecules behave like an electric dipole. There are three mode of polarisations[106]:

- i. Electronic polarisation – this refers to the slight displacement of electrons as regards the nucleus.
- ii. Atomic polarisation – this refers to the distortion of atomic position in a molecule or lattice
- iii. Orientational polarisation – this refers to the tendency for permanent dipole towards electric field alignment to yield a net polarisation in that direction with respect to polar molecules.

Thus, the dipoles present a permanent polarisation, with the application of a static electric field to these materials and give a dielectric constant as ϵ_{static} . Although, the

field change induced with the application of alternating electric current and consequently impact oscillation of the polarisation. It is observed that the oscillating electric field frequency will govern the three modes of polarisation, which underpin the overall dielectric constant. Naturally, the in-phase polarisation with the changing electric field makes it instantaneous as against atomic polarisation. Consequently, atomic polarisation presents a better adherence to the oscillating electric field than the orientational polarisation. As compared to the others, a higher polarisability is seen in certain structures and elements, like bromine, sulphur, iodine and aromatic rings. Correspondingly, the dielectric constant increase was induced by the presence of these groups. It is found easily polarised with the sigma bond presenting stronger aromatic ring attachment than the π bond. It is seen that in bromine and iodine with large size atoms show large electron cloud which is distant from electrostatic attraction influence of the positive nucleus and thus they show an increased probability of a high polarisability. Conversely, fluorine with a small atomic radius as well as concentrated negative charge, allow a tighter electron cloud, thereby resulting in low polarisability, towards a lower dielectric constant.

Towards the determination of dielectric constant, free volume constitutes also an imperative factor, which specifically pertains to the volume that the polymeric material does not occupy. Thus, to compute the free volume evident through one mole of repeat units of the polymer.

$$M/\rho \tag{3.3}$$

This figure may be estimated by subtracting the occupied molar volume of a repeat unit, V_o , from the total molar volume, where M is the molar mass of the repeat unit and ρ is the density. The fractional free volume V_n is given by Equation(3.4)[106]

$$V_n = \frac{M/\rho - v_0}{M/\rho} \tag{3.4}$$

For the free volume enhancement, factors that contribute to the limiting of chain packing density include flexible bridging units, pendant groups' addition and bulky groups[107]. Similarly, free volume presence through pores leads to dielectric constant decrease with the presence of air with about one relative permittivity. Thus, a lower density material is expected with a higher fractional free volume, which in turn provides a lower polarisable group per unit volume-outcome. The high fluorine volume dielectric constant shows a decrease attributed to fluorine replacement of hydrogen. Therefore, fluorine introduction, in addition to low polarisability results in a signifi-

cant dielectric constant decrease through an increase in free volume.

3.2.2 Effect of chain polarity

The polymers can be of two types: (i) polar and (ii) non-polar. The dielectric properties are significantly affected by these characteristics. Some of the polar polymers examples include PVC, PMMA, PC and PA (Nylon) while non-polar polymer examples include, PE, PS, PP and PTFE (and many other fluoropolymers). For the alignment of the dipoles, the particular time is required by the polar polymers, under the alternating electric field. Correspondingly, the dipoles, at very low frequencies, prior to changing direction, have suitable time for field alignment. Sufficient time is not available with the dipoles to align before the change in the field direction. The dipoles do present movement at intermediate frequencies, however, before the field changes direction, they are unable to complete their movement and thus essentially realign with the changed field.

For both polar and non-polar polymers, the electronic polarisation and to some extent atomic polarisation at both high and low frequency is instantaneous. Thus, between 3 and 9 dielectric constants are presented at low frequencies (e.g. 60 Hz) by polar polymers and between 3 and 5 are presented at high frequencies (e.g. 100 Hz). It is observed that the dielectric constant is not dependent on the alternating current frequency for non-polar polymer due to the effective instantaneous polarisation and thus presenting consistently less than 3 dielectric constant. Furthermore, the polar or non-polar quality of the polymer is determined by the chain geometry.

In the case of fix confirmation status of polymer, the dipole moments reinforcement or cancellation governs the resulting dipole. In the extended PTFE configuration, at each alternating carbon backbone, the high dipole moment of $-CF_2-$ units cancelled each other, as the vectors are presented in opposite directions. Thus, presents a low (2.1) dielectric constant. The dipole moment of the PVC are directed parallel to each other and this leads to the dipole reinforcement, wherein figure (3.2) shows the corresponding 4.5 dielectric constant.

As regards dielectric material designing with the aim of desired dielectric properties achievement, requires imperative accounting of net polarity of the structure. This can be demonstrated through the extensive substitution into a polyimide chain of fluorine atom which subsequently lead to increase in otherwise low dielectric constant material[108]. For non-polar polymers, no dipole polarisation contribution is found as seen in polar polymers. This diverse mechanism mode, in the electronic polarisation

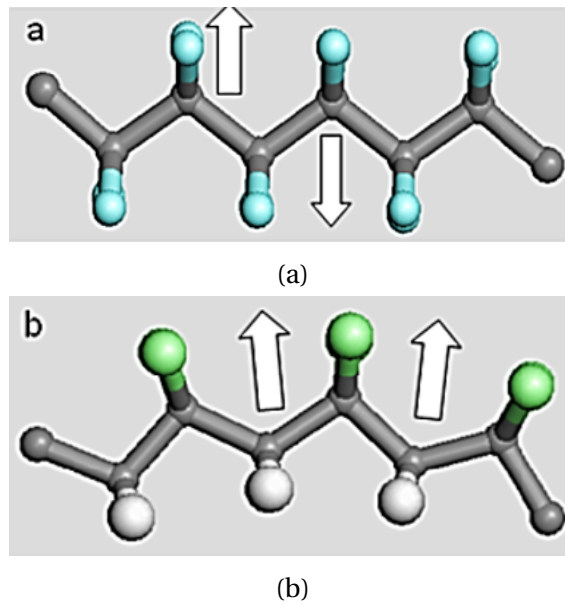


Figure 3.2: PTFE (a) and PVC (b) with arrow showing the net dipole moment[98]

case, to cause the resonance spectra that occurs at the specified frequency beyond 10^{12} Hz. The experimental work shows the constant status of relaxation spectra, below this frequency, which can be associated with the dipole polarisation behaviour. Figure (3.3,) summarizes this observation:

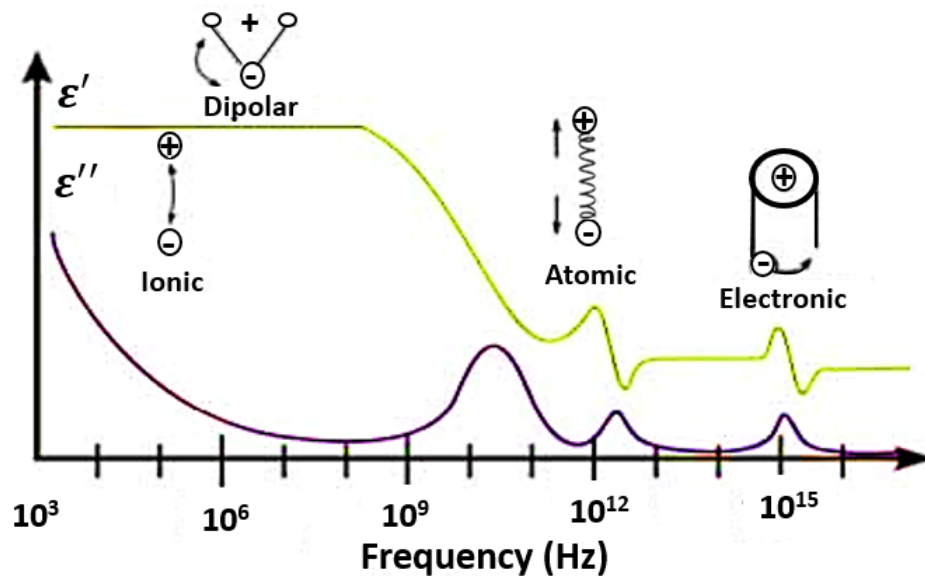


Figure 3.3: Dielectric constant and loss dispersion of dielectric materials against frequency[98]

Relaxation and dielectric loss

The concept of relative permittivity, as presented in Equation (3.5), can be expressed in a complex form:

$$\epsilon^* = \epsilon' - j\epsilon'' \quad (3.5)$$

The equation comprises the real part, i.e. dielectric constant and the imaginary part, i.e. dielectric loss. Subsequently, the dielectric loss and the dielectric constant ratio is quantified as $\tan \delta$ i.e:

$$\tan \delta = \frac{\epsilon''}{\epsilon'} \quad (3.6)$$

In a molecule, the polarisation process unable to follow change rate of the oscillating applied electric field results in a dielectric loss. Similarly, in a polymer, the relaxation time (τ) leads to this process, wherein the time required for the dipoles to return to its original random orientation is entailed. This process does not present an instantaneous occurrence but an exponential diminishing of polarisation. Also, in case the relaxation time is smaller or can be compared with the oscillating electric field rate, the process does not show any or only a minimum loss. Although, in the situations, wherein the electric field oscillates rate is higher compared to the relaxation time, polarisation fails to follow the oscillating frequency and this results in absorption and dissipation of energy as heat. Correspondingly, equation (3.7) presents the dependency of dipole polarisability on the frequency.

$$\alpha_d = \frac{\alpha_0}{1 + j\omega\tau} \quad (3.7)$$

where α_d is the dipole polarisability and α_0 is the low frequency (static) polarisability and are typically evident in the microwave region. Accordingly, Figure (3.3), presents the disparity between real dielectric constant and imaginary dielectric loss. The experimental study showed for dielectric constant ϵ' an unexpected dipole polarisation region drop ($< 10^{12}$ Hz), with the supplementation of maximum dielectric loss ϵ'' . The complete failure for the dipole is presented by this maximum and thus follows the oscillating electric field and external to this, the dipole becomes intact and does not present any effective dielectric constant contribution. It has been observed that higher frequency evidence the electronic and atomic polarisation mechanism, i.e. at a shorter wavelength, for example, infra-red region. The concept of resonance behaviour is evidenced by this region, with quantized energy level due to excitation of

electrons. Also, about a certain frequency dielectric constant reaches a maximal value, prior to a symmetrical drop. Correspondingly, with the oscillating frequency, the optimum polarisation in phase is represented by these maximum and minimum. Natural frequency ω_o is the term accorded to the frequency which evidences the turning point. This point presents the natural frequency's corroboration with the frequency of applied electric field, thus showing maximum absorption, which as a result causes maximum dielectric loss ϵ' .

3.2.3 Effect of temperature

The dielectric properties are affected by temperature and an increase in the temperature, results in augmented thermal agitation, with the breaking of the bond of intermolecular forces between polymer chains. Thus, this relatively frees the polar group, which now permits its analogous movement with the alternating electric field. Correspondingly, with a decrease in temperature, the dielectric constant is reduced with the chain's segmental motion becoming intact. However, the dielectric constant presents a further reduction, at suitably higher temperature, which can be attributed to robust thermal motion causing dipoles' disorientation. A minimal dielectric constant is effectively resulted by the polarisation at this later stage. In addition to the attained kinetic energy, for the induction of segmental movement, the requirement of free space in the polymer matrix is imperative. There is an evident spontaneity in electronic and atomic polarisation all through the measured frequency and temperature. Alternatively, the dipole polarisation, during heat treatment, present a substantial impact by the effective reduction of the relaxation time (τ) and this is due to the reduction in polymer chain τ , with the temperature increase. Thus, within the oscillating electric field, the polymer segment presents a better phase integration. The polymers show important chain and segmental motions, as identified in the following section,[109]:

i. α relaxation: This refers to the micro-Brownian motion involving the whole chain and was previously known as glass transition.

ii. β relaxation: This refers to the polar groups' rotation about the C-C bond. For example conformational flip of the cyclic unit, CH_2Cl and $-\text{COOC}_2\text{H}_5$.

iii. γ relaxation: This refers to the phenyl ring libration as well as limited C-H segmental chain movement.

Moreover, with the increase in temperature, at respective relaxation mechanisms, the dielectric loss shows a maximum. Congruently, Figure (3.4) presents the schematic representation of the dielectric loss.

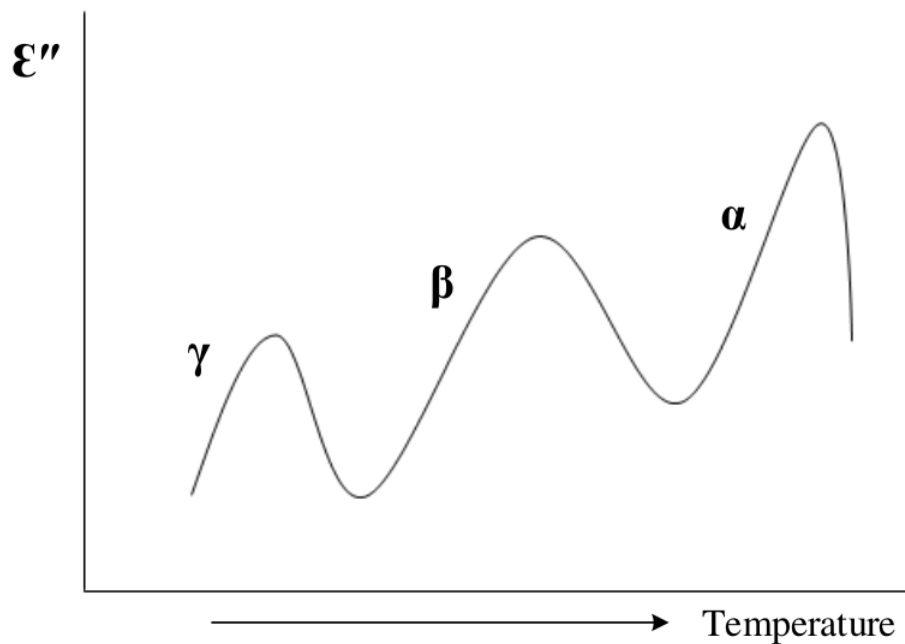


Figure 3.4: Schematic dielectric loss curve for polymer as temperature is increased[98]

Hence, apparently, the involvement of small entities of phenyl rings and C-H units leads to the occurrence of γ relaxation at a lower temperature, attributing to low thermal energy induced readily perturbed motion of the same. Subsequently, β relaxation and then α relaxation follow and these steps are aligned with the longer scale segmental motion. Relaxation time dispersion is identified through the broadness for each peak, which is an outcome of the diverse local environment of polarisable groups.

3.2.4 Effect of a cross-link between chains

To achieve an improvement in properties, oftentimes, polymers are cross-linked with the curing or commonly referred to as the crosslinking process, which presents a convenient monitoring of reaction progress with a change in relaxation time. The curing or crosslinking process of diglycidyl ether bisphenol A (DGEBA) with diethyltetramine (DETA), optimally exemplifies this process, wherein the covalent bonding of chains occurs, resulting in chain rigidity[110].

Also, the rigidity is in direct proportion with the cross-link density, subsequently impacting the relaxation time alteration, as demonstrated in Figure (3.6).

According to Figure (3.6), an increase in α and β relaxation time is seen concur-

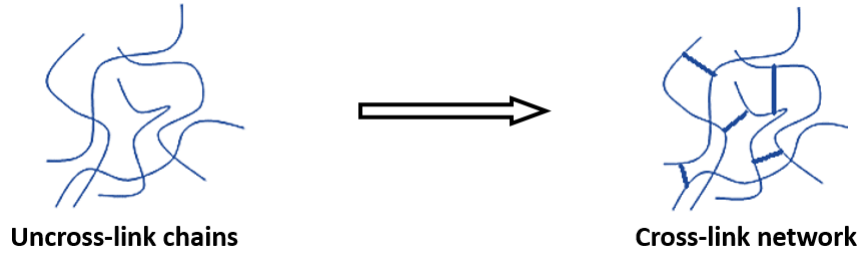


Figure 3.5: Affect of crosslink network on rigidity of polymer chains[98]

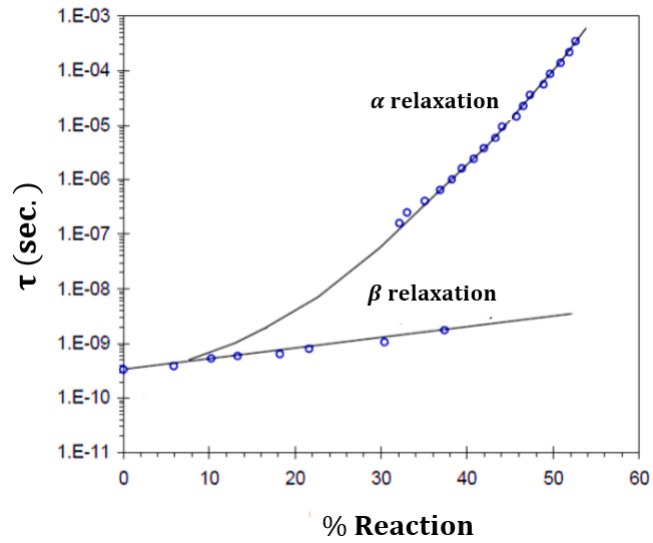


Figure 3.6: Effect of degree of reaction on the α and β relaxation time of DGEBA-DETA system[98]

rent to cross-linking reaction amount increase. It is observed that the polymer chains present an augmented tighter bond with cross-link density increase and thus towards original equilibrium configuration achievement longer time is required. Comparison between α and β relaxation, the former shows a higher rate of increase than the latter, on nearing the glassy state. This can be attributed to larger α relaxation segmental chain motion than β relaxation. Correspondingly, Figure (3.7), presents the dielectric constant ϵ' and loss, while Figure (3.7(a)) presents a substantial dielectric constant drop, aligned with the Figure (3.7(b)) illustration of dielectric loss's maximum frequency. In fact, in the corresponding oscillating electric field, this shift manifests the complete out of phase dipole polarisation frequency value. Herein, to achieve the α relaxation time, maximum frequency ω_{max} (dielectric loss) was computed for use in equation $\tau = 1/\omega_{max}$. A shift of the maximum dielectric loss towards lower frequency is seen with an increase in curing level and conversely, at α_{static} with $\alpha_{infinity}$ dielectric constant change is significantly absent. Thus, this process represents the change of the polymer from the rubbery state to glassy state due to increased density of crosslinking.

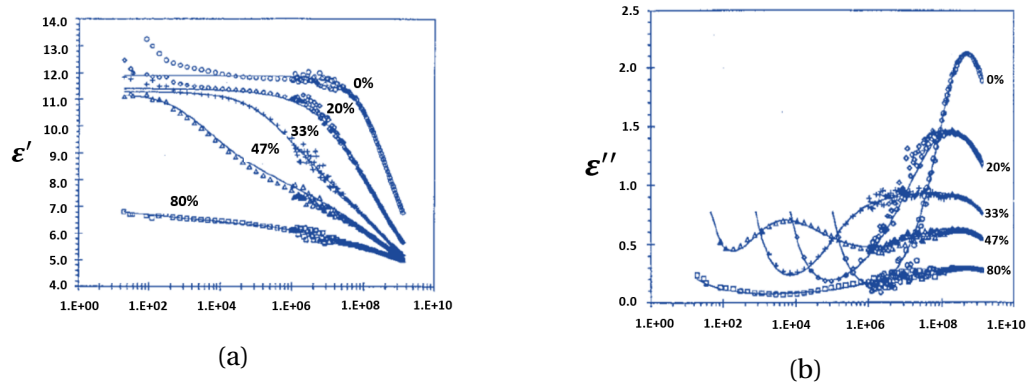
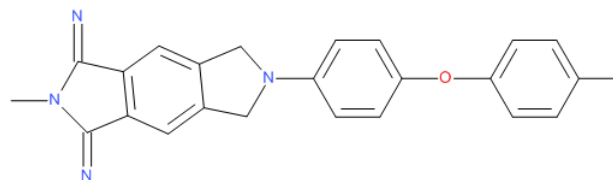


Figure 3.7: (a) Effect of cross-link density on dielectric constant (ϵ' above) (b) dielectric loss (ϵ'' below) for DGEBA-DETA system[98]



Fully cured polyimide

Figure 3.8: Repeat unit of the polyimide[111]

Polarisability and free volume

The Clausius–Mossotti equation presents the two significant factors of polarisability and free volume to impact the dielectric properties. The fluorine introduction into polymer chains, optimally exemplify these impacts[111]. In the experimental works, a vacuum chamber was used to conduct polyimide film fluorination through a gaseous phase. Subsequently, XPS analysis was used to establish the impregnated fluorine content and Table 3.2 correspondingly, presents the consequent dielectric constant.

Sample	$F_{1s}/C_{1s}(\%)$	Dielectric constant (ϵ)	
		$10^2(Hz)$	$10^6(Hz)$
F0	0	2.93	2.90
F2	57.8	2.64	2.60
F3	67.7	2.42	2.41
F4	78.6	2.28	2.27
F5	87.4	2.37	2.26

Table 3.2: The effect of Fluorine content on the dielectric constant of a polyimide[98]

A polyimides series which was generated from the use of starting monomers with a fluorine content of variable percentage, the comparison result was achieved[107]. Correspondingly, fluorine's low polarisability underpins the dielectric constant decrease, concurrent to fluorine content increase. As the fluorine electrons are bonded tightly near to the nucleus. The displacement of a C–F bond's lower electronic polarisability compared to C–H bond causes decrease in fluorinated polyimides' polarisability, concurrent to increase in fluorine atoms[112] [113]. In addition, the polarisable groups per unit volume present a decrease in number, as a result of concomitant free volume increase, owing to large fluorine volume than hydrogen.

The introduction of adamantane into a polyimide chain also evidences the free volume impact[114], due to the bulky nature of Adamantane, which in turn impact free volume increase. At 1 kHz, 2.7 dielectric constant was achieved, which is significantly less than the commercial Kapton H film ($25.4 \mu m$), at 1 kHz approximately 3.5 dielec-

tric constant and at 10 MHz, 3.3 electric constant. In addition, with the reduction of hydrophobicity, moisture absorption was prevented, indicating the significance of low dielectric loss in the context of good capacitors and insulation. The commercial Avatrel™ dielectric polymer furthermore exemplifies the bulky substituents introduction strategy and for passivation applications, it constitutes of polynorbornene. Specifically, it presents 2.55 dielectric constant and less than 0.002 loss tangent. Also, up to above 1 GHz, it was observed that these electrical properties were intact.

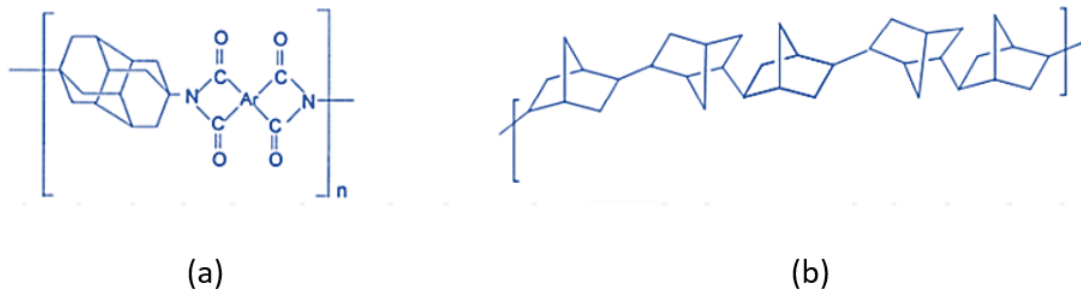


Figure 3.9: (a) Adamantane structure incorporated into polyimide chain[115] (b) the generic structure for polynorbornene[98]

3.3 Structure-properties relationship

3.3.1 Dielectric relaxation

Originally the Debye relaxation model[115] provides the earliest relaxation behaviour model. Correspondingly, Figure (3.10), presents the dielectric constant's real and imaginary parts in this model

where,

$$\epsilon' = \epsilon_{\infty} + \frac{\epsilon_0 - \epsilon_{\infty}}{1 + \omega^2 \tau^2} \quad (3.8)$$

$$\epsilon'' = \frac{\epsilon_0 - \epsilon_{\infty}}{1 + \omega^2 \tau^2} \omega \tau \quad (3.9)$$

Thus, the equation presents the relation of the relaxation time with the dielectric properties in the model. Furthermore, the elimination of parameter $(\omega\tau)$, results in the formulation of relationship between ϵ' and ϵ'' , thereby leading to Equation (3.10)

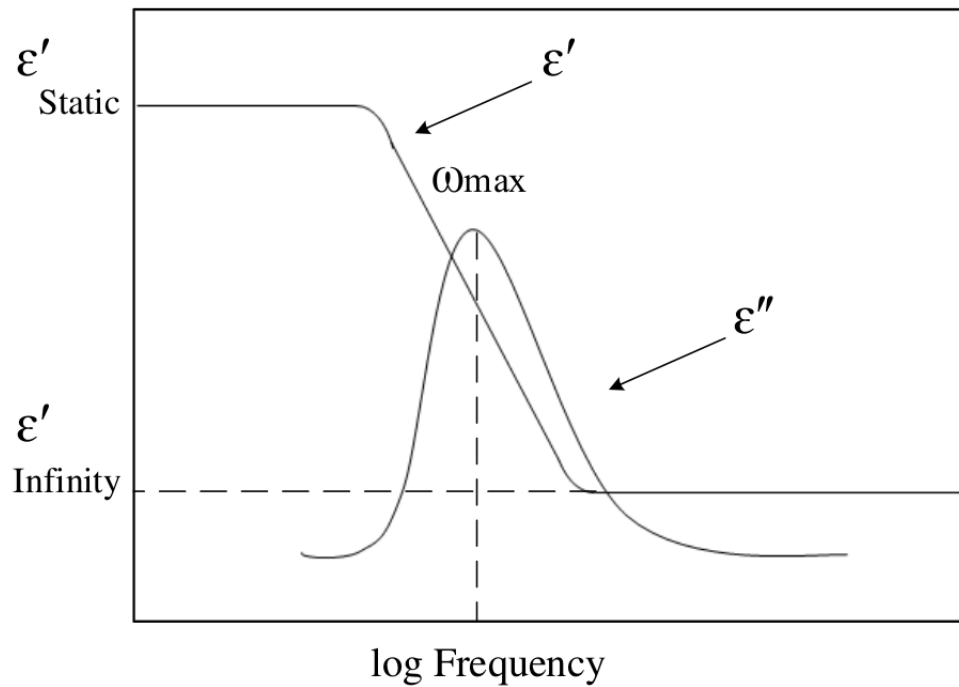


Figure 3.10: Debye dielectric dispersion curve[115]

$$\left(\epsilon' - \frac{\epsilon_s + \epsilon_\infty}{2}\right)^2 + \epsilon''^2 = \left(\frac{\epsilon_s - \epsilon_\infty}{2}\right)^2 \quad (3.10)$$

The equation as presented above demonstrates Cole-Cole plot, which is a form of a semispherical plot, as presented in Figure (3.11).

The plot shows that no loss is evidenced at a dielectric constant of infinite frequency, ϵ_∞ and static dielectric constant, ϵ_s . The maximum loss is seen to occur between the two dielectric values at the midpoint. Thus, the loss is directly proportional to the difference between the static and infinite dielectric constant.

Correspondingly, with polar small molecular liquids, this model presents an ideal fit. Although, bigger six polymeric materials, present higher viscosity in conjunction with in-between chain entanglement. This further adds to the visco-elastic properties that need certain modifications specific to the original model. Notably, only one specific relaxation time was involved in the above relationship. However, this process is to converse in the polymeric system, wherein the relaxation time presents a dependency on dipoles mobility having diverse behaviour in variable local environments. Thus, the outcomes are evident through distribution in relaxation time. The works of Cole and Cole semispherical equation[116] Davidson and Cole[117] Williams and Watt[118] and

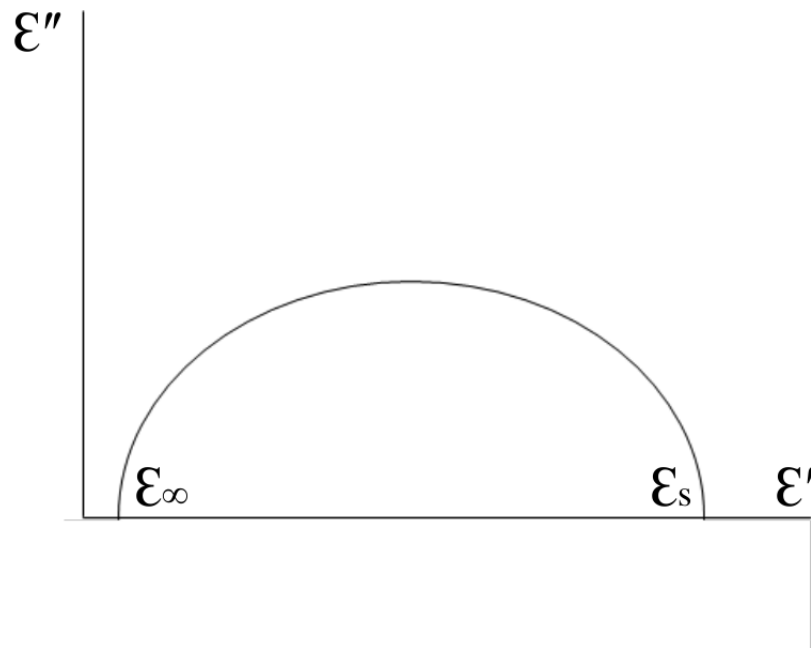


Figure 3.11: Cole-Cole Plot showing the relationship between dielectric constant and dielectric loss[98]

Navriliak and Nagami [119], impacted the modification, thereby leading to the development of the new equation :

$$\epsilon' = \epsilon_{\infty} + \frac{\epsilon_0 - \epsilon_{\infty}}{(1 + (\omega^2 \tau^2)^{\alpha})^{\beta}} \quad (3.11)$$

where α and β is in the range 0 and 1 and yet it is not possible to assign a physical value to these parameters [120].

Furthermore, a broader peak and smaller loss value are resulted by this modification result with asymmetrical features. Figure (3.12), demonstrates, as regards polyvinylchloride the dielectric constant and loss behaviour at variable temperatures and frequencies.

Evidently, in figure (3.12(a)), the polyvinylchloride region of glass transition (85°C) presents the ϵ' and ϵ'' variation. It is observed that initially, within the measured frequency range, the PVC, during glass transition presented a value of 4.1 to 3.2 dielectric constant, which is relatively low. Subsequently, temperature increase impacted an increase in chain mobility and consequent relaxation time reduction. With the changing frequency, the polymer chain dipole polarisation presents an improved alignment in phase, thereby explaining the dielectric constant increase concurrent to increase in

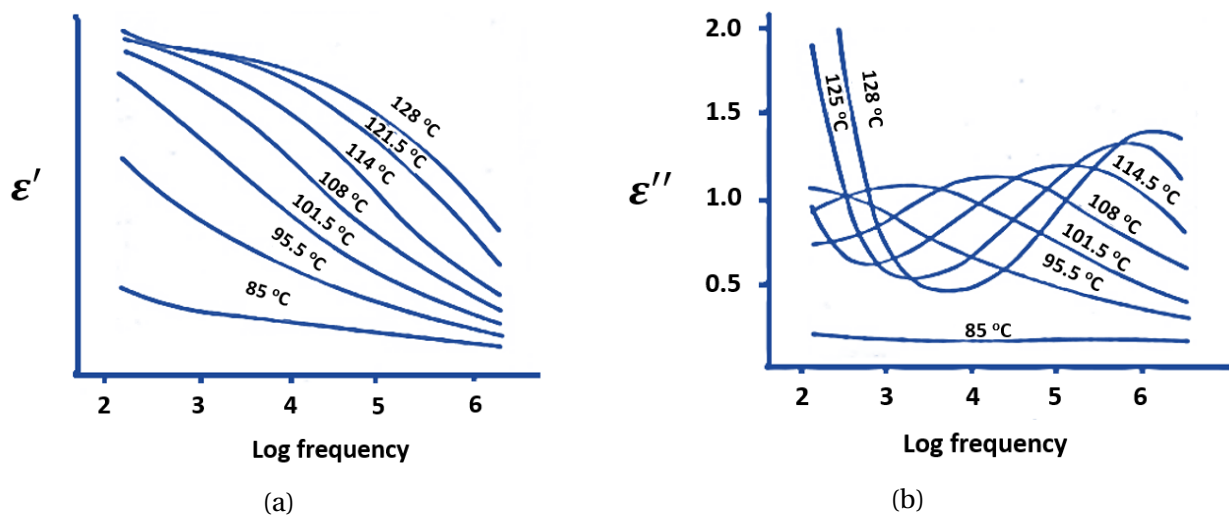


Figure 3.12: Plot of (a) dielectric constant and (b) dielectric loss with the change in frequency and temperature for polyvinylchloride[121].

temperature. Although, increase in frequency resulted in a gradual failure of the alignment within the applied oscillating field. The dielectric constant shows an optimal decrease rate, at a higher frequency, with an increase in temperature.

Correspondingly, Figure (3.12(b)), shows the maximum dielectric loss. Moreover, aligned with the Cole-Cole plot, a correspondingly large dielectric loss is seen during high thermal treatment, which has a significant difference between the static and infinite dielectric constant. A large dielectric loss results at 128 °C temperature than lower temperatures at a higher frequency. Due to the significant impact on the dielectric properties, during polymers use, it is imperative to consider the glass transition of the polymer. For example, in the substitution of fluorine into polyimide, only the electronic polarisation is affected. This could be attributed to the primarily low-temperature use of PI, when its T_g ($<260^\circ\text{C}$), which it is observed that from this mechanism there is an evident lack of effective polar orientation at this temperature towards the reduction of any intrusion effect possibility into the dielectric properties. As regards the commercially used polymers, Table 6.1 shows the dielectric constant and loss.

3.3.2 Dielectric breakdown

It has been observed that on exceeding the maximum electric field which is applicable on the dielectric material, commonly referred to as dielectric strength, results in the electrical breakdown and leads to a blown fuse or short circuit, which is a serious

Materials	Dielectric constant (ϵ')	Loss tangent ($\tan \delta$)	Frequency (Hz)
HDPE	1.0 – 5.0	0.00004 – 0.001	–
Teflon (PTFE)	2.0 – 2.1	0.0005 0.00028	100 Hz 3 GHz
ABS (plastic)	2.0 – 3.5	0.005 – 0.0190	–
Polypropylene	2.2	–	–
Butyl rubber	2.35	0.001 0.0009	1 MHz 3 GHz
Polyamide	2.5 – 2.6	–	–
Polystyrene	2.5 – 2.6	0.0001 0.00033	100 MHz 3 GHz
Gutta percha	2.6	–	–
Polycarbonate	2.8 – 3.4	0.00066 – 0.01	–
Kapton (Type 100) (Type 200)	3.9 2.9	–	–
PVC	3	–	–
Nylon	3.2- 5	–	–
Silicone (RTV)	3.6	–	–
Neoprene rubber	6.26 4.0	0.038 0.34	1 MHz 3 GHz

Table 3.3: Dielectric parameters for some polymers at various frequencies[98]

failure.

Usually, this is evident, high heat is generated from losses in comparison to dissipation, at a specific voltage. The application of this specific voltage, for a long duration, the internal thermal equilibrium is not achieved by the dielectric. The breakdown is typical in the following situations:

- i. Dielectric with a large thickness.
- ii. The dielectric and the surrounding, both displaying high temperature.
- iii. Large dielectric loss (high $\tan \delta$).
- iv. Continuous high voltage application.

Specifically, in the case of large dielectric loss, the failure occurs at high frequency. Also, it can be affected by high humidity in air through an electrolytic process.

3.4 Designing of polymer dielectric materials

Several approaches can be adopted as regards polymer dielectric materials designing, in accordance with the previous discussions. In the following section, two such approaches will be discussed, i.e. (i) free volume; and (ii) copolymerization.

3.4.1 Free volume

The composite presents a substantial decrease in dielectric constant in the second phase as evidenced in Maxwell-Garnet theory[122] In this concept, the foam structure was generated using this concept through air-filled pores introduction, wherein the experiment used the two methods of (i) synthesizing block copolymer with diverse different thermal liability[123]and (ii) solution etching (soluble component in a composite matrix)[124]. In the first method, high temperature and high Tg polymer composed block copolymer was used, with a second component shown in the figure (3.13), with the potential of thermal decomposition due to lower thermal property.

The components of thermally stable polyimide, as well as thermally labile phosphate ester, constituted this triblock. In the experiment, the thermally stable block is left intact with thermal treatment being given to this copolymer at a specific temperature which disintegrated the thermally labile block. This is followed by the generation of microphase separation (small size scale), with a discontinuous, monodispersed size

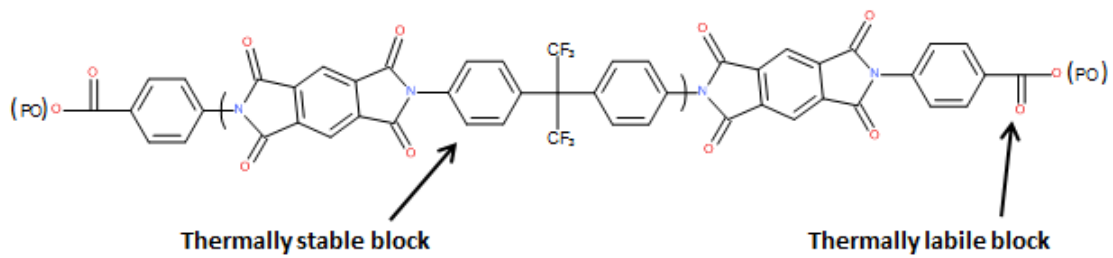


Figure 3.13: Triblock polyimide structure illustrating the thermally labile and stable segments[98]

spherical pore morphology. Moreover, the presence of air in nanopores ($\epsilon = 1.0$) results in a dielectric constant decrease. Also, polymethylmethacrylate, polypropylene oxide and poly methylstyrene constitute the thermally labile oligomers. Furthermore, with a 16% triblock (PPO/ 4BDAF/PMDA) void volume system, the experimental work could achieve a 2.3 dielectric constant of nanofoam and this relationship is illustrated in Figure (3.14)[125].

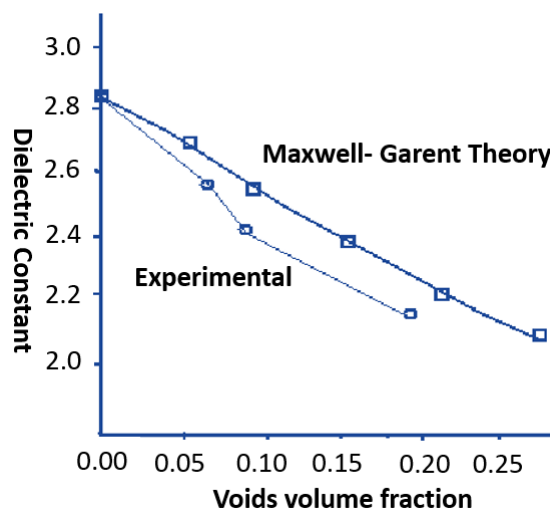
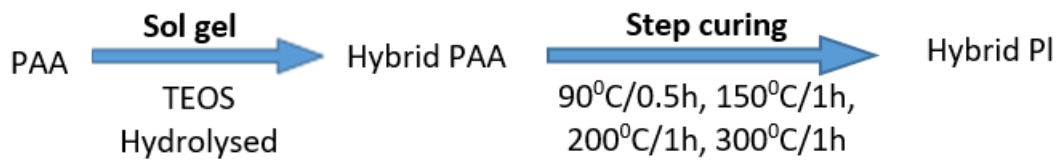


Figure 3.14: Relation between the dielectric constant with the void fractional volume in PMDA/3FDA/PPO triblock system [125]

To achieve porosity in the method of solution etching the soluble component in nanocomposites were subjected to solution etching, which in turn left the chemically stable matrix integrated. The polyimide prepolymer of polyamic acid was used in the process, as the sol-gel method was employed in the inorganic TEOS incorporation in the matrix. The complete homogenous distribution of the inorganic phase, the thermal curing of the composite followed, which subsequently led to hydrofluoride etch-

ing. Thus, nanosize closed cell pore density was achieved uniformly, which occurred due to the dissolution of acid labile inorganic phase. Figure (3.15) presents the fabrication steps as described, in an illustration:

1st Step



2nd Step



Figure 3.15: Preparation of porous Polyimide using sol-gel method[98]

It is observed that the TEOS content, which is added to the polymer matrix decides the porosity level. Correspondingly, this dependency of the dielectric constant on two factors of : (i) fluorine content and (ii) porosity level is presented in Table 3.4.

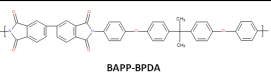


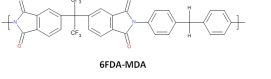
	F(Wt%)	0% TEO	10% TEOS	% TEOS
 BAPP-BPDA	0	2.71	2.84	3.41
 6FDA-BDAF	15	2.45	2.71	3.25
 BDAF-BPDA	17	2.61	2.69	3.18
 6FDA-MDA	33	2.50	2.62	3.98

Table 3.4: Dielectric constant of a series of polyimides at varying TEOS content[98]

Hence, according to the above results a general trend demonstrating a dielectric

constant decrease is evident, with the sol-gel technique using high TEOS concentration. This could be attributed to the void structure increase and a subsequent dielectric constant reduction owing to air. In addition, with the increase of fluorine weight percent in the structures the dielectric constant showed a linear decrease with the decrease rate being constant for different TEOS content. Correspondingly, due to lack of fluorine, BAPP-BPDA amongst the four synthesized polyimides presented the highest dielectric constant. Figure (3.16) depicts the SEM picture specific to the fracture surface morphology.

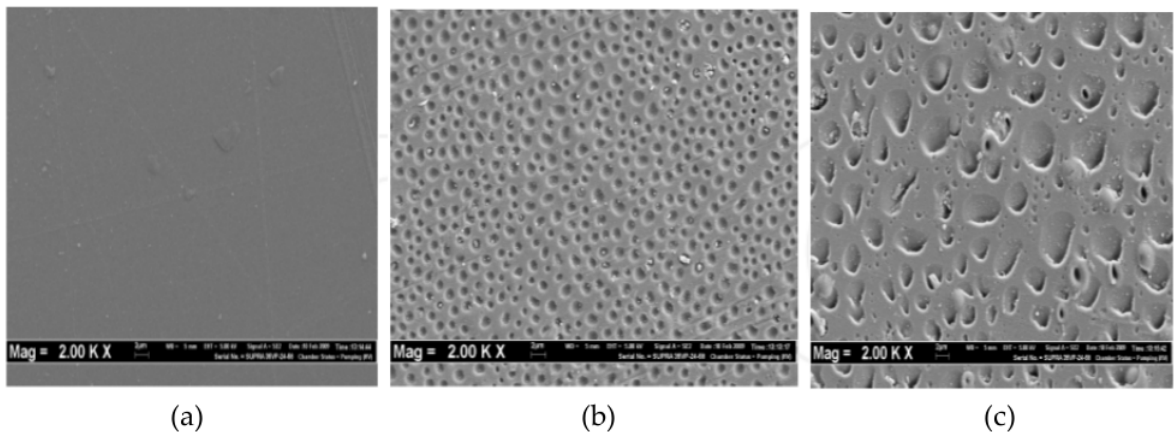


Figure 3.16: SEM scan of fracture surface of pure (a) PI/SiO₂ 10% (b) and PI/SiO₂ 20% porosity (c) [98]

According to Simpsons et al [107] fluorine affects specific developments including free volume increase; lower electronic polarisation; symmetric or asymmetric atoms substitution oriented dielectric constant increase or decrease.

3.4.2 Copolymerisation

For the production of materials with customized dielectric properties, the mechanism in which two or more polymers are copolymerized together offers a significantly useful strategy. Specifically, the process of copolymerization involves the covalent bonding of two or more different monomer units, which in turn, from the respective constituents produces a synergistic effect. Correspondingly, polyimide and polysiloxane present complementary mechanical and chemical properties, attributing to their popular Copolymerisation. It has been observed that despite the superior mechanical and thermal properties, the polyimide is found to be too intractable, particularly as regards the normal processing methods. This is evident through the polyimides

modulus values, which are projected to lie in the range of 10^9 to 10^{12} Pa. However, the value of their T_g is evidenced to be above 260°C . Conversely, the polysiloxane present improved flexibility and processibility, in addition to thermal degradation, which is relatively stable ($> 400^\circ\text{C}$). Correspondingly, within the specific context of electronic packaging, an optimized dielectric material is produced by the copolymers offering practical applications. Within the following structures, the study attempted the experimental works[126].

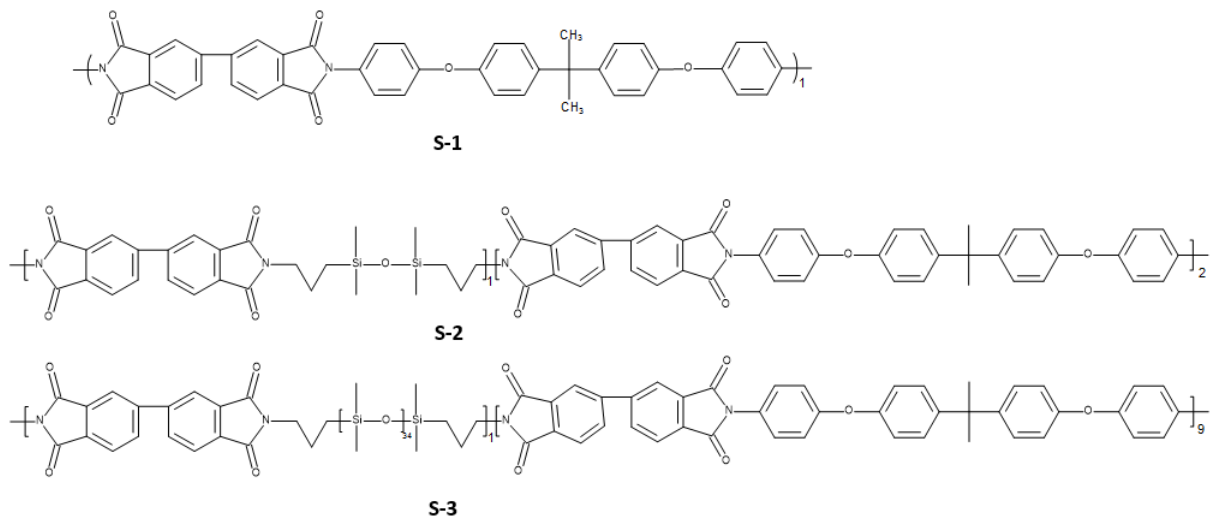


Figure 3.17: Series of PI-polysiloxane copolymers[126]

Their dielectric constant are shown in the following Table

Sample	Dielectric constant at 1 kHz 293°C	n (Si-O repeat unit)
S1	2.90	0
S2	2.57	1
S3	2.43	34

Table 3.5: Effect of silicone content in silicon-polyimide copolymers on dielectric constant[126]

As presented in Table 3.5, the siloxane units increase impacts a direct decrease in dielectric constant. Specifically, the atomic size of silicon is larger than carbon and as compared to C-C bond, the Si-O bond presents more flexibility and hence the mobility of bulky silicone units is less[127]. Thus, the presence of bulky silicone units impacts the whole polyimide network's movement, thereby reducing the dipole efficiency towards polarity change reaction during alternating frequency treatment[127]. In addition, free volume increase results in a significant decrease in molar polarisation. In addition, the latest relevant research illustrates an analogous trend highlighting a decrease in dielectric constant concurrently with an increase of siloxane content, particularly into polyimide structures[127][128].

3.5 Summary

It has been thus observed that with reference to the conventional ceramic and inorganic materials, polymer presents as an alternative dielectric material. This can be attributed to the unique property of high flexibility, manageable and complaint processing, robust chemical stability and prompt tunable properties. However, polymers present the primary disadvantage of thermal stability which is relatively low and this property confines the expensive applications of the compound. In addition, typically polymers present a lower dielectric constant when compared with non-polymeric materials. Particularly, the polymers' dielectric properties can be contributed to the specific mechanism of electric field's interaction with atomic, electronic and dipole polarisation. Correspondingly, the Clausius-Mossotti equation provides the construct for

the formulation of free volume and constituent structure's polarisability, which govern these polarisation mechanisms. Furthermore, throughout the measurable frequencies range; electronic as well as atomic to some extent present an instantaneous polarisation. Although, dipole polarisation entails relaxation time, which towards the return to equilibrium state permits an exponential motion decay. Such diverse behaviour is observed to add an imperative contribution to the dielectric constant as well as loss values. Furthermore, for the detection of segmental as well as local motion during frequency change and temperature treatment, specifically, these properties can be very useful. Particularly, with the processes of the introduction of polarisable groups into polymer chain as well as free volume increase (which can be achieved through copolymerization and porosity promotion); can lead to the designing of dielectric properties. In addition, to increase the dielectric constant, nanocomposites can be produced with inorganic fillers, which present high dielectric constant.

This chapter further gives a brief background about the polymeric dielectric materials and their applications, then the theory of dielectric characteristics in the polymer was discussed. After that, the structure-characteristics relationship was explained. Finally, two approaches used for dielectric materials designing was discussed (free volume and copolymerization)

Chapter 4

CLEANING, FABRICATION AND CHARACTERISATION

There are many fabrication and characterisation techniques which can be used to fabricate semiconductor devices in different designs and scales. This chapter will give an overview of the techniques that are relevant to this work. The practical side of the research will take a linear format as both the fabrication and testing devices will gradually be scaled down to the nanometre range. The purpose of which is to enable the author to develop the relevant skills and experience to a point at which nanoscale devices can be reliably fabricated and tested.

4.1 Plasma Cleaning

This is a vacuum cleaning technique used to remove some suspected impurities on the surface of a substrate by creating a plasma with the help of argon or oxygen gas. The excitation and ionisation of gas atoms take place at the higher energy state in the plasma. The relaxation of the atoms and molecules at lower energy state leads to the evolution of glow light linked with plasma. The colours of the light depend on the different gases used during the plasma process. For argon gas, light purple is observed while oxygen gives light blue colour during the plasma process. The energetic plasma activated species include electrons, ions, photons (Ultra-violet range), metastable and radicals. These energetic species bombard the surface in contact such that energy is transferred on to the solid. The energy transferred by these species releases within the solid by a variety of both physical and chemical processes leads to surface modification and cleaning.

In this work, Bio-Rad PT7100 barrel etcher is used as the pressure in the chamber of this equipment is pumped down to 10^{-2} torr as the oxygen gas is been introduced until the pressure inside the chamber is 10^{-1} torr. The substrate was placed in the chamber horizontally as the radio frequency generator was regulated by tuning of the input power and reflecting power in order to achieve a gas pressure that will aid the cleaning. The glow purple colour appeared on the chamber of the etcher confirming the presence of plasma for the cleaning. The substrate was left in the chamber for twenty minutes for the cleaning and as the temperature of the etcher reduces, the substrate was removed and ready for deposition.

4.2 Thermal Evaporation

Thermal evaporation is a Physical Vapour Deposition (PVD) technique which is used commonly in the semiconductor industry, and it can be defined as the process used for depositing materials in thin films formed on a suitable substrate in the gas phase. This process is taken place in a chamber where sufficient vacuum should be obtained ($\approx 1 * 10^{-6} Torr$). This process is in a vacuum for two main reasons: to clear the contamination, dust particles, and other gases e.g Nitrogen and oxygen which can affect the purity of the deposition. Also, to ensure that the distance between the source and the target is less than the Mean Free Path(MFP).

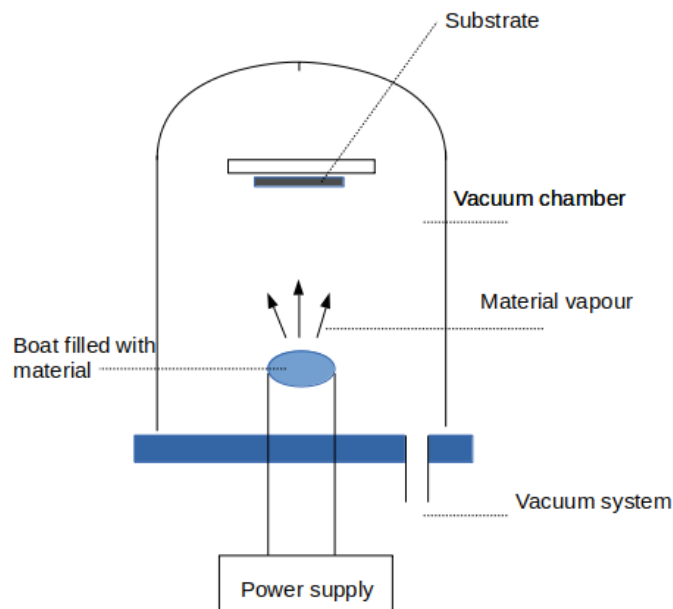


Figure 4.1: Internal structure of thermal evaporator

Thermal evaporation can be obtained by heating materials, often a metal by using a filament or boat which depend on the melting point of the material to be deposited. By applying a current through the filament or boat resistive heating melts the material to be deposited (With consideration of the vapour pressure of each material which plays a significant role in the deposition process), it evaporates then condenses on a prepared substrate. The thickness of the deposition is measured using a quartz thickness monitor.

Thermal evaporation can offer a controlled deposition rate, low impurity, and directionality. On the other hand, the film uniformity across a large substrate is not as high as other deposition techniques such as sputtering. It is also very challenging to deposit less than the 5nm thin film by using this technique. This is one of the techniques used in the fabrication antennas which will be discussed in chapter 6 of this thesis.

4.3 PLASMA – ENHANCED CHEMICAL VAPOUR DEPOSITION (PECVD)

Deposition of thin film materials from a gaseous state to solid state at low temperature with the help of plasma can be done by using Plasma Enhanced Chemical Vapour Deposition Technique. PECVD consists of two parallel electrodes which often arranged in horizontal direction inside reactor chamber which in most cases cylindrical in shape and made of stainless steel as a material, the samples were placed horizontally on the bottom of the down electrode which is grounded and various pipes were connected to the chamber for the supply of gases in order to produce plasma for the deposition as depicted in figure (4.2)[129][130] In this technique, the requirement of external heat energy to excite or to ionize the atoms or molecules of gases leads to the creation of the plasma in the PECVD reactor. The external electrical energy can also be created at a various audio frequency of 10 or 20 KHz, the radio frequency of 13.56 MHz, and a microwave frequency of 2.45 GHz respectively with the presence of carrier gases such as argon, silane, hydrogen, oxygen or nitrogen at low pressure [130][131]. When precursors in form liquids or gases introduced into the chamber PECVD reactor in the presence of plasma, these precursors undergo dissociation and activation at low temperature. As soon as the plasma is in contact with the surface of a particular substrate, the precursors in the plasma stream are deposited at a low temperature as compared to an ordinary chemical vapour deposition. It is a low-temperature de-

position technique with a flexible substrate, precursors can be organic and inorganic, the rate of deposition is high, it is thermally and chemically stable, the deposited films have some uniqueness of chemical properties, high solvent and corrosion resistance [131]. Though this technique has some limitations such as high cost of equipment, the presence of some toxic and explosive gases in the plasma stream, it is time-consuming, the presence of residual and compressive stresses on thin films deposited and the films may be unstable against humidity and aging[131]. At the EMTERC, the deposition was done in the plasma - enhanced chemical vapour deposition system for 10 minutes with 100 sccm Argon (Ar) and 10 sccm methane (CH₄) gases with a total pressure of 100 mTorr and DC radio frequency power of 100 W.

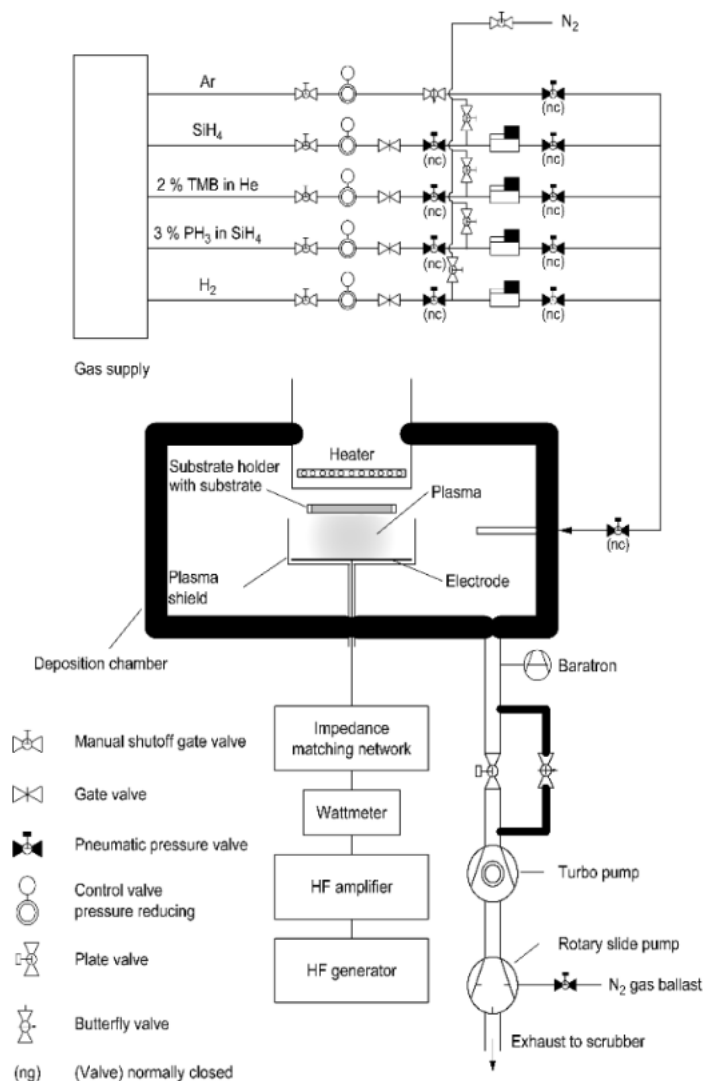


Figure 4.2: The block diagram of Plasma – Enhanced Chemical Vapour Deposition[129]

4.4 Lithography

Lithography is a fabrication technique where the etching operation is used to produce the desired structure from a bulk material. The etching process is done by using a mask to expose and shadow the material from a specific energy source. The perfect control for all the process and for the structure parameters is the most advantage of this technique, however, in an industrial process and very slow to be utilised. There are many different types of lithography such as:

Photolithography is a process used to pattern parts of a thin film or the bulk of a substrate in micro-fabrication. It utilises the light to transfer a specific geometric structure from a photomask to a photoresist (light-sensitive chemical) on the substrate[132].

Reactive-ion etching (RIE) is an etching technology which used chemical reactive plasma to etch material deposited on wafers. In this process, high energy ions from the plasma (which is generated under low pressure) react with the wafer surface. RIE which is also used in micro-fabrication to fabricate devices such as diodes and MPA.

Electron-beam lithography (EBL) is an act of scanning a focused beam of electrons to transfer geometric pattern on a surface covered with an electron sensitive film called a resist[132]. EBL has the advantage it can transfer custom shapes (direct-write) with sub-10 nm resolution which make it suitable technique to fabricate nano-antennas.

4.4.1 Photolithography

In this work, the track layers design was imaged as photo onto the panel, as this is carried out in a clean room to ensure that no dust gets on to the surface of the sample which can cause a short or open circuit on the prepared sample. The panel is first coated with a layer of photosensitive film, the photoresist, which is hot-rolled onto the copper using a cut-sheet laminator as this is carried under the yellow light in a dark room due to the sensitivity of the photoresist to the UV light. The bed of the printer has registration pins matching the holes in the photo tools and the panel. The first track film was loaded onto the pins, then on to the laminated panel and finally to the second track film. The pins ensure that the top and bottom layers are precisely aligned. The printer uses powerful UV lamps to harden the photoresist. The photomask is clear where we want the resist to harden and black where there is no presence of resist. The Mylar film which protected the photoresist is removed and put through a developer which removes the unhardened resist. The unwanted copper was removed using a

powerful alkaline solution to etch away the exposed copper. The process is carefully controlled to ensure that as etch down, sideways will not etch as well. This means that the finished conductor widths are as designed.

4.5 Electrospinning (ES)

Electrospinning technique is an efficient method to fabricate polymeric nanometer scaled fibres in terms of a normally surrounded atmosphere [133][134]. This has led to an improvement of ultra-fine structure in micro and nanometer scale which can enhance the materials characterisations in terms of electrical and mechanical properties such as conductivity, hardness, and so on. These Electro-spun structure materials are promised material for different types of applications, for example, it has been used to fabricate field-effect transistor (FET), chemical and Biological sensors[135][136]. In the first instance, this technique regarded as a very simple and easily controlled where the polymer material is critically examine to the production of fibre materials but fully understand the process reveal it complexity. The basic set up of electrospinning as shown in figure (4.4) consists of syringe pump, metal connecting tube, metal capillary needle (i.e. spinneret), high voltage power supply, Taylor cone and a grounded conductor or collector. The high voltage power supplies usually direct current (DC) potential though alternating current (AC) also practicable. The Taylor cone (with diameter of about 100 μm) connected to the tip of conducting capillary tube, where the syringe play a host to the polymer solution and connected to the metal tube. In view of using syringe pump, the polymer solution feed into the system at a controllable and constant rate for the achievement of fibre materials. The Taylor cone concurrently serves as an electrode where high electric field in the range of 100 to 500 kV/m applied and maintain distance to the collector of about 10 to 25 cm.

The operation process (as shown in figure (4.4)) begins when an adequate voltage is utilized to an electrically conducting solvent, which is streaming in a metallic nozzle, the formulaic hemispherical fluid drop (at the nozzle exit) distorts into a Taylor cone and creates a liquid jet. Following this, the electrified jet undergoes fast expansion and hardening process. The jet becomes stable close to the edge of the nozzle exit. However, while it moves away from the capillary it turns to be elongated and unstable due to whipping movements originating from deflection instabilities. This whipping process occurs in the ES technique caused the uniform fibres to be fabricated.

Theoretically, the drop from the nozzle will experience two electrostatic forces, which include the Coulombic force exerted by the external electric field applied and

the electrostatic repulsion between the charges at the surface of the drop. These electrostatic forces need to be overcome the surface tension of the liquid polymer material and leads to the ejection of the liquid drop from the nozzle. The formation of fibres materials in terms of dimension and shape depend on the properties of the polymer material that include solubility, molecular weight and glass transition temperature. The properties of the solution made from polymer such as electrical conductivity, surface tension, humidity, viscosity, concentration and visco-elasticity will have significant impact on the fibre materials. The properties of the collector, the field strength and geometry of the electrodes as well as the feed rate of the solution also play important role in the formation of fibre materials. In this work, the syringe used was (5ml NORM-JECT), the pump was (Harvard-APPARATUS Pump II) and the metal connection tube made in the laboratory

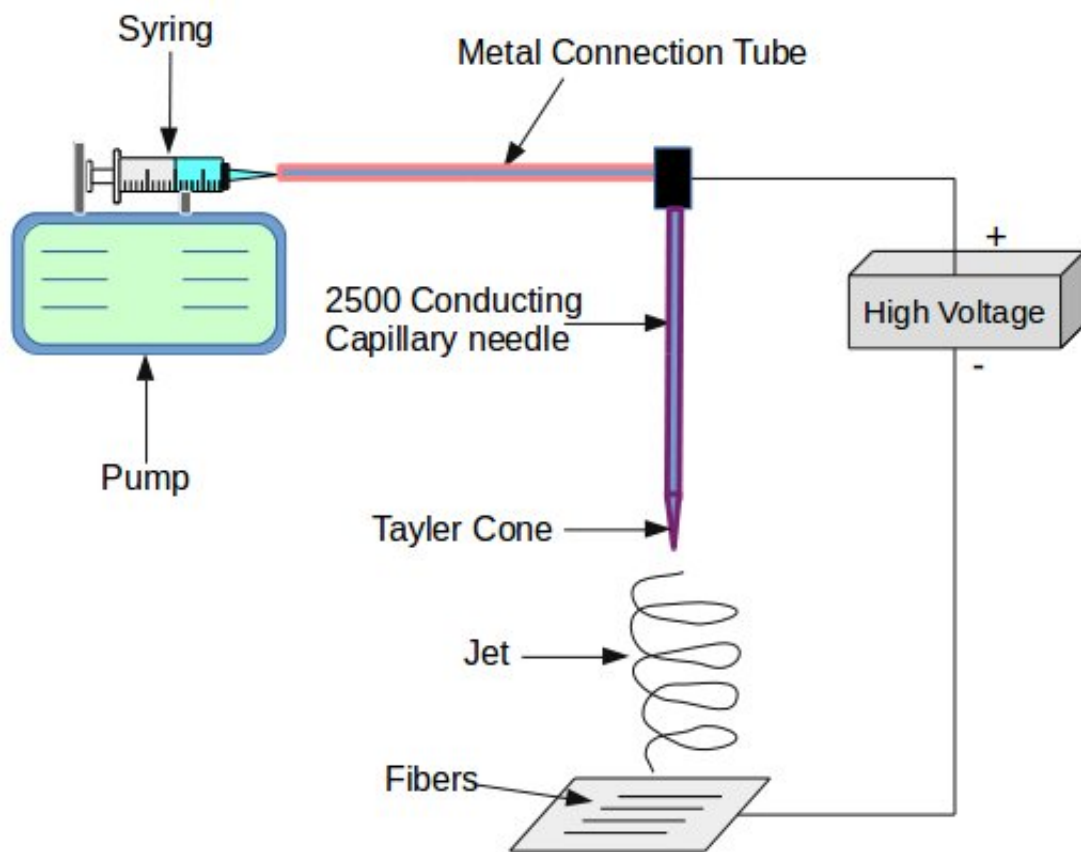


Figure 4.3: Electrospinning set-up

4.6 Focused Ion Beam (FIB)

This is a microscopy technique uses for both the imaging and sputtering of materials[137]. It offers both high-resolution and flexible or robust micromachining in a particular platform[138]. The principle of operation similar to scanning electron microscope (SEM) but uses a beam of positively charged particles to scan across a sample as the resultant signal at each of the scan position are plotted to form an image. The Ga-based blunt needle source is used as the source of positively charged ions due to low melting temperature, low vapour pressure and high stability[137].

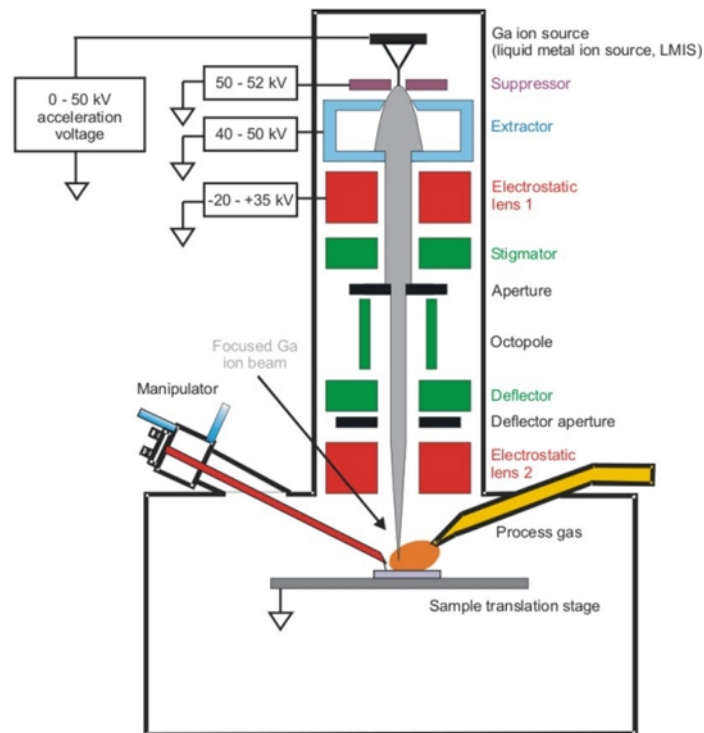


Figure 4.4: Focused Ion Beam set-up

From the reservoir, Ga flows to the tip of the needle and extracted by the field emission. An electric field of magnitude 10^{10} the V/m generated at the tip of the needle between an extraction electrode and the needle[137]. From the needle tip, a beam of an ion travelled through the columns of condenser and objective lens in order to select beam diameter of about 5 nm and current of approximately $2\mu\text{A}$ [137]. A highly focused beam of an ions incident on the sample, scan over the sample surface severally in order to generate signals for the imaging. One of the major advantages of this technique is that the actual shapes and sizes of the sample grains are viewed in the three-dimensional format. For this work, a dual beam FIB that comprises Energy Dis-

persive Spectroscopy (EDS) detectors and electron backscatter diffraction (EBSD) was used and the characterisation was carried out at Loughborough Materials Characterisation Centre situated at the University of Loughborough.

4.7 Profilometer

This is one of the techniques used to measure or determine the thickness of the thin film deposited on a substrate by using surface profiling and the instrument using for this purpose is called profilometer. There are two types of this instrument, the optical-based and the stylus-based profilometer. The most important parts of this instrument are the stage that holds the sample and a detector which determine the points on the sample. Moving the probe physically across the surface of the sample in order to obtain the surface height, in which mechanical feedback provided which monitor the force from the sample by exerting the force against the probe as it scans across the surface of the sample, this feedback is used to position the arm of the probe with a specific amount of force as the set point is determined and this process is called stylus-based profilometry. This technique has two major problems: It requires surface contact which can lead to damage to the sample and sample contamination is inevitable. At the EMTERC, a Tecnor Alpha – Step 200 is used in this work to measure the thickness of the sample deposited on the substrate, aside from the thickness measurement, it can also measure the micro-roughness and etch depth.

4.8 Scanning Electron Microscopy (SEM)

SEM is a method which gives the opportunity to investigate the topography and composition of samples in down to a few nanometres (nm). SEM uses a focused electron beam for scanning and producing images of the sample. The beam (generated in a vacuum) produced by an electron gun moves through different lenses which focus it to a very precise point. (As illustrated in figure (4.5)). After that, when the electron beam touches the surface of the sample, secondary electrons will be produced and emitted as a result of a complex interaction between the beam electrons and the atoms of the specimen. Finally, these secondary electrons will be detected and magnified to produce the final image of the sample. In this work, SEM will be used to verify the geometric space of the nano-antennas. (The impurity can collide and scatter the electron beam for this reason the vacuum is essential in this process) [139] [140] [141]

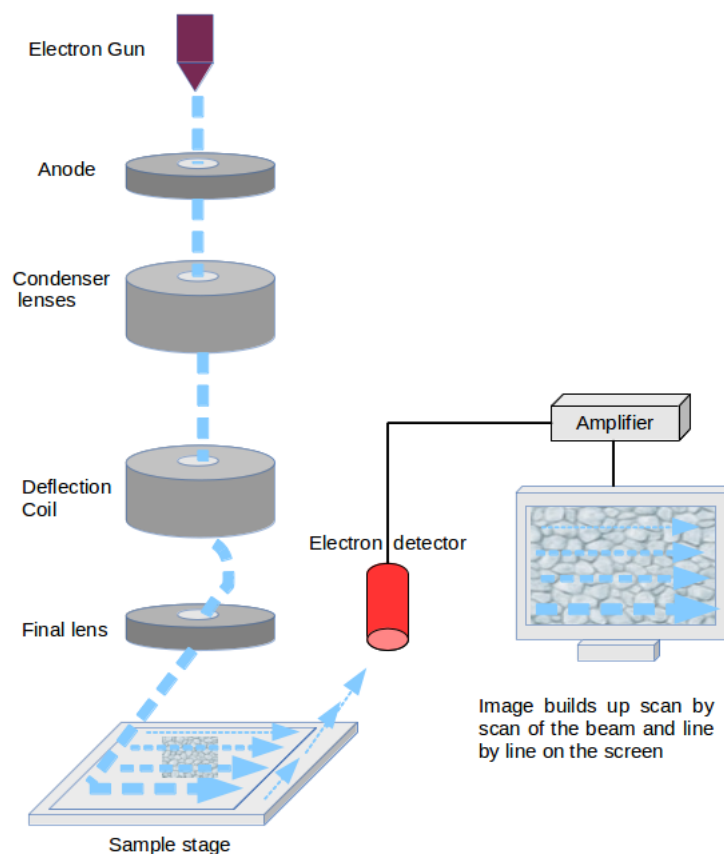


Figure 4.5: Scanning Electron Microscope (SEM)

4.9 Fourier Transform Infra-red Spectroscopy (FTIR)

This is a non-destructive and ambient temperature operation technique used to reveal information about the rotation and vibration of some chemical bonding presence in the sample of a material. FTIR is further used to identify unknown materials, determine the amount or quantity of components in a mixture and determine the standard or stability of a sample in both organic and inorganic forms[142]. This technique has some advantages such as universality (i.e. some molecules have strong absorbance in the near infrared, mid-infrared and near-infrared regions of electromagnetic radiation), provide rich information about the spectra (i.e. the peak positions provide the structures of the molecules, the intensities provide the concentration of molecules and the peak width provide chemical matrix of the sample), fast and easy to use (i.e. many samples can be analysed in 5 to 10 minutes), inexpensive (unlike many spectroscopy equipment is relative to low cost) and sensitive in nature (usable amount of spectra is provided by this equipment). Some of the advantages include the inability to detect some molecules, water and inability to measure the mixtures of some molecules[142][143]. For every FTIR spectrometer comprises of source, interferometer (Michelson interferometer), beam splitter, mirrors (stationary and moving) and detector. When a beam of light from the infrared source travels through an aperture which controls the quantity of light to the sample enters or incident on the interferometer from a particular part of the equipment as shown in figure (4.6)

The interferometer causes the beam to split into two light beams and travel in two different paths at right angles, as one of the beam incidents on the stationary mirror and back to the beam splitter and another beam incident on the moving mirror. The movement of the moving mirror makes the path length varies with respect to the stationary or fixed mirror as the beam incident back on to the beam splitter and recombined. The recombined beam allowed travelling through the sample, as the sample absorb, reflect and transmit some of the beam incidents on the sample as the specific wavelengths or a frequency that determines the characteristic of the sample and finally to the detector where the final measurement takes place[143]. In this work, Bruker Alpha compact spectrometer is used to measure the wave-number vs transmittance or absorbance was recorded accordingly.

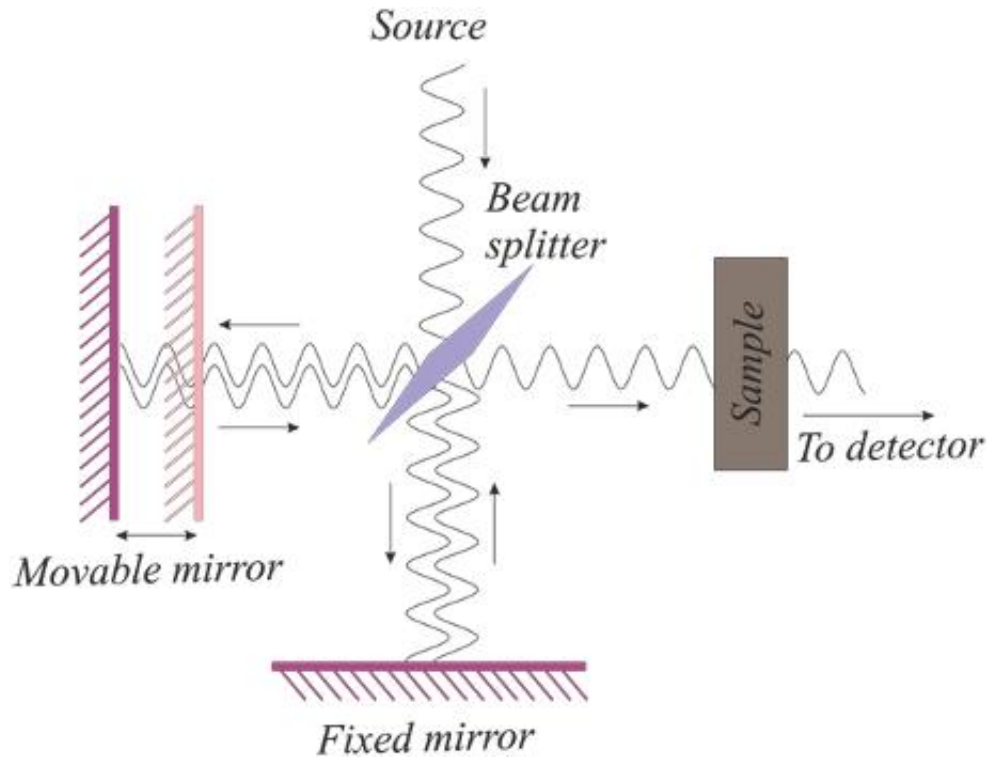


Figure 4.6: FTIR spectrometer set up[144]

4.10 S-Parameter

In order to get introduced into the measurement techniques, it is important to understand the importance of S-parameters in the active and passive device. The S-parameters matrices are useful at low frequency to prove the general analytical results. However, it is very difficult at high-frequency measurements device as it requires open and short circuits termination for evaluating this device and also it is not practical to measure the discrete voltage and currents at high frequency. By using a directional coupler it is easier to measure the travelling wave of a device[145]. To understand the behaviour of a two-port network is to use the incident wave as excitation at each port and to make sure the resulting exiting waves. The exiting waves are called reflected waves [146]. In actual scenario, the wave which is excited in an input port may result in an incident wave in another port and therefore this wave is called an incident wave and the wave which exists from that port is called reflected waves. For a better understanding a block diagram is representing an incident and reflected wave and referred to as S-parameter as shown in figure (4.7)

In this block diagram, a_i represents the incident wave and b_i represents the reflected wave, where i represent the number of port. In S-Parameters both a and b waves

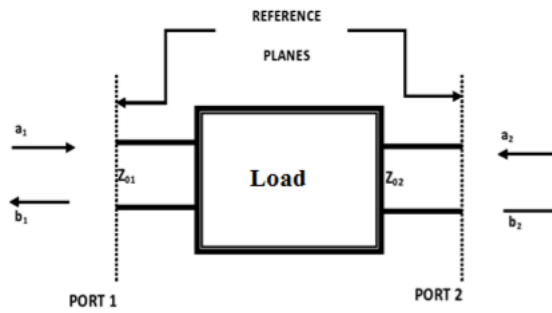


Figure 4.7: Block Diagram of S-Parameters[147]

have both magnitude and phase at each frequency of the input signal. The wave direction and reference planes are shown in the figure (4.7) for a two-port network. However, the same principle can be applied to any number of the ports and the ports need not be of the same type, for example, coaxial port and wave-guide port.

Characteristics impedance of the device is represented as Z . In figure (4.7) Z_{01} & Z_{02} represents the input and output impedance of device from port 1 & port 2. For each port, the characteristics impedance can be defined in terms of incident and reflected waves of the transmission line which is connected to the port. By using a and b waves, a set of the linear network can be characterized by describing the reflected waves from each port in terms of incident waves at all the other ports by using this constant network which is called S-parameters.

For example, for a two port b wave will be leaving the port 1 with respect to the reflected wave from the input port which is $S_{11}a_1$, in addition to that a wave that passes through the two-port network from the port 2 is represented as $S_{12}a_2$.

$$b_1 = S_{11}a_1 + S_{12}a_2 \quad (4.1)$$

Similarly

$$b_2 = S_{21}a_1 + S_{22}a_2 \quad (4.2)$$

The same approach can be applied to 'n' number of the network which connected the transmission line to the ports. For the above equation, the S parameter can be expressed in matrix form which leads to the $n \times n$ matrix, where n represents the number of ports. For the two ports network s parameters matrix can be represented as

$$\begin{pmatrix} b_1 \\ b_2 \end{pmatrix} = \begin{pmatrix} S_{11} & S_{12} \\ S_{21} & S_{22} \end{pmatrix} \begin{pmatrix} a_1 \\ a_2 \end{pmatrix} \quad (4.3)$$

From the above matrix S_{11} represents the forward reflection coefficient or input match and S_{11} is otherwise called the input return loss. S_{22} represents the reverse reflection coefficient or output match. S_{21} forward transmission coefficient otherwise called forward gain or if it is negative then it represents a loss. S_{12} represents the reverse transmission coefficient from the output to the input port which is called isolation. Often S parameters are expressed in a log-magnitude format for example dB. The individual S parameters are evaluated by using these relationships.

$$S_{11} = \left. \frac{b_1}{a_1} \right|_{a_2=0} \quad S_{12} = \left. \frac{b_1}{a_2} \right|_{a_1=0} \quad S_{21} = \left. \frac{b_2}{a_1} \right|_{a_2=0} \quad S_{22} = \left. \frac{b_2}{a_2} \right|_{a_1=0} \quad (4.4)$$

In microwave application, especially transistor characterization, S parameter are particularly desirable because of their evaluation does not require short or open circuit termination. Instead, it requires the matched loads are placed at the input or output port and either the transmission or reflection coefficient is measured[145]. Suppose if the network is reciprocal [148] then

$$S_{ij} = S_{ji} \quad (4.5)$$

S parameters are complex quantities, which consists of phase angles that correspond to the respective network port with reference to the planes used in the measurement. Another advantage of the S parameter is that a change of reference planes farther away from them by the network by an electrical distance θ degree results in negative argument changes in S-parameter. This features of S parameters allows convenient network de-embedding[149] in which S parameters of the network can be easily inferred, even when the measurements are made using the reference planes. For example, when a device measured by using a test reference planes, the S-parameters can be easily calculated by adjusting the only the S parameter phase angles. This is an option which is available in most of the network analyser which will be discussed later in this chapter.

There are many advantages of S parameters, unlike other parameters for example characteristics impedance Z, characteristics admittance Y, and ABCD parameters whose values are independent of the measurement system whereas S parameters de-

pendent on the impedance of the transmission line connected to the ports. The S parameters are only valid when it is associated with the reference planes of the system which is impedance used in their measurements. Usually, 50 ohms is used for the measurements[150].

4.11 Vector Network Analyser (VNA)

Vector Network Analyser (VNA) is the key instrument used for making a variety of measurements on passive as well as active microwaves components and networks. A network analyser measures both amplitude and phase of a signal over a wide frequency range within a reasonable time. The basic measurements involve an accurate reference signal which must be generated with respect to which the test signal amplitude and phase are measured. A schematic block diagram of a complex network analyser is shown on figure (4.8) and a picture of VNA is shown in figure (4.9).

The microwave signal from a sweep generator is first divided by means of a signal splitter into test signal and a reference signal. The test signal is transmitted through the Device Under Test (DUT), while the reference signal passes through a phase equalising the length of the line. Since processing of microwave frequencies is not practical both the test and the reference signal are converted to a fixed intermediate frequency by means of a harmonic frequency converter. The output signal from the harmonic frequency converter is compared to determine the amplitude and the phase of the test signal, the harmonic frequency converter uses a phase-locked loop which helps the local oscillator to track the reference channel frequency. This allows swept frequency measurements. The frequency conversion takes place in two steps. The first mixer converts RF to the fixed if in the MHz range and then after amplification, they are further converted to another fixed RF in the kHz range by means of the second mixer for the final amplitude and phase comparison.

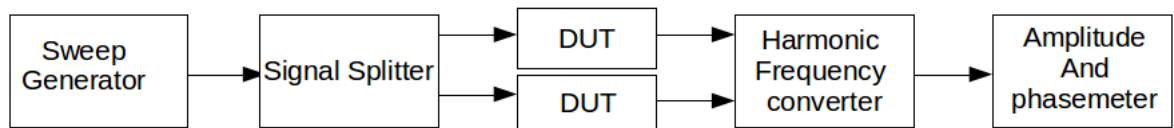


Figure 4.8: A schematic block diagram of a Vector Network Analyser (VNA)

The Vector Network Analyser as shown on figure (4.9) is a test device which is used to measure the network parameters of the electrical network. VNA usually measure S-parameters at high frequencies since the transmission and the reflection of electrical networks are easy to measure there.



Figure 4.9: Vector Network Analyser (VNA)

4.11.1 Networks measuring using VNA

The fundamental 1 and 2 port method used for VNAs calibration can be utilised to measure the active network from DC to 325 GHz. Nottingham University has three different VNA test set-ups to cover this range of the frequency spectrum. Figure (4.10) illustrates the (Test Bench 1) which demonstrates the s-parameters set-up measurement using Agilent E8364B VNA with a cascade probe station to test active elements from DC to 110 GHz. However, figure (4.11) represents (Test Bench-2 and 3) which displays the s-parameters setup measurement with the frequency extenders to measure the s-parameters in two frequency ranges (140 to 220 GHz) and (220 to 325 GHz).

Step 1: Determine the correct VNA for various applications. It is essential to select the right VNA setup to measure the S-parameter of the elements under test. There is a number of parameters should be considered such as availability, operating frequencies, Coplanar waveguide (CPW) probe station and external source.

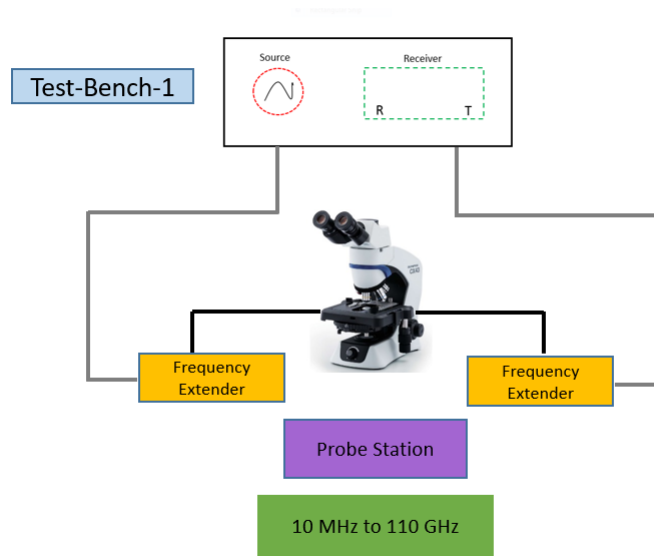


Figure 4.10: S-Parameter measurement setup using Agilent E8364B VNA up to 110GHz

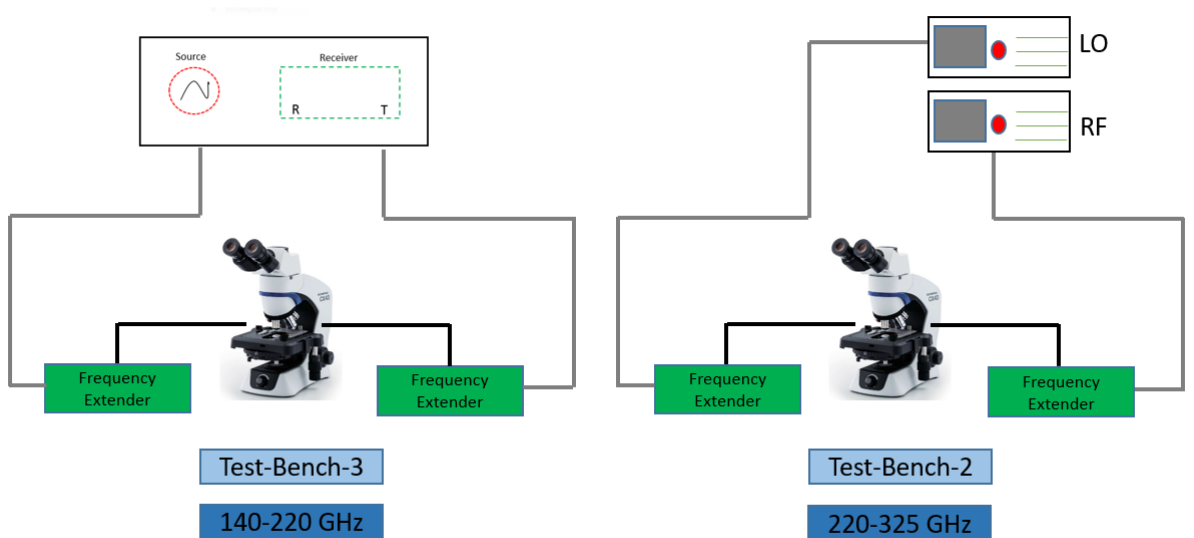


Figure 4.11: Two S-parameter measurement setup using Agilent VNA up to 325GHz

Step 2: VNA Set-up. Setting the VNA to make the experimental measurements needs some parameters to be considered; the start and the ending frequency (frequency span), the amount of frequency measurement points are determined, intermediate frequency bandwidth (IF) and input power level. The IF bandwidth has to be determined carefully, smaller IF bandwidth for normal S-parameter measurements give more accurate measurements but it should be taken into consideration that smaller IF bandwidth takes more time on the measurements. The IF bandwidth is set to 50 kHz for the measurements of the MPA. Moreover, The input RF power level has to be well set, since further high RF power can damage the CPW probe and the DUT. It should be acknowledged that the input power has to be established before the calibration, as an alteration of the input signal level will need the RF attenuator to be reset causing changing the RF match and therefore the calibration conditions.

Step 3: System calibration for S-parameter measurements. It is essential to calibrate a VNA to give accurate measurements if it is going to be used for S-parameters measurements. So, in order to get more accurate and repeatable s-parameters, the frequency response for all the external circuit elements such as cables, waveguide, probes which are connected externally to the VNA should be calibrated. One systematic error is to remove the imperfect elements or mismatch connectors during calibration. There are numbers of calibration options which have been described in table4.1. In general, the calibration is a process which is carried out by measuring a best-known standard elements such as a short, an open, matched load, and various line length depending on the calibration technique used. Almost all the calibration method mentioned are implemented internally in the VNA.

One Port Calibration Procedure

The Short Open Load (SOL) calibration method was utilised In order to calibrate one port network to measure input reflection S-parameters of the antennas from DC to 110 GHz. This technique was introduced first by Eric-Stridin in 1986[151]. It utilised three known standard (i) An Open probe which is set in the air, (ii) A short (a line) and (iii) 50 ohm matched load as illustrated in figure (4.12). Using this method, the VNA was calibrated to the CPW probe tip as the reference plane (as shown in figure (4.13)) and therefore the antenna input was connected to the CPW probe as the reference plane. After that, the calibration results were verified using the Smith chart results using the SOL method for one port calibration for the frequency range from DC to 110 GHz as illustrated in figure (4.14). It is noticeable from the figure that on the open circuit, the

reflected voltage and the incident voltage are equal and in phase. Whereas, at the short circuit the voltage of the reflected wave has to cancel the incident wave. So that zero potential. Moreover, with the load, the reflection coefficient is equal to 1.

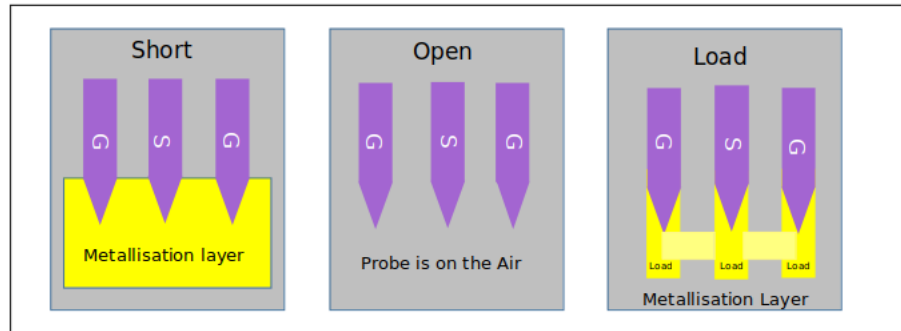


Figure 4.12: Schematic view of the SOL calibration substate

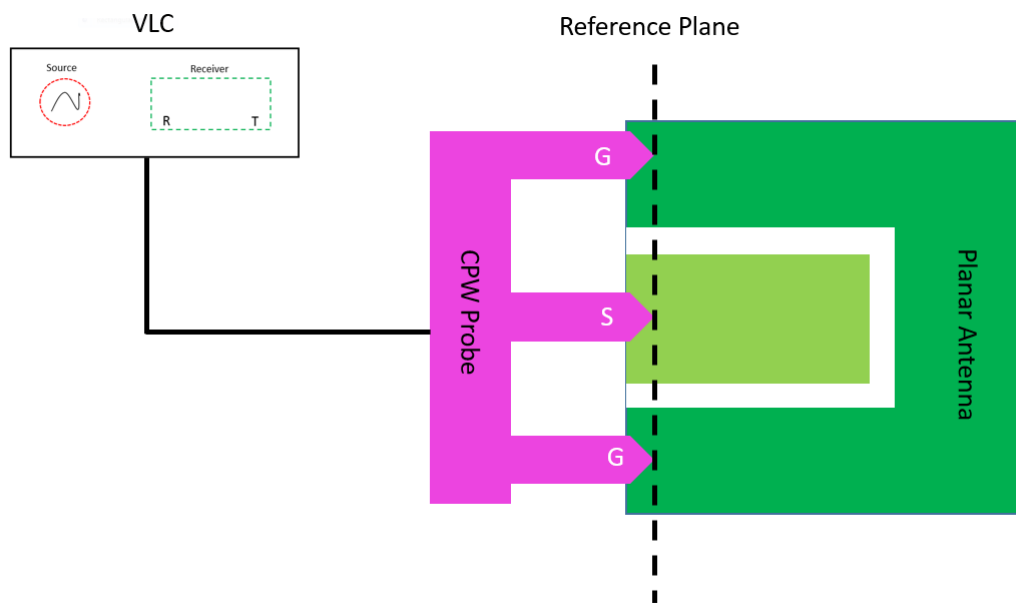


Figure 4.13: set-up of the VNA with the antenna

Two Port Calibration Procedure

The SLOT technique was utilised to calibrate the two-port network on account of its reliability and the other advantages which are mentioned in the table (4.1). Another reason for selecting this method is the absence of suitable calibration parts in

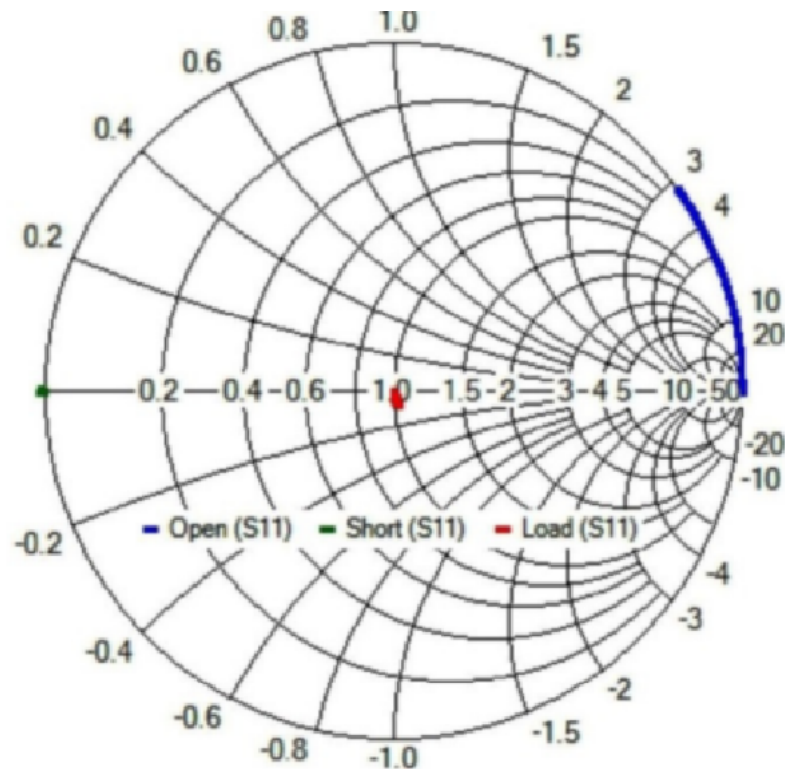


Figure 4.14: One port calibration Smith chart

CPW format on the other calibration techniques i.e. TRL, SSST and SOLR. A schematic presentation of the SOLT method calibration substrate for a CPW probe system is illustrated in figure (4.15). In this method, a measurement sequence is needed in which is represented as a block diagram in figure (4.16). basically, the reference plane of port 1 of the VNA is connected to a calibrated short circuit, then is connected to an open circuit and finally to a matched load (this will covering the whole range of possible reflection coefficients). However, the reference planes of port 1 and port 2 are connected to calibrate out the transmission losses. Again the sequence is repeated at the reference plane of port 2. Finally, the results were verified after calibration. Figure (4.17) illustrated the measured results of the SLOT calibration technique of a two-port network plotted on the Smith chart. It is noticeable form results represented on the Smith chart that the VNA was well calibrated to the CPW probe tip from DC to 110 GHz to measure the S-parameter of the antennas.

Step 4: Verification and Validation. After the process of VNA calibration, it needs to be verified. The verification process started by having a well know standard reference (the ω matched load on the calibration wafer), then measure its S-parameter and

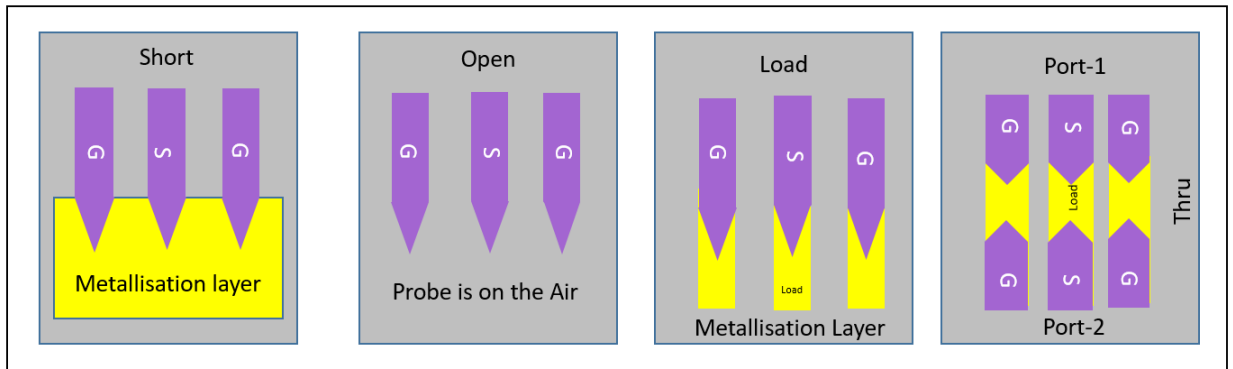


Figure 4.15: Schematic view of the SLOT calibration substrate[147]

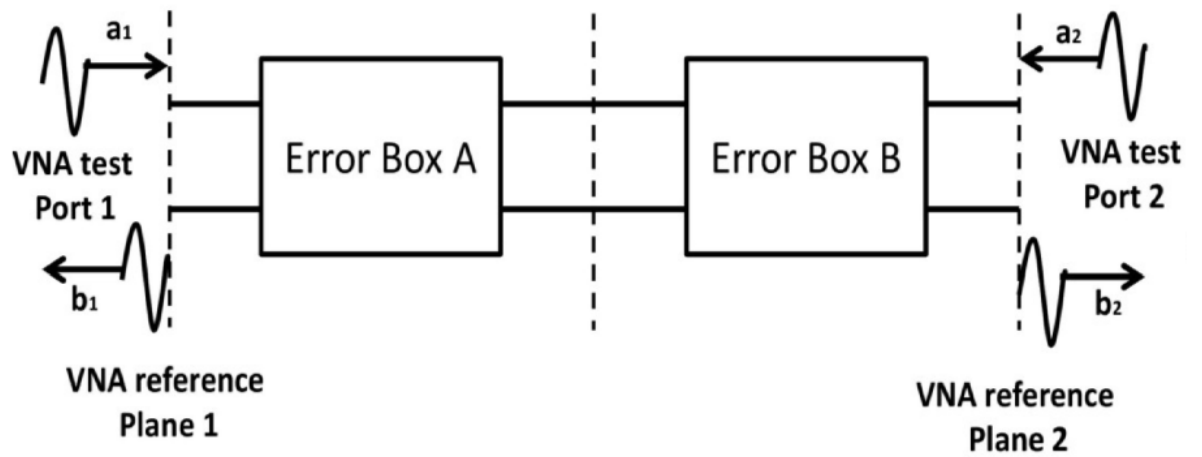


Figure 4.16: Block diagram of two-port network calibration

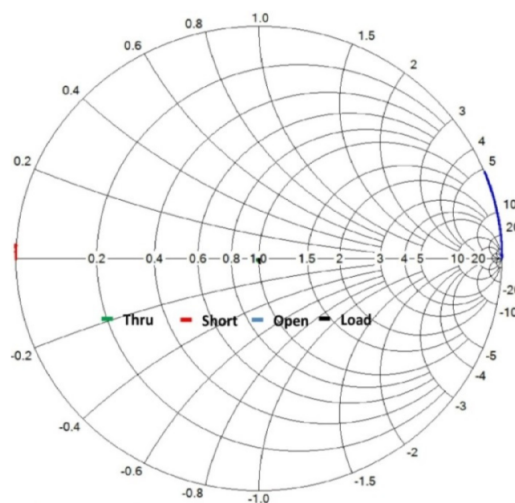


Figure 4.17: Two port calibration Smith chart[147]

compare it with the calibration measurement using (WINCAL) software. This validation procedure was used to proof that the measurements have been conducted without glitches and no resonance.

Step 5: Measurements. After completing the VNA calibration and verification, the probe station is aligned with the test wafer. In order to do this, an alignment marker is attached to the deceive wafer (as seen in figure (4.18)) and used to align the wafer on the right way, so the probes will step automatically from the device to the other device.

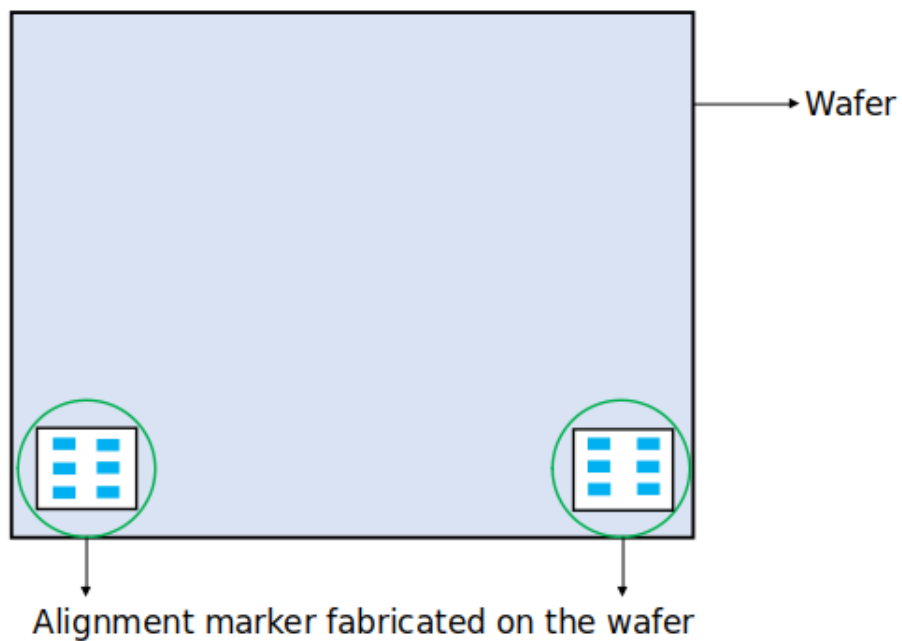


Figure 4.18: Alignment marker on the wafer

Calibration Algorithm	Description	Advantage	Disadvantage
SOLT (short-open-load-thru)	Common coaxially	Simple, redundant standards; not band limited	Requires very well defined standards, poor on the wafer, lower accuracy at high-frequency
SSLT (short-short-load-thru) Short with different offset length	Common in waveguide	Same as SOLT	Same as SOLT but with band limited
SSST (short-short-short-thru) All sorts with different offset lengths	Common in the waveguide or high-frequency coax	Same as SOLT but better accuracy at high frequency	Requires very well defined standards, poor on the wafer, band limited
SOLR/SSLR/SSSR Like as above but with reciprocal instead of thru	Like the above but when the good thru is not available	Does not require well defined thru	Some accuracy degradation, but slightly less definition, another disadvantage of parent calibration
LRL (Line-Reflect-Line) Also called TRL	High-performance coax, waveguide on wafer	Highest accuracy, minimal standard definition	Requires very good transmission lines, less redundancy so more care is required, band limited
LRM (Line-Reflect-Match) Also called TRM	Relatively high performance	High accuracy, only one line length so easier to fixture/on the wafer, not band limited usually	Requires load definition. Reflect standard set-up may require care depending on load model used

Table 4.1: Different kinds of calibration techniques[147][151][152][153][154][155][156]

4.12 Non-Contact THz Probe Measurement

Testing and characterisation of devices working at sub-millimetre wave frequencies and above are very challenging at their intended operation frequencies[157]. A present instrument like contact probes at the THz frequencies are suffering from availability, high costs, fragility issues and the least the difficulty of physical contact (especially with the smaller devices) which is required to conduct the measurements. Caglayan et al[158] presented a novel technique which can be used to test THz frequencies devices with non-contact probes as illustrated in figure (4.19), Device Under Test (DUT) is integrated which is incorporated with planar THz antennas, in which the non-contact probes and connected to VNA test ports through with a quasi-optical coupling setup. This simple configuration is anticipated to cover the THz frequency band (0.3 – 3 THz)

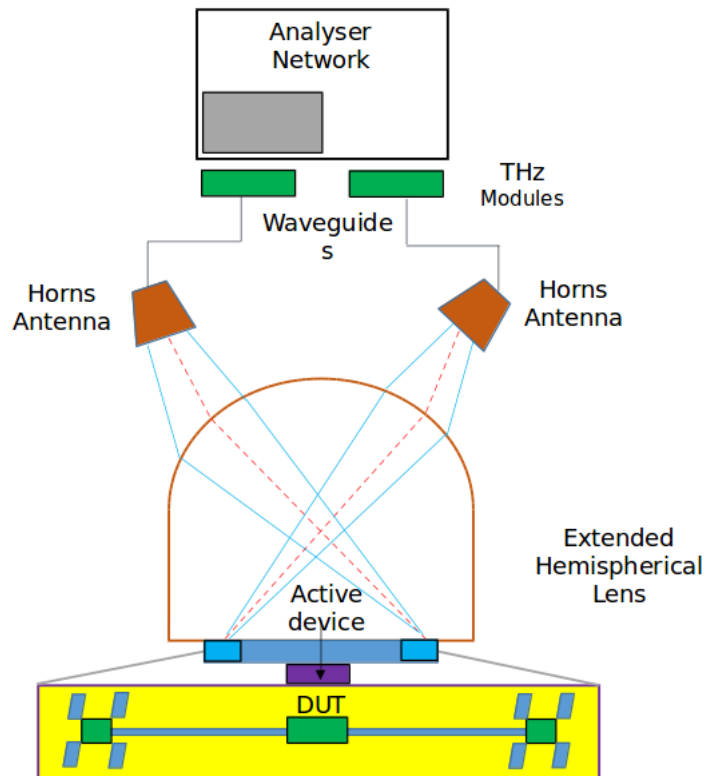


Figure 4.19: Illustration of Non Contact Probes Set-up[158]

4.12.1 Analysis Of The Non-Contact THz Probe

The key characteristic of proposed non-contact probes is the effective coupling of power in and out of DUT. In order to reach an efficient coupling exploitation integrated planar antennas, an extended hemispherical lens is used to devise the quasi-optical set-up. As represented in figure (4.20), the incident beam established from horn antenna connected to THz VNA module is focused upon on-chip antennas by the lens and fed to the device under test through the coplanar situation. The angle among optical axis and transmitting/receiving beam axis is really small, hence allowing effective coupling to planar antennas at broadside. The Butterfly shaped broadband slot antennas proposed in[159], are utilised as non-contact probes. MoM based full-wave simulations are used for the analysis of Coupling performance of non-contact probes. Figure (4.20) shows the radiation pattern of non-contact probe pair under plane wave illumination for a through the connection between the two antennas (no device). This figure illustrated coupling which is achieved over a bandwidth of 400 GHz just about 700 GHz. Half of the incident power is coupled to another antenna at 500 GHz, in contrast at 700 GHz and 900 GHz almost all of the power is coupled. The operation frequency can be extended more by easily scaling and arranging quasi-optical set-up parameters (extension length, lens diameter and so on) proportionately as needed.

4.12.2 Calibration Of Non-Contact Probes

Generally, because of one of the THz ports having only received capability, therefore conventional 2-port calibration techniques are not practicable to be utilised in this system. Hence, only S_{11} and S_{21} can be measured.

In this process, only forward error model of conventional 12-term error model can be utilised[160]. These terms can be extracted by means of 1-port calibration methods and one through measurement. In figure (4.21) functionality of various terminations for calibration purposes is analysed by comparison of scattered fields. Comparing to optimal coupling scenario, scattered fields from an open or short terminated non-contact probe is higher (7-8 dB) on the receiving antenna part, while the situation is reversed at the transmitting antenna. Consequently, short and open standards with various lengths with respect to reference plane can be utilised as the standards for calibration. Non-repeatable errors are anticipated to have a serious impact on calibration accuracy given the nature of the overall setup. So to increase the accuracy of the calibration, an over-determined calibration can be achieved using the least-squares method, as represented by in[161].

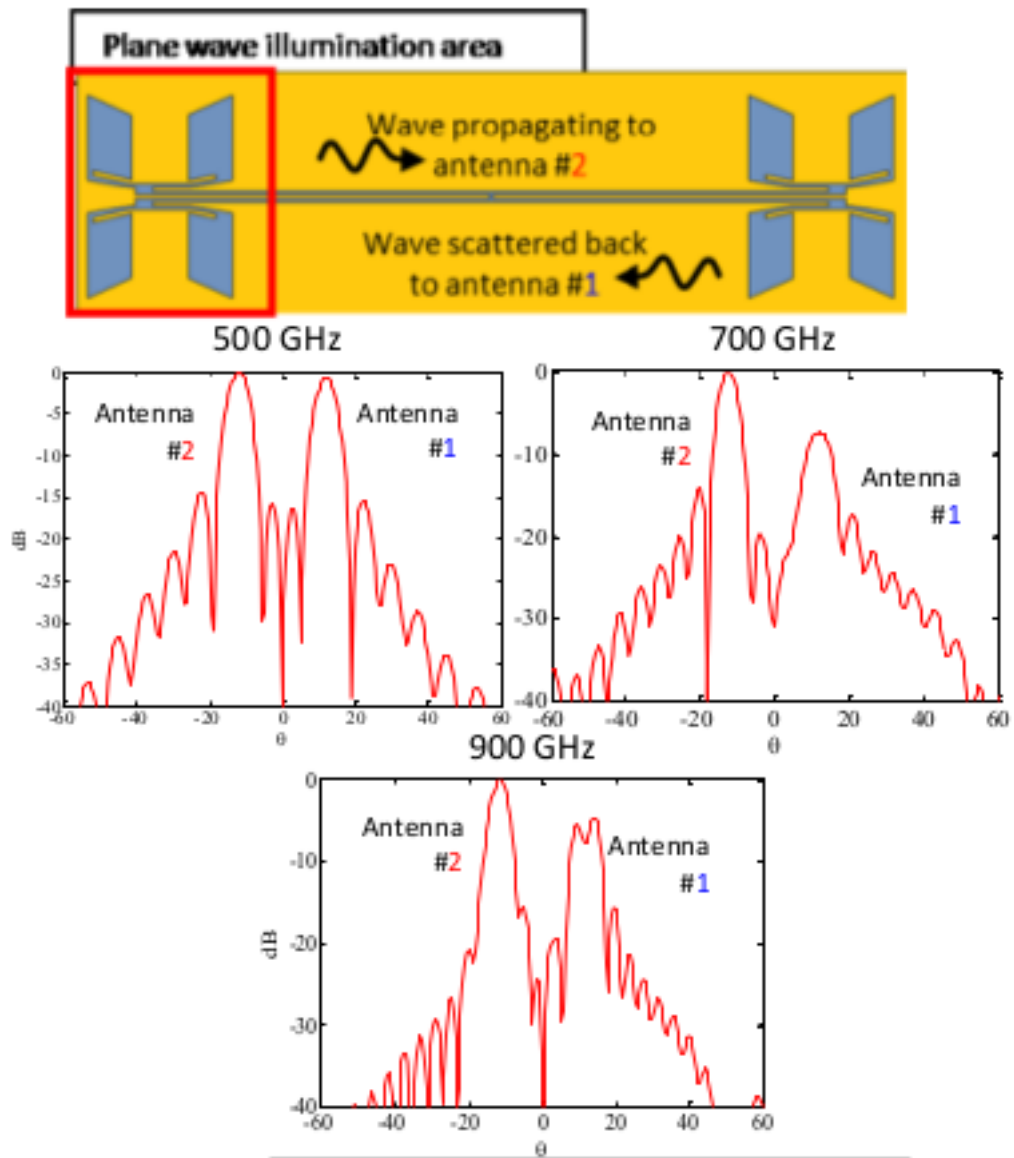


Figure 4.20: Radiation Patterns of Thru Connected Non-Contact Probes[158]

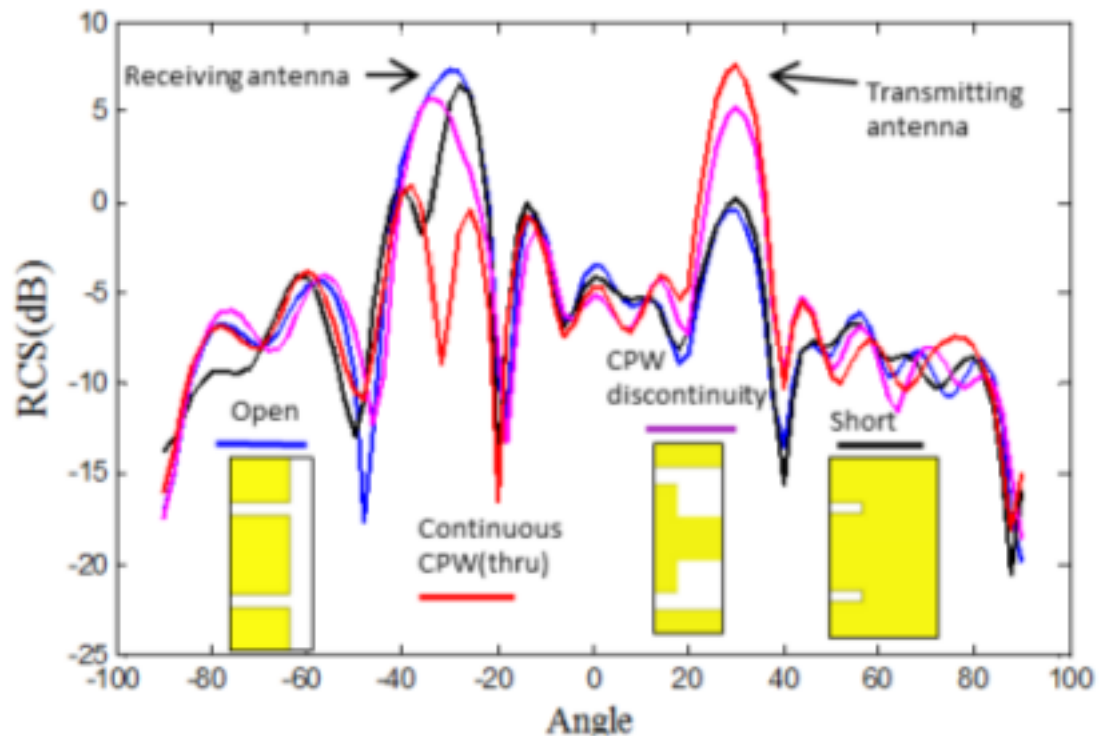


Figure 4.21: Scattering for different terminations of non-contact probes[158]

4.13 Thermal Gravimetric Analysis (TGA)

This is a method used for thermal analysis of a sample or material in which the change in weight or mass of a sample will be measured as a function of the change in temperature over the period of time in the presence of helium gas nitrogen gas, oxygen gas or air atmosphere. This method will assist in determine some of the following profiles of a sample such as thermal stability of a sample, composition of multi-component, decomposition kinetics of samples, oxidative stability of a sample, moisture and volatile contents of a sample, the effect of corrosive or reactive atmosphere on a sample and estimated lifetime of a product[162]. Thermogravimetric analysers or thermo-balance consist of a sample holder within a furnace, the furnace temperature is control by a thermocouple and purge gas system, the photodiode is working with a permanent magnet to provide mass change value and the data is recorded and process within the computer. The sample holder located within the furnace, it is usually made up of platinum due to its inertness and ease cleaning or some time made up of Aluminium or Alumina. It can hold anywhere from 40 to 500 μ L of a given sample or substance. The sensor is placed close to the sample to ensure that recorded temperatures are virtually the same as the sample's temperature. Also located within the

furnace is a connection to a purge gas system. Nitrogen, argon gas is sometimes released within the furnace to prevent the sample from oxidizing as the thermal analysis is taking place. The furnace may have a heating rate from 0.1°C per minute to 100°C or more per minute ranging from room temperature up to 1000°C . The sample holder in the furnace linked to a microbalance apparatus that monitors changes in mass. All fluctuations are detected and put through a data processor. Since a computer controls the furnace, the mass information can be combined in accordance with the temperature change. A sample is placed in the sample holder, as the furnace heats, the sample mass changes and moves the balance beam. This introduces an abnormal flicker between one of the two photodiodes and the lamp. The imbalance supplies the magnetic coil with an amplified current. The magnetic field formed by the coil rebalances the beam. Current produced by the photodiodes is a signal that is turned into mass change data by the computer software where thermogram can then be generated[163].

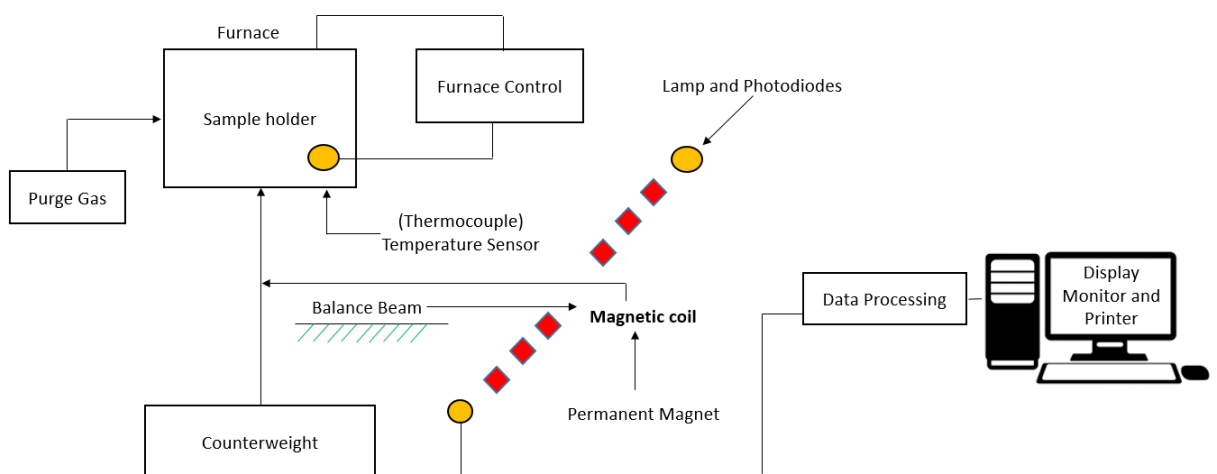


Figure 4.22: Thermal Gravimetric Analysis block diagram[163]

4.14 Differential Scanning Calorimetry (DSC)

This is a technique used for the determination of the rate of heat change in a sample to the heat change in reference sample as a function of temperature in a controlled atmosphere. This method is used to measure the following specific heat capacity, latent heat of fusion, glass and crystalline phase transition temperature, melting temperature, denaturation temperature, enthalpies and melting point of polymeric materials or samples e.t.c [164][165]. DSC consists of two crucibles the sample crucible

which is used for the prepared sample and has a lid with a hole(s) that allow an exchange of heat within the surrounding atmosphere and also the reference crucible as depicted in figure (4.23) It also consists of a thermocouple, the heating resistor and purged gas connector[165]. Once the oven is purged with a sample gas such as nitrogen, oxygen, an environment needed for transition and chemical reactions are created and observed. Furthermore, some of the spaces around the oven are purged with nitrogen gas in order to avoid freezing at low temperature. The heat is supplied to the sample and the reference crucibles through the heat sink such that the temperature difference between the sample and reference were kept constant and the amount of heat energy is recorded[165][166].

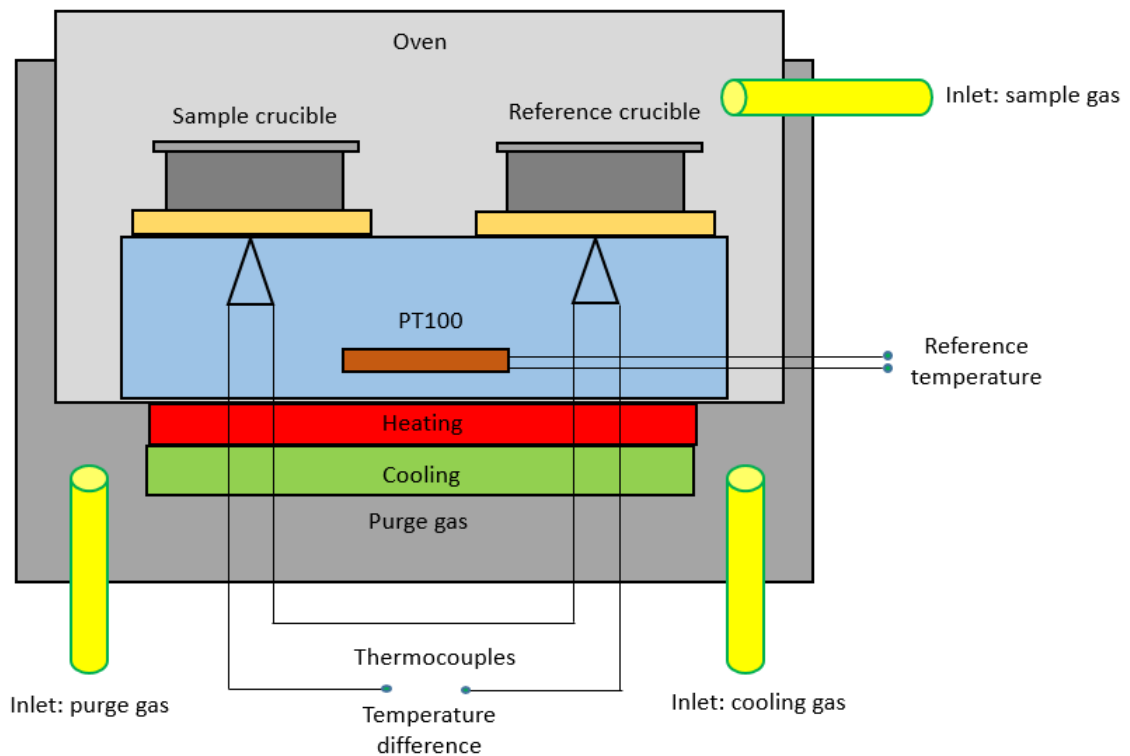


Figure 4.23: Schematic set up of differential scanning calorimetry

4.15 C-V measurements

This is a non-destructive electric measurement technique used in order to determine the response of the fabricated device to the sweep voltage at various frequencies as the capacitance is also been determined. In semiconductor and fabricated poly-

meric devices, some of the quantitative information such as doping concentration, the thickness of oxide layer, interface trapped charge density, electric charge distribution, built-in-voltage, dielectric constant, dielectric charge, dielectric capacitance, and surface density. These parameters can be determined at both low and high frequencies as the voltage applied varied across the device. In this work, HP4192A impedance analyser shown in figure (4.24) is used as the voltage applied is swept between -5V to +5v as the frequencies range between 1 KHz to 1000 KHz and data obtained for this measurement were reported in the results section. This technique is not sufficient enough to reveal the properties of polymeric materials antennae as the higher frequencies are required.

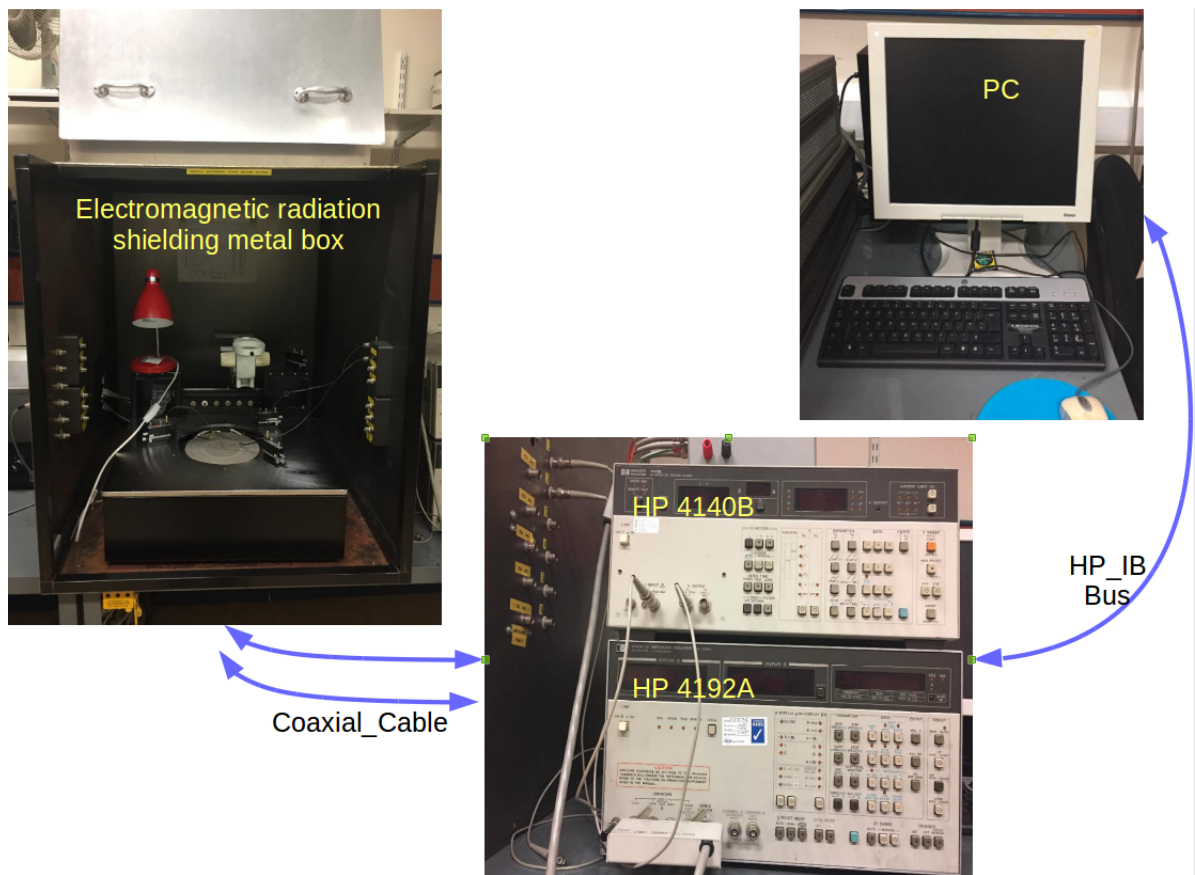


Figure 4.24: CV measurements set-up

4.16 Dielectric Measurements

There are no specific, suitable and accurate single techniques that can be used for the measurement of dielectric constant of materials after fabrication of the devices

over the entire band of frequency [167]. The criteria need to be considered in selecting any methods for the dielectric measurement depend on the frequency, temperature, nature of the material, size or thickness of the sample, required accuracy, destructive or non-destructive, contact or non-contact and cost of the device. In view of the aforementioned factors or criteria, the suitable technique for any dielectric measurement of a material will depend on the frequency needed and type of the materials involved. There are many techniques which can be used for the measurement which can be summarised in table 4.2.

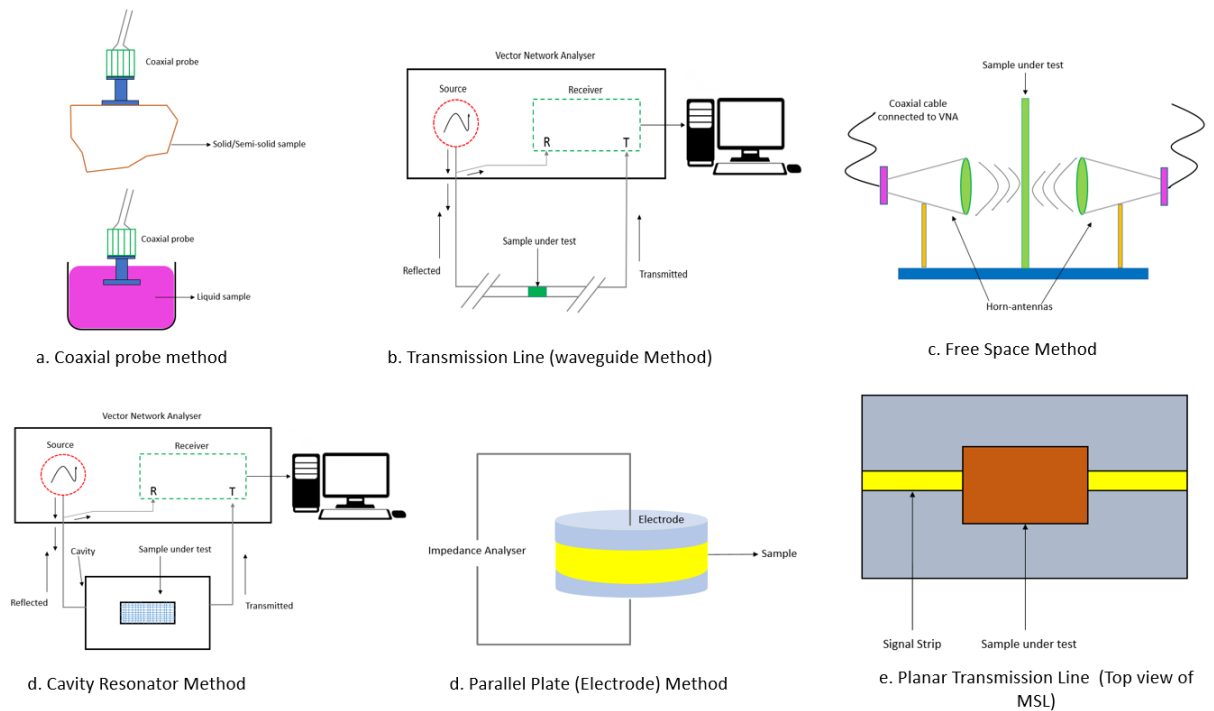


Figure 4.25: Different dielectric measurements methods[167]

Method	Dielectric properties	Materials	S-parameters	Advantages	Drawbacks
Coaxial probe	ϵ_r	Liquids, biological specimen, semi-solids	S11	Broadband frequency, simple and convenient, non-destructive, Isotropic and homogeneous and high accuracy for high-loss materials	Air gaps causes errors and repetitive calibration
Free space	ϵ_r, μ	High temperature material, large flat solid, gas, hot liquids	S11, S21	Wide frequency range support, non-contacting, easy sample preparation, moderate accuracy for high-loss and low-loss materials	Diffraction problem and low end limited by practical sample size
Parallel plate	ϵ_r	Thin, flat solid surface	S11, S21	Higher accuracy, relatively easier measurement and suitable for high-loss materials	Support for low frequency and electrode polarisation effect
Planar transmission	ϵ_r	High temperature material, solid/liquid sample	S11	Simple, cost-effective and rapid, no special sample handling	Low quality factor, air gap causes error

Transmission line	ϵ_r, μ	Coaxial line, waveguides	S11, S21	High frequency, anisotropic materials, and support for both solid and liquid materials	Sample preparation is difficult, unsuitable below a few GHz due to practical sample length limitation
Resonant cavity	ϵ_r, μ	Rod shaped solid materials, waveguides, liquids	Frequencies, Q-factor	Most accurate method, suitable for low-loss materials, no repetitive calibration procedure and high temperature capability	Measurement at only single or at resonant frequency and suitable for small size samples

Table 4.2: Different dielectric measurements methods[167][168]

Split-Post Dielectric Resonators This is one of the easiest, convenient, most accurate and reliable techniques used for the measurements upon low-loss to medium loss solid laminar dielectric materials as compared to other techniques mentioned earlier[167]. The real permittivity ϵ_r thermal coefficient and dielectric loss tangent $\tan \delta$ can be measured over a single fixed frequency or few ranges of frequencies (1 – 36 GHz) with this technique as developed by Krupka and his colleagues[169]. SPDR consists of two identical parallel dielectric resonators with a cylindrical disc placed along z-axis coaxially in order to create a small laminar gap for the placement of sample or specimen for measurement in an enclosed metal as depicted in figure (4.26)

As these two discs resonate together in a particular resonant mode, a circular polarised evanescent electromagnetic field exists in the gap region between them. If these discs were separated and resonate differently, the azimuthal field above and below their plane surfaces of these discs would decay exponentially as a result of the distance from the resonator. Since the resonators are close together with the distance between them (1-5 mm), the electromagnetic field magnitude between them is parabolic as a function of z with a shallow minimum in the centre of the gap[169].

As the samples placed in the specimen gap, the circularly-polarised azimuthal elec-

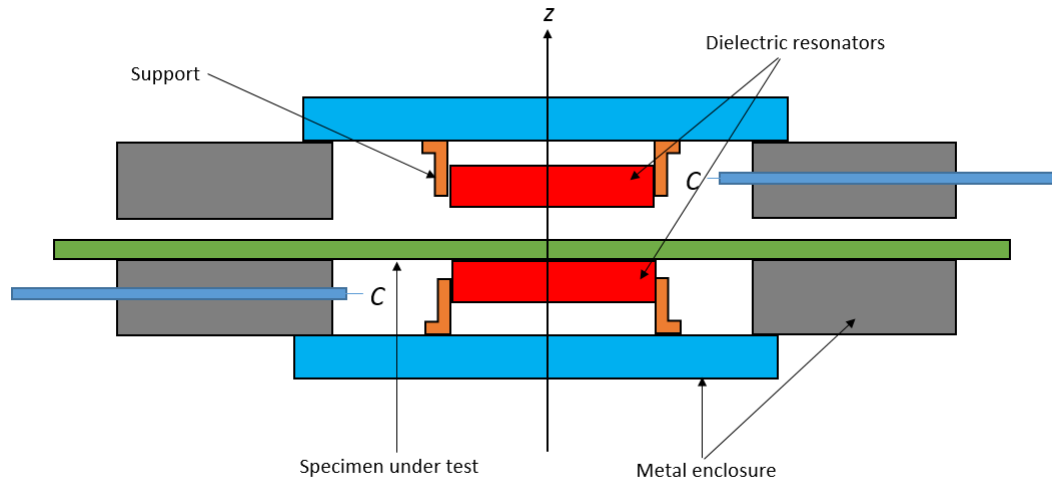


Figure 4.26: A Split-Post Dielectric Resonator (SPDR) cell for dielectric measurements[169]

tromagnetic field in a fixed frequency is continuous across the dielectric above the sample, as the instrument is insensitive to the existence of the air gaps perpendicular to the z-axis of the unit. For the computation of resonant frequencies, unloaded Q-factors, all other related parameters Rayleigh-Ritz method is used. The real permittivity “ of the sample will be determined on the basis of the thickness of the sample and resonant frequencies measurements as an iterative solution to equation (4.6) below[170][171]

$$\epsilon'_r = \frac{1 + f_0 - f_s}{hf_0 K_s(\epsilon'_r, h)} \quad (4.6)$$

Where,

h is the thickness of the sample.

f_0 is the resonant frequency of SPDR without a sample.

f_s is the resonant frequency of SPDR with the sample.

K_s is a function of ϵ' (specimen dielectric constant) and h .

The function K_s is computed and tabulated for every specific SPDR. The actual resonant frequencies and the resulting values of K_s were computed for ϵ'_r and h respectively. The remaining values of ϵ'_r and h was determined based on the interpolation of K_s . The initial value of K_s in the permittivity evaluation using equation (4.6) is taken to be the same as its corresponding value for a given h and $\epsilon'_r = 1$. The subsequent values of K_s are found for the subsequent dielectric constant values obtained in the iterative

procedure. This equation (4.6) converges rapidly as function K_s is varying with ϵ'_r and h [170][171].

However, the loss tangent is computed using the equation

$$\tan\delta = \frac{Q^{-1} - Q_{DR}^{-1} - Q_c^{-1}}{P_{es}} \quad (4.7)$$

Where Q is the unloaded Q-factor of the resonant fixture containing the dielectric sample.

P_{es} is the electric energy filling factor of the sample as shown in equation (4.8)

$$P_{es} = \frac{W_{es}}{W_{et}} = \frac{\int \int \int_{V_s} \epsilon_s EE^* dv}{\int \int \int_{V_s} \epsilon(v) EE^* dv} = h\epsilon'_r K_1(\epsilon'_r, h) \quad (4.8)$$

Q_c is the Q-factor depending on metal losses for the resonant fixture containing the sample as depicted in equation (4.9)

$$Q_c = \frac{\int \int \int_V \mu_0 HH^* dv}{R_s \int \int_S H_t H_t^*} = Q_{c0} K_2(\epsilon'_r, h) \quad (4.9)$$

Q_{c0} is the Q-factor depending on metal losses for the empty resonant fixture.

Q_{DR} is the Q-factor depending on dielectric losses in the dielectric resonators as shown in the equation (4.10)

$$Q_{DR} = Q_{DR0} \frac{f_0 P_{eDR0}}{f_s P_{eDR}} \quad (4.10)$$

where,

P_{eDR} is the sample electric energy filling factor.

P_{eDR0} is electric energy filling factor for the dielectric split resonator.

Similar to the function K_s , K_1 and K_2 are functions of ϵ'_r and h are computed and tabulated.

The interpolation of these functions is used determined the values of ϵ'_r and h [170][171].

The uncertainty of real permittivity The major source of uncertainty of the real permittivity is associated with the uncertainty of the thickness of the sample being under the measurement. The relative error of real permittivity due to thickness uncertainty as shown in the equation (4.11)

$$\frac{\Delta\epsilon_r'}{\epsilon_r'} \leq 0.15 + T \frac{\Delta h}{h} \quad (4.11)$$

In this work, a split-post dielectric resonator that operates at ~ 10.2 GHz with R&S ZVB20 VNA as shown in the figure (4.28) at National Physics Laboratory, Teddington London is used for the measurement. The sample was made to be square in shape with a dimension of 30-mm across for the onward measurement as the tangent loss and dielectric constant were determined respectively.



Figure 4.27: 10 GHz resonator

Broadband Dielectric Spectroscopy (BDS) This is a powerful technique used to measure electric (conductivity and impedance) and dielectric (dielectric constant, permittivity) properties of a material over a wide range of temperature, frequency and relaxation behaviour mode of the material[172]. This technique based on the interaction between an external electric field in conjunction with the electric dipole moment and charges of the material involved at the broadband frequency between 10^{-6} to 10^{12} Hz corresponding to the wavelengths between 3×10^{16} and $0.03cm$. This measurement is carried out by applying a voltage across the electrodes interface such that the amplitude and phase shift of the current can be measured. The ratio of the output signal to the input is referred to as transfer function[173]. When current is the input signal, then the output is the voltage and the transfer function is the impedance of the system. Similarly, when the voltage is the input signal and the current is the output signal, then the transfer function of the system is admittance[173]. The

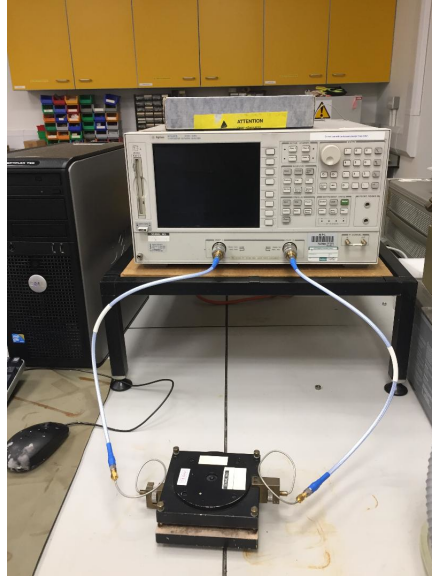


Figure 4.28: SPDR measurements process

admittance and impedance are represented by Y and Z respectively.

The facts that this technique is frequency domain dependent, the measurement of dielectric material can be theoretically related as follows;

Consider a capacitor C , two parallel electrodes filled with a dielectric material under study, the complex dielectric function is given in equation (4.12) as:

$$C(i\omega) = \epsilon(i\omega).C_0 = \epsilon(i\omega).\epsilon_0.\frac{A}{d} \quad (4.12)$$

where,

ϵ_0 is the permittivity of vacuum ($8.85 \cdot 10^{-12}$).

A is the area of electrode [m].

d is the distance [m].

ω is the angular frequency ($2\pi f$).

$$t = \sqrt{-1}$$

In this work, Novocontrol Broadband dielectric / Alpha impedance spectrometer (BDS 40) and Quatro cryo-system which serves as temperature controller used for the dielectric measurement as the schematic diagram of this equipment shown in figure (4.29). Furthermore, this equipment consists of other components such as vacuum pumps, gauges, dewar, gas heater and the active sample cell.

As mentioned earlier, the sample to be measured is placed in between two parallel electrodes separated by a spacer in the active cell. From dewar, the liquid nitrogen of temperature -195.7°C with the pressure of 5 millibar is evaporated with the help of

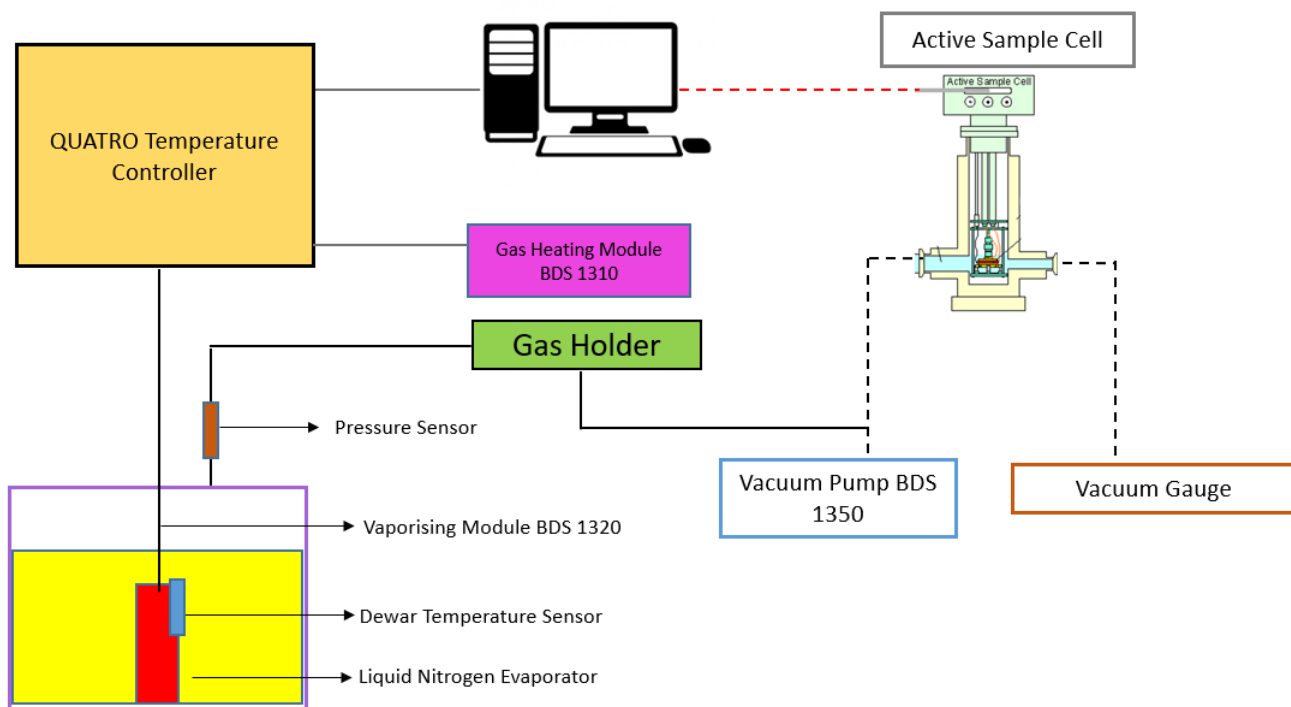


Figure 4.29: Schematic diagram of Broadband dielectric/Impedance Alpha-A-analyser

evaporator and cold gas is allowed to get into the gas heater[174]. The heated nitrogen gas is allowed to flow into the cryostat which controls the temperature of the sample to be measured. On the lower part of the active sample cell, the vacuum pump is connected while the upper part is connected to the Alpha Analyser[174]. This equipment is capable of measuring a sample in the frequency domain within the range of 10^{-5} Hz and 10 MHz. Measurement of the sample at a low frequency of 10^{-5} MHz take many days and high nitrogen consumption at low temperature are the major issues. This can be avoided by setting the equipment at a frequency between 10^{-3} Hz and 10 MHz as the operating temperature range within -155°C and 400°C [174].

The polymer samples to be measure have their diameters of 2.0 mm and thicknesses range between 0.031 mm to 0.75 mm, spacer capacity and the area remain 0 pF. The voltage applied for the measurement is $1 V_{rms}$, frequency varies between 10^{-1} Hz and 10^6 Hz and the dielectric losses measure with the temperature dependence -60°C to 30°C respectively.

4.17 Summary

This chapter gives an overview of the cleaning, fabrications and the measurements techniques used in this research work. Plasma cleaning represents the cleaning process. While the fabrication methods, which were used to fabricate the devices were including thermal evaporation, plasma – enhanced chemical vapour deposition (PECVD), Lithography, Electrospinning (ES) and Focused Ion Beam(FIB). Furthermore, the measurements techniques which were utilised in this work were including profilometer, Scanning Electron Microscopy (SEM), Fourier Transform Infra-red Spectroscopy (FTIR), S-Parameter, Vector Network Analyser (VNA), Thermal Gravimetric Analysis (TGA), Differential Scanning Calorimetry (DSC), C-V measurements and Dielectric Measurements

Chapter 5

POLYMER CHARACTERISATION

5.1 Introduction

As discussed in chapter 2 and 3 the characteristics of the MPAs are dependent on the properties of the dielectric medium used to fabricate them. In this research, different polymer materials were investigated for their suitability for this mode of application. Despite some of these polymer having been used in several electronic devices to date[175], the need to study the dynamic thermal stability of polymer materials over the broad range of frequencies required, where the influence of necessary parameters (dielectric constant and loss tangent) shall be measure for the antenna application.

Until recently conventional dielectric polymers have not been utilised extensively for microelectronic applications, therefore the majority of the information available in the literature refers to the chemical and mechanical properties, with limited information regarding the electrical properties relevant to bulk material insulating applications[175] of vital importance for using a dielectric substrate for patch antennas.

The materials used in this research were dielectric polymers materials:

- Polyethylene (PE)
- Polypropylene (PP)
- Polyvinyl chloride (PVC)
- Polystyrene (PS)

All of these low-cost materials were supplied by a leading company in the petrochemical industry in Saudi Arabia, (Saudi Basic Industries Corporation (SABIC)).

While there have been some reports of the use of e.g. PS in electronic memory devices[176], there has been no systematic exploration of their utilisation as a dielectric substrate for patch antennas. Indeed, despite having a dielectric constant that would render them highly-suitable for high-frequency exploitation, there are no reports on the use of these polymers in this type of application or an assessment of the material properties of relevance. This work will address these issues directly.

5.2 Optimisation of Polystyrene fibre(PSF) Deposition Using Electrospinning

There are a number of methods by which polymer thin and thick films can be deposited such as spin-coating, spray coating, dip-coating chemical vapour deposition (CVD) techniques ink-jet printing, screen printing and slot die[177].

In this work, electrospinning technique has been used to fabricate the dielectric media. It has the benefits of being a low-cost, room temperature process, is highly controllable in terms of the deposited film thickness and can also be used to inject nanoparticles into the materials in order to enhance properties[178].

5.2.1 Electrospinning and Polymer Layer Optimisation

The main parameters of relevance that were likely to impact on the quality of the final electrospun layer were identified as:

- solvent type
- solutions concentration
- flow rate
- applied voltage
- substrate vehicle

Experiments were conducted to evaluate the effect of each of the parameters using grease paper as a substrate to prevent sticking of the material to the collector.

Dichloromethane (DCM) was chosen as solvent because of it volatile and capable of dissolving a large number of organic compounds. At the initial stage, a PS solution was made using 2% of raw polystyrene substance and dissolved in 100% of DCM.

Different PS concentration was made by dissolving using 3%, 4%, 5%, 6% and 7% of the raw PS in 100% DCM and in DCM and Acetone (1:1). The PS solution was electrospun at the flow rate of $50\mu\text{L}/\text{min}$ and $60\mu\text{L}/\text{min}$ respectively with an applied voltage of 14.6 ± 2 KV. For clarity purposed, those parameters used for this purpose are presented in the table(5.1)

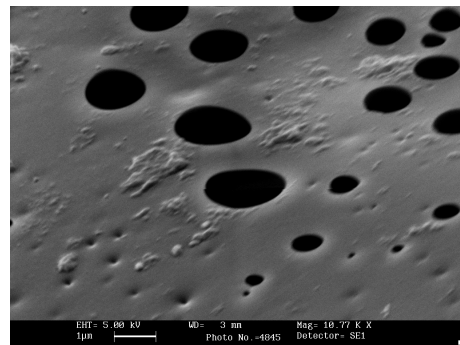
Parameters	Values
Solution concentration	3% , 4% , 5%, 6% and 7%
Flow-rate	$50\mu\text{L}/\text{min}$ and $60\mu\text{L}/\text{min}$
Applied voltage	$14.6\pm\text{kV}$

Table 5.1: Parameters for polystyrene fibre optimisation

The re-construction of polystyrene started with 4% polystyrene concentration using DCM solvent only at $50\mu\text{L}/\text{min}$ (14.6 ± 2)kV. The fabricated material was tested fragile and the SEM image confirmed many pores of different sizes but no presence of fibre as this linked to the vapourisation of DCM solvent.



(a) Photograph of fabricated PSF



(b) SEM image of PSF

Figure 5.1: PSF produced with 4% PS concentration using DCM solvent only at $50\mu\text{L}/\text{min}$ (14.6 ± 2)kV

The flow rate of the polystyrene concentration was increased from $50\mu\text{L}/\text{min}$ to $60\mu\text{L}/\text{min}$ while the concentration remains 4%. It was observed that, there are no different in physical texture of the material but SEM image revealed more pores appeared on the fabricated polymer material with no confirmation the presence of fibre as depicted in figure (5.2) .

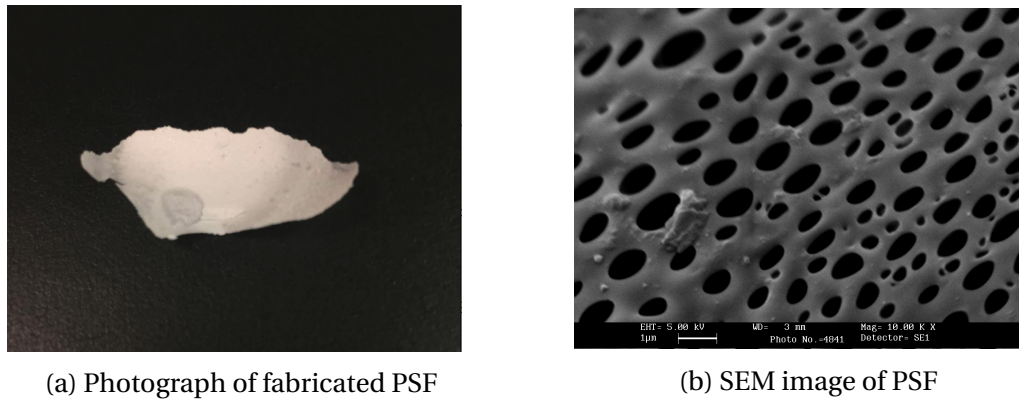


Figure 5.2: Polystyrene fibre produced with 4% PS concentration using DCM solvent only at $60 \mu\text{l}/\text{min}$ (14.6 ± 2)kV

The polystyrene concentration was reduced from 4% to 3% as the flow rate was kept at $60 \mu\text{l}/\text{min}$. The fabricated polymer material appeared homogenous with no presence of pores and fibre as confirmed in the SEM image as presented in figure (5.3).

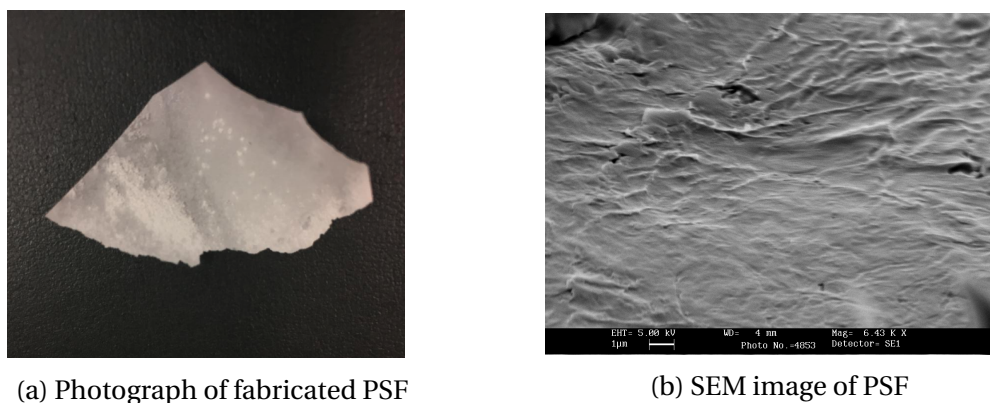


Figure 5.3: PSF produced with 3% PS concentration using DCM solvent only at $60 \mu\text{l}/\text{min}$ (14.6 ± 2)kV

The addition of acetone into the solution provides significant change into the formation of the polystyrene fibre. Acetone is considered because it is a good solvent for synthesising polymer fibres, miscible with other solvents in order to modify the surface tension and viscosity of the solution[179]. The solvent combination is 3% PS concentration with DCM and acetone in ratio (1:1). The material produced appeared harder as compared to those produced earlier but still in fragile state. In the SEM image, the material appeared more homogenous and presence fibre confirmed as depicted in figure (5.4).

The PS concentration was increased from 3% to 5% while other parameters kept constant. The material when it was fabricated it has the dust form, it was not like a

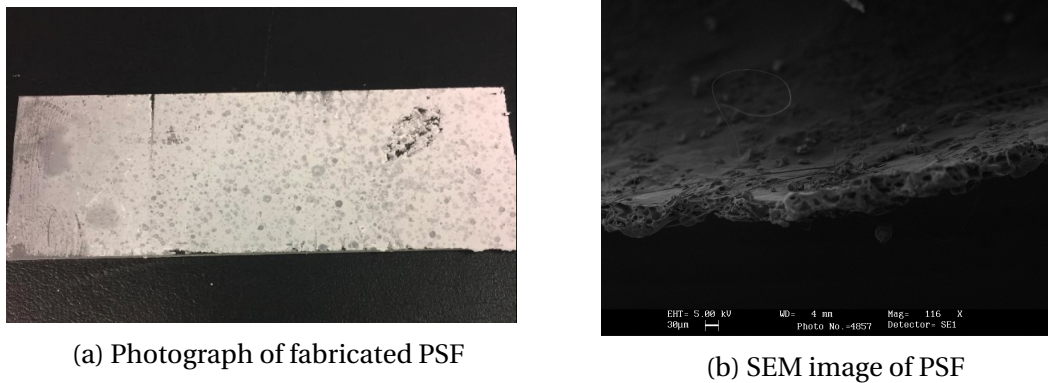


Figure 5.4: PSF produced with 3% PS concentration using DCM and Acetone (1:1) at 60 $\mu\text{l}/\text{min}$ (14.6 ± 2)kV

film. The deposited material structure is shown in figure (5.5), confirmed the presence of fibre, the grown fibre has a very thin diameter (within diameter range of 100 nm to 300 nm), and it is obvious that there are some clusters of polystyrene.

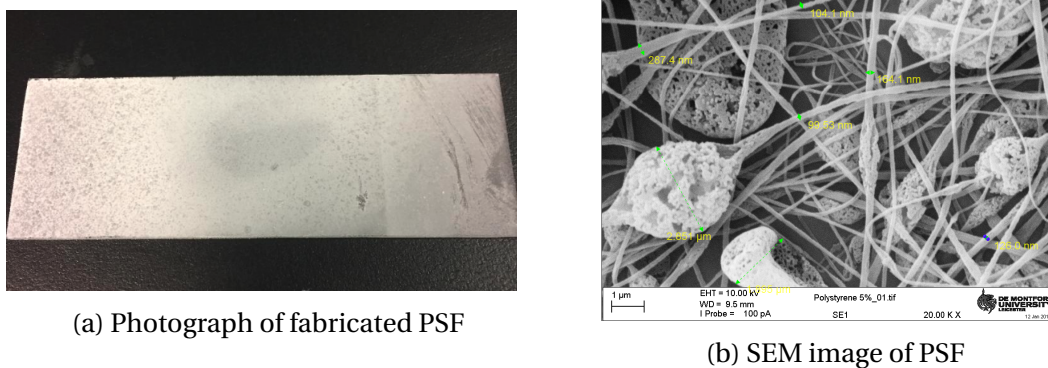


Figure 5.5: olystyrene fibre produced with 5% PS concentration using DCM and Acetone (1:1) at 60 $\mu\text{l}/\text{min}$ (14.6 ± 2)kV

Further increase in the PS concentration from 5% to 7% using DCM and acetone at (1:1) at the flow rate of 60 $\mu\text{l}/\text{min}$, deposited material structure illustrated in figure (5.6) has more fibre appeared with a bigger diameter but the concentration of the fibre is less than the previous 5% PS. Also, this structure has the dust form.

The solvent concentration was reduced to 6%, the deposited material has a thin film form, the structure has a thicker diameter fibre than the 5% PS and they are in mesh shapes. In fact, the deposited structures were more robust and adhered better to the ground plane, enabling them to be used as a dielectric medium more effectively as shown in figure (5.7). The electrospun material was heated to 100°C for 20 minutes in order to make the material more firm, another SEM image has been taken, the image

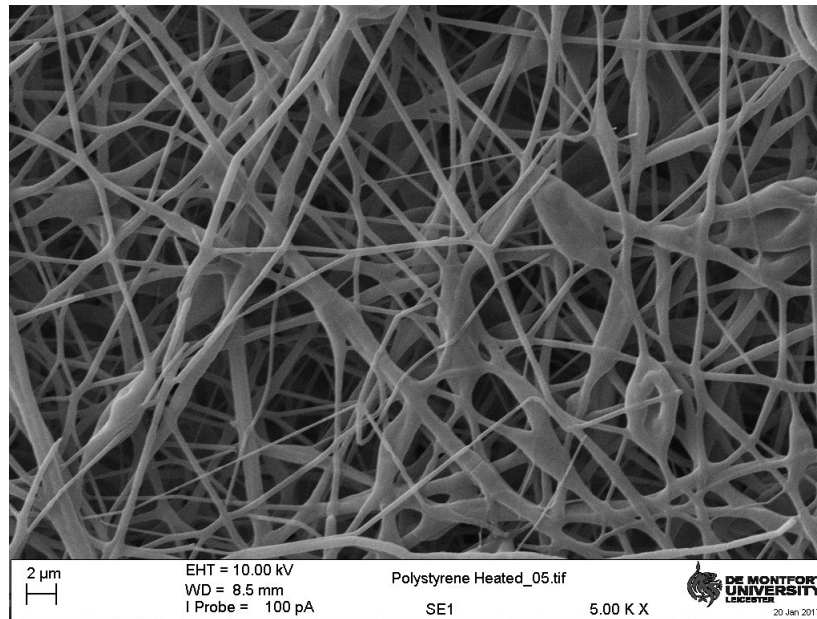


Figure 5.8: SEM image of PSF produced from PS with 6% PS concentration using DCM and Acetone (1:1) at 60 $\mu\text{l}/\text{min}$ (14.6 ± 2)kV after heating

and good performance of the device.

5.3 Characterisation of polymer materials

In order to characterise all the polymers films, analytical tests were conducted on all the specimens including Scanning Electron Microscopy (SEM), Fourier Transform Infra-Red Spectroscopy (FTIR), Thermal Gravimetric Analysis (TGA), Differential Scanning Calorimetry (DSC), Broadband Dielectric Spectroscopy (BDS) and Split-Post Dielectric Resonator (SPDR).

5.3.1 Fourier Transform Infra-Red Spectroscopy (FTIR)

In figure(5.9) the FTIR spectra between 400 cm^{-1} and 4000 cm^{-1} for polymeric materials such as PE, PP, PVC, PS and PFS are presented.

Vibrational bands characteristic of PE are shown in figure peaks were observed at 2916 cm^{-1} , 2850 cm^{-1} , 1461 cm^{-1} and 719 cm^{-1} respectively. A very strong vibration is observed at 2916 cm^{-1} corresponds to C-H asymmetric stretching of the polymeric material (Polyethylene) from CH_2 groups. Another strong band of 2850 cm^{-1} corresponds to C-H symmetric bending from the same group of CH_2 is also observed. At 1461 cm^{-1} , corresponds to the C-H bending vibration as well as deformation of CH_3 (methyl) group in the polymeric material. Furthermore, 719 cm^{-1} represent C-H from methyl group of rocking deformation characteristic as reported[180][181]. The peaks in this material are within the range of those reported in the literature. Some of the weak bands are also observed but due to the conformity of the strong bands to the available literature, the weak bands are not considered.

PP characteristic band shown in figure (5.9b), strong bands observe at 2917 cm^{-1} , 2868 cm^{-1} , 1462 cm^{-1} and 1373 cm^{-1} respectively. 1168 cm^{-1} , 974 cm^{-1} , 836 cm^{-1} and 455 cm^{-1} represent the weak bands in the material. The peaks at 2917 cm^{-1} and 2868 cm^{-1} caused by C-H stretching vibrations occurred in the material. The peaks at 1462 cm^{-1} and 1373 cm^{-1} allocated to both CH_2 and CH_3 bending vibration of polypropylene material under investigation. The small or weak bands such as 1168 cm^{-1} , 974 cm^{-1} , 836 cm^{-1} and 455 cm^{-1} occurred due to symmetric deformation vibration of CH_3 and rocking vibration from CH_2 occurred in the material as reported in the literature[180][182].

PVC characteristic bands shown in figure (5.9c), peaks at 2936 cm^{-1} and 2866 cm^{-1} contributed C-H stretching vibrations of the $\text{C}(\text{CH}_3)$ methylene. At 1269 cm^{-1} and 1105 cm^{-1} peaks occurred due to the CH_2 rocking vibrations while C-Cl stretching bands occurred at 748 cm^{-1} , 615 cm^{-1} and 953 cm^{-1} represent trans deformation of C-H or

wagging vibration [180][183][184]. A sharp spectrum observe at 1717 cm^{-1} is probably due to the vibration of CH_2 occur in the material.

PS characteristic bands are shown in figure (5.9d), peaks at 3020 cm^{-1} , 2931 cm^{-1} and 2856 cm^{-1} observe due to asymmetric and symmetric stretching vibrations of C-H from CH_2 groups. The presence vinyl group of C=C detect at peak 1605 cm^{-1} while at 1456 cm^{-1} , vibration occurred due to the stretching deformation of both CH_2 and benzene ring of styrene molecules. The peaks at 740 cm^{-1} , 694 cm^{-1} and 536 cm^{-1} represent the bending and rocking modes of C-H groups in the polystyrene [180][185][186][187][188]. The peaks at 1024 cm^{-1} and 904 cm^{-1} are notice to represent deformation vibrations occur at C-H group of the polystyrene.

PSF characteristic bands shown in figure (5.9e), feasible peaks both strong and weak are observe at 547 cm^{-1} , 696 cm^{-1} , 1457 cm^{-1} , 2916 cm^{-1} and 3036 cm^{-1} respectively. The C-H stretching of benzene rings is observed at 3036 cm^{-1} and C-H stretching vibration in the CH_2 group at 2916 cm^{-1} is observe. At 1456 cm^{-1} and 1589 cm^{-1} , an aromatic C=C stretching vibration is notice, 1024 cm^{-1} is representing the vibrations of benzene ring, and a strong band is noticed at 696 cm^{-1} , which represent the bending as well as rocking modes of C-H groups in the material. All these peaks are relatively close to those found in the literature supporting the argument for using this technique for polymer deposition in this work[180][185][189]. In this characterisation, obtained are the peaks of different functional groups or molecular structures in the materials and were relatively close to those found in the literature as it confirmed the high quality of these materials used for the fabrication. The performance of the antenna depends on the quality of the materials used during the fabrication process.

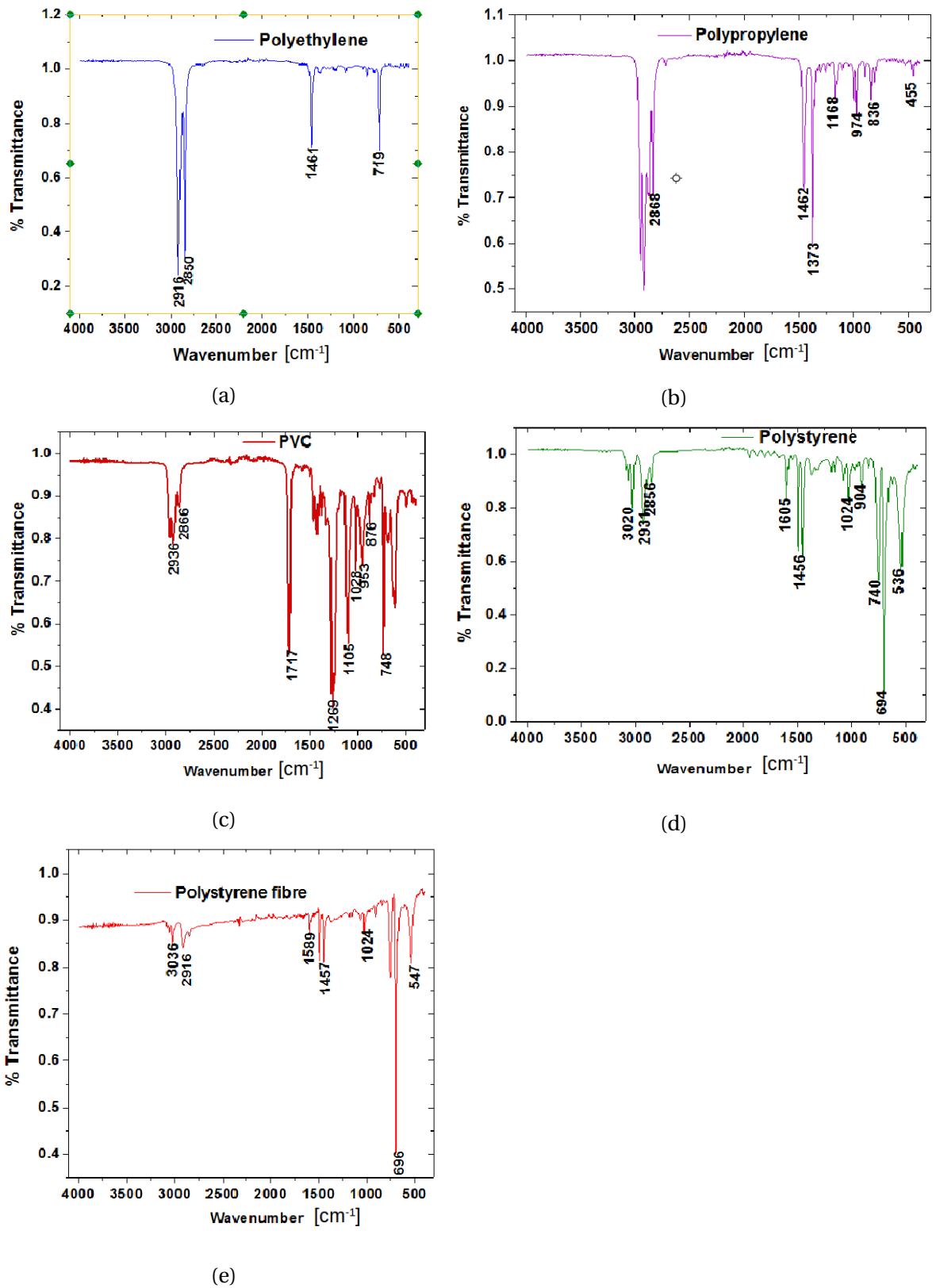


Figure 5.9: FTIR for different polymer materials

5.3.2 Thermogravimetric Analysis (TGA)

Most materials demonstrate single-stage decomposition while PVC material exhibit multistage decomposition thermal process according to figure (5.10) as this is associated to the decomposition of lower molecules (HCl, benzene and vinyl chloride) and a higher molecule of unsaturated hydrocarbon[190]. The initial, maximum and final degradation temperature of these materials were presented in table (5.2) where it formed the basis for the thermal analysis.

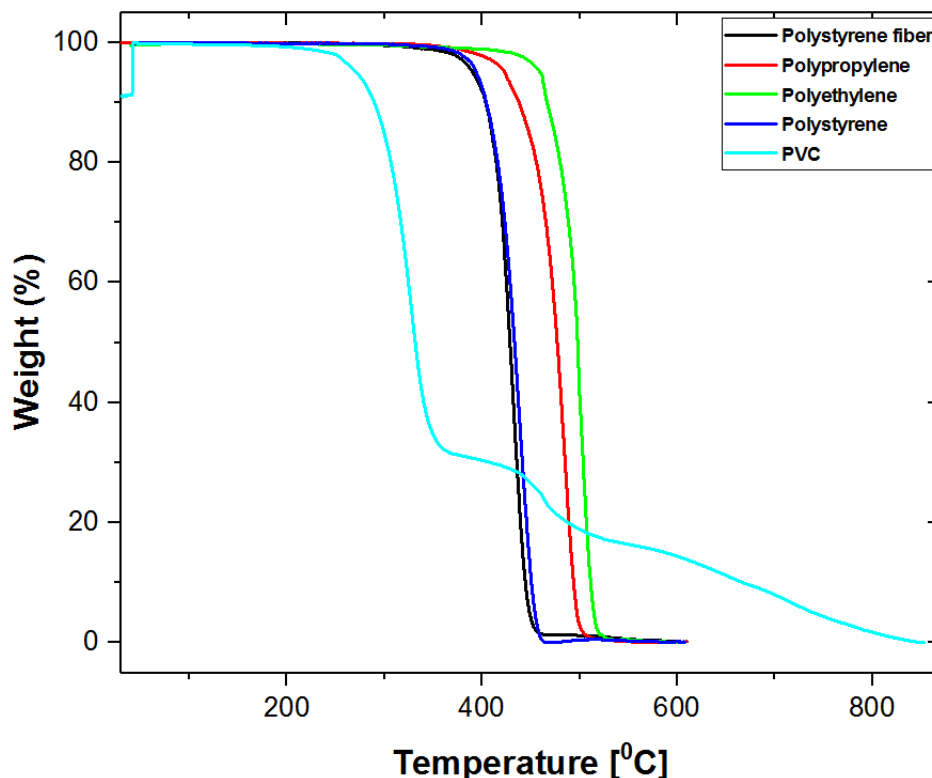


Figure 5.10: Thermogram curve Analysis

PE, PP and PS and PSF have their thermal stability range between 40°C to 354°C while polyvinyl chloride is between 40°C to 323°C. This variation is linked to the presence of different molecules and bonds in the materials as confirmed by the FTIR. The decomposition temperature of the individual polymeric material is presented in a differential format for the better understanding of the thermal decomposition undergone by these materials.

PE thermogram curve presented in the figure (5.11a), from 40°C to 392°C the material is stable as no degradation is noticed suggesting the relative stability of the

Polymeric materials	Initial degradation temperature ($T_{d(1\%)}$)°C	Maximum degradation temperature (T_{max})°C	Final degradation temperature ($T_{d(99\%)}$)°C
Polyethylene	393	499	525
Polypropylene	372	488	510
Polyvinyl chloride	324	461463	790
Polystyrene	357	438	460
polystyrene fibre	355	430	464

Table 5.2: Thermal decomposition of polymer materials

material. The decomposition starts from 393°C ($T_{d(1\%)}$) equivalent to 1%. There is large inverse peak (DTG) noticed at 499°C representing complete decomposition and corresponding to the maximum degradation temperature (100%) (T_{max}). The final degradation temperature of this material is noticed at 525°C. All these values are relatively close to those reported in the literature for low-density polyethylene (LDPE) and pure polyethylene[191][192]. A small peak is also noticeable at 462°C but is not strong enough to claim the degradation of the material under investigation, as this may be linked to the presence of an impurities.

The PP thermogram curve presents in figure (5.11b) show the thermal stability of this material between 26°C to 371°C, the degradation starts at 372°C as corresponding to the decomposition of the material by 1% of weight and 99% of the material decomposition at 510°C. The principal peak noticed at 488°C is the total decomposition of the material comparable to that found in the literature[192]. The thermal decomposition experienced by this material is as a result of thermal scissions of aliphatic C-C backbones linked with hydrogen transfer at the scission sites in a nitrogen gas atmosphere[193]. Some small peaks are evident in the stability region and are again linked to an impurity during the fabrication process of the polymeric material.

The PVC thermogram curve is presented in figure (5.11c), with thermal stability of between 40°C to 321°C; decomposition begins at 322°C corresponding to the decrease of the total weight by 1% (0.098 g,) and 99% of the total weight underwent decomposi-

tion at 792°C. Multistage decomposition of the PVC is clearly evident by the DTG curve as the principal peak appears at the 324°C while other peaks are at 463°C and 790°C respectively. The principal peak corresponding to the dehydrochlorination of PVC is usually found between the temperature of 220°C to 370°C as the formation of conjugated polyenes in the structure[194][195]. The second peak corresponding to the decomposition of the conjugated polyenes structure formed earlier in the structure[194][195]. The third peak can once more be linked to the presence of impurities in the material.

PS thermogram curve is shown in figure (5.11d), with no clear degradation of the material occurring from 50°C to 356°C and degradation beginning at 357°C ($T_{d(1\%)}$) corresponding to 1%. The principal peak observed at 438°C corresponds to the complete degradation or decomposition (100%) (T_{max}) of the polystyrene at the DTG curve while final degradation is noticed at 464°C equivalent to 99% ($T_{d(99\%)}$) of the material decomposition. The initial gradual decrease in the weight of the material when subjected to heat is due to the release or loss of crystalline water and residual organic solute in the polystyrene as reported in the literature. Some of the thermogram values obtained relatively close to those reported in the past works [196][197].

The thermogram curve for PSF is shown in figure (5.11e), this material is shown stability between 60°C and 354°C. The decrease in the weight of 1% and 99% are recorded at 355°C and 464°C respectively. The complete decomposition or degradation is at 430°C. The decomposition is similar to that of the polystyrene as the crystalline water molecule is released and as well as a residual of organic solute in the material.

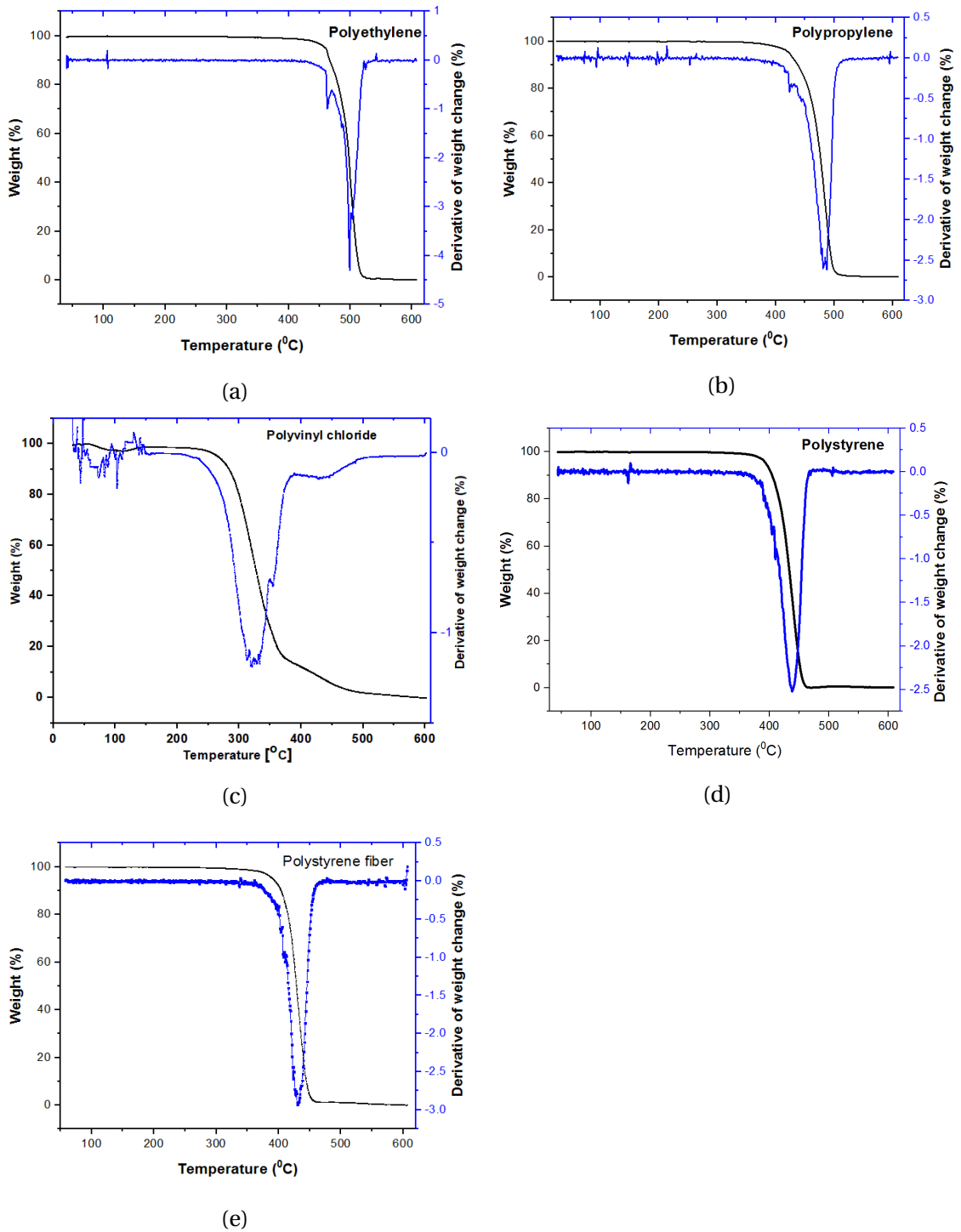


Figure 5.11: Derivative of weight change for different polymers materials

5.3.3 Differential Scanning Calorimetry (DSC)

The determination of thermal stability of the polymeric materials used for the patch antenna continues by using DSC. The temperature range for each of the sample is between 20°C to 380°C in which the count rate is at 20°C per minute. The measurement is carried out in a nitrogen atmosphere with a flow rate of 20ml per minute. The initial temperature is 20°C, the mass of each sample is known and corresponding heat flow rate starts from 0 mW. It should be noted here that the measurement is endothermic in nature. Figure (5.12a) shows the DSC curve for the polyethylene. The glass transition temperature (T_g), crystalline temperature(T_c), specific heat capacity and change in enthalpy can be derived from the figure (5.12a) as shown in figure (5.12b).

At the initial stage, the polymer material is amorphous in nature, when the heat is applied to the material, the amorphous melting temperature is reached and this is called glass transition temperature. The glass transition temperature represents the temperature at which the polymer material starts to lose its solid form and can be found at approximately 75°C relatively close to reported for both low-density polyethylene (LDPE) and high-density polyethylene (HDPE)[198]. Further increases in temperature lead to the crystallinity of the material observed at 162.4°C. However, at the glass transition, amorphous states polymer materials is confirmed. For this purpose, PE is a semi-crystalline polymeric material due to the presence of glass transition[198]. The area under the peak is 233.15 mJ determined from the onset temperature of 101°C to 223.6°C and corresponding to the total energy consumption (heat capacity) for the crystallinity process. The enthalpy change per unit weight for this sample can be determined by dividing the heat capacity by the heating rate and weight of the sample. The weight of PE used for this process is 10.04 mg, the heat rate is 20°C per minute and the enthalpy change per unit weight is 1161 mW/g as this low due to the weight of the material involved.

In figure (5.12c), there is no glass transition temperature present which implies that polypropylene is fully crystalline and the crystallinity is at 173.2°C relatively correspond to those reported earlier[199][200][201]. The total heat consumption for the crystallinity of this material is 553.5 mJ correspond to the area under the crystallisation peak between 128°C and 222°C. Furthermore, the weight of the material used is 27.00 mg and enthalpy change is 1025 mW/g.

As presented in figure (5.12e), the glass transition temperature is approximately 87°C and is not clearly shown but corresponds to those recorded in the

literature[202][203]. The material is semi-crystalline in nature with the crystallinity peak occurred at 258.1°C as shown in the inserted graph. The area of the peak is approximately 16 mJ as corresponding to the heat consumption for the crystallinity of the material as the temperature range between 250°C and 266°C respectively. For this material, the weight is 17.0 mg and calculated enthalpy change is 47.06 mW/g. The low enthalpy change value obtained is as a result of the region where the area of the peak with respect to temperature is taken.

PS is semi-crystalline and the glass transition temperature is approximately 91°C and the crystallisation temperature is 103.5°C respectively in conformity to those reported earlier[204]. The peak area is 4.5 mJ corresponding to the total heat consumption for the crystallinity of the material as the temperature range between 92°C and 125°C respectively. The weight of the sample is 8.4mg and the enthalpy change is 26.8 mW/g at a heating rate of 20°C per minute. There is another peak noticed but not within the range of those reported in the literature.

The PSF DSC curve presented in figure (5.12f) and is similar to figure (5.12e). The semi-crystalline nature of the material is observed when the glass transition temperature is 92°C and crystallisation temperature is 107.8°C and is relatively close to those of polystyrene. The peak which is the total heat capacity for the crystallisation of this material is 3.76 mJ as the temperature range between 97.8°C and 122°C respectively. The enthalpy change for this material is approximately 38.0 m while the weight of the sample is 5.0 mg.

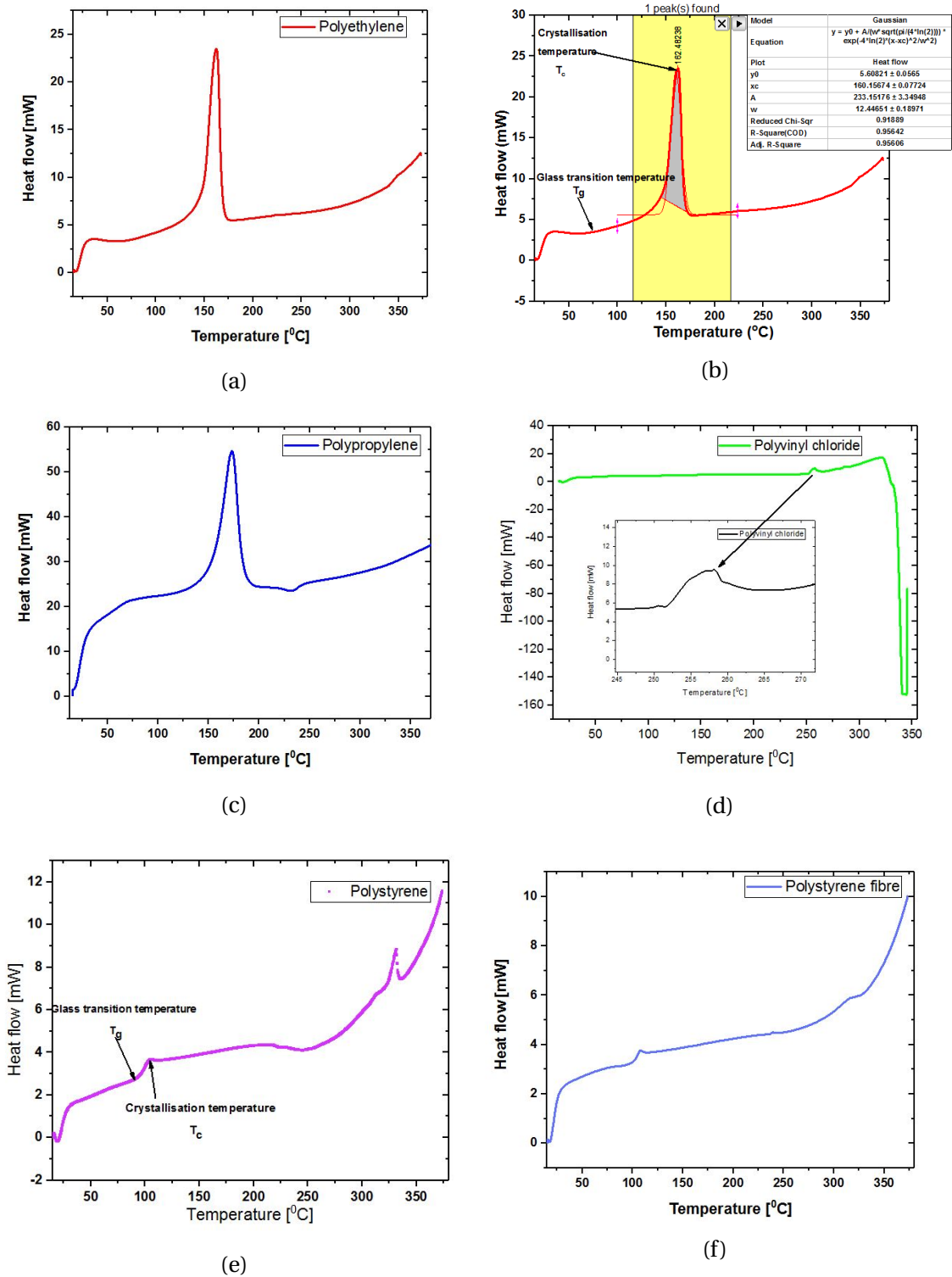


Figure 5.12: DSC for different polymer materials

5.4 Broadband dielectric spectroscopy (BDS)

Broadband dielectric spectroscopy (BDS) is an appropriate technique to obtain information in terms of thermal stability about the dynamic state of polymer materials with respect to the broad range of temperature and frequency[205]. In this work, the dielectric loss of the polymer materials (such as PE, PP, PVC, PS and PSF) is considered as a function of frequency and temperature. Figure (5.13a), represents a three-dimensional rendering of the dielectric measurement for the PE film. The strong dielectric response is observed due to the presence of repeating unit carries no pure dipole moment. The dielectric loss is linked directly to the molecular mobility of the polymer structure or matrix as the presence of impurities and polar carbonyl groups are noticed. The approximate magnitude of dielectric loss within the range of 10^{-4} to 10^{-2} is moderately in conformity to those values quoted in the literature.

The conductivity, α -relaxation, the dielectric active β -process at high temperature and β -relaxation at low temperature. The presence of α -relaxation confirmed a non-polar structure of the material as the segmental motion occurs due to the main chain at the glass transition temperature as earlier shown in differential scanning calorimetry[205][206]. The dielectric loss of this material at the different temperature confirmed it the thermal stability as compared to other polymeric materials. The dielectric loss varies at a lower temperature due to change in the matrix. The fluctuation observed in the lower region is due to the low glass transition temperature as confirmed in DSC [206].

Figure (5.13b) shows three-dimensional rendering of the PP film. The conductivity of this material is quite small approximately (10^{-3}) as compared to the PE and this can be as a consequence of mobile ionic impurities present in the material. Further confirmation of this impurity shown in FTIR as some of the unresolved peaks appeared. The dielectric loss of this material is approximately between 10^{-4} and 10^{-3} and this low loss may be linked to the presence of impurities build up in the material. The α -relaxation process is linked to the higher glass transition temperature while the β -relaxation process is observed at a lower temperature and can be attributed to CH orientation[207]. The fluctuations experienced at low temperature and low frequencies are due to the low glass transition temperature as confirmed in the DSC curve. The three-dimensional broadband dielectric spectroscopy is shown in figure (5.13c) for PVC. The dielectric loss is approximately range between 0 and 10^{-2} . The heterogeneous of the material is confirmed. The conductivity presents linked to the impurities in the material.

The secondary relaxation occurred at the temperature below the glass transition and responsible for the main dielectric loss features in the polymer[208]. As temperature increases close to the glass transition temperature, the primary relaxation begins to be observed with reference to the frequency gaps and the conductivity observed. The shape of this polymer shows the combination of both α -relaxation and β -relaxation as observed[208].

Figure (5.13d) shows the three-dimensional of PS, The dielectric loss is approximately range between 10^{-3} and 10^{-4} as the increase in conductivity is observed in the material. For pure PS, dielectric relaxation behaviour is not strong due to the stability of phenyl groups that are characterised by a high local dipole moment[209]. The α -relaxation occur at a higher temperature which is basically associated with the glass transition temperature while β -relaxation is attributed to the frequent head-to-head polymerisation or rotation of styrene monomers or phenyl groups at lower temperature[209][210]. The γ -relaxation occurs at low temperature linked to the motion of the methylene backbone chains close to head-to-head or tail-to-tail defects occur[210].

The PSF presented in the three-dimensional diagram in figure (5.13e). The dielectric loss of this material is between 10^{-4} and 10^{-5} . The low conductivity of the sample is rarely experienced at low temperature confirming the presence of some impurities in the sample. The presence of α -relaxation, β -relaxation and γ -relaxation can be clearly reflected in the diagram. The thermal instability of polystyrene fibre is confirmed in figure (5.13e) and the peaks observed linked to the distortion in molecular orientation and morphology of the material.

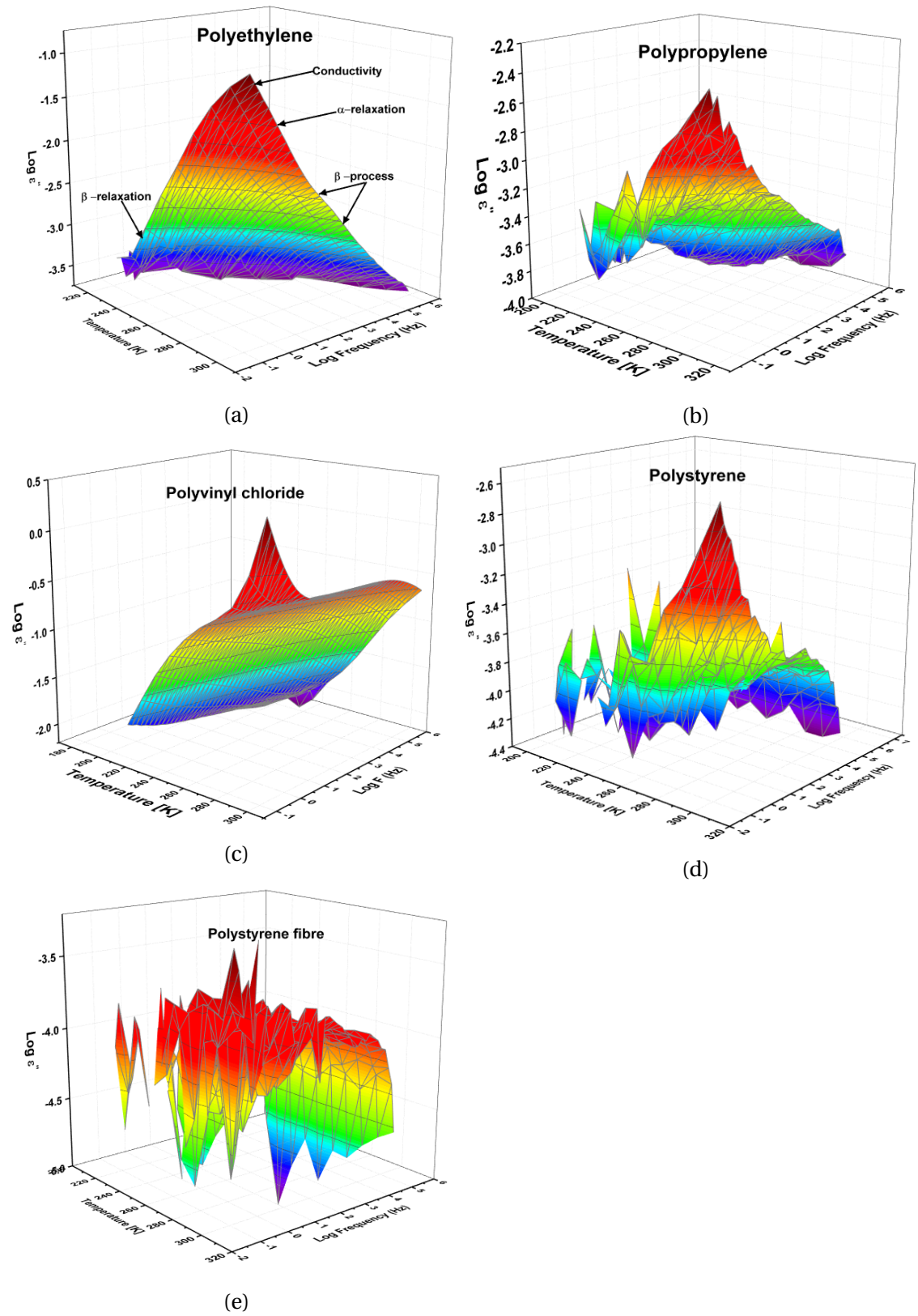


Figure 5.13: Different polymer Broadband dielectric spectroscopy

5.4.1 Split-Post Dielectric Resonator (SPDR)

This technique is used for the measurement of the complex permittivity and dielectric loss tangent at a higher frequency with respect to the thickness of the sample, height of the sample and the number of sample stacking. In this work, the complex permittivity, dielectric loss tangent are determined with respect to the thickness of the polymer materials at the frequency of 10.2 GHz. Three samples for every materials were measured. The thickness of these samples varied significantly and measurements were taken at different locations. The average of the thicknesses, complex permittivities and loss tangents are presented in table(5.3).

SPDR data				Literature		
Polymer materials	Thickness (mm)	Complex permittivity (ϵ_r)	Loss tangent ($\tan\delta$)	Complex permittivity (ϵ_r)	Loss tangent ($\tan\delta$)	Reference F(GHz)
Polyethylene	0.16	2.10± 14%	1.5E-04± 2.9E-04	2.35± 0.3%	1.4E-04± 23%	3.9[171]
Polypropylene	0.39	2.11± 6%	2.3E-04± 1.2E-04			
Polyvinyl chloride	0.21	2.53± 3%	5.8E-03± 2.5E-03	2.7± 0.7%	5.0E-03± 8.0E-05	10[211]
Polystyrene	0.16	2.35± 16%	3.2E-04± 2.6E-04	2.55± 0.4%	4.8E-04± 8%	3.9[171]
Polystyrene fibre	0.15	1.36±5%	2.4E- 04±4.8E- 04			

Table 5.3: SPDR- comparison of some selected polymer materials

Table(5.3), the correlation between the SPDR data obtained from the literature to the measured data is compared. Generally, uncertainties are presented at coverage factor $k = 2$ by the United Kingdom Accreditation Service (UKAS) standard M3003 on the expression of uncertainty and confidence in the measurement. The coverage factor

$K = 2$ equivalent to the 95% level of confidence in measurement and this is used by NPL where the measurement was carried out.

The PE thickness of 0.16 mm gives a complex permittivity of $2.10 \pm 14\%$ and loss tangent of $1.5E-04 \pm 2.9E-04$ is such in a good agreement to the SPDR measurement done at 3.9 GHz by Krupka et.al for the precise measurements of laminar dielectric specimens that provides permittivity of $2.35 \pm 0.3\%$ and loss tangent of $1.4E-04 \pm 23\%$ for high-density polyethylene. However, the thickness of the sample was not mentioned[171]. For the PS, the thickness of 0.16 mm while the complex permittivity is $2.35 \pm 16\%$ and $3.2E-04 \pm 2.6E-04$ for the loss tangent. The complex permittivity shows good agreement with the SPDR measurement by Krupka et.al ($2.55 \pm 0.4\%$) while loss tangent of $4.8E-04 \pm 8\%$ show more variation as this can link to the thickness of the sample which was not mentioned in the literature[171]. The PVC of thickness 0.21mm provides complex permittivity of $2.53 \pm 3\%$ and loss tangent of $5.8E-03 \pm 2.5E-03$. The results are in good agreement with dielectric measurement carried out at 10 GHz for both the complex permittivity ($2.7 \pm 0.7\%$) and loss tangent of $5.0E-03 \pm 8.0E-05$ at unknown thickness[211].

However, the complex permittivities for both PP and PSF are $2.11 \pm 6\%$ and $1.36 \pm 5\%$ while the loss tangents are $2.11 \pm 6\%$ and $1.36 \pm 5\%$ respectively. It should note here that, as at the time of reporting these results, no any literature was found to be used for corresponding data for these two materials and this can serve as the reference data for any future work.

5.5 Summary

The performance of the patch-antennas depends on the quality of the materials used for the fabrication where dielectric substrates play a significant role. In this chapter, the optimised PSF was achieved through variation of parameters such as flow rate, applied voltage, substrate vehicle and loading concentration of the polymer solution such that dielectric medium suitable for the fabrication of MPA. The co-solvent vehicle (50:50) comprised of acetone and DCM was used where a solution infusion flow rate of $60 \mu\text{L}/\text{minute}$ with applied voltage of $12 \pm 2 \text{ kV}$ for a rigid fibrous PS substrates.

The characterisation of PE, PP, PVC, PS and PSF in order to determine the chemical, thermal and mechanical properties of these materials. In the FTIR characterisation, used for the determination of different chemical bonding which include methyl, methylene and vinyl groups in these dielectric materials. The different strong peaks observed in this individual material confirmed the high quality substrates required for the MPAs fabrication. To operate MPA in high temperate region, it is important to know the thermal stability of the substrate materials using both TGA and DSC respectively. Thermal decomposition of the materials confirmed with the analysis using differential TG where different inverse sharp peaks observed for different polymer substrate materials. More so, the glass transition temperature and crystallinity of the materials were obtained at different temperature. Furthermore, SPDR confirmed the loss tangent and complex permittivities which are properties required for the suitability of dielectric substrates for MPAs. These properties were never reported in any literature for both PP and PSF materials before this work. The BDS technique where the ionic conductivity, α – relaxation and dielectric active β – process at both high low temperature were confirmed present in the materials.

Chapter 6

DESIGN AND CHARACTERISATION OF POLYMERS PATCH ANTENNAS AND DLC NANO-PATCH ANTENNAS

6.1 Design And Characterisation Of A Diamond-Shaped Monopole Patch Antenna

6.1.1 Introduction

In regards to the rapid development of wireless communication systems, Electrically Small Antennas (ESAs) have gained increasing interest in the wider area of engineering communities. Compact physical sizes that are small with respect to their operational wavelengths, along with exceptional and multi-functional performance characteristics are high in demand. Over the past decades, researchers have proposed many ESA designs, such as the right/ left-hand composite, transmission line based antennas[212], near-field resonant parasitic antennas[213] and reactive loaded monopole antennas[214]. However, the development of such ESAs are often constrained not only to compact (relative to their operational wavelength) but also have broad impedance bandwidth[215] [216][217]. It is highly desirable to realise an ESA design that is efficient over a wide range of operational frequencies.

This chapter proposes a diamond-shaped monopole antenna to be operated at millimetre wavelengths. It is designed and numerically simulated using the advanced design system ADS-2009 software and the internal package is based on the method of momentum. Method of momentum is an electromagnetic field simulator that compute S-

parameter for general planar circuits including microstrip, slotline, stripline, coplanar waveguide and other technologies. Vias and air-bridge connect topologies between layer; multilayer structures, RF and microwave circuits can also be simulated using ADS-2009. Usually, in the method of momentum, the electromagnetic field problems are classified into two groups. The first one covers directly the electromagnetic field and the second one covers the field source. In both cases, the equation that is to be solved are linear operator equations in terms of unknowns (the field, via and sources). However, in the first case, the equations are differential, whereas in the second case they are integral. Both classes of equations belong to the general class of linear operator equations, which have the common form

$$L(f) = g \quad (6.1)$$

where,

L is the operator.

g is the source of excitation, which is assumed a known function.

I is the field or response, which is the unknown function to be determined.

The linearity of the operator follows from the linearity of Maxwell's equations and the constitutive equations, as only linear media is considered. Also, It is assumed there exists a unique solution to above equation.

For the first group of numerical methods, L is a differential operator. It generally involves derivatives with respect to three spatial coordinates. For the time-domain analysis, derivatives with respect to time are also involved. Furthermore, f is a field vector or potential (depending on the formulation), g is known as quantity, for example, the field or potential due to an incident wave. For the second group of numerical methods L is an integral operator and f represents the field sources. Irrespective of the approach, the operator equation (6.1) can be solved following the numerical procedure recognised under the generic name of the method of moments (MoM). This is a general technique for solving linear operator equations. In this method, it was found that the mesh size was of particular importance to obtain realistic return-losses of the antennas, especially at high frequency. The diamond shaped MPAs were then fabricated on a standard RT duroid material [218] and then it was RF characterised over the frequency range 10 MHz to 20 GHz using a network analyser (E8362B). Initial simulation and measurements result on the high-frequency diamond shaped MPAs show better performance than a standard monopole antenna; it was shorter in physical length and

had a wider bandwidth and higher gain.

6.1.2 Design Of A Diamond-Shaped Monopole Antenna

Figure (6.1) shows a schematic view of the diamond-shaped monopole antenna. The monopole antenna has a metallised thickness of 'T' and an inner length L_1 and a sectorial angle of ' θ_1 '. The corner of the diamond shaped monopole antenna is fed by a 50Ω microstrip-line, which has an inner length of L_1 and sectorial angle of ' θ_2 '. These structures are fabricated on a dielectric substrate with a relative permittivity of ' ϵ ' and a thickness 'H'. The structure is analysed by the method of momentum[90][89]. In the MoM simulation, to ensure a fast simulation with a good accuracy, a graded-mesh is used with the maximum mesh parameter of $\lambda_0/25$ with at least five discretisations on each object. Initially, the diamond-shaped MPA are fabricated on an RT Duroid material, which has the relative permittivity of 2.22 and thickness of 1.6 mm. The 50Ω microstrip line was calculated by using the line formula[219]. It is observed that by decreasing the length L_1 of the monopole antenna the resonant frequency of the diamond-shaped monopole antenna is increased.

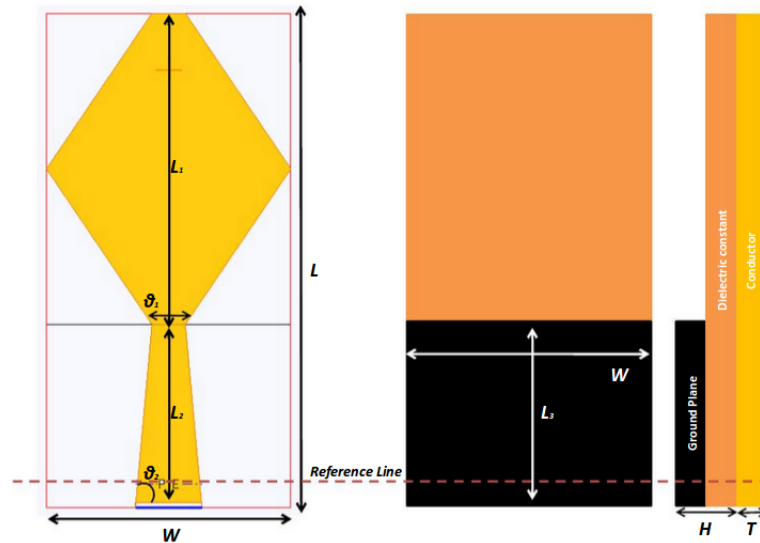


Figure 6.1: Diamond shaped monopole antenna

6.1.3 Simulation Results Of A Diamond Shaped MPA and Fabrication

The resonant frequency of the monopole antenna was calculated using the quarter-wavelength of the resonant frequency. Recently a technique has been developed to calculate the resonant frequency of the radial stub resonators[220][221]. In this work, a similar approach is adopted to calculate the resonant frequency of the diamond-shaped MPA as a function of inner length at a fixed sectorial angle and is given in a polynomial form as

$$f_0 = -3 \times 10^{-6} L_1^5 + 5 \times 10^{-4} L_1^4 - 0.0337 L_1^3 + 1.0827 L_1^2 - 17.29 L_1 + 115.89 \quad (6.2)$$

The polynomial coefficients in equation (6.2) are specific to 45-degree sectorial angle and it needs to be adopted for the different sectorial angle. Figure (6.2) shows a comparison between the simulated diamonds shaped monopole antenna and a monopole wire antenna. The results show that the diamond-shaped monopole antenna resonates at a higher frequency when compared to the monopole wire antenna of a comparable length. The plot shows that for a monopole wire antenna with an inner length of 15 mm resonates at a frequency of 5.1 GHz for the diamond-shaped monopole antenna with an inner length of 15 mm resonate at a frequency of 10.8 GHz. The diamond-shaped monopole antenna has a smaller physical length when compared to the monopole wire antenna.

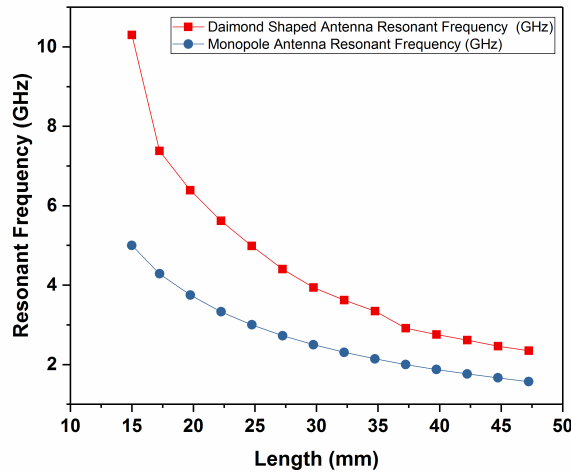


Figure 6.2: Simulated resonant frequency of a diamond-shaped MPAs for different inner length L_1 and by fixed sectorial angle

The antenna has been fabricated using chemical etching process as demonstrated in figure (6.3) and an image of fabricated antennas shown in figure (6.4).

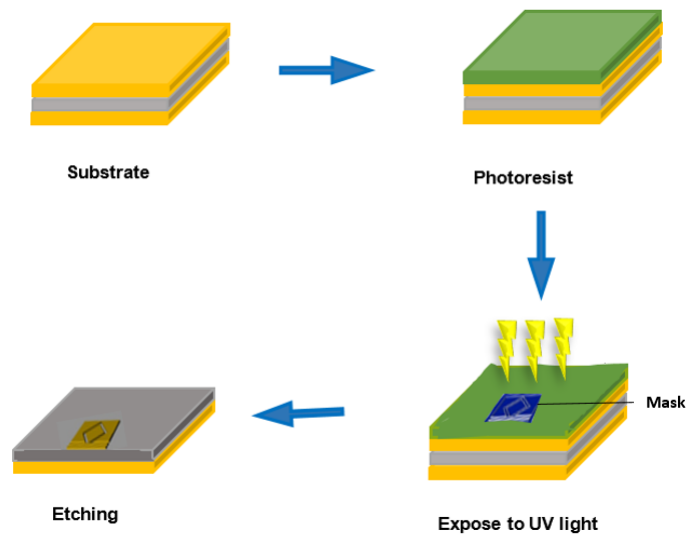


Figure 6.3: Diamond shaped monopole antenna fabrication Process



Figure 6.4: Fabricated diamond shaped antennas

6.1.4 Experimental Results Of A Diamond shaped MPA

A number of diamond-shaped MPAs with a sectorial angle (θ_2) of 45° with an inner length L_1 of 15 to 48 mm are fabricated on a 1.6 mm thick RT Duroid material. The thickness of the metallisation of the monopole antenna structure is $0.5\mu\text{m}$ and the structure is fed by using a $50\ \Omega$ microstrip line which is shown in figure (6.1). The antennas were characterised by using two-port S-parameter measurements from 10 MHz to 20 GHz using a Keysight (E8362B) network analyser. The experimental resonant frequency is determined by using the S_{11} parameter of the monopole antenna.

The measured resonant frequency of a diamond-shaped monopole antenna with an increasing inner length L_1 are compared in figure (6.5). The plot shows that the measured resonant frequencies agree with the simulated results for inner length L_1 varying from 4 mm to 44 mm.

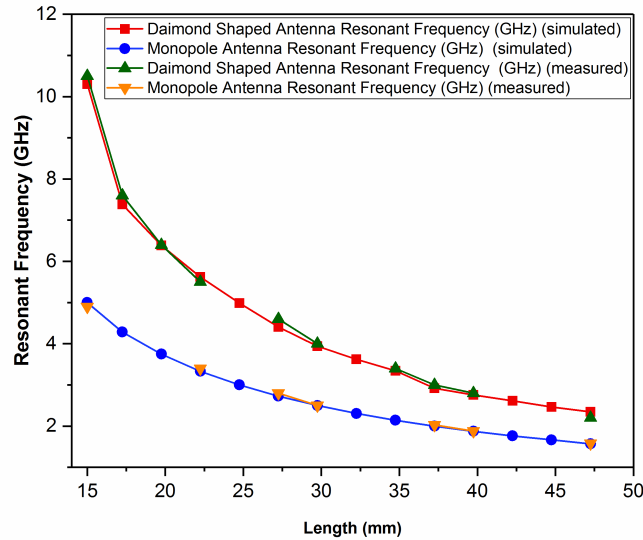


Figure 6.5: Comparison of the resonant frequency of Diamond shaped and monopole antennas as a function of inner length L_1 (simulation and measurements)

The quality factor and bandwidth of diamond-shaped MPAs are calculated by [222]

$$Q = \frac{\text{Energy stored}}{\text{Energy dissipated}} = \frac{f_0}{\Delta f} \quad (6.3)$$

Where Δf is the 3 dB bandwidth. The 8 mm and 45° sectorial angle (θ_2) diamond shaped MPA had a simulated Q-factor of 48; the measured Q-factor was 42, whereas for the monopole antenna the simulated Q-factor was 26. Higher Q-factor is been pos-

sible by increasing the metallisation thickness. Figure (6.6) shows the comparison of the bandwidth of a diamond-shaped monopole and a monopole antenna. It shows that diamond shaped MPA has a higher bandwidth when compared to the monopole antenna.

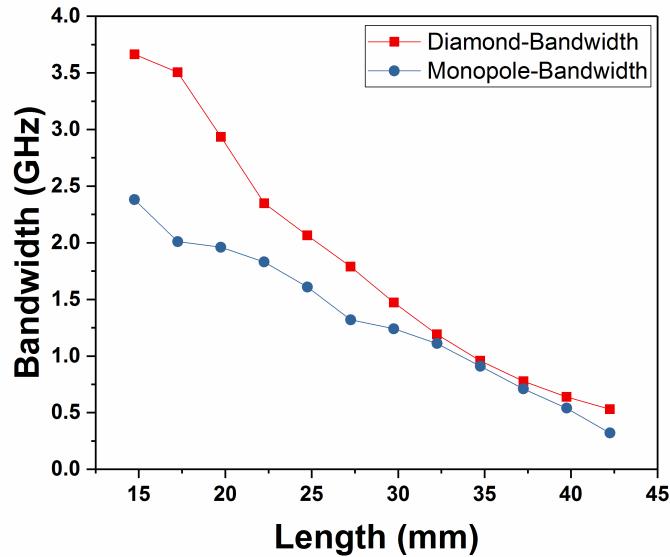


Figure 6.6: Comparison of the bandwidth of diamond-shaped MPAs and monopole antennas for different length

6.2 Coplanar Waveguide (CPW) Diamond Shaped MPAs

High-frequency diamond shaped monopole antennas are designed using coplanar waveguide format structure which has ground-source-ground (GSG) of $(75\mu\ 75\mu\ 75\mu)$ to reduce the parasitic effects. Diamond-Shaped MPAs are designed and developed using the software package Advanced Design systems (ADS-2009). Figure (6.7) shows a typical structure of a CPW diamond shaped MPAs with/without air-bridge, the air-bridge is used to equalise the potential between the ground planes. The simulation results for a 1000μ length CPW diamond shaped MPAs is shown in figure (6.8). The resonant frequency of the CPW diamond shaped antennas was defined when the S_{11} approaches to a low loss and the S_{12} has a high return loss or approaches to zero. From the figure (6.8), it can be seen that CPW diamond shaped MPA with air-bridge is resonating at a higher frequency (≈ 62 GHz) with wider bandwidth when compared to the CPW diamond shaped MPA without air-bridge (≈ 55 GHz). Due to some manufactur-

ing issues, it was difficult to fabricate the air-bridge for the CPW diamond shaped MPA. An important feature of the diamond-shaped MPA was that it took less up circuit space when compared to the other exciting antennas at the same frequency.

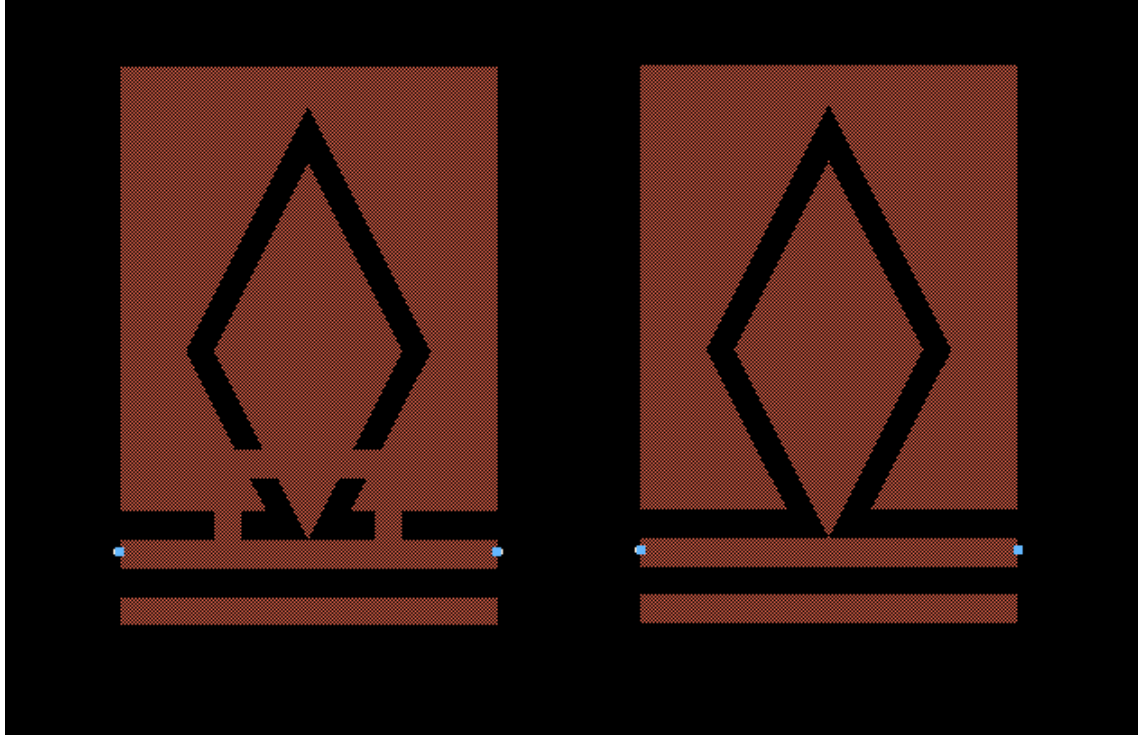


Figure 6.7: Diamond Shaped antenna with and without air-bridge

Figure (6.9) shows a schematic view of the CPW diamond shaped MPA with has a metallised thickness of ($\tau = 300nm$) and a length ($L=1000\mu$) with an inner angle (θ), the apex corner of the resonator is directly fed from a CPW 50Ω line. The diamond shaped MPAs were fabricated by using copper material as a metallisation on a different polymer substrate, which was mentioned in table (6.1) (more details about fabrication process will be discussed in the following section) and RF characterised from 10 MHz to 110 GHz using a high-frequency network analyser. The loaded diamond shaped MPAs were fully characterised using MoM model in an electromagnetic package within the ADS.

Like a diamond-shaped MPA at low frequency, precaution care was taken to choose the correct meshing size ($0.028 * \lambda/4$) in order to obtain a realistic S-parameter for small length CPW diamond shaped MPA. Figure (6.10) illustrated the simulation resonating frequency for each MPA fabricated in different polymer materials.

On the other hand, MPA array was designed and fabricated using the same polymer materials. These MPA arrays are designed using coplanar waveguide format structure

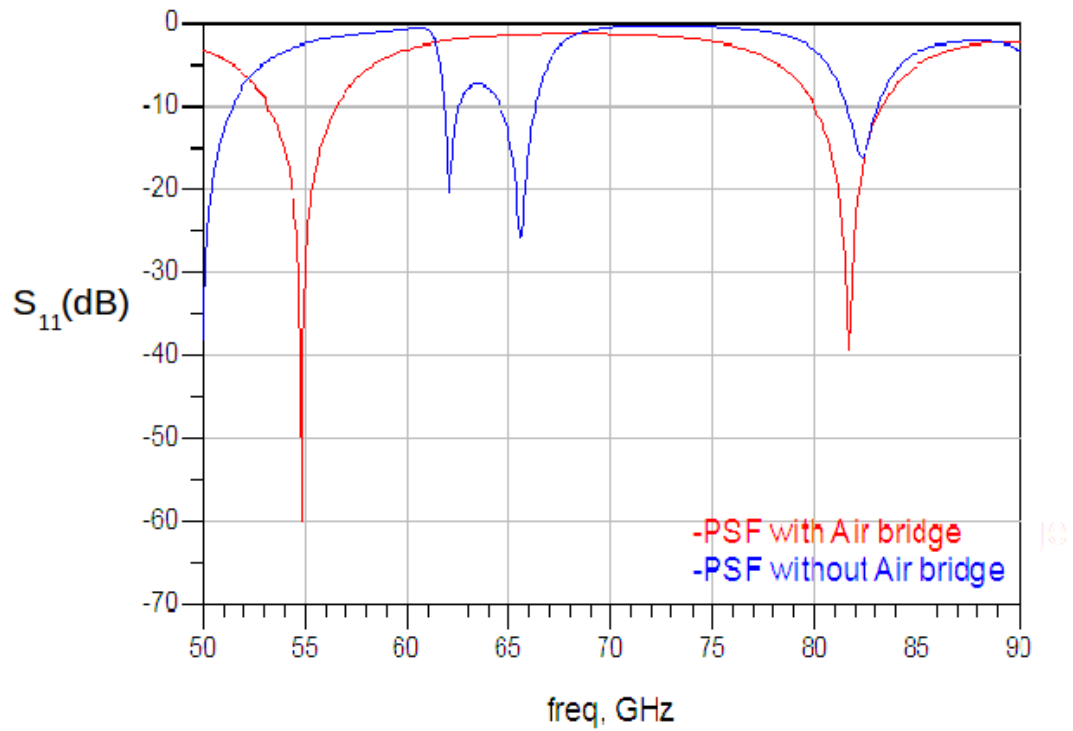


Figure 6.8: Diamond Shaped antenna with and without air-bridge

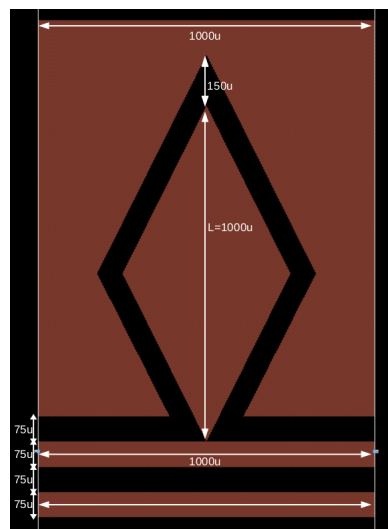


Figure 6.9: Schematic of a CPW Diamond Shaped MPA

Polymer materials	Thickness (mm)	Complex per-mittivity (ϵ_r)	Loss tan-gent ($\tan\delta$)
Polyethylene	0.16	$2.10 \pm 14\%$	$1.5E-04 \pm 2.9E-04$
Polypropylene	0.39	$2.11 \pm 6\%$	$2.3E-04 \pm 1.2E-04$
Polyvinyl chloride	0.21	$2.53 \pm 3\%$	$5.8E-03 \pm 2.5E-03$
Polystyrene	0.16	$2.35 \pm 16\%$	$3.2E-04 \pm 2.6E-04$
Polystyrene fibre	0.15	$1.36 \pm 5\%$	$2.4E-04 \pm 4.8E-04$

Table 6.1: Dielectric parameters for different polymers at various frequencies

which has (GSG) of $(150\mu 150\mu 150\mu)$ as shown in figure (6.11). Figure (6.12) illustrated the simulation resonating frequency for each MPA array in different polymer materials. Further discussion of the simulation results are compared and explained in section (6.2.2)

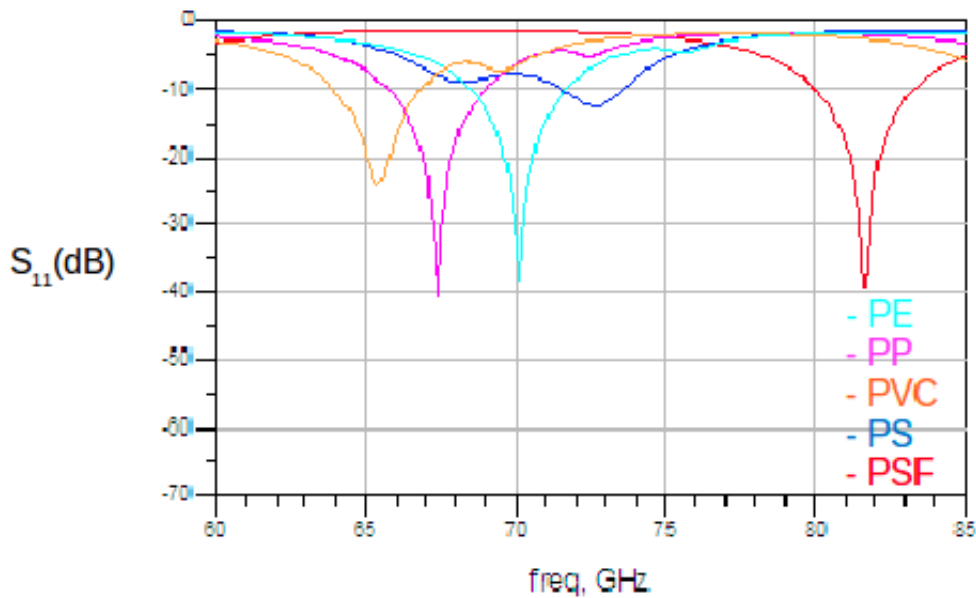


Figure 6.10: Simulation results for different polymers materials (single MPA antennas)

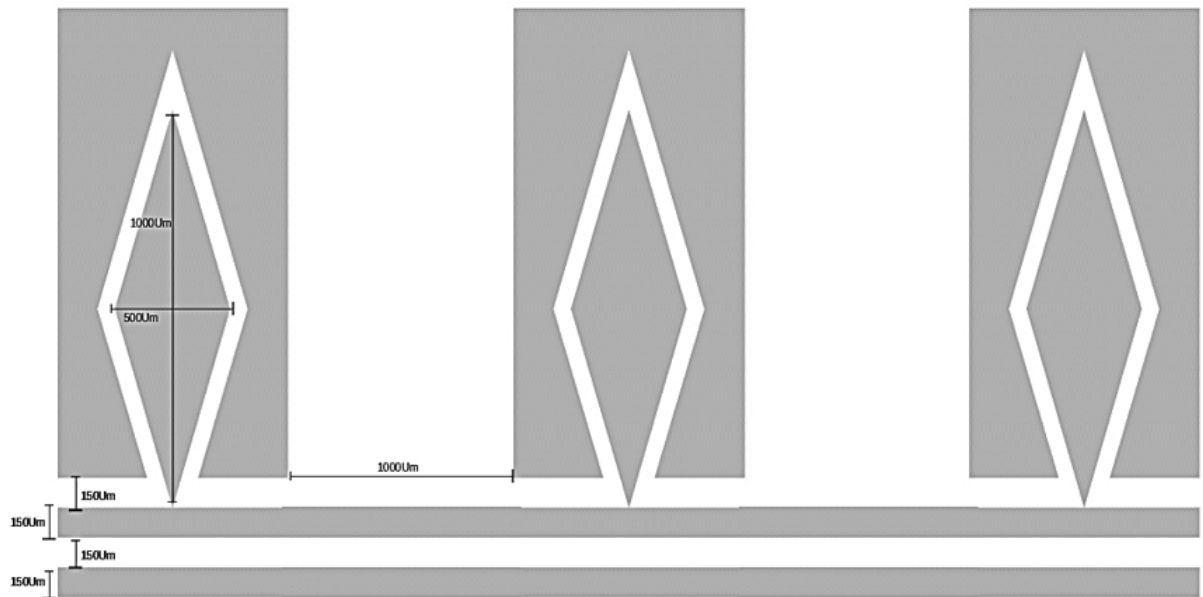


Figure 6.11: Schematic of a CPW Diamond Shaped MPAs

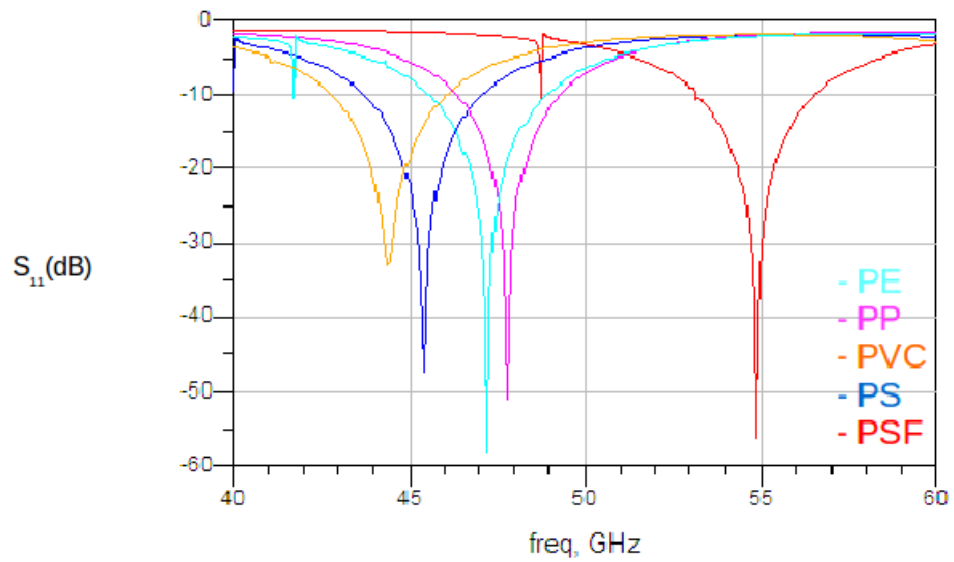


Figure 6.12: Simulation results for different polymers materials (MPA array)

6.2.1 Fabrication process of a CPW Diamond shaped antennas

The antennas were fabricated on the different polymers substrate by using the evaporation technique mentioned on chapter (4). First the polymer samples were cleaned using the barrel etcher as explained also on chapter (4), then the ground plane (Aluminium (Al) material) deposited with thickness ≈ 300 nm using the thermal evaporator on one side of the polymer samples, after that by using the shadow mask, the metallisation layer of the antenna deposited on the other side of the polymer samples with thickness of ≈ 300 nm. The whole process is illustrated in figure (6.13)

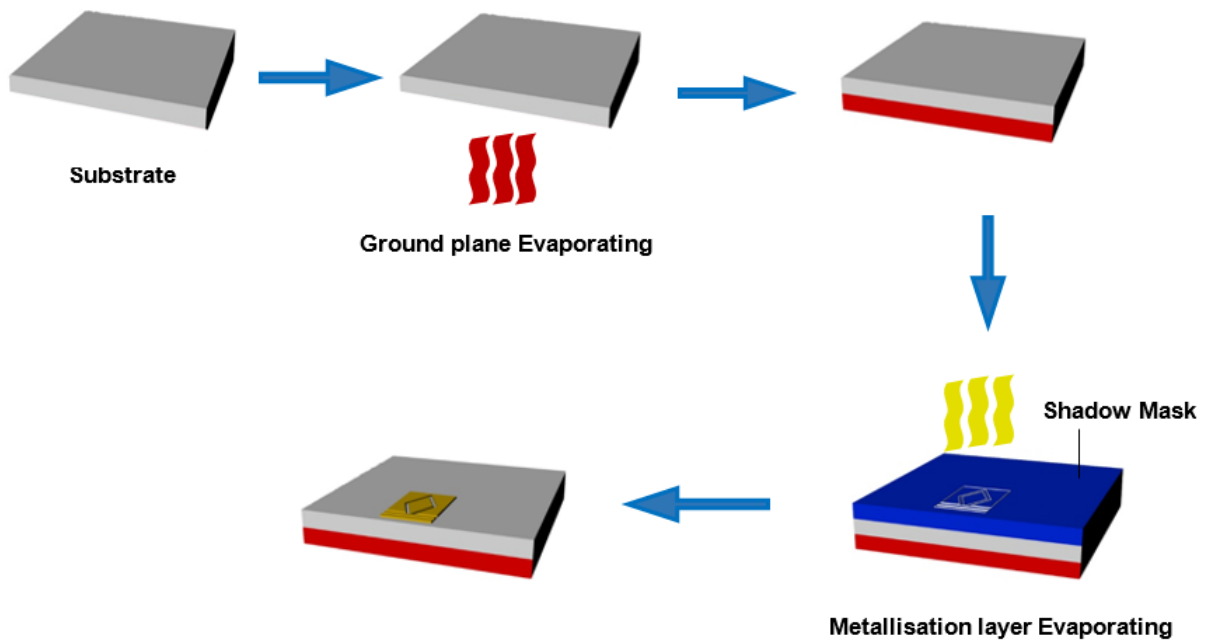


Figure 6.13: High-frequency Diamond shaped antennas fabrication Process

6.2.2 Experimental Results of a CPW Diamond shaped antennas

A number of CPW diamond shaped MPA with a sectorial angle of 45 degrees was fabricated on different material. The metallisation thickness of fabricated antennas was around ≈ 300 nm to minimise the conductor losses and the structure was directly fed by using the 50- Ω CPW lines which are shown in figure (6.9). The CPW diamond shaped MPAs structures were fabricated at DE Montfort University and RF characterisation was carried out at University of Nottingham The CPW diamond shaped MPA were characterised using two-port S-parameter VNA measurements from 100 MHz to 110 GHz and it was calibrated by using RF calibration substrate from picoprobe(CS-5).

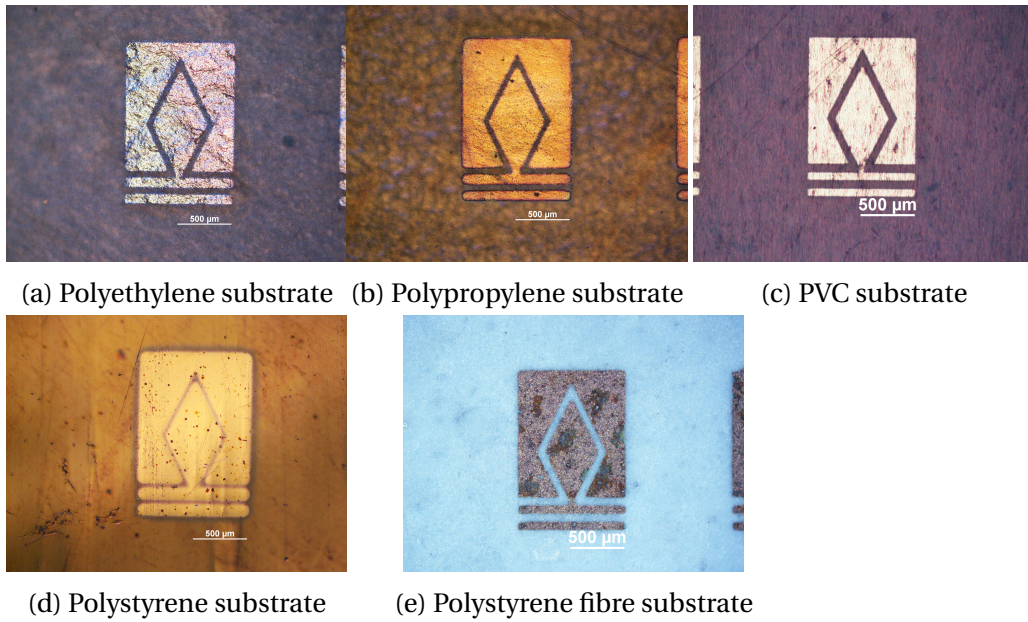


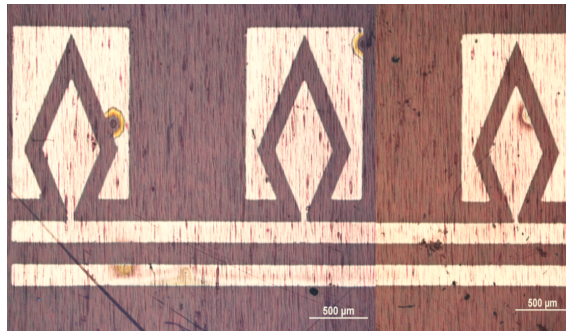
Figure 6.14: Fabricated CPW Diamond Shaped MPAs using different polymers substrates

Figure (6.17) illustrates the measurements and simulation results of diamond-shaped MPA fabricated on a PVC material. The plot displays that the measured resonating frequency was ($\approx 67.2\text{GHz}$ with -41.02dB) while the simulated frequency was (65.42GHz with -24.76dB), the small difference was due to the fabrication problem.

Figure (6.16) shows the comparison between the measured frequency ($\approx 80.58\text{GHz}$ with -52.72 dB) and simulated frequency ($\approx 81.67\text{GHz}$ with -39.57dB) of diamond-shaped MPA fabricated on a PSF material. The plot shows a slight deviation from the resonant frequency when compared to the simulation results, this is also due to the fabrication problem of the diamond-shaped antennas and this can be overcome by a controlled fabrication technology.

The different resonating frequencies illustrated in figure (6.10) and figure (6.12) as well as the measured resonant frequency of the other CPW diamond shaped MPAs with different dielectric materials are directly compared as presented in table (6.2). The different in resonating frequencies for the same antenna design was due to the different characteristics of the different polymers materials i.e dielectric constant and loss tangent.

It should be noted that the measured results for the CPW MPA arrays is not available due to non-availability of GSG probe of (150μ 150μ 150μ)



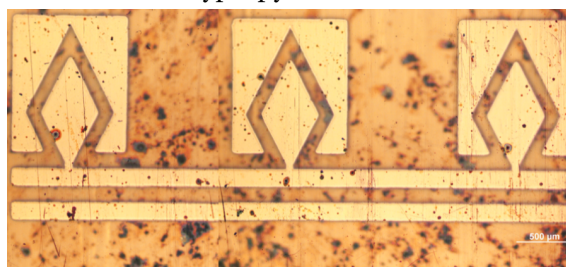
(a) PVC substrate



(b) Polyethylene substrate



(c) Polypropylene substrate



(d) Polystyrene substrate

Figure 6.15: Fabricated high-frequency Diamond Shaped MPAs arrays using different polymers substrates

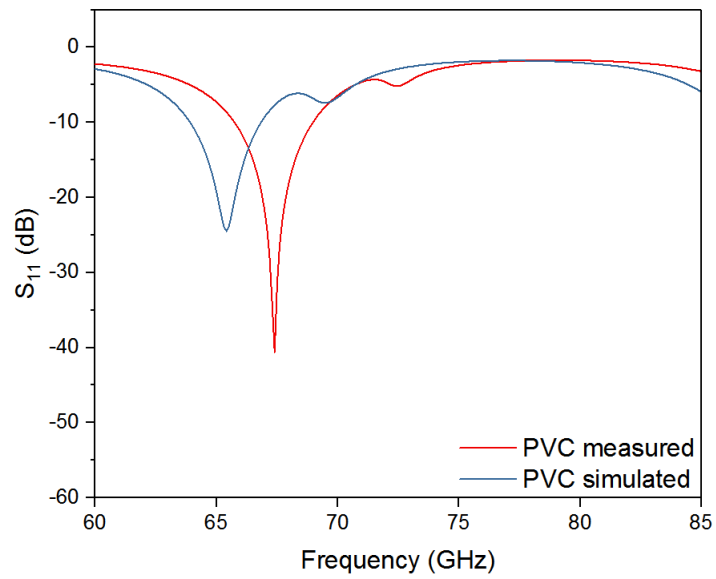


Figure 6.16: Measurements and simulation results of a diamond-shaped MPA fabricated on a PVC

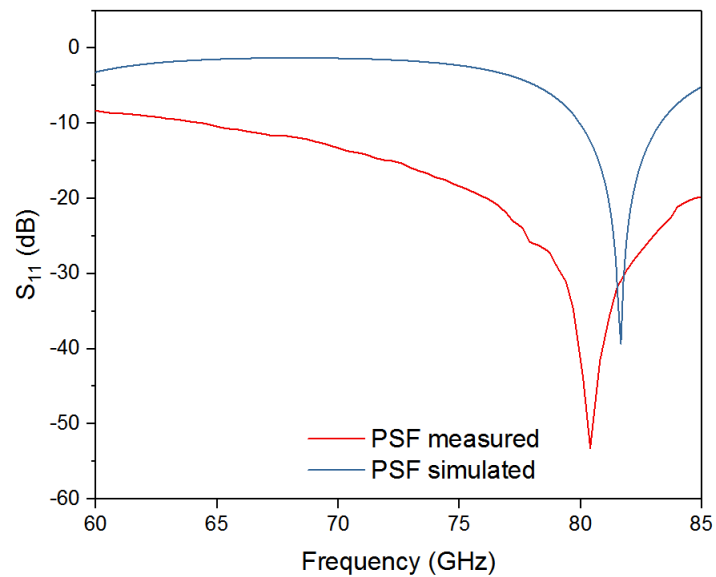


Figure 6.17: Measurements and simulation results of a diamond-shaped MPA fabricated on a PSF

Materials	Simulation frequency (GHz)(single MPA)	Measured frequency (GHz)(single MPA)	Simulation frequency (GHz)(MPA array)
Polyethylene	70.14	67.5	47.24
Polypropylene	67.40	72.36	47.81
PVC	65.42	67.2	44.38
Polystyrene	72.60	63.25	45.42
polystyrene fibre	81.67	80.58	54.84

Table 6.2: Simulation frequency VS Measured frequency for different polymers materials

6.3 Design And Simulation Of Nano-Patch Antennas On Diamond-Like Carbon Substrate

In this recent time, nano-antennas have been explored up to visible range [223][224][225]. There is a wide range of antenna forms that are able to accommodate the stated operating frequency or may be scaled correspondingly for recommended operation.[226][227][228][229]. On the other hand, a greater number of designs feature a wide surface space which may not proper for suitable applications, while a few designs maybe undesired due to the bandwidth limitations[230]. Apparently, the main objective for the present design is to resolve a compact nano-antenna which can provide the recommended impedance and gain achievement over frequency [1 THz–5 THz].

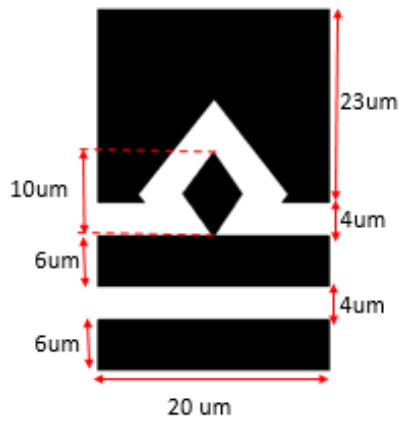
The design of an antenna working at optical frequencies is not a straightforward task, as a result of the inherent nature of the optical radiation and to the dispersive properties of the materials in such a frequency range. Following the previous works by Alú and Engheta [231][232][233], from an electrical engineering perspective, designing nano-antennas can be done using the same electromagnetic concept commonly used in radio and microwave frequencies. Such approach has been successfully employed in the case of simple nano-antennas, for example, the nano-dipoles and nanodimers

[231][232][233] and also applicable for more complex radiators, such as the bowtie, the spiral and the Yagi-Uda antennas[234][235][236]. The concept of the design was to make a radiating device which is able to generate several resonances in the operating spectrum to obtain ultra-wideband performance.

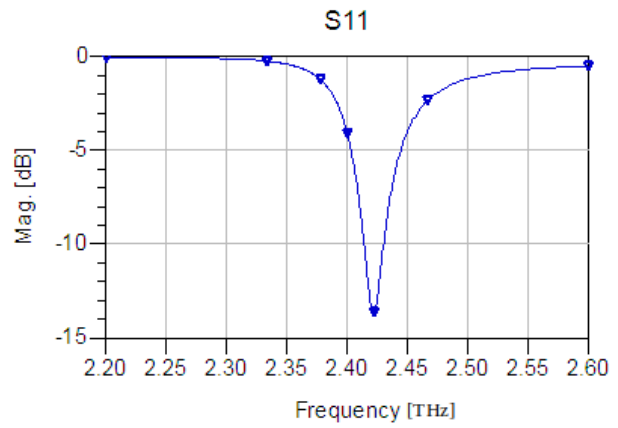
In this section, the same design (diamond-shaped) from the previous section which validate better efficiency, used for nano-patch antennas. Another design (T-shaped) used for this type of antennas as well. Due to the smaller size of nano-patch antennas, a thinner dielectric medium substrate is needed(≈ 100 nm). For this reason, Diamond-like carbon(DLC) material has been used as a dielectric medium since it can be deposited with thickness of (≈ 100 nm) and has dielectric constant (≈ 2.35). It is a metastable, amorphous carbon that comprises a various mixture of sp^3 - and sp^2 -hybridized carbon atoms[237][238]. The amorphous nature of DLC may be hydrogenated or un-hydrogenated depending on the chemical composition used for the deposition[237]. It possesses properties such as optical transparency, excellent insulating material, extremely high corrosion resistance, chemical inertness and above all, these properties are similar to those possessed by diamond[237][238][239]. . DLC found its applications in many areas such as biomedical coating, Micro-Electromechanical devices (MEMs), Automobiles parts, optical windows, memory disks[237][238][239][240]. It is cheaper to produce as compared to the diamond with the following techniques; Filtered Cathodic Vacuum Arc (FCVA), Inductively Coupled Plasma Assisted Sputtering (ICPAS), Pulsed Laser Deposition (PLD) and Plasma Enhanced Chemical Vapour Deposition (PECVD) etc[237][238][241].

6.3.1 Design and simulation of a diamond shaped nano-patch antenna

The diamond shaped nano-patch antenna has been designed using coplanar waveguide format structure (the same method used to design the MPA in chapter 6) which has (GSG) of ($6\mu-4\mu-6\mu$) as shown in figure (6.18a). Figure (6.18b) illustrated the simulation resonating frequency for this nano-patch antenna taking into consideration of the DLC material parameters (thickness ≈ 92.92 nm and the dielectric constant ≈ 2.35). The antenna was resonating at 2.42 THz with (-14 dB) return loss. This antenna has been fabricated using FIB as shown in figure (6.19)



(a) Diamond shaped nano-patch antenna dimensions



(b) S₁₁

Figure 6.18: Diamond shaped nano-patch antenna

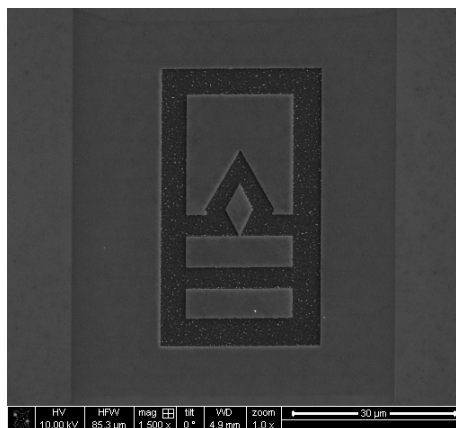


Figure 6.19: FIB fabricated diamond shaped nano-patch antenna on DLC with Si substrate

6.3.2 Design and simulation of a diamond shaped nano-patch antenna array

In order to enhance the gain of the antenna, an array of nano-patch antenna has been designed and simulated(6.20a). Form the simulation shown in figure (6.20b), the resonating frequency is 1.42 THz with (-19 dB) return loss. This array has been fabricated using FIB as illustrated in figure (6.21)

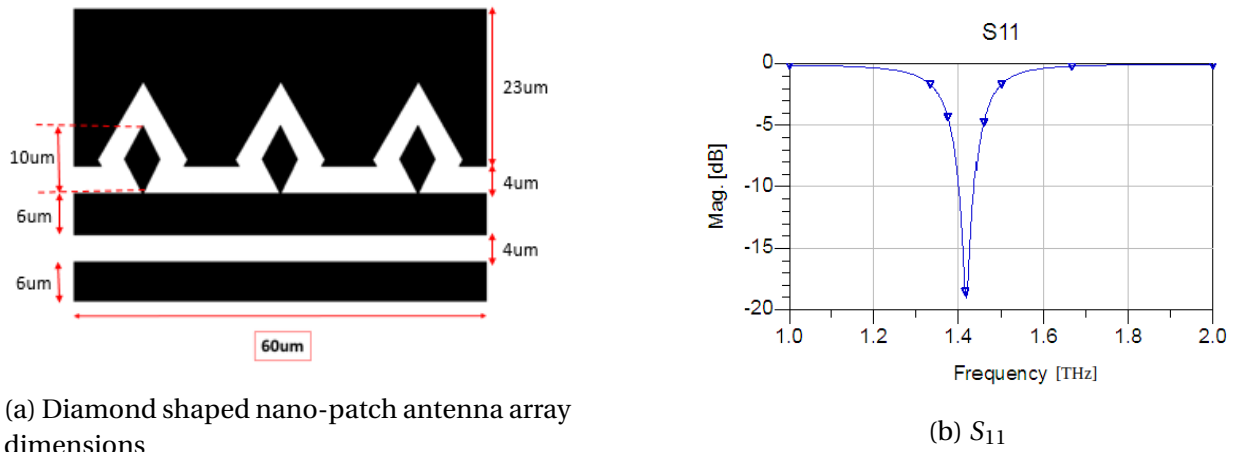


Figure 6.20: Diamond shaped nano-patch antenna array

6.3.3 Design and simulation of T-Shaped nano-patch antennas

The proposed T-shaped nano-patch antenna is capable of preserving a low profile and fitting in a tiny area and gaining resonances for wideband performance at the same time. The following stage of the design focused on further improvements for the overall performance of this antenna.

The structure was designed to achieve the circular polarisation in terahertz frequencies. The novel T-shaped nano-patch antenna was found to have a higher bandwidth and return loss when compared to the other nano-patch antennas[242][243][244].

A schematic view of the T-shaped nano-patch antenna illustrated in figure (6.22a) and (6.22b) respectively. The nano-patch antenna has a T-shaped with an inner length of L . the apex corner of the nano-patch antenna straight fed from a $50\text{-}\Omega$ microstrip line.

The simulated result for a T-shaped nano-patch antenna having an inner length of 400 nm and sectorial angle of 60 degrees is shown in figure (6.23a). The simulated

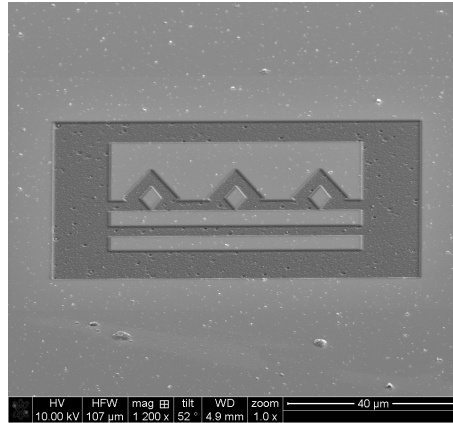


Figure 6.21: FIB fabricated diamond shaped nano-patch antenna arrays on DLC with Si substrate

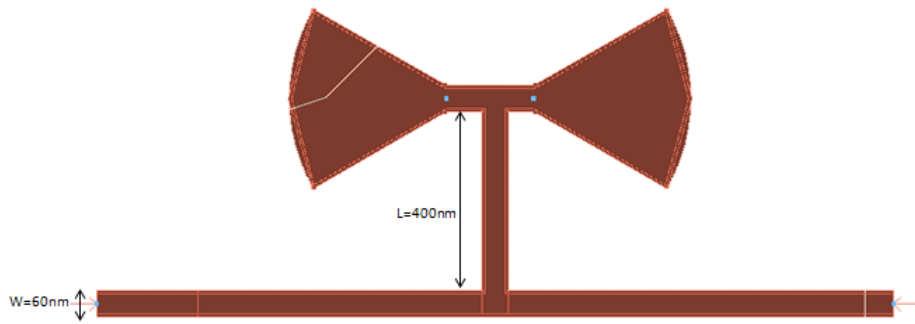
results show that the T-shaped antenna was resonating at 1.3 THz and 3.3 THz with an operational bandwidth of more than 100% performs significantly better than the traditional nano-antenna.

Simulated gain and directivity performance for T-shaped nano-patch antenna is shown in figure (6.23b), which shows that a gain of 1.8 dBi at 1.3 THz, 1.1 dBi at 3.3 THz and the almost flat response observed through out the majority of the frequency. A typical radiation pattern for the novel T-shaped nano-patch antenna is shown in figure (6.24). The antennas were designed to radiate in broadside i.e. perpendicular to the axis of the patch. The main beam is sharp between 90° and 270° while minimum is in between 0° and 180° .

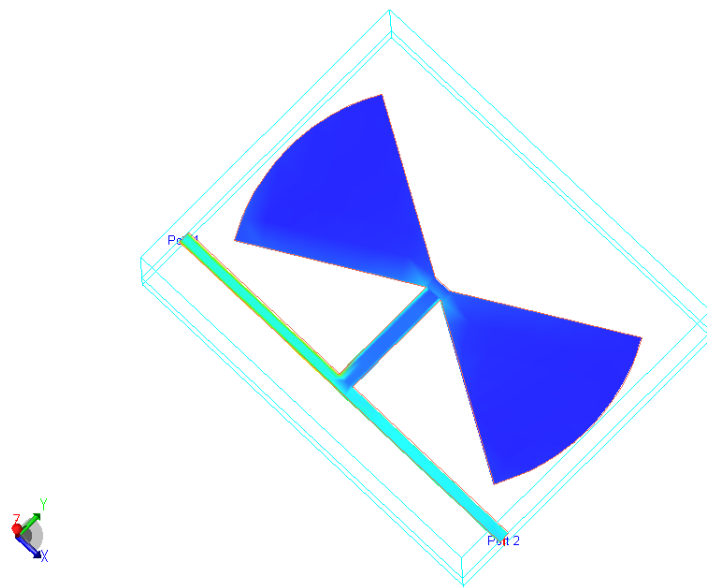
6.3.4 Fabrication process for nano-patch antennas

The fabrication process started by the deposition of a ground plane layer using Al with a thickness of ≈ 200 nm on a Si substrate using thermal evaporation technique, then a deposition of ≈ 93 nm DLC was carried out using PECVD technique and the deposition parameters are presented in table (6.3). The metallisation layer of Al was done using thermal evaporation technique to give ≈ 200 nm.

The nano-patch antennas of different shapes (T-shaped, Diamond-shaped and arrays patterned on DLC with Si substrate using FIB technique with dwell time of 1.000 μ s as the Al was etched to the shape required.

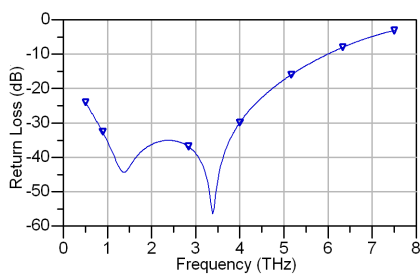


(a) (top-view)

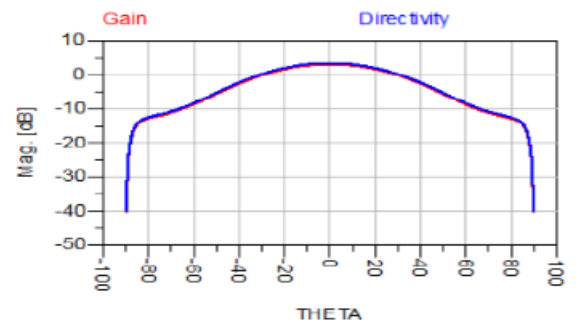


(b) (angular-view)

Figure 6.22: Schematic view of the T-shaped nano-patch antennas



(a) Simulated return loss response of the designed T-Shaped nano-patch antennas



(b) Gain and directivity of the T-shaped nano-patch antennas

Figure 6.23: Return loss, gain and directivity of the T-shaped nano-patch antennas

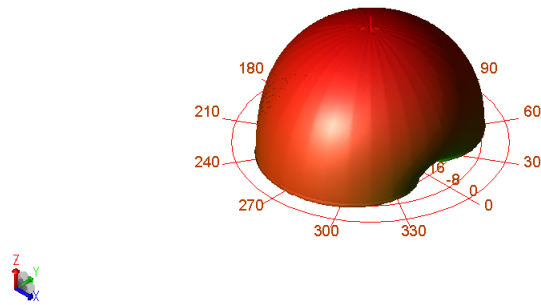


Figure 6.24: Front view of 3D directivity pattern

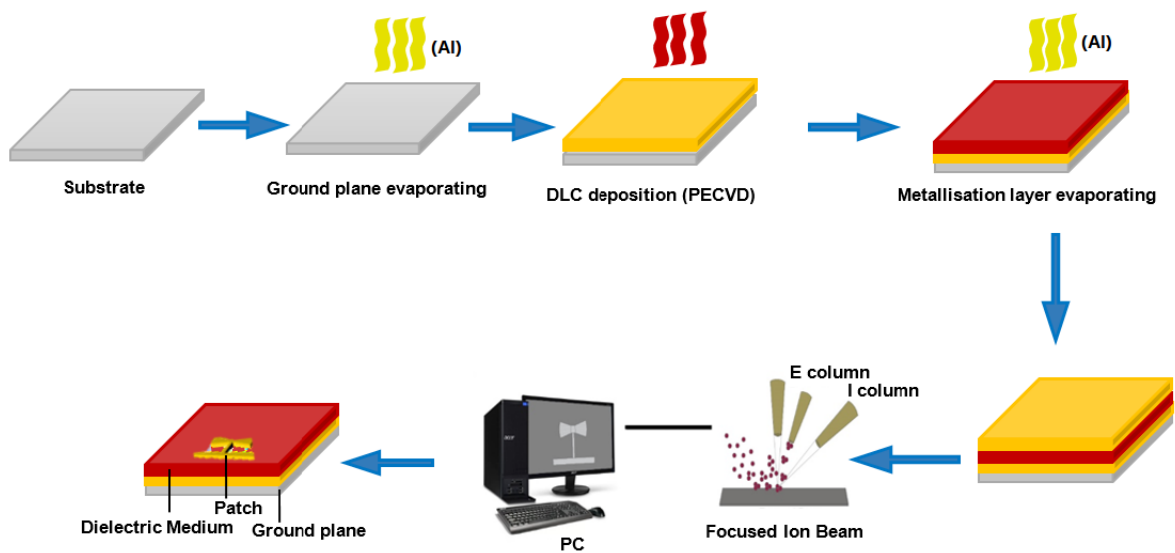


Figure 6.25: FIB fabrication

Parameters	Values
Gas flow rate CH_4	100 sccm
Gas flow rate Argon	100 sccm
RF	100 w
Deposition pressure	100 mTorr
Deposition time	10 minutes

Table 6.3: PECVD deposition parameters for growth of DLC

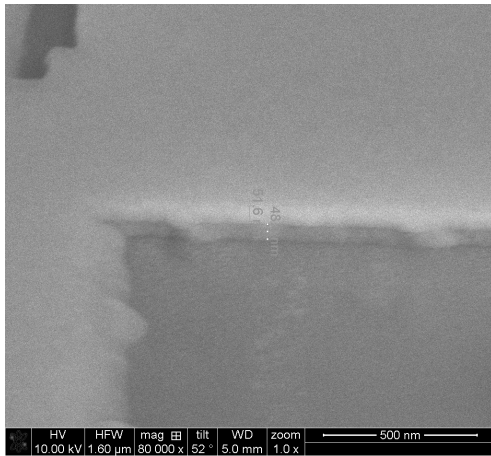


Figure 6.26: Cross section on copper on DLC

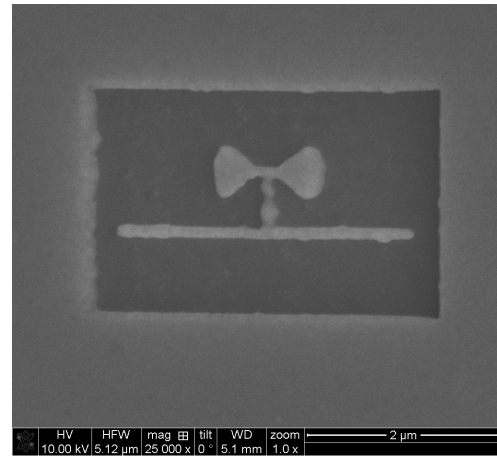
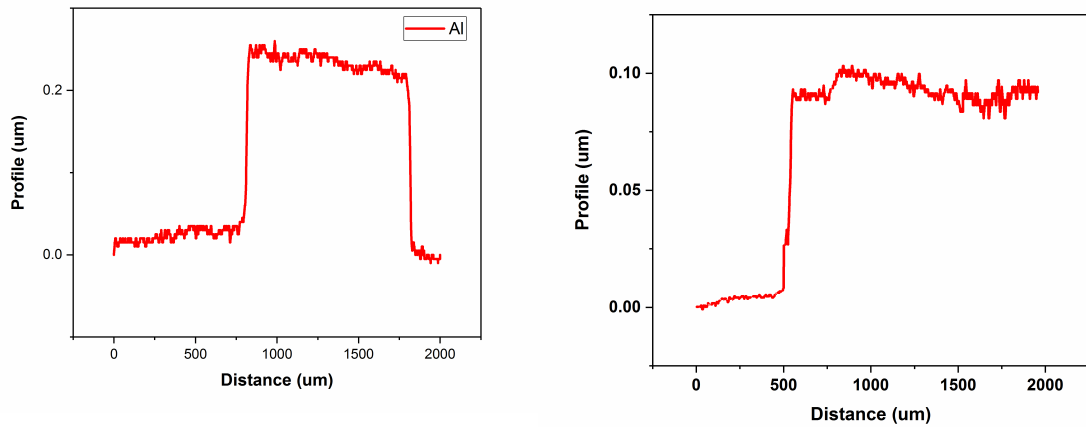


Figure 6.27: Fabricated t-shaped nano-patch antenna

6.3.5 DLC Measurements

6.3.6 Thickness

The thickness for metallisation layer (Al), the ground plane (Al) and the dielectric medium (DLC) were measured using the step profilometer. Two samples (Al and DLC) were prepared for this purpose by creating a step for each sample. The Al thickness measured was ≈ 200 nm thickness as illustrated in figure (6.28a) and the DLC thickness for the material is ≈ 93 nm as shown in figure (6.28b).



(a) Thickness of the Al layer on plain glass substrate

(b) Thickness of the DLC layer

Figure 6.28: Thickness measurements for Al and DLC layers

6.3.7 C-V measurements

The C-V measurement (described in 4) has been used to determine the dielectric constant of the medium substrate. The result of this measurement is illustrated in figure (6.5).

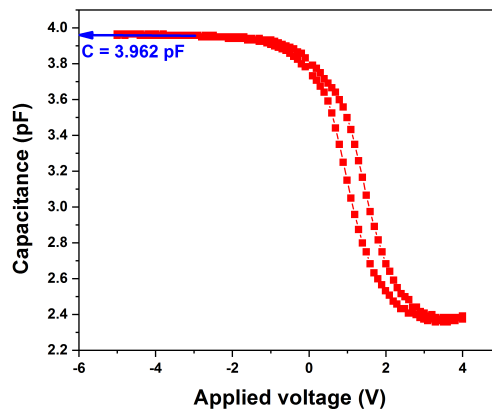


Figure 6.29: Capacitance of DLC materials

$$C = \frac{\epsilon_0 \epsilon_r A}{D} \quad (6.4)$$

From equation (6.4), the dielectric constant of the DLC materials has been calculated as follows; $C = 3.962 * 10^{-12} F$

$$A = 1.77 * 10^{-6} m^2$$

$$\epsilon_0 = 8.85 * 10^{-12} F/m$$

$$D = 92.91 nm$$

$$C = \frac{3.962 * 10^{-12} * 92.91 * 10^{-9}}{8.85 * 10^{-12} * 1.77 * 10^{-6}} \quad (6.5)$$

so the DLC $\epsilon_r = 2.35$

6.3.8 RF measurements of the nano-patch antennas

As discussed earlier in the chapter 4, RF measurements for this kind of antennas is challenging. Due to this reason, proposed "**Non-contact probes set-up**" can be used for the measurements. It should also be noted that no literature as stated this measurement technique for this purpose. Presently, non-availability of this instrument hindered the measurements of these fabricated antennas in order to compare the resonating frequencies between the simulated and fabricated antennas.

6.4 Conclusion

A diamond shaped MPA on RT Duriod material has been simulated and fabricated for different inner lengths. The resonant frequency is approximated as a function of inner length L_1 in the form of a polynomial equation. It was observed that the diamond-shaped MPA is more compact (physical length) compare to conventional monopole antenna, making it attractive for wireless communication technology applications. Diamond shaped MPA was fabricated and experimentally measured with a good agreement with the simulation results.

CPW diamond shaped MPA were fabricated on different polymer materials (including PSF which was fabricated at De Montfort University) and characterised at the University of Nottingham. The resonant frequency of the CPW diamond shaped MPA fabricated on PSF was resonating at a higher frequency and a wider bandwidth when compared to the other polymers materials. CPW diamond shaped MPA was fabricated and experimentally measured with a good agreement with the simulation results, a slight deviation from the resonant frequencies when compared to the simulation results is due to the fabrication issue which can be overcome by a controlled fabrication technology.

The nano-patch antennas of different shapes were designed, simulated and fabricated. These antennas were designed and analysed by using momentum model in ADS software. The fabrication was done on DLC with Si substrate, which was growth using both thermal evaporation and PECVD as the antennas were fabricated on the substrate using FIB. The results indicate that the novel T-shaped nano-patch antenna had a smaller physical size and higher bandwidth when compared to the other nano-antennas at terahertz frequency. Though, fabricated antennas were not measured due to non-availability of suitable instrument (non-contact probes set-up).

Chapter 7

CONCLUSION AND FUTURE WORK

7.1 Conclusion

This chapter sum up all the findings through this research work. First, The initial characterisation and justification for the choice of polymer materials (PE, PP, PVC, PS and PSF) as dielectric medium substrates for MPAs working in MMW region. The techniques employed include FTIR, DSC, TGA, BDS and SPDR. These analysis confirmed the suitability of these materials as dielectric medium for MPAs operating in MMW spectrum due to their high thermal stability, lower permittivity and low loss tangent.

Furthermore, A co-solvent vehicle (comprising 50:50 ratio) of DCM and acetone was used with processing conditions of solution infusion flow-rate of $60\mu\text{L}/\text{min}$ and an applied voltage of $12\pm\text{kV}$ for the production of PSF using Electrospinning technique. This material posses lower complex permittivity of $1.36\pm 5\%$ and lower loss tangent of $2.4\text{E-}04\pm 4.8\text{E-}04$ as compared to PS ($2.35\pm 16\%$ and $3.2\text{E-}04\pm 2.6\text{E-}04$).

Designing, simulation and fabrication of a diamond-shaped MPAs working in spectrum (1-10 GHz) has been carried out using Photolithography. Diamond-shaped MPAs were fabricated and experimentally measured with a good agreement with the simulation results. It has been found that the diamond-shaped MPAs is more compact (physical geometry) and efficient as compared to traditional monopole antenna.

Moreover, Design, simulation and fabrication of CPW diamond shaped MPA using polymer materials (PE, PP, PVC, PS and PSF) as substrates. Fabrication process was done by thermal evaporation. The resonant frequencies of the CPW diamond shaped MPAs for PE, PP, PVC, PS and PSF are 67.5 GHz, 72.36 GHz, 62.41 GHz, 63.25 GHz and 80.58 GHz respectively. The antenna fabricated on PSF was found to resonate at a higher frequency when compared to the other polymers materials. Also, the effect of

adding an air-bridge to the CPW diamond-shaped MPA has been studied which verify an increase in the resonate frequency from 55 GHz to 62 GHz.

Finally, three different nano-patch antennas (Diamond shaped, diamond shaped array and T-shaped) were designed, simulated and fabricated on Si substrate with DLC. The DLC was deposited by PECVD technique, with CH_4 gas flow rate of 10 sccm, 100 sccm of Argon gas flow rate, RF power 100 w, deposition pressure of 100 mTorr, deposition time of 10 minutes. DLC has thickness of ≈ 93 nm while the metallisation layer Al has ≈ 200 nm of thickness using thermal evaporation. The final shape were patterned using FIB with dwell time of $1.000 \mu s$ as the Al was etched. The simulation illustrated that Diamond shaped and diamond shaped array were resonated at 1.42 THz with (-19 dB return loss) and 2.42 THz with (-14 dB return loss) respectively and T-shaped resonated at 1.3 THz and 3.3 THz (with -45 dB and -55 dB).

7.2 Future Work

One aspect that should be undertaken is to reconstruct the polymer materials (PE, PP, PVC and PS) using electrospinning technique. This will probably modify the material by lower relative permittivity (dielectric constant ϵ_r and the loss tangent δ) and help to improve the performance of antennas by increasing the resonating frequency, bandwidth, gain and directivity.

Antennas of different shapes can be designed and fabricated on the different modified polymer materials in order to further confirm the suitability of these materials and enhancement of their performance in MPAs.

The injection of gold nanoparticles into the PSF can also be investigated in order to reduce the dielectric constant ϵ_r and the loss tangent δ by enhancing the performance of the substrate for MPAs.

Furthermore, measuring the loss tangent of DLC using Atomic Force Microscopy (AFM) can help to establish the loss tangent of this material is not available presently in any literature. This value will help with the simulation accuracy of the nano-patch antenna.

The GSG-type of $150\mu-150\mu-150\mu$ probes needed for the measurements of CPW diamond-shaped MPA array fabricated should be made available in order to measure the fabricated array and make a comparison between the measurement and simulation results.

GSGs smaller than 40μ is not available, which raises the need for non-contact probes measurement. Consequently, the design and construction of non-contact

probes could be investigated to help ameliorate for this issue and facilitate measurement of the fabricated nano-patch antennas here and hence compare experimental results with simulated results.

References

- [1] Siva Viswanathan Thyagarajan. *Millimeter-Wave/Terahertz Circuits and Systems for Wireless Communication*. PhD thesis, University of California, Berkeley, 2014.
- [2] Siva Viswanathan Thyagarajan. Millimeter-wave/terahertz circuits and systems for wireless communication. 2016.
- [3] Fuad E Doany, Benjamin G Lee, Clint L Schow, Cornelia K Tsang, Christian Baks, Young Kwark, Richard John, John U Knickerbocker, and Jeffrey A Kash. Terabit/s-class 24-channel bidirectional optical transceiver module based on tsv si carrier for board-level interconnects. In *Electronic Components and Technology Conference (ECTC), 2010 Proceedings 60th*, pages 58–65. IEEE, 2010.
- [4] Traian Andrei. An overview of long term evolution advanced. Technical report, Washington University in St Louis.
- [5] M Barrett. The 60-ghz band cuts 4g backhaul cost. *Electronic Design*, Nov, 5, 2013.
- [6] Yikun Yu, Peter GM Baltus, and Arthur HM van Roermund. Millimeter-wave wireless communication. In *Integrated 60GHz RF Beamforming in CMOS*, pages 7–18. Springer, 2011.
- [7] Kenneth J Button. Infrared and millimeter waves v. 14: millimeter components and techniques, pt. v. 1985.
- [8] GR Davis, MJ Griffin, DA Naylor, PG Oldham, BM Swinyard, Peter AR Ade, SB Calcutt, Th Encrenaz, Th De Graauw, D Gautier, et al. Iso lws measurement of the far-infrared spectrum of saturn. *Astronomy and Astrophysics*, 315:L393–L396, 1996.
- [9] Chris Koh. The benefits of 60 ghz unlicensed wireless communications. *YDI Wireless Whitepaper*, pages 1–7, 2002.

- [10] Wi-Fi Alliance. Wigig® and the future of seamless connectivity, 2013.
- [11] Wireless backhaul spectrum policy recommendations & analysis. Technical report, GSMA, 2014.
- [12] Mario Weiß, Mathieu Huchard, Andreas Stohr, Benoît Charbonnier, Sascha Federwitz, and Dieter Stefan Jager. 60-ghz photonic millimeter-wave link for short-to medium-range wireless transmission up to 12.5 gb/s. *Journal of Lightwave Technology*, 26(15):2424–2429, 2008.
- [13] Byoung-Nam Kim, Seong-Ook Park, Jung-Keun Oh, and Gwan-Young Koo. Wideband built-in antenna with new crossed c-shaped coupling feed for future mobile phone application. *IEEE antennas and wireless propagation letters*, 9:572–575, 2010.
- [14] Rolf Kraemer and Marcos Katz. *Short-range wireless communications: Emerging technologies and applications*. John Wiley & Sons, 2009.
- [15] Thomas Kaufmann, Akhilesh Verma, Van-Tan Truong, Bo Weng, Roderick Shepherd, and Christophe Fumeaux. Efficiency of a compact elliptical planar ultra-wideband antenna based on conductive polymers. *International Journal of Antennas and Propagation*, 2012, 2012.
- [16] Boddapati Taraka Phani Madhav, Harish Kaza, Vidyullatha KAZA, Ponnamm MANIKANTA, Siddharth DHULIPALA, Sravan Kumar KONIJETI, Anvesh BONA-GIRI, and Fayaz SHAIK. Liquid crystal polymer substrate based wideband tapered step antenna. *Leonardo Electronic Journal of Practices and Technologies*, 26:103–114, 2015.
- [17] Jovanche Trajkovikj, J Francois Zurcher, and Anja K Skrivervik. Soft and flexible antennas on permittivity adjustable pdms substrates. In *Antennas and Propagation Conference (LAPC), 2012 Loughborough*, pages 1–4. IEEE, 2012.
- [18] Emranul Haque, Subaha Mahmuda, and Feroz Ahmed. A flexible polymer substrate based wideband antenna for wban applications. In *Telecommunications and Photonics (ICTP), 2017 IEEE International Conference on*, pages 190–194. IEEE, 2017.
- [19] Reshma Lakshmanan and Shinoj K@inproceedingshaque2017flexible, title=A flexible polymer substrate based wideband antenna for WBAN applications,

- author=Haque, Emranul and Mahmuda, Subaha and Ahmed, Feroz, booktitle=Telecommunications and Photonics (ICTP), 2017 IEEE International Conference on, pages=190–194, year=2017, organization=IEEE Sukumaran. Flexible ultra wide band antenna for wban applications. *Procedia Technology*, 24:880–887, 2016.
- [20] Yi Huang and Kevin Boyle. *Antennas: from theory to practice*. John Wiley & Sons, 2008.
- [21] Kai Chang. *RF and microwave wireless systems*, volume 161. John Wiley & Sons, 2004.
- [22] August E Grant and Jennifer H Meadows. *Communication technology update and fundamentals*. Routledge, 2016.
- [23] Ramiro Jordan and Chaouki T Abdallah. Wireless communications and networking: an overview. *IEEE Antennas and Propagation Magazine*, 44(1):185–193, 2002.
- [24] ATTILA GULYÁS. British radar in wwii. *AARMS*, 2008.
- [25] Tapan K Sarkar, Robert Mailloux, Arthur A Oliner, Magdalena Salazar-Palma, and Dipak L Sengupta. *History of wireless*, volume 177. John Wiley & Sons, 2006.
- [26] JE Brittain. Pierce and kompfner on earth satellite communications systems. *Proceedings of the IEEE*, 72(12):1704–1705, 1984.
- [27] Steven J Dick. *Societal Impact of Spaceflight*. Government Printing Office, 2007.
- [28] Federal Standard et al. Telecommunications: Glossary of telecommunication terms. *Retrieved January*, 15(2004):69–72, 1996.
- [29] Constantine A Balanis. *Antenna theory: analysis and design*. John Wiley & Sons, 2016.
- [30] Richard C Johnson and Henry Jasik. Antenna engineering handbook. *New York, McGraw-Hill Book Company, 1984, 1356 p. No individual items are abstracted in this volume.*, 1, 1984.
- [31] Ludwig Reinhold and Bretchko Pavel. Rf circuit design: theory and applications, 2000.

- [32] Constantine A Balanis. *Advanced engineering electromagnetics*. John Wiley & Sons, 2012.
- [33] Prakash Bhartia, RS Tomar, and KVS Rao. *Millimeter-wave microstrip and printed circuit antennas*. Artech House, 1991.
- [34] Terence Charles Edwards and Michael Bernard Steer. *Foundations of interconnect and microstrip design*, volume 3. John Wiley, 2000.
- [35] Ramesh Garg, Prakash Bhartia, Inder J Bahl, and Apisak Ittipiboon. *Microstrip antenna design handbook*. Artech house, 2001.
- [36] RS ELLIOT. Ieee standard definitions of terms for antennas. *IEEE Transactions on Antennas and Propagation*, 31(6):1–29, 1983.
- [37] L Volakis John and L Volakis. *Antenna engineering handbook*. McGraw-Hill, Toronto, 2007.
- [38] Constantine A Balanis. *Antenna theory: analysis and design*. John Wiley & Sons, 2012.
- [39] J Howell. Microstrip antennas. *Antennas and Propagation, IEEE Transactions on*, 23(1):90–93, 1975.
- [40] Ahmed Fatthi Alsager. *Design and analysis of microstrip patch antenna arrays*. 2011.
- [41] Ahmed A Kishk. *Fundamentals of antennas*, 2009.
- [42] Dhunish Kumar. *DESIGN AND ANALYSIS OF MICROSTRIP ANTENNAS FOR ULTRA-WIDE BAND APPLICATIONS*. PhD thesis, National Institute of Technology Rourkela, 2014.
- [43] J Howell. Microstrip antennas. *IEEE Transactions on Antennas and Propagation*, 23(1):90–93, 1975.
- [44] John D@bookschaub2004production, title=Production Testing of RF and System-on-a-chip Devices for Wireless Communications, author=Schaub, Keith B and Kelly, Joe, year=2004, publisher=Artech House Kraus. Ronald j. marhefka. *Antenna for all applications third edition*.

- [45] Keith B Schaub and Joe Kelly. *Production Testing of RF and System-on-a-chip Devices for Wireless Communications*. Artech House, 2004.
- [46] Trevor S Bird. Definition and misuse of return loss [report of the transactions editor-in-chief]. *Antennas and Propagation Magazine, IEEE*, 51(2):166–167, 2009.
- [47] A Rahim and Mohamad Kamal. Electromagnetic band-gaps structure in microwave device design. 2008.
- [48] James R James. *Handbook of microstrip antennas*, volume 28. IET, 1989.
- [49] Indrasen Singh and VS Tripathi. Micro strip patch antenna and its applications: a survey. *Int. J. Comp. Tech. Appl*, 2(5):1595–1599, 2011.
- [50] Rajeswari Chatterjee. *Antenna theory and practice*. New Age International, 1996.
- [51] Robert A Sainati. *CAD of microstrip antennas for wireless applications*. Artech House, Inc., 1996.
- [52] Georges A Deschamps and W Sichak. Microstrip microwave antennas. In *third USAF Symposium on Antennas*, volume 84, 1953.
- [53] JT Bernhard, PE Mayes, D Schaubert, and RJ Mailloux. A commemoration of deschamps and sichak's microstrip microwave antennas: 50 years of development divergence and new directions. Technical report, DTIC Document, 2003.
- [54] Randy Bancroft. *Microstrip and printed antenna design*. The Institution of Engineering and Technology, 2009.
- [55] H Gutton and G Baissinot. Flat aerial for ultra high frequencies. *French patent*, 703113, 1955.
- [56] WL Stutzman and GA Thiele. Antenna theory and design. *New York, John Wiley and Sons, 1981. Chap. 10.*, 1981.
- [57] AW Rudge, K Milne, AD Olver, and P Knight. *The handbook of antenna design*, volume 16. IET, 1983, pp. 73-79.
- [58] J Ashkenazy, P Perlmutter, and David Treves. A modular approach for the design of microstrip array antennas. *IEEE Transactions on Antennas and Propagation*, 31(1):190–193, 1983.

- [59] Yong Liu, Li-Ming Si, Meng Wei, Pixian Yan, Pengfei Yang, Hongda Lu, Chao Zheng, Yong Yuan, Jinchao Mou, Xin Lv, et al. Some recent developments of microstrip antenna. *International Journal of Antennas and Propagation*, 2012, 2012.
- [60] Zi-bin Weng, Nai-Biao Wang, and Yong-Chang Jiao. Study on high gain patch antenna with metamaterial cover. In *Antennas, Propagation & EM Theory, 2006. ISAPE'06. 7th International Symposium on*, pages 1–2. IEEE, 2006.
- [61] SUNIL KUMAR THAKUR. Design & analysis of microstrip patch antenna using metamaterial. Master's thesis, 2012.
- [62] Afzal Syed, Kenneth Demarest, and Daniel D Deavours. Effects of antenna material on the performance of uhf rfid tags. In *RFID, 2007. IEEE International Conference on*, pages 57–62. IEEE, 2007.
- [63] PA Wäger, M Eugster, LM Hilty, and C Som. Smart labels in municipal solid waste—a case for the precautionary principle? *Environmental Impact Assessment Review*, 25(5):567–586, 2005.
- [64] Camille Ramade, Sébastien Silvestre, Frédérique Pascal-Delannoy, and Brice Sorli. Thin film hf rfid tag deposited on paper by thermal evaporation. *International Journal of Radio Frequency Identification Technology and Applications*, 4(1):49–66, 2012.
- [65] Pavel V Nikitin, Sander Lam, and KVS Rao. Low cost silver ink rfid tag antennas. In *Antennas and Propagation Society International Symposium, 2005 IEEE*, volume 2, pages 353–356. IEEE, 2005.
- [66] Asadullah Noor. Design of microstrip patch antennas at 5.8 ghz. 2012.
- [67] David M Pozar and Daniel H Schaubert. *Microstrip antennas: the analysis and design of microstrip antennas and arrays*. John Wiley & Sons, 1995.
- [68] Robert S Elliot. *Antenna theory and design*. John Wiley & Sons, 2006.
- [69] Bikram Patir. A review on various techniques of microstrip patch antenna design for wireless application. In *International Journal of Computer Applications (IJCA), National Conference on Recent Trends in Information Technology (NCIT 2015)*, pages 0975–8887.

- [70] Binu Paul, S Mridula, CK Aanandan, and P Mohanan. A new microstrip patch antenna for mobile communications and bluetooth applications. *Microwave and Optical technology letters*, 33(4):285–286, 2002.
- [71] Erhan Budak, Bulent Catay, Ibrahim Tekin, Husnu Yenigun, Mehmet Abbak, and Sergei Drannikov. Microstrip patch antenna for rfid applications. In *RFID Eurasia, 2007 1st Annual*, pages 1–3. IEEE, 2007.
- [72] Raied AR Ibrahim, Mustapha CE Yagoub, and Riadh WY Habash. Microstrip patch antenna for rfid applications. In *Electrical and Computer Engineering, 2009. CCECE'09. Canadian Conference on*, pages 940–943. IEEE, 2009.
- [73] Rida el Messari, José Carlos Reyes Guerrero, Otman el Mrabet, Abdellatif Medouri, and Luis Antonio Mariscal Rico. Broadband circular microstrip patch antenna for wimax marine application. *Instrumentation viewpoint*, (11):56–56, 2011.
- [74] Chien-Yuan Pan, Tzyy-Sheng Horng, Wen-Shan Chen, and Chien-Hsiang Huang. Dual wideband printed monopole antenna for wlan/wimax applications. *IEEE Antennas and Wireless Propagation Letters*, 6:149–151, 2007.
- [75] Heng Li, Zhen Chen, Liang Yong, and Stephen CW Kong. Application of integrated gps and gis technology for reducing construction waste and improving construction efficiency. *Automation in Construction*, 14(3):323–331, 2005.
- [76] E Alboni and M Cerretelli. Microstrip patch antenna for gps application. *Ancona, Italy*, pages 16–19, 2004.
- [77] D Orban and GJK Moernaut. The basics of patch antennas, updated. *RF Globalnet (www.rfglobalnet.com) newsletter*, 2009.
- [78] DC Nascimento and JC da S Lacava. Design of low-cost probe-fed microstrip antennas.
- [79] MANIK GUJRAL. *Bandwidth enhancement of dual patch microstrip antenna array using dummy EBG patterns on feedline*. PhD thesis, 2008.
- [80] Girish Kumar and KP Ray. *Broadband microstrip antennas*. Artech House, 2003.
- [81] Warren L Stutzman and William A Davis. Antenna theory. *Wiley Encyclopedia of Electrical and Electronics Engineering*, 1998.

- [82] Punit S Nakar. Design of a compact microstrip patch antenna for use in wireless/cellular devices. 2004.
- [83] Erik O Hammerstad. Equations for microstrip circuit design. In *Microwave Conference, 1975. 5th European*, pages 268–272. IEEE, 1975.
- [84] Inderjit Bahl and Prakash Bhartia. *Microstrip antennas*. Artech house, 1980.
- [85] Edgar J Denlinger. Losses of microstrip lines. *IEEE Transactions on Microwave Theory and Techniques*, 28(6):513–522, 1980.
- [86] Terry C Edwards and Michael B Steer. *Foundations for microstrip circuit design*. John Wiley & Sons, 2016.
- [87] Robert A Pucel. Design considerations for monolithic microwave circuits. *IEEE Transactions on microwave theory and techniques*, 29(6):513–534, 1981.
- [88] WF Richards. Microstrip antennas, chapter 10 in antenna handbook: Theory applications and design (yt lo and sw lee, eds.), 1988.
- [89] E Newman and Pravit Tulyathan. Analysis of microstrip antennas using moment methods. *IEEE Transactions on Antennas and Propagation*, 29(1):47–53, 1981.
- [90] RF HARRINGTON. Field computation by moment methods. *The Macmillan Comp.*, 130(6):276–280, 1968.
- [91] LV Kantorovich and GP Akilov. Functional analysis in normed spaces. translated from the russian by de brown. edited by ap robertson. international series of monographs in pure and applied mathematics, vol. 46, 1964.
- [92] John Dunlop. *Telecommunications engineering*. Routledge, 2017.
- [93] R Méjard, A Verdy, O Demichel, M Petit, L Markey, F Herbst, R Chassagnon, G Colas-des Francs, B Cluzel, and A Bouhelier. Advanced engineering of single-crystal gold nanoantennas. *Optical Materials Express*, 7(4):1157–1168, 2017.
- [94] Ibrahim Khan, Khalid Saeed, and Idrees Khan. Nanoparticles: Properties, applications and toxicities. *Arabian Journal of Chemistry*, 2017.
- [95] and others. Electric capacitor, March 28 1967. US Patent 3,311,801.
- [96] Alfred S Cummin and Jr Charles E Watts. Electric capacitor and method for making the same, May 24 1966. US Patent 3,252,830.

- [97] 1979.
- [98] Zulkifli Ahmad. Polymer dielectric materials. In *Dielectric material*. InTech, 2012.
- [99] Yuxing Ren and David CC Lam. Properties and microstructures of low-temperature-processable ultralow-dielectric porous polyimide films. *Journal of Electronic Materials*, 37(7):955–961, 2008.
- [100] Rao R Tummala, Eugene J Rymaszewski, and YC Lee. *Microelectronics packaging handbook*, 1989.
- [101] Vivek Ranjan, Liping Yu, Marco Buongiorno Nardelli, and Jerry Bernholc. Phase equilibria in high energy density pvdf-based polymers. *Physical review letters*, 99(4):047801, 2007.
- [102] Shu-Hui Xie, Bao-Ku Zhu, Ju-Biao Li, Xiu-Zhen Wei, and Zhi-Kang Xu. Preparation and properties of polyimide/aluminum nitride composites. *Polymer testing*, 23(7):797–801, 2004.
- [103] Lizhu Liu, Bing Liang, Wei Wang, and Qingquan Lei. Preparation of polyimide/inorganic nanoparticle hybrid films by sol–gel method. *Journal of composite materials*, 40(23):2175–2183, 2006.
- [104] Hongyan Li, Gang Liu, Bin Liu, Wei Chen, and Shoutian Chen. Dielectric properties of polyimide/al₂O₃ hybrids synthesized by in-situ polymerization. *Materials Letters*, 61(7):1507–1511, 2007.
- [105] CS Indulkar. *An introduction to electrical engineering materials*. S. Chand Publishing, 2008.
- [106] Anthony R Blythe and David Bloor. *Electrical properties of polymers*. Cambridge University Press, 2005.
- [107] JO Simpson and AK St Clair. Fundamental insight on developing low dielectric constant polyimides. *Thin Solid Films*, 308:480–485, 1997.
- [108] G Hougham, G Tesoro, A Viehbeck, and JD Chapple-Sokol. Polarization effects of fluorine on the relative permittivity in polyimides. *Macromolecules*, 27(21):5964–5971, 1994.
- [109] Robert J Young and Peter A Lovell. *Introduction to polymers*. CRC press, 2011.

- [110] Jose M Kenny and Marica Oplicki. Influence of the chemorheology of toughened epoxy matrices on the processing behavior of high performance composites. In *Macromolecular Symposia*, volume 68, pages 41–56. Wiley Online Library, 1993.
- [111] Soo-Jin Park, Ki-Sook Cho, and Sung-Hyun Kim. A study on dielectric characteristics of fluorinated polyimide thin film. *Journal of colloid and interface science*, 272(2):384–390, 2004.
- [112] G Nansé, E Papirer, P Fioux, F Moguet, and A Tressaud. Fluorination of carbon blacks: an x-ray photoelectron spectroscopy study: Iii. fluorination of different carbon blacks with gaseous fluorine at temperatures below 100 c influence of the morphology, structure and physico-chemical characteristics of the carbon black on the fluorine fixation. *Carbon*, 35(4):515–528, 1997.
- [113] PS Alegaonkar, AB Mandale, SR Sainkar, and VN Bhoraskar. Refractive index and dielectric constant of the boron and fluorine diffused polyimide. *Nuclear Instruments and Methods in Physics Research Section B: Beam Interactions with Materials and Atoms*, 194(3):281–288, 2002.
- [114] Yaw-Terng Chern and Chin-Min Huang. Synthesis and characterization of new polyimides derived from 4, 9-diaminodiamantane. *Polymer*, 39(25):6643–6648, 1998.
- [115] Peter Josef William Debye. *Polar molecules*. Chemical Catalog Company, Incorporated, 1929.
- [116] Kenneth S Cole and Robert H Cole. Dispersion and absorption in dielectrics i. alternating current characteristics. *The Journal of chemical physics*, 9(4):341–351, 1941.
- [117] DW Davidson and Robert H Cole. Dielectric relaxation in glycerine. *The Journal of Chemical Physics*, 18(10):1417–1417, 1950.
- [118] Graham Williams and David C Watts. Non-symmetrical dielectric relaxation behaviour arising from a simple empirical decay function. *Transactions of the Faraday society*, 66:80–85, 1970.
- [119] Stephen Havriliak and Stephen James Havriliak. *Dielectric and mechanical relaxation in materials: analysis, interpretation and application to polymers*. Hanser, 1997.

- [120] AA Lukichev. Graphical method for the debye-like relaxation spectra analysis. *Journal of non-crystalline solids*, 358(3):447–453, 2012.
- [121] Yōichi Ishida, Yūjirō Takada, and Motowo Takayanagi. Studies on dielectric properties of polyvinyl alcohol. *Colloid & Polymer Science*, 168(2):121–124, 1960.
- [122] David J Bergman and David Stroud. Physical properties of macroscopically inhomogeneous media. *Solid state physics*, 46:147–269, 1992.
- [123] J Hedrick, J Labadie, T Russell, D Hofer, and V Wakharker. High temperature polymer foams. *Polymer*, 34(22):4717–4726, 1993.
- [124] Muhammad Bisyrul Hafi Othman, Nicholas Ang Soon Ming, Hazizan Md Akil, and Zulkifli Ahmad. Dependence of the dielectric constant on the fluorine content and porosity of polyimides. *Journal of Applied Polymer Science*, 121(6):3192–3200, 2011.
- [125] JL Hedrick, KR Carter, JW Labadie, RD Miller, W Volksen, CJ Hawker, DY Yoon, TP Russell, JE McGrath, and RM Briber. Nanoporous polyimides. In *Progress in Polyimide Chemistry II*, pages 1–43. Springer, 1999.
- [126] Muhammad Bisyrul Hafi Othman, Mohamad Riduwan Ramli, Looi Yien Tyng, Zulkifli Ahmad, and Hazizan Md Akil. Dielectric constant and refractive index of poly (siloxane–imide) block copolymer. *Materials & Design*, 32(6):3173–3182, 2011.
- [127] Liming Tao, Haixia Yang, Jingang Liu, Lin Fan, and Shiyong Yang. Synthesis and characterization of highly optical transparent and low dielectric constant fluorinated polyimides. *Polymer*, 50(25):6009–6018, 2009.
- [128] Anindita Ghosh and Susanta Banerjee. Thermal, mechanical, and dielectric properties of novel fluorinated copoly (imide siloxane) s. *Journal of applied polymer science*, 109(4):2329–2340, 2008.
- [129] Chetan Singh Solanki. *Solar photovoltaics: fundamentals, technologies and applications*. PHI Learning Pvt. Ltd., 2015.
- [130] Wolfgang Fahrner. *Nanotechnology and nanoelectronics: materials, devices, measurement techniques*. Springer Science & Business Media, 2005.

- [131] Yasaman Hamedani, Prathyushakrishna Macha, Timothy J Bunning, Rajesh R Naik, and Milana C Vasudev. Plasma-enhanced chemical vapor deposition: Where we are and the outlook for the future. In *Chemical Vapor Deposition-Recent Advances and Applications in Optical, Solar Cells and Solid State Devices*. InTech, 2016.
- [132] Prosenjit Rai-Choudhury. *Handbook of microlithography, micromachining, and microfabrication: microlithography*, volume 1. Iet, 1997.
- [133] Dan Li and Younan Xia. Electrospinning of nanofibers: reinventing the wheel? *Advanced materials*, 16(14):1151–1170, 2004.
- [134] Andreas Greiner and Joachim H Wendorff. Electrospinning: a fascinating method for the preparation of ultrathin fibers. *Angewandte Chemie International Edition*, 46(30):5670–5703, 2007.
- [135] Xiaofeng Lu, Ce Wang, and Yen Wei. One-dimensional composite nanomaterials: Synthesis by electrospinning and their applications. *Small*, 5(21):2349–2370, 2009.
- [136] Jun-Chuan Wang, Ming-Wei Chang, Zeeshan Ahmad, and Jing-Song Li. Fabrication of patterned polymer-antibiotic composite fibers via electrohydrodynamic (ehd) printing. *Journal of Drug Delivery Science and Technology*, 35:114–123, 2016.
- [137] Cynthia A Volkert and Andrew M Minor. Focused ion beam microscopy and micromachining. *MRS bulletin*, 32(5):389–399, 2007.
- [138] Paul Richard Munroe. The application of focused ion beam microscopy in the material sciences. *Materials characterization*, 60(1):2–13, 2009.
- [139] D McMullan. An improved scanning electron microscope for opaque specimens. *Proceedings of the IEE-Part II: Power Engineering*, 100(75):245–256, 1953.
- [140] M Von Ardenne. The scanning electron microscope. theoretical fundamentals. *Z. Phys*, 109:553–572, 1938.
- [141] M Von Ardenne. Improvements in electron microscopes. *GB patent*, 511204, 1937.

- [142] Brian C Smith. *Fundamentals of Fourier transform infrared spectroscopy*. CRC press, 2011.
- [143] Ftir spectroscopy (fourier transform infrared). online available at <https://chemistry.oregonstate.edu/courses/ch361-464/ch362/irinstrs.htm>, 2017. Accessed [03.01.2018].
- [144] Dieter K Schroder. *Semiconductor material and device characterization*. John Wiley & Sons, 2006.
- [145] Joseph F White. *High Frequency Techniques: An Introduction to RF and Microwave Design and Computer Simulation*. John Wiley & Sons, 2004.
- [146] Joseph F White. *Microwave semiconductor engineering*. Springer Science & Business Media, 2012.
- [147] Mohamed Ismaeel Maricar. Design of circuits to enhances the performace of high frequency planar gunn diodes. 2014.
- [148] David M Pozar. *Microwave engineering*. John Wiley & Sons, 2009.
- [149] Agilent Technologies. *Agilent De-embedding and Embedding S-Parameter Networks Using a Vector Network Analyzer*. Agilent Technologies, may 2004.
- [150] Kenneth Rasmussen. *Measuring the S-Parameters of a 50 to 75 Ohm impedance matching device using the Vector Network Analyzer ZVA*. Rohde & Schwarz, 03 2009.
- [151] Eric Strid. Planar impedance standards and accuracy considerations in vector network analysis. In *ARFTG Conference Digest-Spring, 27th ARFTG*, volume 9, pages 159–166. IEEE, 1986.
- [152] Anritsu. Understanding vna calibration, 2012.
- [153] Andrea Ferrero and Umberto Pisani. Two-port network analyzer calibration using an unknown'thru'. *IEEE Microwave and Guided Wave Letters*, 2(12):505–507, 1992.
- [154] H-J Eul and B Schiek. Thru-match-reflect: One result of a rigorous theory for de-embedding and network analyzer calibration. In *Microwave Conference, 1988. 18th European*, pages 909–914. IEEE, 1988.

- [155] Keith Jones and Eric Strid. Where are my on-wafer reference planes? In *ARFTG Conference Digest-Winter, 30th*, volume 12, pages 27–40. IEEE, 1987.
- [156] Wei-Kung Deng and Tah-Hsiung Chu. A three-port vector network analyzer-measurement system, calibration and results. In *Microwave Symposium Digest, 2001 IEEE MTT-S International*, volume 3, pages 1531–1534. IEEE, 2001.
- [157] Theodore J Reck, Lihan Chen, Chunhu Zhang, Alex Arsenovic, Christopher Groppi, Arthur Lichtenberger, Robert M Weikle, and N Scott Barker. Micromachined probes for submillimeter-wave on-wafer measurements—part ii: Rf design and characterization. *IEEE Transactions on Terahertz Science and Technology*, 1(2):357–363, 2011.
- [158] Cosan Caglayan, Georgios C Trichopoulos, and Kubilay Sertel. On-wafer device characterization with non-contact probes in the thz band. In *Antennas and Propagation Society International Symposium (APSURSI), 2013 IEEE*, pages 1134–1135. IEEE, 2013.
- [159] Georgios C Trichopoulos, H Lee Mosbacker, Don Burdette, and Kubilay Sertel. A broadband focal plane array camera for real-time thz imaging applications. *IEEE Transactions on Antennas and Propagation*, 61(4):1733–1740, 2013.
- [160] Doug Rytting. Network analyzer error models and calibration methods. *White Paper, September*, 1998.
- [161] Ken Wong. Uncertainty analysis of the weighted least squares vna calibration. In *Microwave Measurements Conference, Fall 2004. 64th ARFTG*, pages 23–31. IEEE, 2004.
- [162] Derrick Dean. Thermal gravimetric analysis. online available. Accessed [03.01.2018].
- [163] Douglas A Skoog, F James Holler, and Stanley R Crouch. *Principles of instrumental analysis*. Cengage learning, 2017.
- [164] Principle of differential scanning calorimetry (dsc). online available at <https://www.hitachi-hightech.com/global/products/science/tech/ana/thermal/descriptions/> 2017. Accessed [03.01.2018].
- [165] Differential scanning calorimetry (dsc) thermal analysis. online available at <http://www.andersonmaterials.com/dsc.html>, 2017. Accessed [03.01.2018].

- [166] Amal Elkordy. *Application of Calorimetry in a Wide Context-Differential Scanning Calorimetry, Isothermal Titration Calorimetry and Microcalorimetry*. In-Tech, 2013.
- [167] Muhammad Talha Khan and Syed Muzamil Ali. A brief review of measuring techniques for characterization of dielectric materials. *International Journal of Information Technology and Electrical Engineering*, 1(1), 2012.
- [168] Kubík Zdeněk, Nikolayev Denys, Karban Pavel, Skála Jiří, and Hromádka Miroslav. Optimization of electrical properties of parallel plate antenna for emc testing. *Journal of Computational and Applied Mathematics*, 270:283–293, 2014.
- [169] RN Clarke, AP Gregory, D Cannell, M Patrick, S Wylie, I Youngs, and G Hill. A guide to the characterisation of dielectric materials at rf and microwave frequencies. *Institute of Measurement and Control/National Physical Laboratory*, 2003.
- [170] Keysight Technologies. Split post dielectric resonators for dielectric measurements of substrates, August 2014.
- [171] J Krupka, RN Clarke, OC Rochard, and AP Gregory. Split post dielectric resonator technique for precise measurements of laminar dielectric specimens-measurement uncertainties. In *Microwaves, Radar and Wireless Communications. 2000. MIKON-2000. 13th International Conference on*, volume 1, pages 305–308. IEEE, 2000.
- [172] Andreas Schönhals and F Kremer. Analysis of dielectric spectra. In *Broadband dielectric spectroscopy*, pages 59–98. Springer, 2003.
- [173] Jovan Mijovic and Benjamin D Fitz. Dielectric spectroscopy of reactive polymers. *Mater. Sci*, 2(5):1531–9, 1998.
- [174] Jan Leys. Broadband dielectric spectroscopy of confined liquid crystals and hydrogen bonded liquids. 2007.
- [175] Dominic Charles Prime. Switching mechanisms, electrical characterisation and fabrication of nanoparticle based non-volatile polymer memory devices. 2010.
- [176] Cheng-Liang Liu, Jung-Ching Hsu, Wen-Chang Chen, Kenji Sugiyama, and Akira Hirao. Non-volatile memory devices based on polystyrene derivatives with electron-donating oligofluorene pendent moieties. *ACS applied materials & interfaces*, 1(9):1974–1979, 2009.

- [177] Saleem Khan, Leandro Lorenzelli, and Ravinder S Dahiya. Technologies for printing sensors and electronics over large flexible substrates: a review. *IEEE Sensors Journal*, 15(6):3164–3185, 2015.
- [178] Kazem Nazari, Eleni Kontogiannidou, Rita Haj Ahmad, Dimitrios Andreadis, Manoochehr Rasekh, Nikolaos Bouropoulos, Susanna M van Der Merwe, Ming-Wei Chang, Dimitrios G Fatouros, and Zeeshan Ahmad. Fibrous polymeric buccal film formulation, engineering and bio-interface assessment. *European Polymer Journal*, 97:147–157, 2017.
- [179] Sabine Enders, Heike Kahl, and Jochen Winkelmann. Surface tension of the ternary system water+ acetone+ toluene. *Journal of Chemical & Engineering Data*, 52(3):1072–1079, 2007.
- [180] M Yahya, HV Lee, SK Zain, and SB Abd Hamid. Chemical conversion of palm-based lignocellulosic biomass to nano-cellulose. *Polymers Research Journal*, 9(4):385, 2015.
- [181] JV Gulmine, PR Janissek, HM Heise, and L Akcelrud. Polyethylene characterization by ftir. *Polymer Testing*, 21(5):557–563, 2002.
- [182] Koay Seong Chun, Salmah Husseinsyah, and Hakimah Osman. Utilization of cocoa pod husk as filler in polypropylene biocomposites: effect of maleated polypropylene. *Journal of Thermoplastic Composite Materials*, 28(11):1507–1521, 2015.
- [183] RD Mathad, HG Harish Kumar, B Sannakki, S Ganesh, KSS Sarma, and MV Badiger. High energy electron irradiation effects on polystyrene films. *Radiation Effects & Defects in Solids*, 164(10):656–664, 2009.
- [184] S Ramesh, Koay Hang Leen, K Kumutha, and AK Arof. Ftir studies of pvc/pmma blend based polymer electrolytes. *Spectrochimica Acta Part A: Molecular and Biomolecular Spectroscopy*, 66(4-5):1237–1242, 2007.
- [185] Meenashi Subramani and Umamaheswari Sepperumal. Ftir analysis of bacterial mediated chemical changes in polystyrene foam. *Ann. Biol. Res.*, 7(5):55–61, 2016.
- [186] Adan-Yovani León-Bermúdez and Ramiro Salazar. Synthesis and characterization of the polystyrene-asphaltene graft copolymer by ft-ir spectroscopy. *CT&F-Ciencia, Tecnología y Futuro*, 3(4):157–167, 2008.

- [187] WT Tan, MM Radhi, MZB Ab Rahman, and AB Kassim. Synthesis and characterization of grafted polystyrene with acrylonitrile using gamma-irradiation. *Applied Sciences*, 10:139–144, 2010.
- [188] Heartwin A Pushpadass, Robert W Weber, Joseph J Dumais, and Milford A Hanna. Biodegradation characteristics of starch–polystyrene loose-fill foams in a composting medium. *Bioresource technology*, 101(19):7258–7264, 2010.
- [189] Chen Huang, Haitao Niu, Jinglei Wu, Qinfei Ke, Xiumei Mo, and Tong Lin. Needleless electrospinning of polystyrene fibers with an oriented surface line texture. *Journal of nanomaterials*, 2012:7, 2012.
- [190] D Braun. Thermal degradation of polyvinyl chloride. *Pure and Applied Chemistry*, 26(2):173–192, 1971.
- [191] M Blazso, B Zelei, and E Jakab. Thermal decomposition of low-density polyethylene in the presence of chlorine-containing polymers. *Journal of analytical and applied pyrolysis*, 35(2):221–235, 1995.
- [192] A-HI Mourad, Rania O Akkad, AA Soliman, and TM Madkour. Characterisation of thermally treated and untreated polyethylene–polypropylene blends using dsc, tga and ir techniques. *Plastics, Rubber and Composites*, 38(7):265–278, 2009.
- [193] Qingliang He, Tingting Yuan, Suying Wei, and Zhanhu Guo. Catalytic and synergistic effects on thermal stability and combustion behavior of polypropylene: influence of maleic anhydride grafted polypropylene stabilized cobalt nanoparticles. *Journal of Materials Chemistry A*, 1(42):13064–13075, 2013.
- [194] Arturo Salazar Avalos, Minna Hakkarainen, and Karin Odelius. Superiorly plasticized pvc/pbsa blends through crotonic and acrylic acid functionalization of pvc. *Polymers*, 9(3):84, 2017.
- [195] Zhi Ping Xu, Susanta K Saha, Paul S Braterman, and Nandika D’Souza. The effect of zn, al layered double hydroxide on thermal decomposition of poly (vinyl chloride). *Polymer degradation and stability*, 91(12):3237–3244, 2006.
- [196] Jiezhao Xiao, Zhengbo Zhang, and Jin Nie. Preparation, characterization and catalytic activity of polystyrene with pendent perfluoroalkylsulfonylimide groups. *Journal of Molecular Catalysis A: Chemical*, 236(1-2):119–124, 2005.

- [197] Hou Xuemei and Ying Hao. Fabrication of polystyrene/detonation nanographite composite microspheres with the core/shell structure via pickering emulsion polymerization. *Journal of Nanomaterials*, 2013:8, 2013.
- [198] Abdullah Ashraf. Thermal analysis of polymers (ldpe, hdpe) by differential scanning calorimetry technique. December 2014.
- [199] Cheng-Fang Ou. The crystallization characteristics of polypropylene and low ethylene content polypropylene copolymer with copolyesters. *European Polymer Journal*, 38(3):467–473, 2002.
- [200] Hitachi. Dsc measurement of polypropylene. Technical report, HitachiHigh-Tech Science Corporation, August 2008.
- [201] SADDYS RODRÍGUEZ-LLAMAZARES et al. Polypropylene/starch blends: Study of thermal and morphological properties. *Journal of the Chilean Chemical Society*, 58(1):1643–1646, 2013.
- [202] Hye Been Pyeon, Jeong Eon Park, and Dong Hack Suh. Non-phthalate plasticizer from camphor for flexible pvc with a wide range of available temperature. *Polymer Testing*, 63:375–381, 2017.
- [203] Teng-Chun Yang, Takafumi Noguchi, Minoru Isshiki, and Jyh-Horng Wu. Effect of titanium dioxide on chemical and molecular changes in pvc sidings during quv accelerated weathering. *Polymer Degradation and Stability*, 104:33–39, 2014.
- [204] Rui-Ying Bao, Wei Yang, Zheng-Ying Liu, Bang-Hu Xie, and Ming-Bo Yang. Polymorphism of a high-molecular-weight racemic poly (l-lactide)/poly (d-lactide) blend: effect of melt blending with poly (methyl methacrylate). *RSC Advances*, 5(25):19058–19066, 2015.
- [205] Huajie Yin, Pavel Chapala, Maxim Bermeshev, Andreas Schonhals, and Martin Bohning. Molecular mobility and physical aging of a highly permeable glassy polynorbornene as revealed by dielectric spectroscopy. *ACS Macro Letters*, 6(8):813–818, 2017.
- [206] T Seghier and F Benabed. Dielectric proprieties determination of high density polyethylene (hdpe) by dielectric spectroscopy. *J. Materi., Mecha. and Manufac.*, 3(2):121–124, 2015.

- [207] Abdelkader Kahouli, Olivier Gallot-Lavallée, Pascal Rain, Olivier Lesaint, Laurent Heux, Christophe Guillermin, and Jean-Marc Lupin. Structure effect of thin film polypropylene view by dielectric spectroscopy and x-ray diffraction: Application to dry type power capacitors. *Journal of Applied Polymer Science*, 132(39), 2015.
- [208] A Arbe, A Moral, A Alegria, J Colmenero, W Pyckhout-Hintzen, D Richter, B Farago, and B Frick. Heterogeneous structure of poly (vinyl chloride) as the origin of anomalous dynamical behavior. *The Journal of chemical physics*, 117(3):1336–1350, 2002.
- [209] Jin Liu, Hanzheng Guo, Xinchang Pang, Xiaoli Tan, Mufit Akinc, Zhiqun Lin, and Nicola Bowler. Dynamics of polystyrene-block-poly (methylmethacrylate) (ps-b-pmma) diblock copolymers and ps/pmma blends: A dielectric study. *Journal of Non-Crystalline Solids*, 359:27–32, 2013.
- [210] A Wypych, E Duval, G Boiteux, J Ulanski, L David, G Seytre, A Mermet, I Stevenson, M Kozanecki, and L Okrasa. Physical aging of atactic polystyrene as seen by dielectric relaxational and low-frequency vibrational raman spectroscopies. *Journal of non-crystalline solids*, 351(33-36):2593–2598, 2005.
- [211] James Baker-Jarvis, Richard G Geyer, Chriss A Grosvenor, Christopher L Holloway, Michael D Janezic, Robert T Johk, P Kabos, and James Baker-Jarvis. *Measuring the permittivity and permeability of lossy materials: Solids, liquids, metals, building materials, and negative-index materials*. 2005.
- [212] Sen Yan. Metamaterial design and its application for antennas. 2015.
- [213] Peng Jin and Richard W Ziolkowski. High-directivity, electrically small, low-profile near-field resonant parasitic antennas. *IEEE Antennas and Wireless Propagation Letters*, 11:305–309, 2012.
- [214] Fei-Fei Zhang, Bao-Hua Sun, Xiaohui Li, Wei Wang, and Jin-Yuan Xue. Design and investigation of broadband monopole antenna loaded with non-foster circuit. *Progress In Electromagnetics Research C*, 17:245–255, 2010.
- [215] Randy Bancroft. Fundamental dimension limits of antennas. *Centurion Wireless Technologies*, pages 1–14, 2002.
- [216] S Best. Optimization of the bandwidth of electrically small planar antennas. In *Antenna Applications Symposium, Allerton Park, Monticello, IL*, 2009.

- [217] Yu Yu Kyi and Jian-Ying Li. Analysis of electrically small size conical antennas. *Progress In Electromagnetics Research Letters*, 1:85–92, 2008.
- [218] ROGERS CORPORATION. Rt/duroid ® 5870 /5880 high frequency laminates.
- [219] KC Gupta and P Garg. Barl. i. and bhartia, p., " microstrip lines and slotlines", arhech house, 1996.
- [220] Chong Li, Ata Khalid, Sonia H Paluchowski Caldwell, Martin C Holland, Geoff M Dunn, Iain G Thayne, and David RS Cumming. Design, fabrication and characterization of in 0.23 ga 0.77 as-channel planar gunn diodes for millimeter wave applications. *Solid-State Electronics*, 64(1):67–72, 2011.
- [221] Mohamed Ismaeel Maricar, James Glover, Gwynne Evans, Ata-ul-Habib Khalid, David Cumming, and Chris Oxley. Design and characterization of a novel diamond resonator. *Microwave and Optical Technology Letters*, 56(7):1691–1693, 2014.
- [222] RC Hansen. Q and bandwidth of electrically small antennas. *Microwave and Optical Technology Letters*, 49(5):1170–1171, 2007.
- [223] Javad N Farahani, Hans-Jürgen Eisler, Dieter W Pohl, Michaël Pavius, Philippe Flückiger, Philippe Gasser, and Bert Hecht. Bow-tie optical antenna probes for single-emitter scanning near-field optical microscopy. *Nanotechnology*, 18(12):125506, 2007.
- [224] Alberto G Curto, Giorgio Volpe, Tim H Taminiau, Mark P Kreuzer, Romain Quidant, and Niek F van Hulst. Unidirectional emission of a quantum dot coupled to a nanoantenna. *Science*, 329(5994):930–933, 2010.
- [225] TH Taminiau, FD Stefani, FB Segerink, and NF Van Hulst. Optical antennas direct single-molecule emission. *Nature Photonics*, 2(4):234–237, 2008.
- [226] AA Lestari, AG Yarovoy, and LP Ligthart. An efficient ultra-wideband bow-tie antenna. In *Microwave Conference, 2001. 31st European*, pages 1–4. IEEE, 2001.
- [227] Ben Allen, Mischa Dohler, Ernest Okon, Wasim Malik, Anthony Brown, and David Edwards. *Ultra wideband antennas and propagation for communications, radar and imaging*. John Wiley & Sons, 2006.

- [228] Yan-Lin Chen, Cheng-Li Ruan, and Lin Peng. A novel ultra-wideband bow-tie slot antenna in wireless communication systems. *Progress In Electromagnetics Research Letters*, 1:101–108, 2008.
- [229] Katsuki Kiminami, Akimasa Hirata, and Toshiyuki Shiozawa. Double-sided printed bow-tie antenna for uwb communications. *IEEE Antennas and Wireless Propagation Letters*, 1(3):152–153, 2004.
- [230] Manas Sarkar, Santanu Dwari, and Anitha Daniel. Compact printed monopole antenna for ultra-wideband application with dual band-notched characteristic. *Microwave and Optical Technology Letters*, 55(11):2595–2600, 2013.
- [231] Andrea Alu and Nader Engheta. Tuning the scattering response of optical nanoantennas with nanocircuit loads. *Nature photonics*, 2(5):307–310, 2008.
- [232] Andrea Alù and Nader Engheta. Input impedance, nanocircuit loading, and radiation tuning of optical nanoantennas. *Physical review letters*, 101(4):043901, 2008.
- [233] Andrea Alù and Nader Engheta. A hertzian plasmonic nanodimer as an efficient optical nanoantenna. *arXiv preprint arXiv:0807.1783*, 2008.
- [234] Hongcang Guo, Todd P Meyrath, Thomas Zentgraf, Na Liu, Liwei Fu, Heinz Schweizer, and Harald Giessen. Optical resonances of bowtie slot antennas and their geometry and material dependence. *Optics express*, 16(11):7756–7766, 2008.
- [235] Ranjan Singh, Carsten Rockstuhl, Christoph Menzel, Todd P Meyrath, Mingxia He, Harald Giessen, Falk Lederer, and Weili Zhang. Spiral-type terahertz antennas and the manifestation of the mushroom principle. *Optics express*, 17(12):9971–9980, 2009.
- [236] Davide Ramaccia, Filiberto Bilotti, Alessandro Toscano, Alessandro Massaro, and Roberto Cingolani. Electrical and radiation properties of a horn nanoantenna at near infrared frequencies. In *Antennas and Propagation (APSURSI), 2011 IEEE International Symposium on*, pages 2407–2410. IEEE, 2011.
- [237] Aiping Zeng, Victor F Neto, Jose J Gracio, and Qi Hua Fan. Diamond-like carbon (dlc) films as electrochemical electrodes. *Diamond and Related Materials*, 43:12–22, 2014.

- [238] S Khatir, A Hirose, and C Xiao. Coating diamond-like carbon films on polymer substrates by inductively coupled plasma assisted sputtering. *Surface and Coatings Technology*, 253:96–99, 2014.
- [239] John Robertson. Diamond-like amorphous carbon. *Materials Science and Engineering: R: Reports*, 37(4-6):129–281, 2002.
- [240] L Anne Thomson, Frances C Law, Neil Rushton, and J Franks. Biocompatibility of diamond-like carbon coating. *Biomaterials*, 12(1):37–40, 1991.
- [241] Alfred Grill. Diamond-like carbon: state of the art. *Diamond and related materials*, 8(2-5):428–434, 1999.
- [242] Shailesh Raut and Aldo Petosa. A compact printed bowtie antenna for ultra-wideband applications. In *Microwave Conference, 2009. EuMC 2009. European*, pages 081–084. IEEE, 2009.
- [243] HaiWen Liu, Hao Jiang, Xuehui Guan, JiuHuai Lei, and Shen Li. Single-feed slotted bowtie antenna for triband applications. *Antennas and Wireless Propagation Letters, IEEE*, 12:1658–1661, 2013.
- [244] A Thabet, Adel Z El Dein, and A Hassan. Design of compact microstrip bandpass filter by using new nano-composite materials. In *Nanoelectronics Conference (INEC), 2011 IEEE 4th International*, pages 1–2. IEEE, 2011.